Impact of Damages on the Stability and Reliability of Pattern-Placed Revetments

M.Sc. Thesis

N. van der Vegt

Technische Universiteit Delft

TU Delft Delft University of Technology

Challenge the future

Cover:
A Basalton revetment on a dike along the river IJssel in Kampen

Impact of Damages on the Stability and Reliability of Pattern-Placed Revetments

by

N. (Niels) van der Vegt

to obtain the degree of Master of Science
at the Delft University of Technology,
to be defended publicly on Friday October 8, 2021 at 16:00.

Department of Hydraulic Engineering
Faculty of Civil Engineering and Geosciences
Delft University of Technology

Version: Final (01-10-21)
Student number: 4956656

Graduation Committee:

Chairman:	
Dr. ir. B. Hofland	Delft University of Technology
Daily supervisor:	
Ir. W. J. Klerk	Delft University of Technology
Other members:	
Dr. ir. D. J. Peters	Delft University of Technology
Prof. dr. ir. M. R. A. Van Gent	Delft University of Technology

TU Delft

Preface

This study represents the conclusion of my Master Hydraulic Engineering at the TU Delft. Over the past year, I have enjoyed working on this study, resulting in a report of which I am proud. However, I could never have done this entirely on my own, so I would like to thank the following people:

First of all, I would like to thank my committee: Bas Hofland, Dirk Jan Peters, Marcel van Gent, and Wouter Jan Klerk. Thank you for your time to give me feedback and guidance. I really enjoyed working with you all. A special thanks to my daily supervisor Wouter Jan, thank you for your enthusiasm and your time to guide me throughout the process.

I would like to thank Deltares and Mark Klein Breteler for providing data on the old flume experiments. I would also like to thank the pavement engineering section for hosting my models on their High-Performance Computer (HPC), and in particular, Cor Kasbergen, who has arranged access to the HPC.

Finally, I would like to thank my family and friends who always supported me. Without your support, I would never have come this far.

Niels van der Vegt
Kampen, September 2021

Abstract

Over time, degradation processes might cause damage to pattern-placed revetments. Examples of such damages are missing elements, deformation, and the loss of joint filling. Little is known about the exact consequences of those damages. Therefore, when damage is observed during an inspection, it is estimated based upon experience what the possible consequences are and when a maintenance intervention is planned. If the consequences are misjudged, this will lead to one of the following two scenarios:

1. The consequences of the damage are believed to be more significant than they are. This results in an immediate maintenance intervention and causes more costs to be made.
2. The consequences of the damage are believed to be less significant than they are. This results in postponement of the maintenance intervention to a moment when large maintenance is executed. Consequentially, the hinterland may temporarily be exposed to a larger flood risk than required by law.

Better insight into the exact consequences of damages will expand the possibilities of how risk-based maintenance can be used to maintain revetments. Consequentially, maintenance interventions can be planned more efficiently, reducing the societal costs incurred due to the two described scenarios. This study contributes to this topic by investigating whether it is possible to estimate the impact of damages on the stability and reliability of a revetment using a model.

First, a qualitative analysis of the different types of damage for a pattern-placed revetment is done to obtain an overview of the most common damages. Within this analysis, all damages are related to root causes, and the impact on the stability is analyzed. Based on the results, it is concluded that missing elements and deformation can initiate positive feedback loops. These damages are able to affect their own root causes, resulting in a faster progression of the damage when the intensity of the damage becomes larger.

Subsequently, data of old flume experiments with Basalton and basalt revetments are analyzed to study and quantify damages to implement the damages within the model. This analysis focused on the uplift of elements, deformation around the wave impact zone (S-profile), and washed-out joint filling. For the studied revetments, the data showed that most elements were uplifted due to wave impact and that most joint filling is washed-out around the wave impact zone. Finally, the S-profile has been parameterized, and equations are derived to estimate the location and the width. Analysis showed that most elements were uplifted from the hump of the S-profile, which indicates that this is a weak spot.

Next, a finite element model (FE-model) is created to simulate the wave impact on pattern-placed revetments. The main focus of the FE-model is to study the uncertainty due to structural changes, which are the damages. To achieve this, a script is created which allows for fully automatic generation of a finite element model (FE-model) of a pattern-placed revetment based upon a predetermined set of parameters. The damages quantified during the analysis of the flume experiments are also included in order to be able to assess damaged revetments. We think an FE-model as developed within this study may be a valuable tool next to flume experiments that allow for a quick evaluation of different scenarios. Three types of damage are included and assessed with the FE-model: deformation (S-profile), reduced clamping (washed-out joint filling), and a missing element. For deformation, it is assumed that the migration of the filter material solely causes the S-profile. Therefore, a varying leakage length as a function of the slope coordinate is introduced within the FE-model to model the effect of the varying filter layer thickness on the filter response. Based on the analysis of the different damages, it was found that an S-profile has the most significant impact on the stability of top layer elements during wave loading, followed by a revetment without joint filling. Furthermore, the analysis showed that a missing element has relatively little impact. Important to note is that the analysis of a missing element only resembles

the case in which an element is removed caused by vandalism or woody vegetation.

The final part of the study uses the FE-model within a sensitivity analysis to study the most important uncertain parameters. The results show that the dimensionless loading and the dimensionless leakage length are the most important parameters. Furthermore, the sensitivity analysis shows that the reduced stability caused by deformation primarily results from an increase in loading under the hump of the S-profile. This increase in loading happens because the filter material migrates, increasing the layer thickness under the hump and changing the leakage length. Based on the samples used in the sensitivity analysis, response surfaces are fitted to obtain a model that can predict the damage for any set of parameters. With those models, the impact of the leakage length and Iribarren number on the stability number is studied. For a typical column-type pattern-placed revetment under wind wave loading, the stability number is expected to decrease 25% to 50% for a deformed revetment. For no joint filling about 25%, and for a missing element 0% up to 25% depending on the leakage length. Finally, a case study of a coastal dike near Den Helder is done to assess the impact of damages on the failure probability. For small deformations, an increase of 10^1 – 10^2 of the failure probability has been observed, while for medium to large deformations, the failure probability is 10^3 – 10^4 times increased. For no joint filling or a missing element, an increase of the failure probability of 10^1 – 10^2 is observed.

This study showed that it is possible to create a finite element model that can estimate the impact damage has on the stability and reliability of a pattern-placed revetment. The obtained results can be used within the daily practice as part of risk-based maintenance as the study provides a way to obtain a first indication of the impact of missing elements, deformation, and washed-out joint filling. Additionally, the developed methodology can be used to obtain the impact of other types of damage. Although Basalton is the primarily investigated type of top layer, analysis of the flume experiments showed that basalt revetments are subject to identical types of damage. Therefore, it is expected that the findings within this study can be applied to a broader range of top layer elements with similar characteristics to Basalton (e.g. basalt, C-Star, and Hydroblocks).

Contents

List of Symbols

Symbol	Definition	Unit
a_s	Amplitude of the S-profile	[m]
B	Width of an element	[m]
B_m	Width of the model	[sets]
B_s	Width of the S-profile	[m]
$B_{s;hump}$	Width of the hump of the S-profile	[m]
$B_{s;trough}$	Width of the trough of the S-profile	[m]
b	Thickness of the filter layer	[m]
D	Thickness of the top layer	[m]
d	Water depth	[m]
E_e	Young's modulus of top layer elements	[Pa]
g	Gravitational acceleration	[m/s^2]
$H_{2\%}$	Wave height exceeded by 2% of the waves	[m]
H_b	Breaking wave height	[m]
H_{m0}	Spectral wave height	[m]
H_s & $H_{1/3}$	Significant wave height	[m]
i_{st}	Storm intensity	[-]
k	Permeability of the filter	[m/s]
k'	Permeability of the top layer	[m/s]
L_{0p}	Deep water peak wave length	[m]
n	Number of waves	[-]
$P_{max;2\%}$	Pressure exceeded by 2% of the wave impacts	[Pa]
$R_{d;2\%}$	2% Exceedance run-down height of irregular waves	[m]
s_{0p}	Offshore peak wave steepness	[m]
T_p	Peak period	[s]
U_e	Washed-out joint filling	[m]
z_{bot}	Bottom of the revetment	[mREF]
z_{top}	Top of the revetment	[mREF]
α	Angle of the revetment slope	[°]
γ	Breaker index	[-]
γ_B	S-profile width coefficient	[-]
γ_z	S-profile location coefficient	[-]
Δ	Relative density of the top layer	[-]
Λ	Leakage length	[m]
μ_e	Coefficient of friction between elements	[-]
μ_f	Coefficient of friction between elements and filter	[-]
ν_e	Poisson ratio of the top layer elements	[kg/m^3]
$\xi_{m-1,0}$	Iribarren number based on H_{m0} and $T_{m-1,0}$	[-]
ξ_{op}	Iribarren number for the offshore peak conditions	[-]
ρ_e	Mass density of the top layer elements	[kg/m^3]
ρ_w	Mass density of water	[kg/m^3]
Φ_F	Hydraulic head in the filter layer	[m]
Φ_T	Hydraulic head on the top layer	[m]

1

Introduction

1.1. Background

With more than 17,500 kilometers of flood protection in the Netherlands, dikes have become an essential part of the Dutch landscape. The construction of dikes has been a craft practiced since the seventh century. Since then, people have tried to find ways to determine how to shape dikes in order to prevent flooding of the hinterland. Back in the day, the typical way to determine the height of a dike was to look at previous storms and adjust the crest height of the dike such that it was a bit higher than the observed water level. During the first part of the 20th century, dikes often were raised 0.5 – 1.0 meters above the highest observed or measured water level (TAW, 1989b).

After the floods in Zeeland in 1953, the first Delta Committee is installed. Their goal was to advise the government which measures were required to prevent a flood as in 1953 from happening again. One of the findings of the committee is that there is some regularity in the water level. Consequentially, this opens the possibility to describe the water level using statistics and led to the introduction of the 'delta height' in the Deltawet of 1958 (Delta Committee, 1960. The newly introduced DeltaWet then required dikes to withstand a predetermined extreme storm event. The delta height was determined for each dike ring and is based on a cost-benefit analysis of the hinterland resulting in exceedance probabilities varying from 1/1.250 for dike rings along the IJssel to 1/10.000 for dike rings in Noord-Holland at the coast (Rijksoverheid, 1958).

In 2017, new standards were introduced with the Water Act (Waterwet) (Rijksoverheid, 2017). For each dike trajectory, a target probability of failure is derived based on individual risk, group risk, and a cost-benefit analysis of the hinterland. In addition, the new method also requires all uncertainties to be considered when assessing a dike trajectory (STOWA, 2021). The main difference with the preceding standards is the definition of failure. Whereas with the preceding standards, dikes were assessed based upon the exceedance of critical hydraulic loading conditions, the new method assesses based upon flooding of a dike trajectory (Kok et al., 2016).

Once every 12 years, all dikes in the Netherlands are comprehensively assessed. Between those assessments, the manager of the dike trajectory is required to maintain the dike so that it continues to meet the safety standard by the 'Duty of Care for Primary Flood Defences' (Zorgplicht Primaire Waterkeringen), hereafter called 'duty of care' (Ministerie van Infrastructuur en Milieu, 2015). In order to maintain the dike efficiently, risk-based maintenance is used to strategically plan inspections and prioritize maintenance interventions of damages based on the impact it has on the probability of failure (Faber, 2002). However, often the impact of damage is unknown, and thus judgment is based upon experience. Therefore, to make more efficient use of risk-based maintenance, the impact of damage needs to be better understood and quantified.

1.2. Problem Statement

This study focuses on damaged pattern-placed revetments located on the outer slope of a dike. The primary purpose of pattern-placed revetments is to protect the outer slope against erosion caused by either flow or wave loading. Additionally, sometimes revetments are also made rougher to reduce overtopping (Schiereck and Verhagen, 2019). In the Netherlands, pattern-placed revetments are commonly used as revetments for dikes under wave loading and are a common sight along the IJsselmeer, estuaries, and the coast. Within this study, the impact damage has on a pattern-placed revetment under wave loading is investigated. A few examples of possible types of damage are shown in Figure 1.1.

Figure 1.1: Damaged pattern-placed revetments, left: a missing element, right: washed-out joint filling (Waterschapshuis, 2019)

In order to efficiently maintain the dike with the use of risk-based maintenance, the consequences of damage should be clear. However, this is currently not the case for pattern-placed revetments on dikes. As a result, when during inspection damage is observed, the consequences are estimated based on experience. If the consequences are misjudged, this will lead to inefficient maintenance and, therefore to one of the following two undesirable scenarios:

1. Overestimation of the impact of the damage
2. Underestimation of the impact of the damage

In the first scenario, the consequences of the observed damage are overestimated. This will result in the manager believing that the consequences of the damage are more severe than they are. As a result, a maintenance intervention with a high priority is planned instead of postponing the intervention for the next major round of maintenance. By prioritizing and therefore planning additional maintenance interventions, more costs will be made. In the second scenario, the consequences of the observed damage are underestimated. This will result in the manager believing that the consequences of the damage are less severe than they are. In this case, the manager assumes the dike still fulfills the requirements and will likely include the maintenance intervention in the next major round of maintenance. In reality, the dike trajectory will have a higher probability of failure than the manager believes and may expose the hinterland to a higher probability of flooding than required by the Water Act.

At the moment of this study, no scientific insight is available into the impact damage has on pattern-placed revetments. Therefore, the consequences of most damages are evaluated based upon experience in maintenance as written in reports such as ‘Maintenance requirements for revetments on dikes’ (Klein Breteler, 2018). However, by studying the impact of damage on pattern-placed revetments, an estimation of the impact on the stability and failure probability can be made. These estimations can then be used to more efficiently plan maintenance using risk-based maintenance and reduce societal costs due to inefficient maintenance.

1.3. Research Objective and Questions

From the problem statement, we identify that it is unknown what the exact impact of damage is on the stability and reliability of a pattern-placed revetment. Therefore, we aim in this study to explore this topic with the use of finite element simulations. As a result, this study will contribute to two gaps in the knowledge. First, the impact of damage on the stability and reliability of the revetment. Second, how a finite element model can be used to simulate pattern-placed revetments under wave loading.

Based on the identified gaps in the knowledge, we define two objectives. The first objective is to assess how different types of damage impact the stability and reliability of a pattern-placed revetment. The second objective is to determine whether a finite element model can be used to simulate a (damaged) pattern-placed revetment. Based on both objectives, the following research question is formulated:

Can a model be used to estimate the impact of damage on the stability and reliability of a pattern-placed revetment under wave loading?

To answer the research question, a literature review is conducted and the research question is divided into four sub-questions:

1. What are the different types of damage that can occur on a pattern-placed revetment, how are they caused, and what is the qualitative effect on the top layer stability?
2. How can data from old flume experiments be used to quantify the impact of damage on a pattern-placed revetment?
3. What is the impact damage has on the stability of a pattern-placed revetment, and can this be modeled with a finite element model?
4. What is the impact damage has on the reliability of a pattern-placed revetment, and which uncertain parameters are the most important?

Figure 1.2 provides a graphical overview how the literature review and different sub-questions relate to each other and how the research objectives will be accomplished.

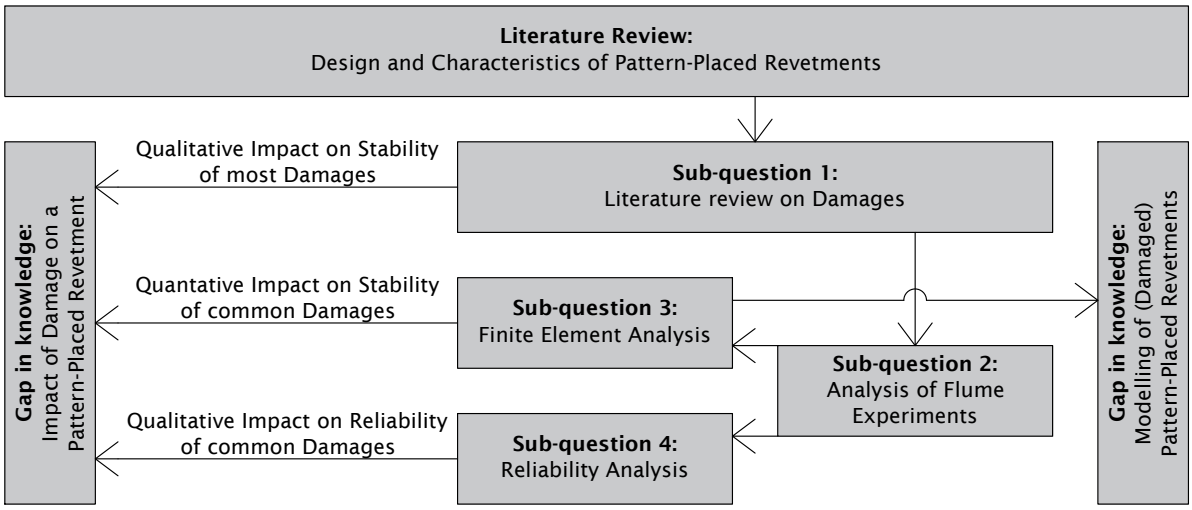

Figure 1.2: Relation between literature review, different sub-questions and the two objectives

1.4. Research Scope

Pattern-placed revetments can be found on dikes in different locations under different circumstances. Therefore, it is essential first to define the scope of the study.

Top Layer Elements
The primarily investigated type of top layer will be non-clamped column-type elements, such as Basalton. In the first chapters, the study will be broader and focus on the pattern-placed revetments in general. However, from the analysis of the flume experiments, the focus will be on column-type pattern-placed revetments, specifically basalt and Basalton revetments. For the finite element model, we choose to study a revetment made of Basalton STS+, as this is a modern set of elements and is commonly used on dikes in the Netherlands and other places around the world.

Geometry
The investigated revetment will be on a simple slope with no berm. The studied slope will range from 1:3 up to 1:4 as this slope is the most common for dikes in the Netherlands, and most research is done for slopes within this range. Within the study, only normally incident waves will be considered.

Loading
There are two main types of loads on which a pattern-placed revetment can be designed, waves and longitudinal flow. This study will focus on wave loading, as this is often more important than longitudinal flow when considering a revetment on the slope of a dike, and most pattern-placed revetment can be found along dikes prone to wave loading. When considering column-type revetments, chosen is only to consider the wave impact, as this turned out to be the most critical loading for column-type revetments.

Failure Mechanisms
The main focus of the study is to find the impact on the stability of the top layer. Geotechnical failure mechanisms are out of scope.

1.5. Significance

This study will provide insight into the impact of certain types of damage typical for a column-type pattern-placed revetment. This is important as little research has been conducted on this topic. Although the main focus of this research is Basalton STS+, it is found that most of the findings may apply to similar types of top layer elements as well.

The main benefit of obtaining more insight into the impact of damage on the stability and reliability is to improve the maintenance of a dike. Maintenance is often carried out conservatively because it is only known how reliable an undamaged pattern-placed revetment is; therefore, damages are often judged based on expertise. However, assessing based on expertise may lead to misjudgment by either underestimating or overestimating the impact of the damage. By improving our insight into the impact damage has on a pattern-placed revetment, we can reduce inefficiencies caused by misjudgment and either result in maintaining too early or too late. As a result, societal costs incurred due to inefficient maintenance can be reduced, and the hinterland can be better protected.

New insights into the impact on the reliability of a pattern-placed revetment can find a wide national application since many outer slope revetments in the Netherlands have a top layer of Basalton or any other similar type of top layer elements. The studied revetments are also regularly used internationally, which implies that the findings of this research can also provide new insights globally.

Finally, this study provides insights into how finite element models can be used next to flume experiments. For example, in some cases, it may be helpful to use a finite element model as a first estimate to optimize the pilot program of flume experiments. Furthermore, a finite element model is also beneficial to obtain more specific data about the revetment during the simulation of wave loading.

1.6. Outline

In this section, an overview is given of the outline of this study and is briefly touched upon the methodology. At the beginning of each chapter, the methodology is discussed in more detail.

- **Chapter 1: Introduction**

  In Chapter 1, the reader is given an introduction to the study, the research problem, scope and significance of the study.

- **Chapter 2: Physical Behaviour of Pattern-Placed Revetments**

  In Chapter 2, a literature review is done on the design of pattern-placed revetment. This chapter will discuss different characteristics of pattern-placed revetments, hydraulic loading, the strength of the revetment, and design equations.

- **Chapter 3: Damaged Pattern-Placed Revetments**

  In Chapter 3, a literature review into the different types of damage for pattern-placed revetments is done. Furthermore, a framework is introduced to relate damage with their corresponding root causes and their impact on the resistance of the revetment.

- **Chapter 4: Analysis of Old Flume Experiments**

  In Chapter 4, old flume experiments are reviewed and analyzed on the reported damage. Based on the analysis results, this study hopes to give more insight into the most common types of damage and to parameterize and quantify those damage.

- **Chapter 5: Impact of Damage on the Strength**

  In Chapter 5, a finite element model is created to simulate (damaged) revetments. With this model, different simulations are done with different types of damage to study the impact of damage on the stability of a revetment. Furthermore, this chapter gives insight into whether it is possible to simulate (damaged) revetments using a finite element model.

- **Chapter 6: Impact of Damage on the Reliability**

  In Chapter 6, the finite element model from the previous chapter is used to assess the reliability of a damaged revetment. First, a study into the most uncertain parameters is done, followed by the creation of a response surface model which can be used to estimate the impact damage has. Finally, this model is applied within a case study in which damaged pattern-placed revetments are assessed for a coastal dike in the Netherlands.

- **Chapter 7: Discussion**

  In Chapter 7, the methodology of the finite element model and what the implications are on the findings are discussed. After that, the meaning of the findings for daily practice is discussed.

- **Chapter 8: Conclusions and Recommendations**

  In Chapter 8, conclusions are given and recommendations are made for implementation of the findings in the daily practice and further research.

2

Physical Behaviour of Pattern-Placed Revetments

In this literature review, we introduce the topic of pattern-placed revetments in four main sections. First, in Section 2.1, a general introduction into pattern-placed revetments is given by discussing: the general purpose, the different types of elements, and the failure mechanisms of a pattern-placed revetment. Next, the top layer stability is studied; first, the different kinds of loads are reviewed in Section 2.2, next, the factors determining the strength of a revetment in Section 2.3. Finally, in Section 2.4, the different design methods and stability equations are discussed.

2.1. Pattern-Placed Revetments

The first part of the literature review is an introduction of pattern-placed revetments. In Section 2.1.1, the general purpose of pattern-placed revetments on dikes is explained. Next, in Section 2.1.2, the different types of pattern-placed revetments are discussed, and in Section 2.1.3, the different pattern-placed elements. Finally, in Section 2.1.4, the most common failure mechanisms are addressed for pattern-placed revetments.

2.1.1. Pattern-Placed Revetments on Dikes

Pattern-placed revetments are used as protection on outer slopes of dikes to prevent erosion due to the hydraulic loading caused by waves and flow. Dorst et al. (2012) describe pattern-placed revetments as “A protection of a shoreline with stony material, usually natural stone or concrete, with a thickness of only one layer of elements, and of which the elements are placed in a pattern. The elements might have connections.” In Figure 2.1, a typical cross-section of a pattern-placed revetment revetment is shown.

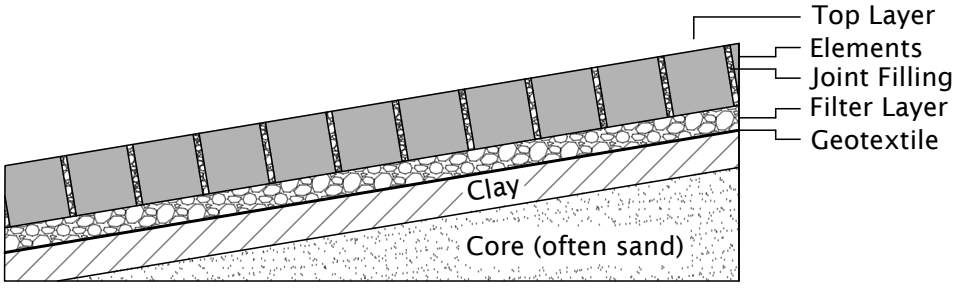

Figure 2.1: Detailed cross-section of a pattern-placed revetment on a dike

The layer with elements is called the top layer and is often placed on a layer of granular material called the filter layer. The goal of the filter layer is to prevent the migration of the soil particles through the revetment. For pattern-placed revetments made of column-type elements (for example, Basalton), the revetment is washed in with granular material between the joints called the joint filling. The primary purpose of the joint filling is to clamp the elements in place. It will also act as a drainage for the filter and, therefore, also impacts the filter response (Cirkel et al., 2015). More on the filter response will be discussed in Section 2.2.3.

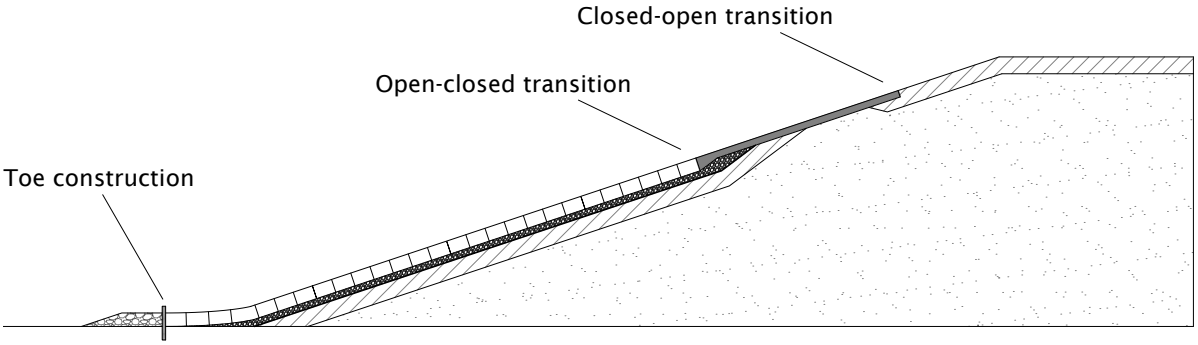

Figure 2.2: Typical cross-section of a pattern-placed revetment on a dike with no berm

In Figure 2.2 a typical cross-section of a dike with a pattern-placed revetment is shown. At the outer edges of the revetment, a transition can be found between two types of revetment. However, those transitions are weak spots as, over time, a gap may form at the transition, for example, due to deformation (Section 2.1.4). Therefore, transitions are often specially designed to ensure a smooth transition between the two revetments (Schiereck and Verhagen, 2019). At the lower end of the slope, the edge of the revetment is protected by a toe structure. The primary purpose of the toe is to prevent the toe structure from sliding down the slope. The toe structure is often a wall or sheet pile combined with a rubble mound berm to act as a counterweight. One disadvantage for revetments with small joints is that the use of an embedded wall will make the release of pressure in the filter more difficult. As a result, this will increase water pressure in the filter near the toe. This can be prevented by using a permeable structure instead of a sheet pile.

2.1.2. Types of Pattern-Placed Revetments

Below, the differences between the different types of revetment will be briefly discussed. Next, a more in-depth review of the most commonly used block and column-type elements is done. A closer look into the different types of pattern-placed revetments learns there are generally four different types of pattern-placed revetments (Dorst et al., 2012):

- Pattern-placed revetments with column-type elements;
- Pattern-placed revetments with block-type elements;
- Pattern-placed revetments with interlocking elements;
- Block mats.

All four types of pattern-placed revetments are shown in Figure 2.3. The top left image of this plot shows basalt columns, the top right image Haringman blocks, the bottom left image interlocking Verkalit elements, and the bottom right shows a block mat.

Figure 2.3: Different types of pattern-placed revetments: top left: basalt columns (Stenen zoeken.nl, 2020), top-right: Haringman blocks (DeltaExpertise, 2020), bottom-left: Interlocking Verkalit elements (LBN Beton, 2020), bottom-right: RonaTon block mats (Altena Infra-materialen, 2019)

The main two types of top layer elements are column-type and block-type elements. Both elements are similar, and a clear division has not been defined. However, the Dutch guidance on pattern-placed revetments names some differences between pattern-placed revetments using columns or blocks. The most important one is that the shapes of block elements are often regular while columns are often irregular (Cirkel et al., 2015). As a result, revetments made of column-type elements have larger joints between the elements than revetments made of block-type elements. To increase the clamping of the column-type elements, the joints between the elements are washed in with granular material.

Interlocked elements are similar to other artificially shaped elements except that they have an interlocking mechanism. With the use of this mechanism, the element is force-locked over either one or two directions. Gier et al. (2012) showed in experiments with interlocking Verkalit elements that interlocking elements have a much higher stability number than usual column-type and block-type elements.

Block mats are artificially shaped elements that are attached to a geotextile, often using plastic pins (Schiereck and Verhagen, 2019). The failure mechanisms for such mats are different than for loose pattern-placed revetments as the mats function as a system instead of multiple small elements.

This study will focus on pattern-placed revetments made of loose elements without interlocking. Therefore interlocking elements and block mats are out-of-scope for this study. This distinction is important to make because interlocking elements and block mats behave differently and therefore have different failure mechanisms.

2.1.3. Different Column and Block Elements

Basalt

Basalt elements are column-type elements made of natural stone. Basalt was a popular choice for a pattern-placed revetment in the last century because the basalt is harder and more resistant against wave attacks than the elements used at that time. Nowadays, basalt quarries are either exhausted or protected as nature reserves and are hardly ever used in new pattern-placed revetments in the Netherlands. In addition, due to the natural shape of basalt stones, each stone is different. This natural difference makes automating the stone placing process difficult, resulting in much manual labour when constructing a revetment made of basalt.

Figure 2.4: Basalt (Stenen zoeken.nl, 2020)

Basalton®

Basalton® is the concrete alternative to basalt elements and a product of Holcim Coastal gamma. Currently, Basalton is one of the most widely used element types for pattern-placed revetments in the Netherlands. Basalton was developed because basalt was becoming scarcer and was difficult to place due to the varying thickness of elements. According to the manufacturer Holcim Coastal (Holcim Coastal, 2013), Basalton is specially developed to function as pattern-placed revetment on slopes and does have a fixed form of 18 standard elements spanning a total area of about 1.3 m^2 per set. The joints between the elements are filled with granular material to ensure that the elements stay in place. The fixed shape of each Basalton set makes it suitable to be placed mechanically on straight trajectories.

Figure 2.5: Basalton (DeltaExpertise, 2020)

C-Star®

C-Star® elements are made of concrete and are a product of LBN Betonproducten. The column-type elements do have a repeating patron and can be easily placed by machines. Because of the remarkable shape of the elements, C-Star elements have high stability due to the clamping generated by the shape of the element (Wolters, 2016b). Also, because of the rounded edges, the manufacturer LBN suggests it has a long life span (LBN Betonproducten, n.d.). The joints are filled with granular material and are large enough to provide good ecological soil for sea organisms.

Figure 2.6: C-Star (DeltaExpertise, 2020)

Haringman® blocks

Haringman® blocks are block-type elements and were popular in the Netherlands during the nineteen-sixties. The most notable feature of the Haringman block is that it has a dent on the top of the block to reduce wave run-up. Later, during the nineteen-eighties, it turned out that the dent did not reduce the wave run-up as expected. Although nowadays, Haringman blocks are no longer being used in revetments, old Haringman blocks are sometimes being reused in a revetment by placing the block on its side, which makes it similar to a revetment made of rectangular blocks.

Figure 2.7: Haringman blocks (Nationaal Park Oosterschelde, 2020)

Hillblock®
Hillblock® elements are made of concrete and are a product of Hillblock BV. The Hillblock has a unique shape as between the base and the top of the element, the element becomes more narrow, creating hollow spaces. According to the manufacturer Hillblock BV, the main benefit from the Hillblock is a reduction in wave run-up as the water can flow into the hollow spaces created by the geometry of the block (Hillblock BV, 2018). In addition, the Hillblock is generally more stable than the more common types of elements (Van Steeg, 2016).

Figure 2.8: Hillblocks (DeltaExpertise, 2020)

Hydroblock®
Hydroblocks® are elements made of concrete and is a product of Haringman Betonwaren. Haringman Betonwaren developed the Hydroblock after it turned out that the Haringman blocks did not meet the expectation. Due to the fish-shaped elements, Hydroblocks can be placed in a repeated pattern on straight and curved trajectories. According to the manufacturer, Hydroblocks are much easier to place mechanically than other elements because of their simple pattern (Haringman Betonwaren, n.d.).

Figure 2.9: Hydroblocks (DeltaExpertise, 2020)

Rectangular blocks
Rectangular blocks are block-type elements often made of concrete. In some cases, rectangular element revetments are made from Haringman blocks placed on its side. Because of the shape of the blocks, rectangular blocks have very narrow joints between the elements. As a result, the leakage length for this type of element is relatively large compared to other elements.

Figure 2.10: Rectangular blocks (DeltaExpertise, 2020)

RONA®Ton
RONA®Ton are column-type elements of concrete and are a product of Altena Infra-materialen. The columns are hexagonal shaped and are placed in a honeycomb pattern. RONA®Ton follows a similar design as Hillblock elements to reduce wave run-up. When constructing a new revetment, RONA®Ton can mechanically be placed and does not require a lot of granular material to be washed in. (Altena Infra-materialen, 2019)

Figure 2.11: Ronaton (DeltaExpertise, 2020)

2.1.4. Failure Modes for Revetment Failure

In the next part, the most common failure modes for pattern-placed revetments are briefly described based on the 'Handreiking Dijkbekledingen' (Cirkel et al., 2015). It is important to note that if a revetment fails, it will usually not lead directly to flooding of the hinterland. The strength left in a dike after the revetment fails is called the residual strength and has, until recently, been barely considered in the assessment of dikes. However, ongoing research has led to a better understanding of residual strength and therefore, it will first be introduced in the next assessment round for dikes in the Netherlands (BOI 2023) (Rijkswaterstaat, 2019).

Pressure differences over the top layer due to wave impact

Pressure differences over the top layer can occur due to wave impact. Pattern-placed revetments made of column-type elements are most prone to this type of failure. During wave impact, the top layer is exposed to large pressures. Due to the wide joints, the filter layer will adjust fast to those pressures. This will increase the filter pressure locally around the wave impact location, exposing the elements near the wave impact location to a large pressure from the filter. This may eventually lead to either single element failure or group failure.

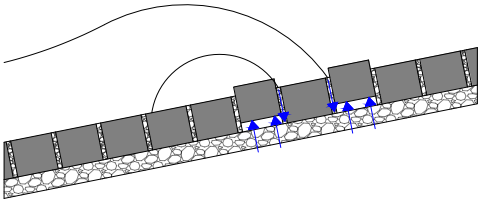

Figure 2.12: Overpressure due to wave impact can cause single element failure (drawn) or group uplift (blue arrow is water pressure)

Pressure differences over the top layer due to wave run-down

Pressure differences over the top layer can also occur due to wave run-down. However, to pressure differences due to wave impact, this failure mode affects primarily pattern-placed revetments with block-type elements under loading of waves with a large Iribarren number (Klein Breteler and Van der Werf, 2006). With those types of revetment, it takes a long time before the filter pressure adjusts to changes in the water pressure on the top layer. Therefore, during run-down, the pressure on the top of the top layer significantly decreases while the filter layer keeps most of its pressure. As a result, elements near the wavefront are exposed to a large filter pressure while experiencing almost no pressure from the wave. This may eventually lead to either single element failure or group failure.

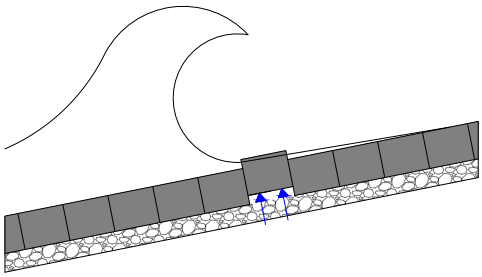

Figure 2.13: Overpressure due to wave run-down can cause single element failure (drawn) or group uplift (blue arrow is water pressure)

Migration of joint filling out of the top layer

Due to the hydraulic loading of the waves, the joint filling may migrate out the joints. This may be caused by pressure from the filter or turbulence caused by the waves on the top layer. Generally, the insufficiently clamped joint filling is more vulnerable to being washed-out. However, some damages, such as deformation or damaged elements, may cause wider joints, making it easier for the joint filling to migrate out of the top layer.

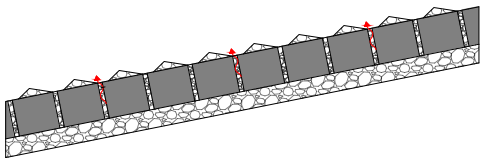

Figure 2.14: Failure due to migration of joint filling out of the top layer (red arrow is migration joint filling)

Migration of filter material through the top layer

The flow from water in and out the filter layer may cause filter material to migrate through the top layer. This can be prevented by having enough joint filling clamped between the joints and designing the gradation of the joint filling to act as a geometrically closed filter for the filter material. However, when the migration of the filter material happens, this will lead to a decreasing thickness of the filter layer and deformation, which may decrease the stability of the revetment.

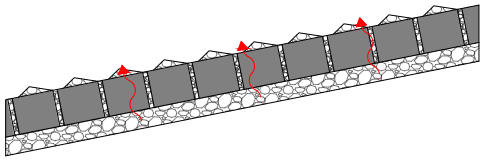

Figure 2.15: Failure due to migration of filter material through the top layer (red arrow is migration filter material)

Migration of core material into the filter layer
Due to the hydraulic loading of the waves, currents will develop in the filter layer due to pressure differences. Those currents can erode the core material and transport it into the filter layer creating hollow spaces underneath the revetment. This could lead to local subsidence of the revetment and clogging of the filter. This failure mechanism can be largely avoided by designing a geometrically closed filter layer.

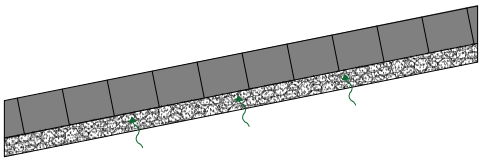

Figure 2.16: Failure due to migration of core material into the filter layer (green arrow is migration core material)

Migration of filter material within the filter layer
The filter material may migrate in the filter layer due to the translation of the elements caused by wave loading as it is no longer held in place by the element's weight. The migration of the filter material will result in a thicker filter layer down the slope and a thinner filter layer up the slope. This could locally impact the revetment as a change in filter thickness deform the revetment and may change the filter response. In addition, the deformation can also negatively affect the clamping of the elements.

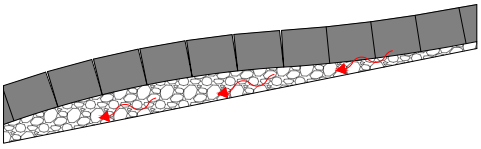

Figure 2.17: Failure due to migration of the filter material within the filter layer (red arrow is migration filter material)

Liquefaction of the core
Liquefaction of the core is a failure mechanism that has only been reported on dikes where the pattern-placed revetment is placed directly on the core, without a clay layer. Due to a high phreatic level inside the core, the wave impact can liquefy the core material, leading to large deformations of the revetment (Klein Breteler et al., 2014). However, this failure mode can often be neglected in practice as pattern-placed revetments are usually placed upon a clay layer.

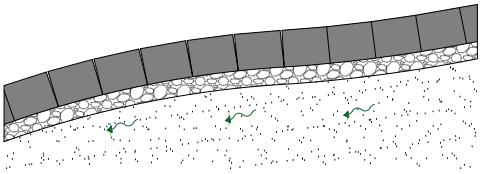

Figure 2.18: Failure due to liquefaction of the core (green arrow is migration core material)

Failure of the toe construction
A pattern-placed revetment is generally supported at the bottom by a toe construction. Failing the toe construction could lead to the sliding of elements down the slope, creating large joints between two elements. In addition to this, the sliding of elements also leads to decreased clamping, which results in less stability.

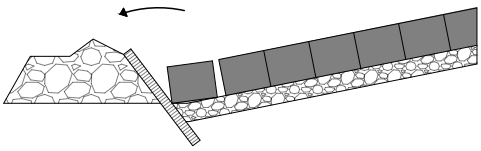

Figure 2.19: Failure due to deformation of the toe

Sliding of the elements
Sliding of the elements is generally caused by one of the two causes: compaction and reordering of the elements and deformation of the toe structure. Sliding may induce the widening of joints at the outer edge of the revetment, which makes the transition prone to failure. In addition, it may also affect the joints between the elements as due to sliding, the joints become wider, which results in a reduction in clamping.

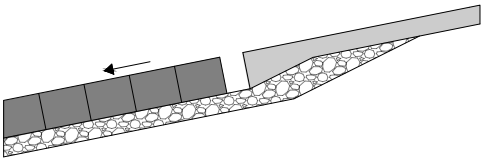

Figure 2.20: Failure due a sliding elements

External influences
There are also external influences that may impact the stability of a revetment. This mainly concerns the damage to the top layer as filter layers are not accessible on the surface. Some examples of causes are vandalism, washed-up stones or objects, or collision with the bow of a ship.

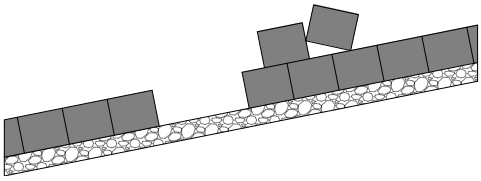

Figure 2.21: Failure due to external influences

2.2. Hydraulic Loading on a Revetment

The next part of the literature review will focus on the physics of the top layer stability. In this section, the main hydraulic loads for a revetment on the outer slope will be discussed. First, the most important aspects for the design water level are listed in Section 2.2.1. Next, the wave loading is discussed in Section 2.2.2. Last in Section 2.2.3, the filter pressure is discussed.

2.2.1. Water Level

The water level near the dike determines where on the slope the wave impact will take place. However, for dikes along the coast, lakes, or estuaries, this is more complicated as five other factors could influence the local water level (Figure 2.22):

- Tides
- Storm surge
- Sea-level rise
- Wave setup
- Lake level

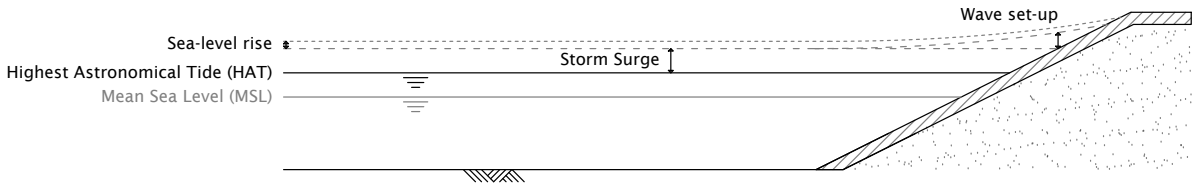

Figure 2.22: Impact of sea-level rise, tides, surges, and wave setup on the water level near a dike

2.2.2. Waves

In hydraulics, a wave is often referred to as a periodic fluctuation in water height. There are two main types of waves, swell and wind waves (Holthuijsen, 2007). Swell waves are gentle waves generated during a storm far away in the ocean. Swell waves will take a long to dissipate energy, allowing them to travel thousands of kilometers overseas. It is not uncommon to expect swell waves from another direction than the wind is blowing as the wind is no longer a significant driving force for those kinds of waves. Wind waves are steep waves and are locally generated by the wind. In contrast to swell waves, wind waves dissipate energy faster and can travel only relatively short distances (Holthuijsen, 2007). For revetments, wind waves are the most common type of wave expected in the Netherlands. Although swell waves generated by storms are less common due to the geographical location of the Netherlands, low-frequency waves can be expected due to wind waves breaking before they reach the dike.

2.2.2.1. Generation of Waves

In the literature, two types of wave fields are commonly used, regular and irregular. The main difference between the two types of wave fields is that a regular wave field has non-varying characteristics and is described by fixed values denoted by H, T, L_0. While, an irregular wave field does have varying characteristics and is described by statistical parameters denoted by H_s, T_p, L_{0p}. The development over the last few decades shows that irregular wave fields have become more the norm as they better reflect reality (Holthuijsen, 2007).

The two most important parameters required when describing waves are the wave height and the wave period. The significant wave height H_s represents the average wave height of the one-third highest waves. To denote the significant wave height, sometimes also $H_{1/3}$ or H_{m0} is used. H_s and $H_{1/3}$ are defined the same and are based on field observations and measurements of waves, while H_{m0} is based on spectral analysis. H_{m0} is generally almost equal to H_s in deep water. However, in shallow water, it will slightly overestimate H_s. The spectral analysis can be used to model waves if the surface elevation can be seen as a stationary Gaussian process (Holthuijsen, 2007). The second important

design parameter is the peak period T_p, which represents the wave period of the wave with the largest amount of energy. With the wave period known the length of the wave can be estimated using linear wave theory. To estimate the wave length of a regular wave on deep water, Equation 2.1 can be used (Holthuijsen, 2007).

$$L_0 = \frac{gT^2}{2\pi} \tag{2.1}$$

The same equation can also be applied for irregular waves. For example, when replacing the wave period T by the peak period T_p the equation can be used to find the deep water peak wavelength L_{0p}. The most common wave period for the spectral analysis is the spectral mean wave energy period $T_{m-1,0}$.

The representative wave height for a dike can be obtained using different methods. The most straightforward method is to obtain an estimation for the significant wave height using literature, for example, using the given hydraulic boundary conditions by the government (Rijkswaterstaat, 2007). It is also possible to estimate the wave height based on a model like Bretschneider as described in 'Design of River Dikes' (TAW, 1989a). In addition to deterministic models, computer models like SWAN are available to include more details into a calculation and make more accurate predictions (Holthuijsen, 2007). For this study, the wave height at the toe is taken as starting point.

2.2.2.2. Breaking Waves

A wave will break when the particle velocity of the water exceeds the wave velocity resulting in the particles leaving the wave. When a wave breaks, this is most likely caused when the wave is on deep water by a too steep wavefront and shallow water because the wave speed too much decreased (Schiereck and Verhagen, 2019). When a wave reaches a slope, it can break in four different ways, of which three are relevant for dikes. With the use of the Iribarren number, it can be determined which breaker type will occur. Battjes (1974) defined the Iribarren parameter for regular waves as shown in Equation 2.2.

$$\xi = \frac{\tan \alpha}{\sqrt{H/L_0}} \tag{2.2}$$

In which:

ξ	=	Iribarren number	[-]
H	=	Incident wave height at toe of the slope	[m]
L_0	=	Deep water wave length	[m]

The expression H/L_0 in the denominator of Equation 2.2 can be seen as an approximation of the wave steepness. Which is for wind waves rarely larger than 0.05 and swell waves 0.01 or less (Schiereck and Verhagen, 2019).

The EurOtop (2018) suggests the use of the spectral Iribarren number $\xi_{m-1,0}$ in order to determine the most likely breaker type for an irregular wave field. The spectral Iribarren number is defined by replacing the incident wave height H by the spectral significant wave height H_{m0}, and the deep water wavelength L_0 by the deep water spectral wavelength $L_{m-1,0}$. For the spectral Iribarren number, the corresponding breaker types are shown in Figure 2.23. A standard dike usually has a slope between 1:3 and 1:4, which results in a spectral Iribarren number between 1 and 1.5, resulting in plunging breakers.

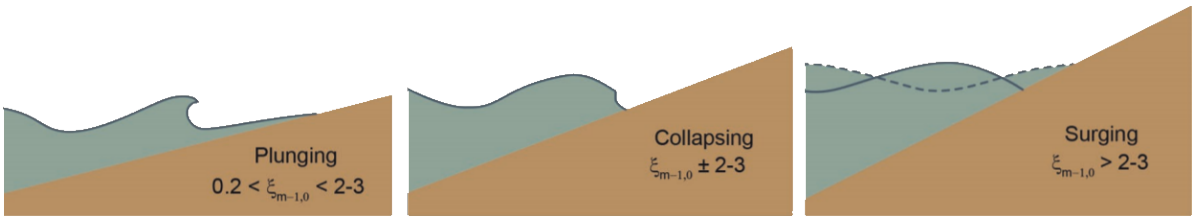

Figure 2.23: Breaker types for different spectral Iribarren numbers (EurOtop, 2018)

2.2.2.3. Wave Run-Down

As described in Section 2.1.4, overpressure over the top layer can be caused by wave run-down or wave impact. The following sections consider how these two physical processes can be parameterized, starting with top layer instability due to wave run-down. This failure mode is often governing for revetments with a large leakage length, such as revetments made of block-shaped elements.

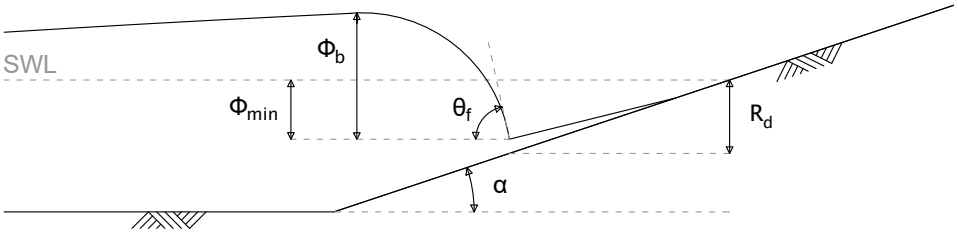

Figure 2.24: Wave run-down schematized with the key parameters

The main parameters for failure due to wave run-down are the run-down location (R_d or x_s in Figure 2.24) and the breaker height and angle (ϕ_b and θ_b in Figure 2.24). In this section, we first discuss the run-down location and then the breaker height.

Run-down Location

Run-down is defined as the minimum elevation of the waterline reached by waves. It is an important parameter when considering pattern-placed revetments as it determines the location of the wavefront (Klein Breteler et al., 2012). The largest pressure difference between the top and filter layers is expected at this specific location during run-down. As a result, elements near the wavefront are most prone to be uplifted due to this pressure difference.

For an irregular wave field, The Rock Manual (CIRIA, 2007) suggests Equation 2.3 to determine the 2% exceedance height for the run-down on straight smooth slopes.

$$\begin{aligned} \frac{R_{d2\%}}{H_s} &= 0.33\ \xi_{0p} \quad \text{for} \quad 0 < \xi_{0p} < 4 \\ \frac{R_{d2\%}}{H_s} &= 1.5 \qquad\quad \text{for} \quad \xi_{0p} \geq 4 \end{aligned} \tag{2.3}$$

In which:

$R_{d2\%}$	=	2% Exceedance run-down height	[m]
ξ_{0p}	=	Iribarren number based on H_s and T_p	[-]

More background information on this equation cannot be traced other than it appearing in The Rock Manual (CIRIA, 2007). This makes it difficult to interpret how this equation is derived, especially because earlier studies suggest more conservative equations, for example, by adding an extra constant to Equation 2.3 to make it fit better for lower Iribarren numbers (TAW, 1984).

Bezuijen et al. (1990) suggest an equation for wave run-down based on analysis of flume experiments done between 1980 and 1988. This run-down equation is later also used in the quantification of wave loading by Klein Breteler et al. (2012) and is shown in Equation 2.4.

$$\frac{R_{d2\%}}{H_s} = 0.6\ \xi_{0p} - 0.2 \tag{2.4}$$

Other studies suggest the use of a quadratic fit. Van der Meer and Klein Breteler (1991) derived an equation based on a quadratic fit to determine the run-down of regular waves on a smooth slope based on experiments done in the Delta Flume. Peters (2017) used the same approach as Van der Meer and Klein Breteler to derive Equation 2.5 for the run-down of irregular waves on a smooth slope. For this derivation, he used multiple experiments and used a quadratic fit such that the fit represents the 5% exceedance value of all large scale tests, resulting in Equation 2.5.

$$\frac{R_{d2\%}}{H_s} < -0.0344\ \xi_{m-1,0}^2 + 0.55\ \xi_{m-1,0} + 0.4 \tag{2.5}$$

In which:

$\xi_{m-1,0}$ = Iribarren number based on H_{m0} and $T_{m-1,0}$ [-]

In Figure 2.25 the three discussed equations are illustrated. The Iribarren number ξ_{0p} is expressed into $\xi_{m-1,0}$ using the rule of thumb: $T_p \approx 1.1\ T_{m-1,0}$ (Holthuijsen, 2007). In order to be able to model pattern-placed revetments in the finite element model, a choice has to be made which run-down equation will be used. While Equation 2.3 is based on experiments with smooth straight slopes, Equations 2.4 and 2.5 are based on experiments with pattern-placed revetments. Based on the publications behind those equations, chosen is to use Equation 2.5 within this study. The main reason behind this choice is that this equation is the most recent and based on the largest group of experiments.

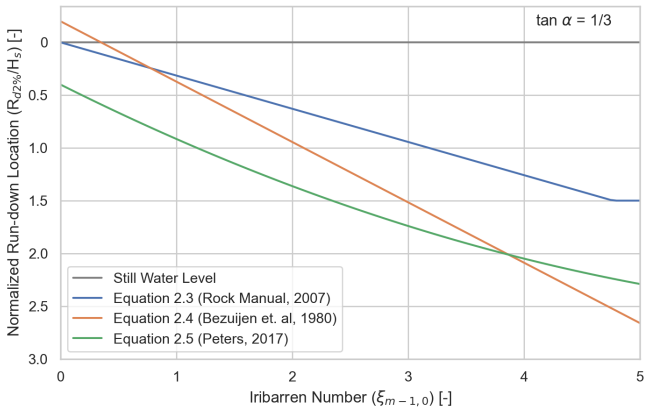

Figure 2.25: Comparison between the different run-down equations

Breaker Height

The breaker height is defined as the difference in the hydraulic head from the run-down location up to the top of the wavefront. This parameter is the most important for revetments with large leakage lengths, such as block-shaped elements. However, this study will mainly focus on revetments made from column-type elements for which the leakage length is smaller and thus the breaker height is of lower significance. Therefore, a summary of publications will be given in order to parameterize the breaker height.

The most important parameters used to define the breaker height are the difference in the hydraulic head just before and after the breaker front (ϕ_b). Other important parameters are the water head gradient of wavefront $d\phi_b/dx$, which is often expressed with an angle denoted by θ_b and the difference between the still water level and the lowest point just in front of the wavefront ϕ_{min}.

Klein Breteler et al. (2012) parameterized the wave front loading as part of the research program 'Kennisleemtes Steenbekledingen' based on an older parameterization from De Waal et al. (1995). As part of this report, the equations for the wavefront parameters were improved based on new large and small-scale flume experiments. Two categories of wavefronts were parameterized, steep and high. It is difficult to point out which one is critical as it is dependent on the considered revetment. Therefore both profiles are assessed within SteenToets (Klein Breteler and Kaste, 2019).

A disadvantage of the parameterization done by Klein Breteler et al. (2012) is that the used experiments only had slopes varying between 1:3 and 1:4. Therefore, Peters (2017) collected data for more steeper and shallower slopes and found that when the breaker parameter is increasing, the dependency of the breaker index on the wave steepness and the slope angle is decreasing. Based on those findings, he proposed two new sets of equations for high and steep wavefronts. Those sets of equations are more suitable for a larger domain of slopes.

2.2.2.4. Wave Impact

The most important parameters affecting top layer instability due to wave impact are discussed in the next part. This failure mode is especially applicable to relative open revetments, such as revetments made of column-shaped elements such as basalt and Basalton. First, the wave impact location is discussed. After that, the wave impact pressure is discussed.

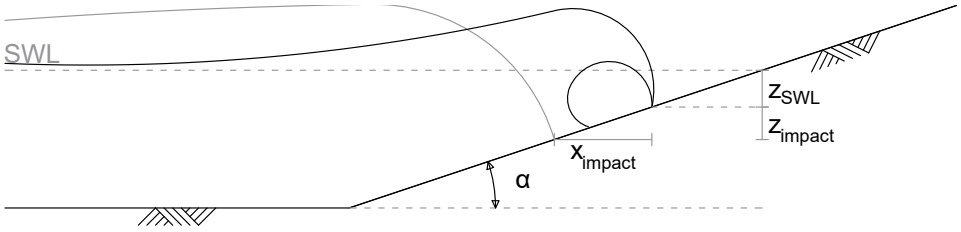

Figure 2.26: Wave impact schematized with the key parameters

The main parameters for failure due to wave impact are illustrated in Figure 2.26. The most important parameters are the location, pressure (P), and the duration (t_d) of the wave impact.

Wave Impact Location

The wave impact location is the location on the slope where the peak pressure during wave impact is expected. Coeveld (2003) did a literature study into wave impact as part of the national research program regarding pattern-placed revetments in the Netherlands. He compared different studies performed during the 1990s about wave impact and came to the conclusion that multiple studies concluded that the largest wave impacts take place about 0.5 H_s below still water length.

Schüttrumpf (2001) quantified the wave impact location by analysing video material wave by wave of flume experiments. He did his experiments on a 1:4 and 1:6 slope and came to Equation 2.6 to determine the impact location of regular and irregular breaking waves.

$$\frac{z_{SWL}}{H_s} = 0.8 + 0.6 \cdot \tanh\left(\xi_m - 2.1\right) \quad \text{for} \quad \xi_m < 3 \tag{2.6}$$

In which:

z_{SWL}	=	Wave impact location below SWL	[m]
ξ_m	=	Iribarren number based on H_s and T_m	[-]

Peters (2017) determined the wave impact location by using the fall time and the horizontal particle velocity from a wave. He suggests that the wave impact point is related to the run-down point due to the horizontal distance a plunging wave can travel. In his Ph.D. thesis, he used the horizontal particle velocity and the fall time to determine the impact point. He found that the horizontal distance between the run-down location and the impact point is about 0.7 H_s (x_{impact}). Based on those findings, he suggests the use of the set of Equations 2.7 to locate the wave impact zone.

$$\begin{aligned} \frac{x_{impact}}{H_s}\tan\left(\alpha\right) &< 0.4 + 0.55\ \xi_{m-1,0} - 0.0344\ \xi_{m-1,0}^2 - 0.7 \\ \frac{x_{impact}}{H_s}\tan\left(\alpha\right) &> 0.45\ \xi_{m-1,0} - 0.3 \\ z_{impact} &= \tan\left(\alpha\right)\ x_{impact} \end{aligned} \tag{2.7}$$

x_{impact}	=	Wave impact location in the x direction with reference to the wave front	[m]
z_{impact}	=	Wave impact location in the z direction with reference to the wave front	[m]

In Figure 2.27, the three described equations are illustrated. The wave impact location is important in this study as it will be used to later model the wave impact location in the finite element model. Chosen is to use the equation by Peters (2017), mainly because the equation is derived based upon large-scale flume experiments on pattern-placed revetments while Schüttrumpf (2001) derived his equation on small-scale flume experiments with regular and irregular waves. Although the rule of thumb of Coeveld (2003) is easy to implement, it seems to deviate a lot for higher Iribarren numbers in comparison to the other two equations.

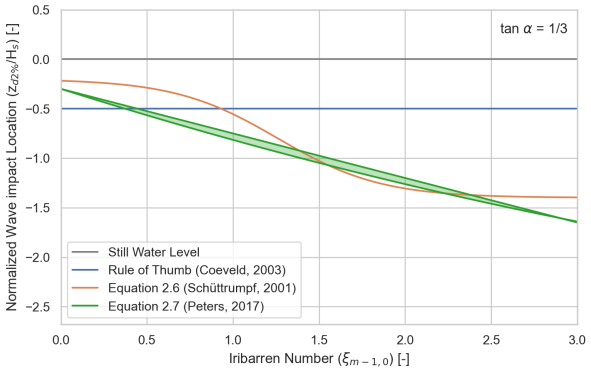

Figure 2.27: Comparison between the different wave impact locations

Wave Impact Pressure

The wave impact pressure is the peak pressure generated by the wave impact on the slope. The pressure from the wave impact and the filter response will determine the residual loading of the elements in the revetment. When the wave impacts the revetment, a short and high impact will occur. TAW (2002) gives a first approximation to determine the maximum load by using Equation 2.8.

$$p_{max} = \rho_w \; g \; q \; H \tag{2.8}$$

q	=	The impulse factor (appendix 6 of the report of TAW)	[-]
ρ_w	=	Density of water	[kg/m^3]

Klein Breteler et al. (2012) parameterized the wave impact loading profile by two profiles of 8 points as part of a study to expand SteenToets. Within this report, two types of wave impacts are described, the first one with a trough and the second one without a trough (Figure 2.28). Both profiles are derived from pressure sensor data during flume experiments. It is difficult to predict which wave impact type is the most representative and may vary between different revetments. Therefore both wave impact profiles are used within SteenToets to assess pattern-placed revetments. The sets of equations used to define the points of both profiles can either be found in the report 'Kwantificering golfbelasting en invloed lange golven' (Klein Breteler et al., 2012) or the SteenToets documentation (Klein Breteler and Kaste, 2019).

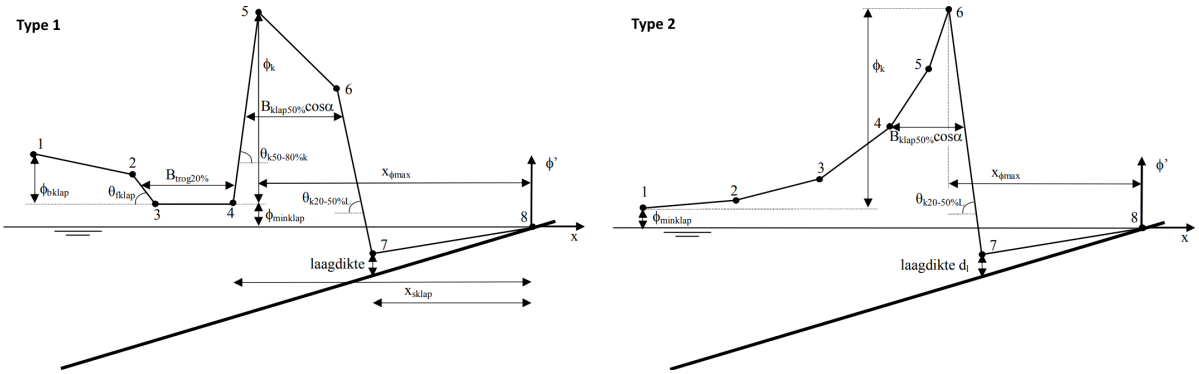

Figure 2.28: Wave impact profiles type 1 with trough (left) and type 2 without trough (right) (Klein Breteler et al., 2012)

Peters (2017) gives in his Ph.D. thesis a new equation to determine the $P_{max2\%}$ for irregular waves. This equation is shown in Equation 2.9 and is based on measured pressure of wave impacts during large scale tests and review of earlier studies. He noted that the peak pressure could up to 1.6 times larger than $P_{max2\%}$.

$$\frac{P_{max2\%}}{\rho_w \; g \; H_s} = 8 - 1.6 \; \xi_{m-1,0} - \frac{2}{\left(\xi_{m-1,0} - 0.2\right)^2} \tag{2.9}$$

Peters also noted that the duration of the wave impact is between 0.16 and 0.22 seconds. The time it takes to reach the peak pressure is defined by the rise time denoted by t_r for which he proposed Equation 2.10.

$$t_r = 0.10 \left(\frac{p_{max}}{\rho_w \; g \; H_s} \right)^{-1} \qquad 0.15 < t_r < 0.18 \tag{2.10}$$

Based on his findings, Peters proposed a idealized time signal and space diagram to simulate wave impact. This diagram is shown in Figure 2.29.

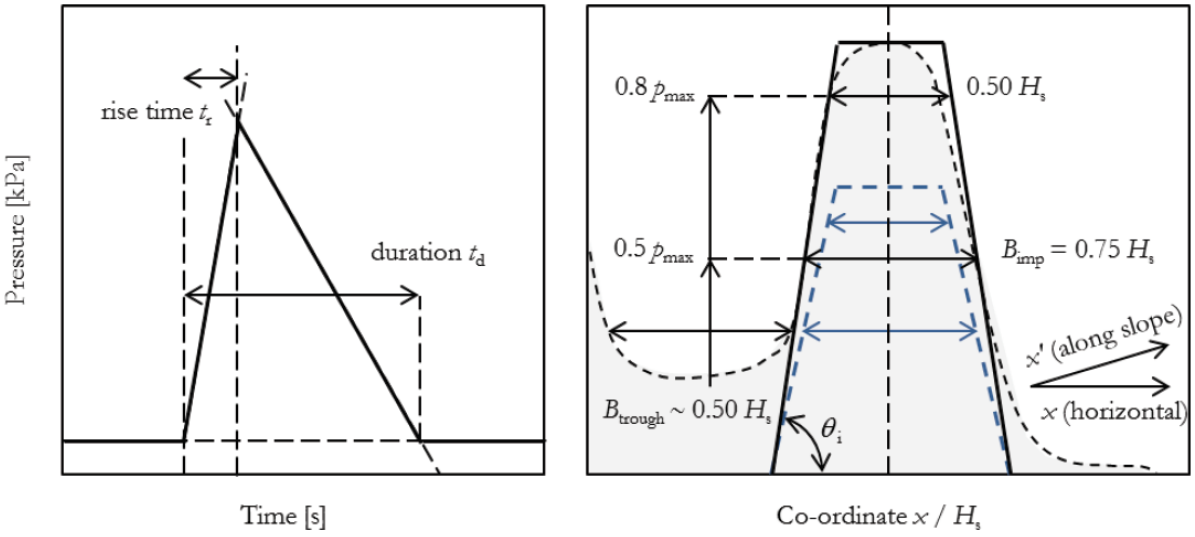

Figure 2.29: Idealised time signal and space diagram (Peters, 2017)

In order to model the wave impact in the finite element model, a wave impact profile is required. Because the aimed way of creating this model is on an explicit basis, it is desirable to have a wave profile in space and time. The wave impact profile from Peters (2017) seems a reasonable choice to model the wave impact. This model is chosen because it is based upon a review of the models of TAW (2002) and Klein Breteler et al. (2012). In addition to this, the model of Peters (2017) is also defined in space and time, whereas Klein Breteler et al. (2012) only defines the maximum loading in space and TAW (2002) only the maximum pressure.

2.2.3. Filter Pressure

The residual loading on the elements can be expressed as the difference between the pressures on the top layer caused by the wave loading and the filter pressure. We use the leakage length Λ to define the filter response, which is a linearized approximation of the non-linear resistance. The leakage length is used in different models to measure the exchange between the wave loading and the filter pressure (Equation 2.11). For example, in Figure 2.30, the wave loading and filter pressure for a revetment with a large and small leakage length are illustrated. A large leakage length is expected when the top layer permeability is low, resulting in a slow adjustment of the filter pressure to the pressure on the top layer. On the other hand, a small leakage length is expected when the top layer permeability is high, resulting in a fast adjustment of the filter pressure (Cirkel et al., 2015).

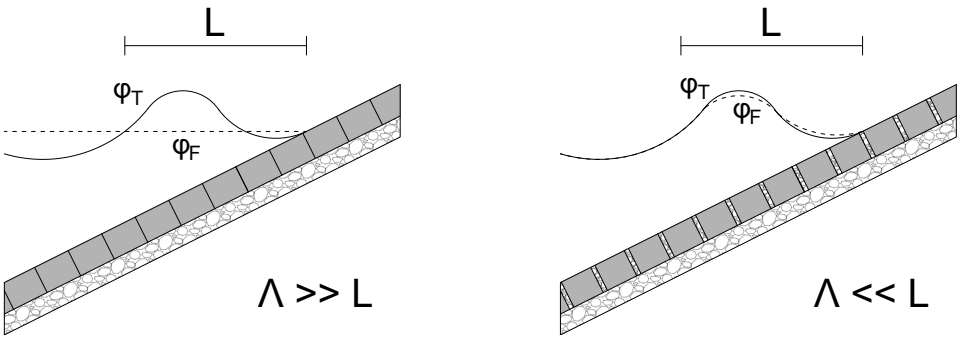

Figure 2.30: Differences in leakage length (Based on figure 8-5 in Schiereck and Verhagen (2019))

$$\Lambda = \sqrt{\frac{bDk}{k'}} \tag{2.11}$$

In which:

Λ	=	Leakage length	[m]
b	=	Thickness of the filter layer	[m]
D	=	Thickness of the top layer	[m]
k	=	Permeability of the filter	[m/s]
k'	=	Permeability of the top layer	[m/s]

The parameters required in Equation 2.11 are often based on measurements. Within models, the leakage length is often assumed to be a constant used for the whole slope. While it is easy to measure the thickness of the top and filter layer, it is more difficult to estimate the permeability of both layers. Therefore, the permeability can be estimated based on the gravel grading with the use of models as is done in SteenToets (Klein Breteler and Kaste, 2019) or by performing experiments with the gravel grading.

With the leakage length, the filter pressure can be estimated. In the report 'Waterspanning bij dijken' (Van der Meer et al., 2004), a combination of the continuity equation and Darcy's law is used to estimate the hydraulic head difference between the outside and the inside of the dike. When the flow in the filter is assumed to be laminar or when the resistance is linearized, this same principle can also be used for pattern-placed revetments, which gives Equation 2.12 (Schiereck and Verhagen, 2019).

$$\Lambda^2 \frac{d^2\Phi_F}{dx^2} - \Phi_F = -\Phi_T \tag{2.12}$$

In which:

Φ_T = The hydraulic head on the outside of the top layer		[m]
Φ_F = The hydraulic head in the filter layer		[m]

Together with the wave loading, the filter pressure is crucial in order to simulate loading on the elements of a pattern-placed revetment. Equation 2.12 seems to be a reasonable choice to model the filter pressure as it is also used within in the Dutch software to assess pattern-placed revetments (SteenToets) (Klein Breteler and Kaste, 2019). Furthermore, combining differential Equation 2.12 with the wave pressure profile from Peters, 2017 (Peters, 2017) from the previous section will allow for a simplified model to simulate a wave impact. For certain types of damage, such as deformation, the filter layer thickness varies along the slope. In this case, the leakage length can instead be implemented as a function of the slope coordinate.

2.3. Resistance of a Pattern-Placed Revetment

After reviewing the different physical processes of loading on a revetment, this section will review the physics behind the resistance of the pattern-placed revetment on a slope. Below, in Figure 2.31, a free body diagram is drawn of a pattern placed revetment with all aspects of loading and resistance on a single element of the revetment.

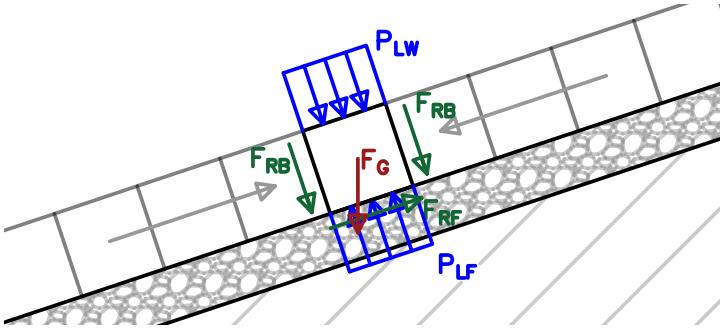

Figure 2.31: Force balance on a single element in a pattern-placed revetment

In this figure, the wave impact loading is governed by P_{LW} and the filter response is governed by P_{LF}. For the resistance, three important forces are determining the strength of a single element:

- Self-weight F_G;
- Block-Filter friction F_{RF};
- Block-Block friction F_{RB};

2.3.1. Self-Weight

Self-weight is, together with clamping, the most important aspect regarding stability. In the case pattern-placed revetments, the strength is expressed as ΔD, in which Δ is the relative density of the top layer and D is the thickness of the top layer. Based on the force balance shown in Figure 2.32, ΔD turns out to be the most important parameter when considering stability due to self-weight. In addition, Peters (2017) concludes in his Ph.D. thesis that elements with a higher thickness over width ratio tend to be more stable. This is because a taller column can distribute the flexural and shear deformation over more joints. This makes column-shaped elements generally more stable than block-shaped elements.

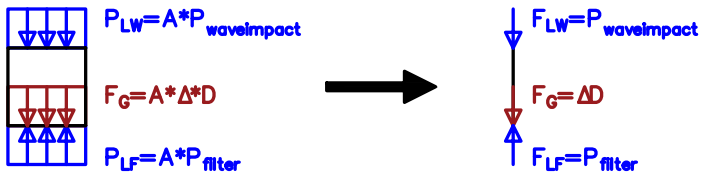

Figure 2.32: Stability based on self-weight for a pattern-placed revetment

2.3.2. Clamping

When the slope exceeds a certain angle, elements will start interacting as block-filter friction is not enough to obtain a force equilibrium. This interaction will generate a normal force within the revetment. For pattern-placed revetment, it is expected that the normal force within the revetment increases significantly over time (Vrijling et al., 2001). As a result, a toe construction that can withstand the weight of the revetment becomes much more critical. The generated normal force in the revetment will induce friction between the elements which makes the elements more resistant against single element pull-out (Figure 2.33) (Peters, 2017).

Furthermore, Vrijling et al. (2001) and Peters (2017) describe both in the literature that the loading history is also important, as it is believed that normal force develops over the area of the wave run down. Vrijling et al. conclude that due to the generated normal force, the stability of a revetment can increase by 35% with a variation coefficient of 17% as they confirmed by using model tests.

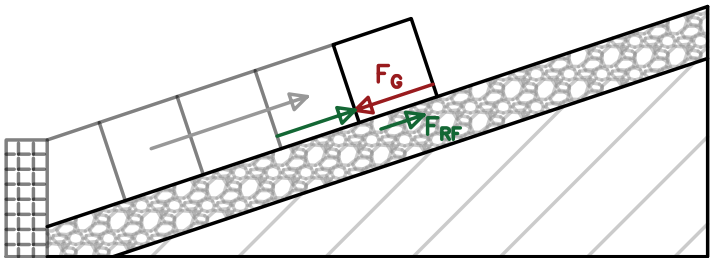

Figure 2.33: The interaction between elements with a toe construction

2.3.3. Block-Filter Friction

Block-Filter friction will act as resistance to prevent the element from sliding over the filter layer. The amount of resistance induced by block-filter friction is determined by the revetment slope and the element's self-weight. For shallow slopes, the block-filter friction is enough to prevent the elements from sliding. However, for a steeper slope, the parallel component of the force generated by the self-weight will exceed the friction. In that case elements will start 'resting' on each other resulting in the generation of the normal force (Figure 2.34) (Vrijling et al., 2001).

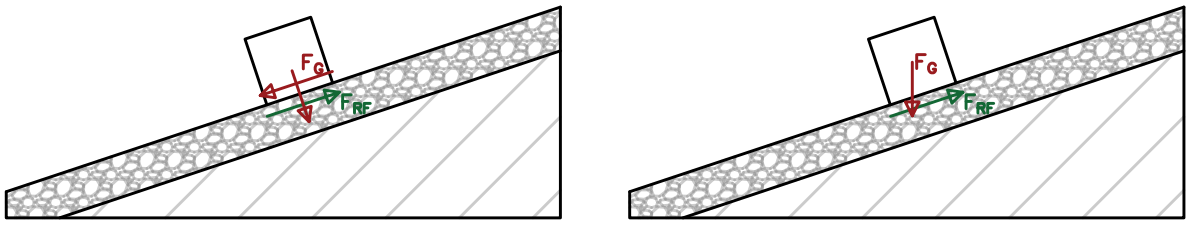

Figure 2.34: Block-Filter interaction on a single element

2.4. Design Models

In this section, models for the design of pattern-placed revetments are discussed. One key parameter for almost all stability equations is the stability parameter. In the case of a revetment on a slope under wave attack, this is expressed as the stability number which is defined in Equation 2.13.

$$\frac{H_s}{\Delta D} \tag{2.13}$$

In which:

H_s	=	Significant wave height	[m]
Δ	=	Relative density of the top layer	[m]
D	=	Thickness of the top layer	[m]

The higher the stability parameter, the more stable the revetment is for a specific wave height. The highest stability number is often found for revetment types like interlocking blocks like Verkalit. The stability number for those blocks is determined to be around 5 - 7, while a relatively low stability number can be found for a revetment made of loose elements, for which the stability number is often around 2 - 3 (Gier et al., 2012). Over time, several equations have been derived to estimate the stability number of revetments. In the following sections, some of the most important stability equations are discussed.

2.4.1. Force Balance

Over the past decades, a lot of research has been done into the stability of pattern-placed revetments under wave loading (Coeveld, 2003). One of the first and most simple stability equations is the force balance of a single element. This equation can be used to design a revetment on single element failure due to the uplift of the element. The stability equation is given in Equation 2.14 (Schiereck and Verhagen, 2019).

$$\frac{H_s}{\Delta D} = 3\frac{\cos\alpha}{\xi_{op}} \tag{2.14}$$

In which:

α	=	Angle of the revetment slope	[°]
ξ_{op}	=	Iribarren number for the offshore peak conditions	[-]

In this equation, the strength is solely determined by the self-weight of the block, while the load is determined by the uplift pressure on the block just before the wavefront during maximum run-down. Important to note is when this equation is applied, it often leads to conservative results. This is mainly because pressure release through pores and friction forces caused by neighboring blocks is not taken into account (Schiereck and Verhagen, 2019).

2.4.2. Black Box Models

In Pilarczyk et al. (1995) a new stability equation is derived that can be approximated by Equation 2.15.

$$\frac{H_s}{\Delta D} = f\left(\frac{D}{b}\frac{k'}{k}\right)\xi^{-0.67} = f\left(\frac{D}{\Lambda\,\xi}\right)^{0.67} \tag{2.15}$$

In Equation 2.15, it is observed that the leakage length comes into the equation, which is missing in the force balance equation. The paper mentions the equation can be used for pattern-placed revetments and block mats within the ranges $0.01 < k'/k < 1$ and $0.1 < D/b < 10$. The coefficient f is the stability coefficient and can be used in a range of $5 < f < 15$, for which a higher value refers to the presence of higher friction between the elements.

However, the practical applicability is limited as the permeability of the top layer is difficult to determine and some of the theoretical and empirical bases are poor. Also, Equation 2.15 is only usable for pattern-placed revetments on a granular filter. Therefore, the authors of the paper reduced the Equation 2.15 to Equation 2.16 and used large-scale model studies to determine the factor F for different cases. The results can be found in graphs in the paper (Pilarczyk et al., 1995).

$$\frac{H_s}{\Delta D} = F\xi_{op}^{-0.67} \tag{2.16}$$

In the pattern-placed revetment guidelines published in 2003 by TAW/ENW (Flikweert, 2003), Equation 2.16 is given as the '6-ksi-rule' by assuming 6 for F. This rule is suggested as an upper limit for relative open pattern-placed revetments and is derived from experiments in the Delta flume and results from ANAMOS (CUR, 1995). The 6-ksi-rule is generally sufficient conservative for top layers with little clamping (Flikweert, 2003).

Another black box model is proposed within the safety regulations for the assessment of dikes (Ministry of Infrastructure and Water Management, 2004). In comparison to the other described black box models, this model proposes two curves. One defining the boundary between safe and uncertain, and one defining the boundary between uncertain and unsafe. This models differs from the other models by assuming that plunging waves cause the most damage. As a result, the models will give the lowest stability number for an Iribarren number of 2.0. For Iribarren number larger than 2.0, the predicted stability number increases.

2.4.3. Beam Models

Next to black-box models which are equations fitted on data of experiments, there are also analytically derived equations. Vrijling et al. (2001) developed a model that describes the mechanical behavior of pattern-placed revetments on a dike under wave loading. In his paper, pattern-placed revetments are modeled as a beam on a stiff foundation. Using this model he finds two stability relations, one that describes the limit as imposed by the bending moment capacity and one that describes the limit as imposed by the shear capacity. As a result, the paper states that the interaction between blocks and the generation of normal force can increase stability by 35% with a coefficient of variation of 17% as confirmed by model tests. The paper also states that the loading history on a pattern-placed revetments is important, as loading will cause small realignments of the elements in the revetment which increases the stability of time. To keep the generated normal force, the stiffness of the toe is also important to maintain the normal force in the revetment.

Peters (2017) describes several experiments investigating the build-up of the normal force in revetments. He found that the lower elements in the revetment are more stable than higher elements due to the normal force generated by the elements above and that elements around the toe are generally less stable than expected due to the stiffness of the toe. In addition to this, it turned out that a lower outside temperature and a younger age of the revetment can also have a negative impact on the stability of the revetment. Also, a stiff and robust toe structure is a critical factor in developing the potential resistance of pattern-placed revetments, and that long gentle slopes have a lower in-plane force than short and steep slopes.

Wave impact:

$$N_x = r_8\rho_s g D B_y \left(0.5R_{u;2\%} + z_{SWL} - z\right) - r_6 P_{max} D B_y \not< c_{Nmin}\rho_s g D^2 B_y$$

Wave run-down:

$$N_x = r_8\rho_s g D B_y \left(0.5R_{u;2\%} + z_{SWL} - z\right) - r_7\rho_w g \phi_b D B_y \not< c_{Nmin}\rho_s g D^2 B_y$$

With:

$$r_6 = 0.25$$

$$r_7 = 0.10$$

$$r_8 = 0.8 - 0.1\left(\cot\alpha - 2.5\right)^{1.5} \not> 0.8$$

$$c_{Nmin} = \frac{5}{1 + \frac{1}{3}\cot\alpha}$$

$$0.5R_{u;2\%} + z_{SWL} \not> z_{top}$$

(2.17)

In his publication, Peters proposed the stability equation shown in Equation 2.17 with the following new findings:

- The stability curve $H_s/\Delta D$ versus breaker parameter ξ has an extra dependency on the slope angle α;
- The stability curve $H_s/\Delta D$ versus breaker parameter ξ has an extra dependency on the revetment thickness D;
- The tallness (D/B) plays a role, resulting in elements with larger tallness being more stable;
- Patterns with an overlap in the x-direction are better resistant.

Last, he notes that there are still differences in the performance of different types of elements. In particular, the column types of elements, as it is related to the ability of those columns to keep the joint fill and filter material in place.

2.4.4. SteenToets

SteenToets is a program to design pattern-placed revetments often used in the Netherlands. SteenToets is created and maintained by Deltares on behalf of the Dutch Ministry of Infrastructure and Water Management (Klein Breteler, 2020). Within Steentoets, all publications are combined into one model to assess and design pattern-placed revetments. The program can assess all kinds of failure mechanisms such as migration of material, shearing, and stability of the top layer. In this section, the focus will be on how the top layer stability is assessed.

Pattern-placed revetments on a filter layer are assessed for four different loading profiles, two representing wave impact and two representing wave run-down (Klein Breteler and Kaste, 2019). The loading profiles are based upon experiments with pressure sensors in the flume to expand SteenToets as part of the research program 'Kennisleemtes Steenbekledingen' (Klein Breteler and Van der Werf, 2006).

The most important difference between the two wave impact profiles is the trough at the seaward side of the impact. It is difficult to predict which of the two wave impacts profiles is the most representative. Therefore, both profiles are used within SteenToets. The same goes for the wave run-down profiles, and again there are two types of wavefronts, steep and high. Depending on the leakage length, either one may have the largest impact on the stability of the revetment. Therefore, both are also used when assessing a revetment within SteenToets (Klein Breteler and Van der Werf, 2006).

Using those four loading profiles as loading on the top layer, SteenToets uses an analytical solution to the differential Equation 2.11 to determine the filter response pressure. SteenToets assumes the filter layer thickness to be constant, this is an important assumption as this will lead to a constant leakage length as the top layer thickness and the permeability of the top and filter layer is also constant (Klein Breteler and Kaste, 2019). Taking the difference between the loading profile and the filter response will yield the residual pressure on the elements.

The first step in assessing the stability of the top layer is to check whether the pattern-placed revetment is still stable when the element is loose. In this case, a force balance between the self-weight of the element, the pressure by the wave loading, and the filter pressure as described in the previous paragraph is considered. If the revetment is deemed to be stable, the self-weight of the element is sufficient to prevent the element from being lifted (Section 2.3). If this is the case, the revetment is considered to be stable. If this is not the case, the residual strength of the top layer, filter layer, and clay layer is calculated to check whether the revetment and the clay layer are strong enough to resist a storm if a hole occurs due to the uplift of some elements. If the residual strength is not sufficient, the impact of clamping is determined, and the resistance of the elements with clamping is assessed (Peters, 2007). If the revetment with the impact of clamping is considered stable, the revetment is found to be safe (Klein Breteler and Kaste, 2019).

3

Damaged Pattern-Placed Revetments

In this chapter, a qualitative analysis of the impact damages have on pattern-placed revetments is done. First in Section 3.1 the methodology of this chapter is outlined. Next, in Section 3.2 the framework used in the qualitative analysis is introduced. In Section 3.3, the different components of the framework are defined for pattern-placed revetments. In Section 3.4, the different types of damages are analyzed using the framework. Finally, in Section 3.5 the results are discussed, and some final remarks are given.

3.1. Methodology

This chapter aims to identify the different types of damage that can occur on a pattern-placed revetment, how they are caused, and the qualitative effect on top layer stability. These objectives will be achieved by performing a qualitative analysis with a framework developed upon the paper 'Time-dependent reliability analysis of flood defences' by Buijs et al. (2009) and the report 'A semi-probabilistic assessment rule for the stability of block revetments under wave attack' by Jongejan and Klein Breteler (2015). The different types of damage are identified by doing a literature review on the different maintenance guidelines and publications. Based on this literature review and with the use of the framework, we will relate how each damage is caused and what the qualitative effect is on the top layer stability.

3.2. Framework for Qualitative Assessment of Damages

In this section, we present the framework we will use to assess the different types of damage. We structure our analysis using the framework sketched in Figure 3.1. This framework is based upon the earlier mentioned paper by Buijs et al. (2009) and the report by Jongejan and Klein Breteler (2015).

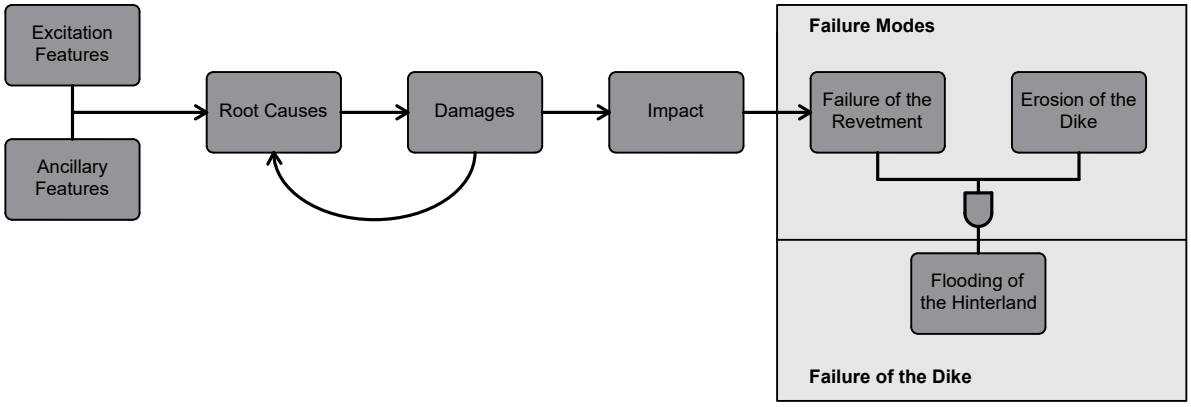

Figure 3.1: Lay-out of the used framework to qualitatively assess the different types of damage

In the next part, we will briefly explain the different parts of the framework. In our framework, **damage** is a physical state of the structure different from the initial state. This change often has a negative impact on the resistance of the structure. Examples of damages could be a missing element, deformation, or washed-out joint filling for pattern-placed revetments.

Damage does not occur all at once; it is a process that develops over time. Therefore, the process leading up to this change in the physical state we identify as the **root cause**. For example, when we observe a deformed revetment, a root cause could be that this deformation occurred due to consolidation of the body of the dike or due to migration of the filter material within the filter layer. In some cases, damage may have an incentive effect on other root causes, allowing other damages to develop faster. For example, it becomes easier for filter material to migrate through the top layer if the joint filling is washed out. When damage has an incentive effect on one of its root causes, a positive feedback loop will occur, allowing the damage to increase in intensity quickly.

Behind every root cause, there are two types of features unrelated to damages which are the main drivers: excitation features and ancillary features. Both are based on the paper of Buijs et al. (2009) in which **excitation features** are defined as ”flood defence properties that actively initiate or drive the time-dependent process” (Buijs et al., 2009). Examples of excitation features are the wave climate, river current velocities, and third-party interference. Next, **ancillary features** are defined as ”flood defence properties that additionally influence the time-dependent process by transforming the excitation features into the time-dependent process” (Buijs et al., 2009). Examples of ancillary features may be the slope of the revetment, the thickness of the top and filter layer and the mass of the elements.

With the above described four definitions, we can describe within our framework how damage occurs. However, a damaged revetment does not lead to immediate failure of the dike, nor does it always lead to failure of the revetment. Therefore, for each type of damage, we first relate it to the **impact**, which is the impact the damage has on the stability of the revetment. In the case of pattern-placed revetments, damage may either impact the stability by affecting the loading or resistance of the revetment.

If the impact is significant enough, it may lead to **failure of the revetment**. The exact definition of when a pattern-placed revetment fails is a grey area and difficult to define. Therefore, our analysis will not define when a revetment fails but only acknowledge that failure will eventually happen when the impact becomes too large.

Failure of a dike is commonly defined as **flooding of the hinterland** (CIRIA, 2013). Therefore, when a revetment fails, it does not lead to immediate failure of the dike as there is some residual strength left in the body of the dike. Within our framework, we simplified the residual strength into **erosion of the dike**. It should be noted that this is a simplification of a complex failure mode based on a more comprehensive analysis and fault tree by Jongejan and Klein Breteler (2015). Only when the revetment has failed and the body of the dike is eroded, the dike will fail.

3.3. Defining the Components of the Framework

In this section we will define the different components of the framework discussed in the previous section. We will apply the framework to qualitatively assess the impact of damages on the top layer of pattern-placed revetments. Within our analysis we will consider the process from the excitation and ancillary features up to failure of the revetment.

3.3.1. Excitation and Ancillary Features

First, we will consider the excitation and ancillary features. Because little is known about damages on pattern-placed revetment, it is difficult to relate what the impact is of, for example, a change in slope or top layer thickness on the different root causes. Therefore, we will acknowledge that ancillary features exist but do not directly relate them to the different root causes. For the excitation features, we will consider the following list:

- **Wave Climate:** loading by the wave impact and run-down of waves.
- **Other Environmental Influences:** environmental influences not related to waves. (UV radiation, temperature differences, growth of vegetation, etc.).
- **Construction Errors and Structural Degradation:** degradation of the structure over time or caused by errors made during construction and maintenance.
- **Third-party interference:** degradation of the structure caused by third parties.

3.3.2. Root Causes

The second step is to compose a list of root causes based on our findings in Section 2.1.4. Next, we complemented this list using the publications describing maintenance procedures for different types of damage by Van Der Meer and Moens (1990) and Klein Breteler (2018). This leads to the list of root causes shown below:

- Pressure differences over the top layer
- Migration joint filling through the top layer
- Migration filter material within the filter layer
- Migration filter material through the top layer
- Migration core material into the filter layer
- Material fatigue
- Washing-up of objects
- Consolidation and creep
- Deformation of the toe construction
- Shearing of the revetment
- Liquefaction
- Growth of woody vegetation
- Growth of non-woody vegetation
- Vandalism

3.3.3. Damages

The third step is to compose a list with all damages for pattern-placed revetments. We based our list on the following three publications:

1. Van Der Meer and Moens (1990) wrote a catalog describing damages for several different types of revetments. For a basalt revetment, it gives a brief overview with several types of root causes and damages. The catalog also provides an overview of damages relating to transitions between different types of revetments.

2. Klein Breteler (2018) describes in the report 'Maintenance requirements for revetments on dikes' different kinds of damages relating to basalt and Basalton revetments. The report also includes experience-based recommendations when different damages should be repaired.

3. The DigiGids (Waterschapshuis, 2019) is a catalog to identify and classify damages on revetments developed by STOWA and the Dutch Department of Public Works (Rijkswaterstaat).

For now, we will only show a list of the different types of damage down below. Then, in Section 3.4, we will further touch upon the damages and lay relations with the root causes and the impact using our framework.

- Missing elements
- Partial uplift of elements
- Damaged elements
- Washed-out joint filling
- Wide joints between elements
- Clogged top or filter layer
- Deformation of the revetment
- Rotation of elements

3.3.4. Impact

The fourth step is to identify in what ways damages can affect the stability of the revetment. Based on the literature review in Chapter 2, we can identify four different ways this can happen. The first three are related to the resistance of an element and the fourth one to the loading. As discussed in Section 2.3, an element's resistance consists of three components: self-weight, clamping, and block-filter friction. As a result, damages can affect the resistance of the revetment by affecting one of these three components. In addition to this, from Section 2.2.3, it is known that a change in leakage length affects the filter pressure. Therefore, when damages can affect one of the parameters related to the leakage length, it is possible that the filter response changes in a negative way, causing more residual pressure on the elements during the wave loading. In conclusion, the stability of the revetment can be affected by damages in the following four ways:

- Self-weight
- Clamping
- Block-Filter friction
- Leakage length (Loading)

3.3.5. Failure of the Revetment

Our final step is to identify failure of the revetment. It is a difficult objective to do this quantitative, therefore we will assess failure of the revetment qualitative. First, we consider the purpose of an outer slope revetment, which is to protect the outer slope from erosion (Schiereck and Verhagen, 2019). Consequentially, failure of the revetment does imply the moment waves are able to erode the outer slope. Although it is not exactly clear at which point this moment happens, based on flume experiments done by Klein Breteler and Eysink (2007) show that revetments with some missing elements are still able to fulfill their function. In conclusion, within our framework we assume that when the impact of damages on the stability of the revetment becomes too large, the revetment fails.

3.4. Analysis of the Damages

With the components of the framework identified, the different types of damage are in this section qualitatively analyzed. During the analysis, we will discuss the how the damage is caused and what the expected impact is based on the physics. At the end of the section, all findings are summarized in Figure 3.10. For each damage a cross-section is provided with different colors of arrows used to indicate the impact. The following color-coding is used:

- **Red arrows** indicate the migration of either filter material, joint filling or core material;
- **Orange arrows** indicate the displacement of the revetment;
- **Green arrows** indicate the force created by the resistance. A reduction of this force is denoted by a grey dashed line;
- **Blue arrows** indicate a change in the loading.

3.4.1. Missing Elements

When elements are fully lifted from the revetment, they leave a hole behind, exposing the filter layer to wave loading. In the left pane of Figure 3.2, an example of a missing element is shown, and in the right pane, the impact on the stability is illustrated.

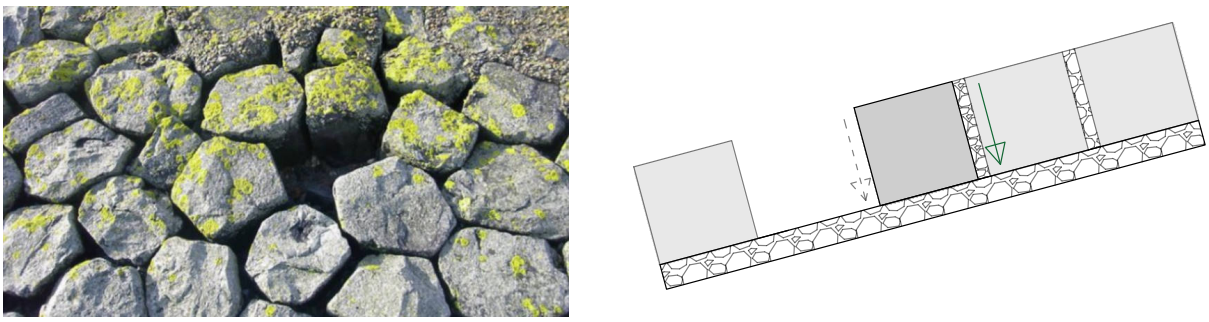

Figure 3.2: Missing elements (left, Waterschapshuis, 2019) causes a loss of clamping (right)

When elements are fully uplifted from the revetment, this is typically caused by a pressure difference over the top layer due to wave impact or wave run-down. In addition, some other less common root causes may cause the element to be lifted from the revetment, such as the growth of woody vegetation or vandalism (Klein Breteler, 2018). Due to the missing element, the elements surrounding the hole in the revetment experience a reduction in clamping. Based on the physics, it is expected that the normal force within the revetment will be redirected around the hole due to the arching of the elements. This may cause elements below the hole to experience less normal force than they usually would.

3.4.2. Partial Uplift of Elements

Partially uplifted elements are elements that are partially protruding above the revetment. In the left pane of Figure 3.3 an example of a partially uplifted element is shown, and in the right pane, the impact on the stability is illustrated.

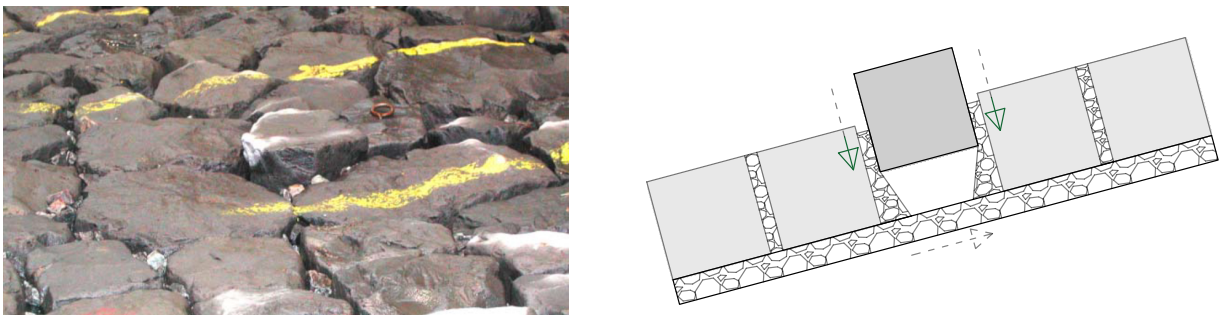

Figure 3.3: Partially uplifted elements (left, Klein Breteler and Eysink, 2005) causes loss of clamping (right)

Partially uplifted elements are typically caused by a pressure difference over the top layer due to wave impact or run-down. In addition, some other less common root causes may cause the element to be partially lifted from the revetment, such as the growth of woody vegetation or vandalism. As the elements protrude above the revetment, they experience less clamping and are therefore at risk of being fully lifted from the elements. In some cases, elements cannot fall back into their original place as joint filling and filter material may migrate under the element's open space.

Missing and partially uplifted elements are a common type of damage in the field and are also well documented in old flume experiments. It is also believed that those types of damage may have a significant impact on the stability of the revetment. Therefore both types of damage will be assessed further in-depth in the following chapters.

3.4.3. Damaged Elements

Elements can be damaged in different ways, the most common two kinds of damaged elements are chipped-off corners or elements broken in half (Waterschapshuis, 2019). In the left pane of Figure 3.4, both types of damaged elements are illustrated, and in the right pane, the impact on the stability is illustrated.

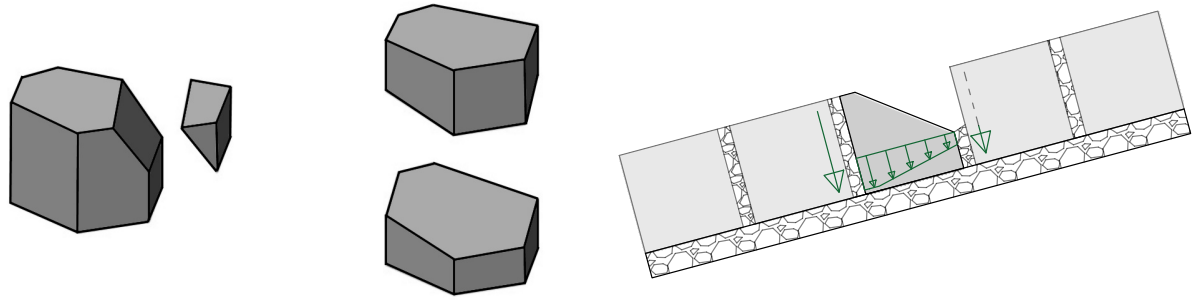

Figure 3.4: Elements with chipped off corners or broken in half (left) and can cause a reduction in clamping and self-weight (right)

Damages to elements are primarily caused due to material fatigue. Examples of aspects contributing to material fatigue are temperature differences, UV radiation from the sun, and constant wave loading. Occasionally, elements can get damaged by other root causes such as washing up of debris or vandalism. The consequences for damaged elements could be reduced clamping due to less contact area and decreased self-weight due to the parts broken off the elements.

3.4.4. Washed-out Joint Filling

Joint filling is granular material used within the joints between the elements to enhance clamping. However, the joint filling may come loose and wash out because elements translate and rotate under wave loading. In the left pane of Figure 3.5, an example of a revetment with washed-out joint filling is shown, and in the right pane, the impact on the stability is illustrated.

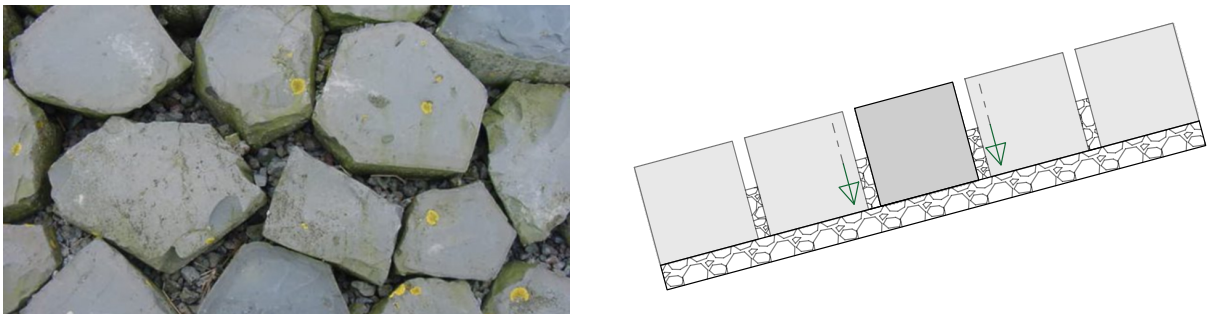

Figure 3.5: Washed-out joint filling (left, Waterschapshuis, 2019) cause a loss of clamping (right)

Washed-out joint filling is typically caused by wave loading on the revetment. Pressure difference over the top layer can result in the translation or rotation of elements, which may loosen the joint filling. Consequentially, turbulence caused by the wave loading may wash out the joint filling that is not clamped enough out of the joints. Additionally, joint filling may be pushed out the joints by the growth of woody vegetation or removed due to vandalism. When a revetment is (partially) washed-out, the clamping between the elements reduces, which increases the risk of elements being lifted up from the revetment (Klein Breteler, 2018). An additional purpose of joint filling is to act as a geometrically closed filter for the filter material (Cirkel et al., 2015). Therefore, washed-out joint filling affects the root causes related to the filter material as without joint filling, the filter material can easier migrate out of the top layer.

Washed-out joint filling is a common and important type of damage and well-reported during old flume experiments. Therefore, this type of damage will be assessed further in-depth in the following chapters.

3.4.5. Wide Joints between Elements

Due to various root causes, such as deformation, the joints between elements may become wider. In the left pane of Figure 3.6, an example of a revetment with wider joints than usual is shown, and in the right pane, the impact on the stability is illustrated.

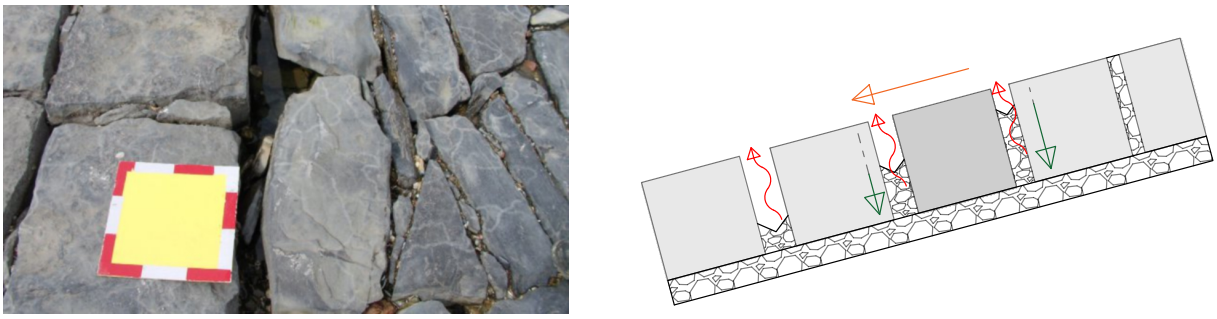

Figure 3.6: Wider joints (left, Waterschapshuis, 2019) can cause a reduction in clamping and easier migration of the joint filling (right)

Widening of joints can occur due to shearing of the revetment, which may be the result of a deformed toe. Additionally, deformation or the growth of woody vegetation can push elements away from each other, resulting in wider joints. Wide joints will negatively affect the clamping of the revetment as the clamping by the joint filling decreases or even entirely disappears. In addition to this, wide joints affect the migration of joint filling over the top layer. Because the joint filling is less clamped, the migration out of the top layer becomes easier (Klein Breteler, 2018). The widening of joints may impact the loading on the revetment as it changes the permeability of the top layer of the revetment. It also impacts the root causes related to the filter material and joint filling, as the widening of joints will result in less clamped joint filling allowing for better migration of the filter material and joint filling.

3.4.6. Clogged Top or Filter Layer

Over time, the joint filling and the filter may get clogged. This will affect the way the filter pressure will respond to the wave loading, as explained in Section 2.2.3. In the left pane of Figure 3.7, an example of a revetment with a clogged top layer is shown, and in the right pane, the impact on the stability is illustrated.

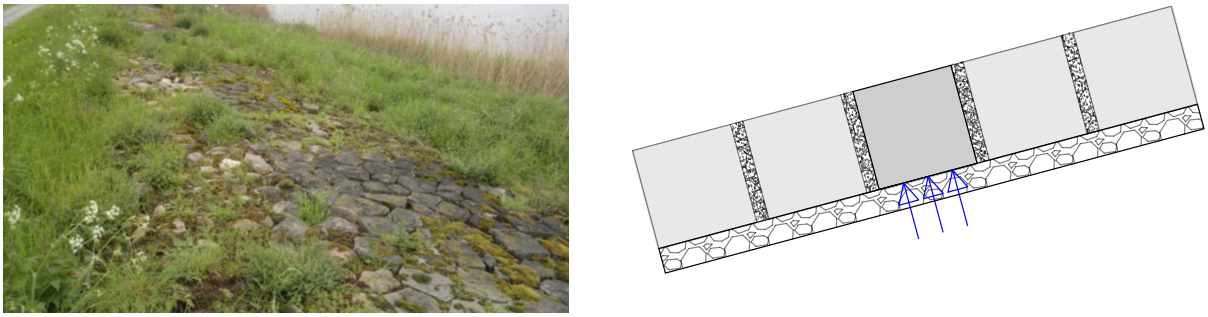

Figure 3.7: A clogged top layer (left, Waterschapshuis, 2019) may change the loading on the elements (right)

Clogging of the top and filter layer is usually caused by the growth of non-woody vegetation or by the washing up of sand caused by the waves. In addition to this, the filter layer may also experience clogging from the migration of the core material. However, this is often easy to prevent by using a geotextile. A clogged top or filter layer impacts the leakage length, therefore the filter response, and thus residual pressure changes on the elements. Furthermore, a clogged filter layer may affect the root cause liquefaction as the top layer becomes less permeable, and higher pressures within the filter layer and dike body can build up.

3.4.7. Deformation of the Revetment

When a part of the revetment is subsided or lifted up, we call this deformation. In the left pane of Figure 3.8, an example of a deformed revetment is shown, and in the right pane, the impact on the stability is illustrated.

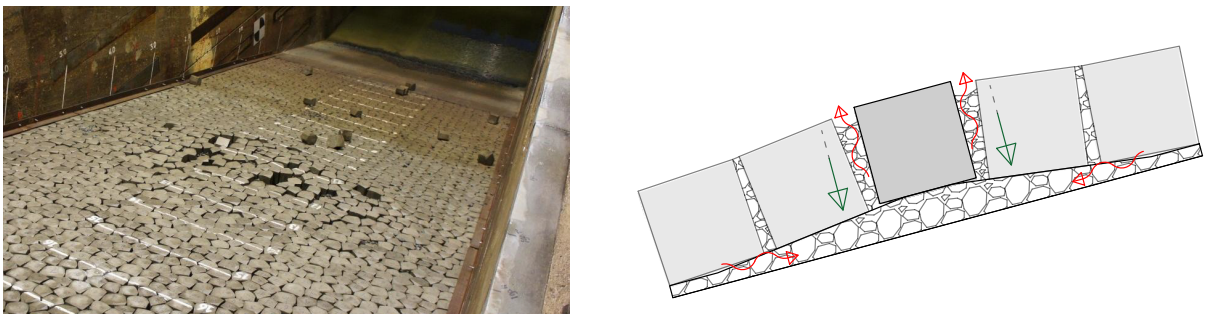

Figure 3.8: Deformation of a revetment (left, Wolters, 2016a) decreases the clamping and causes easier migration of the joint filling (right)

Deformation occurs mainly due to two root causes. The first root cause is the migration of filter material within the filter layer. Due to wave loading, currents will develop within the filter layer, which will transport filter material. The filter material can migrate because, during wave impact or wave run-down, the residual pressures on the element will lift the elements from the filter layer. A second root cause is the consolidation of the soil, which happens over time. In general, deformation will decrease the clamping of elements. In case deformation is caused by filter migration, the changes in filter layer thickness over the slope will also affect the residual loading on the elements. Furthermore, deformation may make it easier for the joint filling to be washed-out as joints become wider.

Deformation, especially the formation of the S-profile at the wave impact location, is a common and important type of damage for a column-type pattern-placed revetment. The formation of the S-profile is also well-reported during old flume experiments. Therefore, this type of damage will be assessed further in-depth in the following chapters.

3.4.8. Rotation of Elements

Rotation of elements often occurs when the support at the bottom of the revetment is displaced. In the left pane of Figure 3.9, an example of rotated elements is shown, and in the right pane, the impact on the stability is illustrated.

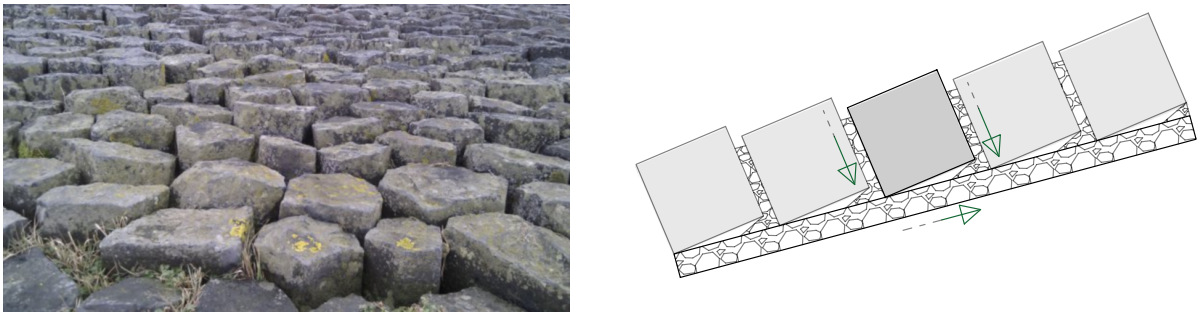

Figure 3.9: Rotation of elements (left, Waterschapshuis, 2019) decreases the clamping and friction with the filter (right)

Shearing of the revetment can cause rotation of elements. Often, the revetment can shear because the support at the toe is lost due to a displaced or deformed toe structure. As a result of this type of damage, the top of the element will shift more towards the toe than the bottom, causing a rotation. This rotation negatively impacts the friction with the filter and clamping of the revetment (Flikweert, 2003). In addition to this, it will also give space to the joint filling to migrate under the elements, which creates less area of contact.

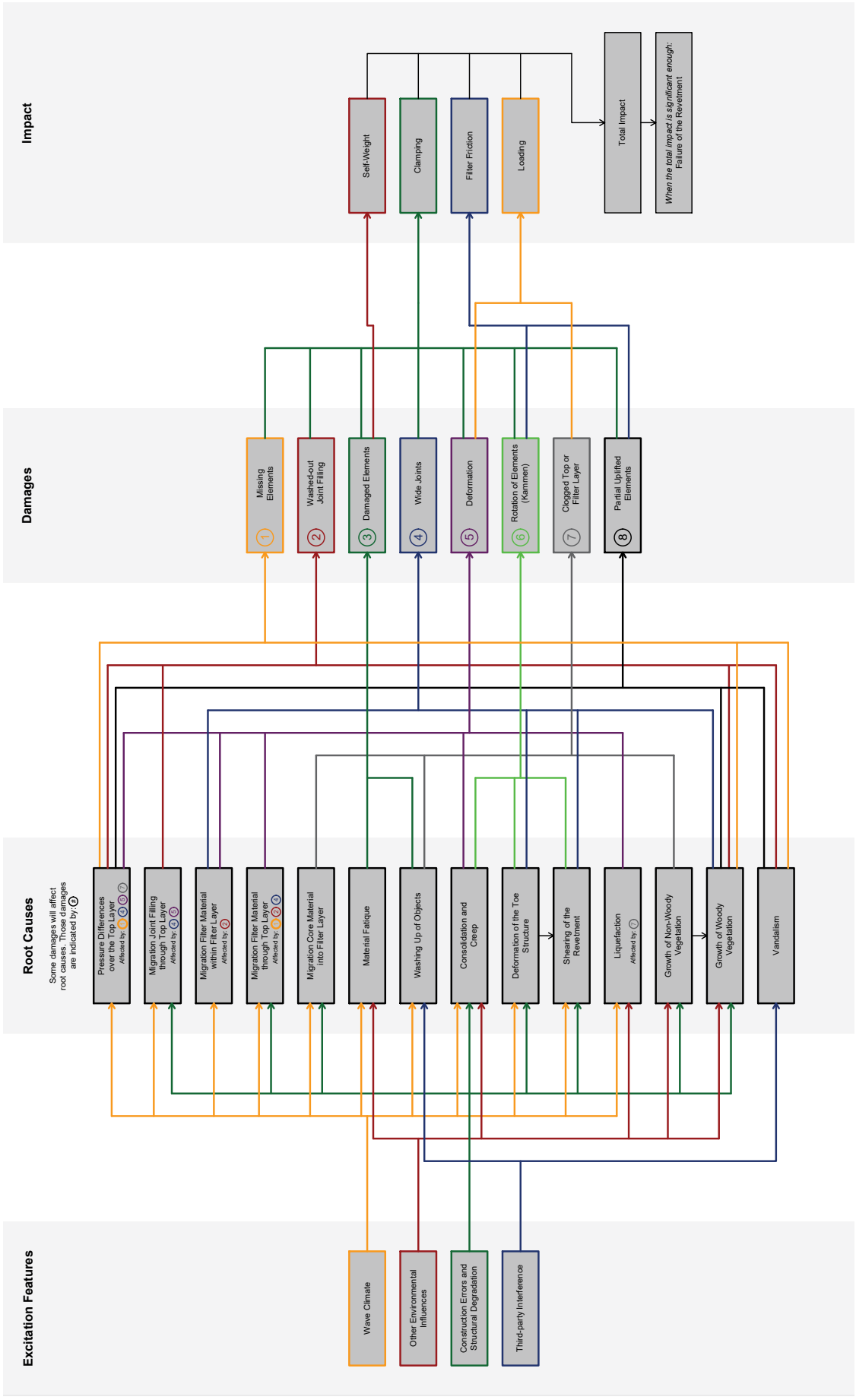

Figure 3.10: Relations between the excitation features, root causes, damages and the impact on the stability of the revetment

3.5. Concluding Remarks and Summary of Findings

This chapter aims to qualitatively assess the different types of damage for a pattern-placed revetment. Using our framework, we identified for eight common types of damage, the root causes, and the impact on the stability of the revetment. This analysis is summarized in Figure 3.10.

As the last part of the qualitative analysis, we would like to touch upon the results. Within our analysis, we found two positive feedback loops. The first feedback loop is for deformation and the root cause migration of filter within the filter layer. For deformations caused by migration of the filter layer, the filter layer thickness varies along the slope. This also impacts the leakage length along the slope and thus the wave loading. Areas to which the filter material migrates will get a thicker filter layer increasing the residual loading on the elements at these areas. As a result, those elements are more prone to be lifted from the filter layer during wave impact, allowing more filter material to migrate towards this area, increasing the thickness of the filter layer. Eventually, this will lead to the failure of the revetments as the elements are fully uplifted by the increased residual pressure and the reduced clamping.

The second positive feedback loop is between the uplift of elements and the pressure over the top layer. When an element is removed from the revetment, it leaves a hole behind. This hole will affect the neighboring elements as they experience less clamping due to less contact area. As a result, these elements are more prone to be also uplifted from the revetment. Therefore, this feedback loop could induce a domino effect of elements being lifted from the revetment. It is expected that this only happens when the revetment is loaded close to its stability number. When the revetment is subjected to a lower loading, it is expected that the elements do have enough residual resistance from a combination of the self-weight and the reduced clamping.

Last, we would like to discuss the growth of vegetation. Based on the analysis, the growth of non-woody vegetation mainly causes clogging of the top and filter layers, which is not mainly a critical type of damage. However, if non-woody vegetation is not well maintained, it can grow into woody vegetation, which does have severe consequences for the stability of the revetment (Klein Breteler, 2018). Woody vegetation can cause the uplift of elements and also make it easier for the joint filling to migrate out of the joints by either pushing it out of the joints with the roots or loosening the joint filling by widening the joints. Additionally, the growth of non-woody vegetation can also make the revetments more challenging to inspect as damages can be hidden by the vegetation. In conclusion, although the growth of non-woody vegetation does not seem like a critical root cause, it is vital to maintain it well.

4

Analysis of Old Flume Experiments

In the previous chapter, different types of damage for pattern-placed revetments were qualitatively analyzed within a framework. This chapter will continue this analysis by reviewing and parameterizing the most common types of damage using data from old flume experiments.

First, in Section 4.1 the methodology is introduced. Next, in Section 4.2, the used flume experiments are listed. In Section 4.3, the different experiments are analyzed, and in Section 4.4, the data of damages during the experiments are analyzed. All this is summarized in a summary of findings in Section 4.5.

4.1. Methodology

This chapter aims to analyze and parameterize the most common types of damage based on old flume experiments (Figure 4.1). The analysis and parameterization of damages are essential as the results will be used in the next chapter to model the damages in the finite element model. In order to accomplish this goal, we will first collect data from old flume experiments. It is chosen to collect data from old Basalton, and basalt experiments as both are a common type of revetment in the Netherlands and have been tested regularly in the past. The data from the old flume experiments were primarily found in online repositories. Deltares also provided some data when some data could not be obtained from the report.

By analysing the data of the flume experiments, it turned out three types of damage are well reported in all research programs: uplifted elements, deformation, and the washing out of joint filling. Based on Chapter 3, it also turns out that those damages are expected to be able to have a significant impact on the stability of a revetment. It is therefore chosen to focus the analysis on those three types of damage. All data regarding those damages are collected and put into an Excel sheet and can also be found in Appendix A. The data is analyzed and parameterized with the use of Python.

Figure 4.1: Basalton STS+ revetment in the Delta flume (Kaste and Mourik, 2016)

4.2. Flume Experiments

In this section, we will list all flume experiments we will use in this chapter. Chosen is to only include flume experiments with simple slopes in this analysis to ensure consistency of the data. This means that flume experiments with shallow foreshores, low berms, and other anomalies are excluded from the data set. In total, 56 suitable experiments with a Basalton revetment and 33 suitable experiments with a basalt revetment were found in 6 research programs. A summary of those research programs is given below:

(1) Stability of a Basalton 30 STS revetment under wave loading
Wolters (2016a)
This research program contains 13 experiments executed on a scale of 1:2 as part of a program to determine the stability of modern types of pattern-placed elements (Vergelijkend Onderzoek Zetsteen). The goal of this research program is to test the stability of Basalton STS elements. The experiments were done in the old Deltagoot in De Voorst in 2013 and 2014.

(2) Stability of a Basalton 30 STS+ revetment under wave loading
Kaste and Mourik (2016)
This research program contains 14 experiments executed on a scale of 1:1.6 as part of a program to determine the stability of modern types of pattern-placed elements (Vergelijkend Onderzoek Zetsteen). The goal of this research program is to test the stability of Basalton STS+ elements. The experiments were done in the new Deltagoot in Delft in 2015.

(3) Residual strength of a pattern-placed revetment with initial damage
Klein Breteler and Eysink (2007)
This research program contains 4 experiments on a scale of 1:1 as part of a program to learn more about the behavior of pattern-placed revetments (Onderzoeksprogramma Kennisleemtes Steenbekledingen). During the experiments, artificial damage is created by removing elements to analyze how the damaged revetment behaves. The experiments were performed on a Basalton SS/VS revetment in the old Deltagoot in De Voorst.

(4) Long-term strength of pattern-placed revetments
Klein Breteler and Eysink (2005)
This research program contains 30 experiments on a scale of 1:1 as part of a program to learn more about the behavior of pattern-placed revetments (Onderzoeksprogramma Kennisleemtes Steenbekledingen). The specific goal of those experiments was to analyze the stability of pattern-placed revetments under wave loading over a long period. This research program contains both experiments with Basalton SS/VS revetments and basalt revetments. The experiments were done in the old Deltagoot in De Voorst.

(5) Flume research to the stability of basalt, phase 1 and 2
Eysink and Klein Breteler (2003)
This research program contains 24 experiments on a scale of 1:1 as part of a program to learn more about the behavior of pattern-placed revetments (Onderzoeksprogramma Kennisleemtes Steenbekledingen). The specific goal of those experiments was to determine the strength of both a Basalton SS/VS revetment and basalt revetment under wave loading. The experiments were done in the old Deltagoot in De Voorst.

(6) Residual strength of a clay dike with a pattern-placed revetment
Wolters and Klein Breteler (2011)
This research program contains 4 experiments on a scale of 1:1 as part of a program studying important aspects of the strength and loading of a dike (Sterkte en Belastingen Waterkeringen). The specific goal of those experiments was to determine the residual strength of a clay dike with a Basalton STS revetment. After the first four experiments, the Basalton revetments failed. Therefore only the first four experiments will be included in the data set. The experiments were done in the old Deltagoot in De Voorst.

4.3. Data of the Experiments

For all research programs, data on the used geometry of the flume experiments are collected from the corresponding reports. This chapter will touch upon the geometry of the used models in the flume and the used top layer elements. At the end of this section, a table can be found summarizing the most important data on the studied flume experiments. (Table 4.1).

Revetment Model in the Flume

For each research program, the structure of the revetment model is almost identical. The core of the model in the flume is made of sand. A sand-cement mixture in most cases replaces the clay layer. The sand-cement mixture creates a layer with similar characteristics to clay (Kaste and Mourik, 2016). On this layer, a geotextile is placed, followed by the granular filter and the top layer. The slope at the upper and lower end of the revetment is made of concrete. As a result, the revetment is supported by a (concrete) stiff toe. Because Basalton and basalt are column-type pattern-placed revetments, the joints between the elements are washed in with granular material. The slopes used within the experiments are either 1:3 or 1:3.5.

The top and bottom of the revetment will be expressed as the dimensionless top and bottom levels ($z_{top;d}$ and $z_{bot;d}$). This is required as the flume experiments are performed on different scales, ranging from 1:1 to 1:2, depending on the research program. The top and bottom levels are made dimensionless with the water depth using Equation 4.1 (Figure 4.2).

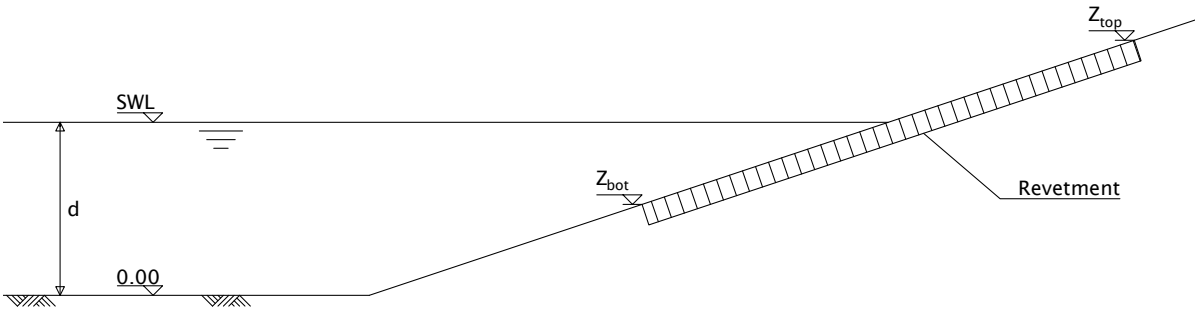

Figure 4.2: Parameters required to determine the dimensionless top and bottom levels (Equation 4.1)

$$z_{top;d} = \frac{z_{top} - d}{d} \qquad z_{bot;d} = \frac{z_{bot} - d}{d} \tag{4.1}$$

Based on the collected data, an average dimensionless top level of 0.26 and an average dimensionless bottom level of -0.55 were found. It should be noted that the no significant differences were found when comparing the dimensionless top and bottom level of Basalton and basalt experiments.

The leakage length will be expressed as the dimensionless leakage length (Λ/D) to account for scaling. On average, the dimensionless leakage length for the Basalton STS(+) experiments is 1.3 meters, and for the Basalton SS/VS and basalt experiments the average leakage length is 2.5 meters. The leakage length is retrieved from the report, and if not available, calculated based on parameters given in the report using the method described in the SteenToets documentation (Klein Breteler and Kaste, 2019).

Top Layer Elements

There are four different types of top layer elements within the selected experiments for this study: Basalton STS, Basalton STS+, Basalton SS/VS, and basalt. Below, the difference between the three different Basalton sets will be discussed. Basalt elements are already discussed in Section 2.1.3.

Basalton SS/VS (Steunset / Vervolgset) is the first set of Basalton elements. The 'Vervolgset' (VS) variant is mainly used in a Basalton revetment. The 'Steunset' (SS) variant is used along the edges of the revetment because it has one straight edge, which will provide a good connection to the adjacent revetment (the bottom edge in Figure 4.2).

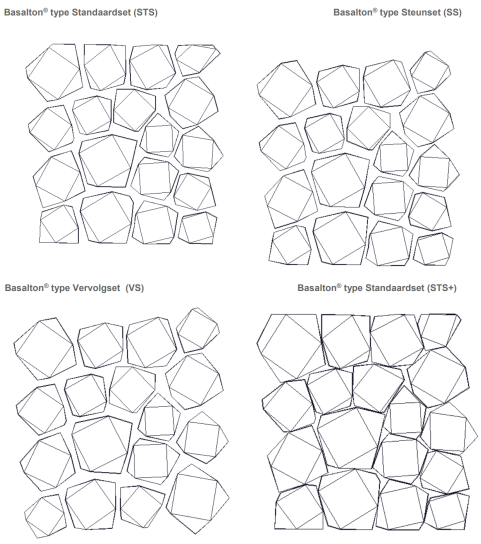

Figure 4.3: Different Basalton sets (KOMO, 2018)

Basalton STS (Standardset) was released in 2004. The average percentage of open area for the STS variant is about 10%. The advantage of the STS variant over the SS/VS variant is that it is easier to place on curved dike segments due to the straight line at the bottom and the top of the set. In addition to this, no longer specific set for the edges is required.

Basalton STS+ (Standardset+) was released in 2016 and is an improved version of the STS variant. The main difference between the STS and STS+ variants is the shape of a few elements. The main benefit of this change is that the distribution of the open spaces is more equally divided over the STS+ set. The mean percentage of open area is about 10%, which is similar to the STS variant.

Data on Used Models

Below, Table 4.1 summarizes the most important data on the studied flume experiments. A more detailed overview of the data can be found in Appendix A.

Program / Top Layer		Slope [-]	Exp[1] [-]	H_s[2] [m]	D [m]	b [m]	Λ [m]	ρ_s [kg/m^3]	Df;15[3] [m]	Di;15[4] [m]
			3	0.62 - 1.12	0.15	0.095	0.20	2293	0.014	0.009
(1)	STS	1:3	4	0.67 - 1.18	0.15	0.069	0.14	2293	0.007	0.009
			6	0.70 - 0.90	0.15	0.071	0.16	2293	0.011	0.009
(2)	STS+	1:3	14	0.75 - 1.96	0.18	0.079	0.24	2297	0.011	0.006
(3)	SS/VS	1:3.5	4	1.47 - 1.53	0.20	0.12	N/A	2827	0.022	0.005
(4a)	SS/VS	1:3.5	14	1.22 - 1.42	0.20	0.12	0.50	2827	0.022	0.005
(5a)	SS/VS	1:3.5	7	0.70 - 1.57	0.20	0.12	0.52	2827	0.022	0.007
(6)	STS	1:3.5	4	1.00 - 1.60	0.15	0.07	0.32	2388	0.015	0.008
(4b)	Basalt	1:3.5	16	0.88 - 1.66	0.20	0.12	0.50	2955	0.022	0.005
(5b)	Basalt	1:3.5	17	0.66 - 1.74	0.20	0.12	0.52	2955	0.022	0.007

Table 4.1: Data on the model setup of the analyzed Basalton and basalt flume experiments

[1]: The number of flume experiments within the research program

[2]: Range of the significant wave height in the experiments

[3]: The diameter where 15% of the filter material is smaller

[4]: The diameter where 15% of the joint filling material is smaller

4.4. Analysis of Damage occurred in Flume Experiments

In this section, the data collected on the damages will be analyzed and parameterized. First, in Section 4.4.1, two ways of measuring damage over time are compared to find the most suitable way to analyze damage over time. Next, three of the most common types of damage are analyzed. In Section 4.4.2, the uplift of elements, in Section 4.4.3 washing out of the joint filling, and in Section 4.4.4 deformations of the revetment.

4.4.1. Development of Damage over Time

In order to study the progression of deformation and the washing out of joint filling, we combined the experiments into groups. Within one group, all experiments are collected between two interventions done at the revetment. We made two sets of groups, one for deformation and one for joint filling (Figure 4.4). This is necessary because it turned out that more often is intervened to wash in the joint filling than to remove the deformation. With the use of those groups, we will study the development of damage over time.

Research Program	Basalton STS													Basalton STS+					
Experiment	P01	P02	P03	P04	P05	P06	P07	P08	P09	P10	P11	P12	P13	B01	B02	B03	B04	B05	...
Joint Filling	1	2	3	4	5	6	7	8	9			10		11	12	13	14	15	...
Deformation	1			2				3						4					...

Figure 4.4: Combining all experiments in groups based on when certain types of damage are repaired

In the case of waves breaking on a slope, it is expected that the damage will become slightly more prominent for each wave attack. This raises the question of what time scale should be used to quantify damage over time. To answer this question, we will consider two time scales and compare them to each other. First, we consider a time scale based upon the number of waves. This time scale is the most common and is used in well-known equations. An example is the Van der Meer equations (Van der Meer, 1988), which are used to determine the required diameter of rubble mound on a slope taking into account damage development and the number of waves. Reasons to use the cumulative number of waves are because it is often known, and when it is unknown, it can be easily estimated.

However, the cumulative number of waves does not say anything about the impact each wave has on the slope. Based on Section 2.2.2.4, the height of a wave also plays an important role in the magnitude of impact. Therefore, we hypothesize that a time scale based on wave energy can better describe the progression of damage. Based on this, the second time scale we consider is the cumulative wave energy, which is proportional to the number of waves times the amplitude squared (Bosboom and Stive, 2015). An important assumption for the second time scale is that the energy of a propagating wave is related to the load of the wave on impact. An energy-based time scale is proposed in Equation 4.2, which takes into account the significant wave height for each experiment i for each group of x experiments.

$$E_{wave} \propto a^2 \propto H^2$$
$$E_{tot} \propto \sum_{i=1}^{x} n_i \cdot H_{s;i}^2 \tag{4.2}$$

Both time scales are compared against each other in Figure 4.5. Over the x-axis, we illustrated the cumulative number of waves, while over the y-axis, we illustrated the cumulative wave energy. Then for all experiments, we calculated the cumulative number of waves and the cumulative wave energy after the experiment and illustrated this as a point in the graph. The results show that there is a linear relationship between both time scales. This demonstrates that although we thought that the cumulative wave energy could better describe the progression of damage over time, it does not differ much from the cumulative number of waves. Therefore, we will use the cumulative number of waves in the study.

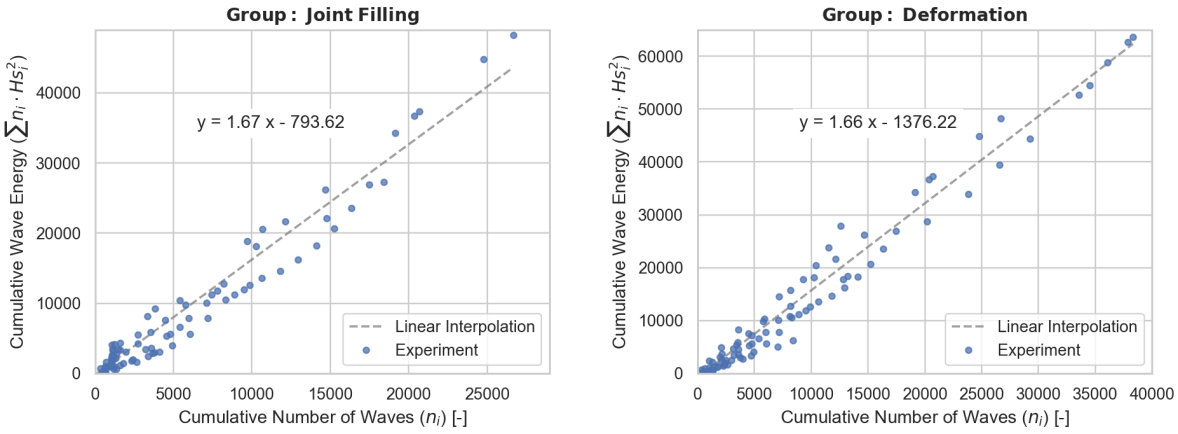

Figure 4.5: The cumulative number of waves illustrated against the cumulative wave energy for the group relating to joint filling (left) and deformation (right)

4.4.2. Uplift of Elements

The first type of damage we will assess is the uplift of elements due to either wave impact or wave run-down. For this analysis, we collected all experiments where elements were partially or fully lifted from the revetment. Next, we assigned to each experiment one of four categories based on how much the element has been uplifted (z_e) with respect to the top layer (D):

- **Damage category 1**: Small uplift of an element ($0 < z_e/D < 0.33$);
- **Damage category 2**: Medium uplift of an element ($0.33 < z_e/D < 0.67$);
- **Damage category 3**: Large uplift of an element ($0.67 < z_e/D < 1$);
- **Damage category 4**: Element fully lifted from the revetment ($z_e/D > 1$).

As uplift of elements is always reported, all data could be obtained from the reports. In total, 25 Basalton elements and 22 basalt elements were (partially) uplifted during the flume experiments.

Cause of Uplift

There are two driving mechanisms related to wave loading that can cause an element to be lifted from the revetment: wave impact and wave run-down. Both of those failure modes are covered in the literature review in Section 2.1.4. The location of the elements most prone to being lifted from the revetment is dependent on the location where the largest residual pressure on the elements will occur. During wave impact, the elements just above and below the wave impact location are most critical. While, during wave run-down, the elements just in front of the wavefront are the most critical. In Figure 4.6, all locations of the reported uplifted elements are illustrated together with the 2% run down location (Equation 2.5), and the wave impact location based on the 2% and maximum value (Equation 2.7). In this case, it is justified to use the 2% values for this analysis as higher waves cause a higher impact and, therefore, a larger chance for elements to being lifted from the revetment.

For revetments made of Basalton, it is evident that most elements are being lifted around the wave impact zone. This is expected as Basalton is a relatively open revetment and thus more vulnerable to uplift due to wave impact than wave run-down. For revetments made of basalt, the data is more scattered. Because basalt is similar to Basalton as it is also a relatively open revetment, it is expected that most elements are also being lifted around the wave impact zone. However, because basalt is a natural stone, the elements have more natural variations. This increases the spatial variability and possibility of weak spots, which also may explain the outliers in Figure 4.6. For example, one outlier occurred during the long-term experiments. From the report, we know that Klein Breteler and Eysink (2005) noted that a basalt element was instantaneously lifted from the revetment. After inspection, it was found that the stone was very tapered in shape and was then replaced with another element.

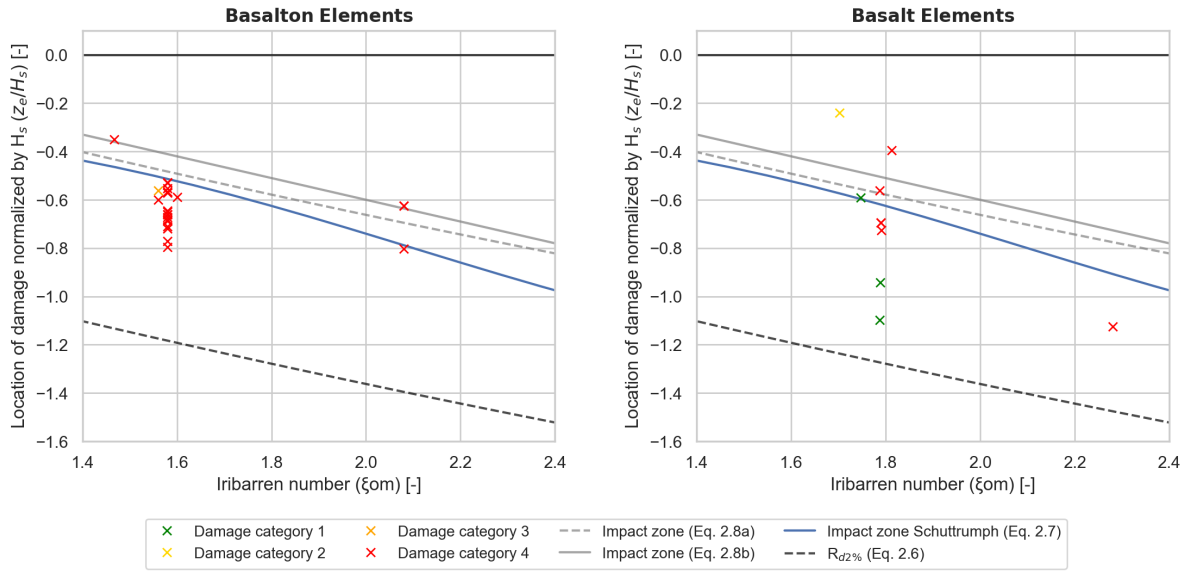

Figure 4.6: Locations of damaged elements normalized by the significant wave height in respect to the wave run-down and impact locations

From this analysis, we can conclude that for revetments made of Basalton, and to a certain extent, basalt, wave impact is the driving failure mode. This is crucial information to correctly model the load in the finite element model in Chapter 5.

4.4.3. Washing Out of the Joint Filling

The second type of damage we will assess is the washing out of the joint filling. For this analysis, only three research programs are used, the Basalton STS and STS+ programs (1) and (2) and the long-term basalt experiments (5b), as the others programs lack detailed information on the inspection of the joint filling. We divided the slope into three different zones to analyze if there is a difference in the loss of joint filling between the zones. The following three zones are defined:

- **Zone 1, Above SWL:** This zone is largely influenced only by wave run-up.
- **Zone 2, Between SWL and SWL-H_s:** In this zone the wave impact takes place;
- **Zone 3, Below SWL-H_s:** This zone is largely influenced only by wave run-down.

For further references, the average amount of washed-out joint filling for the zones described above is given as z_1, z_2, and z_3. A cross-section with the different zones is given in Figure 4.7. In total, we found data on the amount of joint filling left for 29 Basalton experiments and 16 basalt experiments.

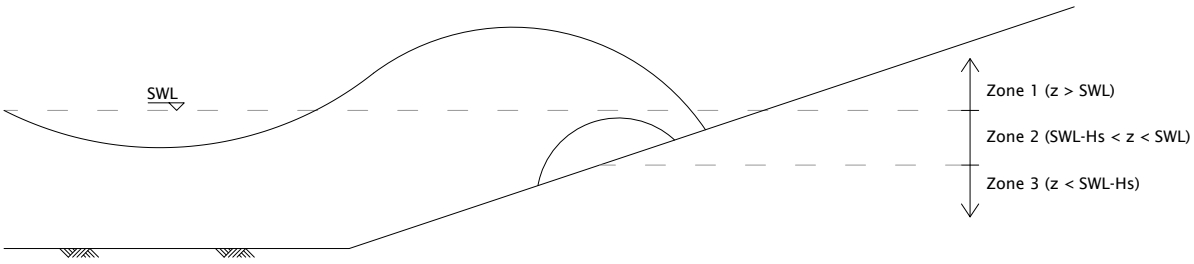

Figure 4.7: Different zones used in the analysis of the joint filling

In the first part of the analysis, we will study the washing out of the joint filling over the different zones. In Figure 4.8, plots are shown in which the amount of washed-out joint filling of the wave impact zone (zone 2) is compared with the run-up zone (zone 1) in the left plot, and with the run-down zone (zone 3) in the right plot. From both plots, it can be concluded that the joint filling around the wave impact zone is the most prone to be washed-out. This may be explained by the fact that the wave impact on the slope will induce large pressures and turbulence over the elements and joints. Additionally, the wave impact will cause the elements near the wave impact location to be lifted up. The displacement of the elements during wave impact may also make it easier for the joint filling to migrate out of the joints.

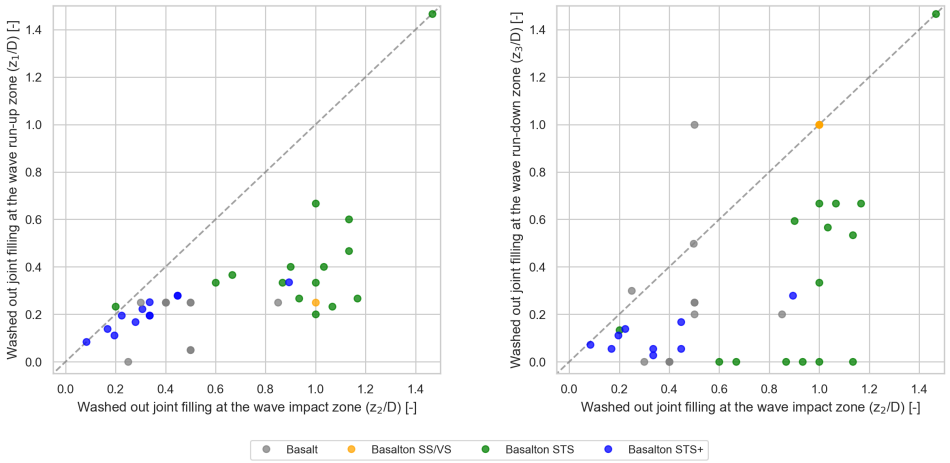

Figure 4.8: Loss of joint filling of the different zones

Next, we will study the washing out of joint filling over time. In Figure 4.9, the amount of washed-out joint filling of the wave impact zone (zone 2) is illustrated against the cumulative number of waves. In this figure, the Basalton STS variant stands out in particular because the joint filling is washed-out faster than the other variants. Wolters (2016a) concluded that this may have happened because the surface of the used scaled elements was smoother than typical STS elements as they were made through a different process. Almost all Basalton STS data, except the most upper line, are from this research program. Hence, those results are likely not to be representative and are therefore faded in the graph.

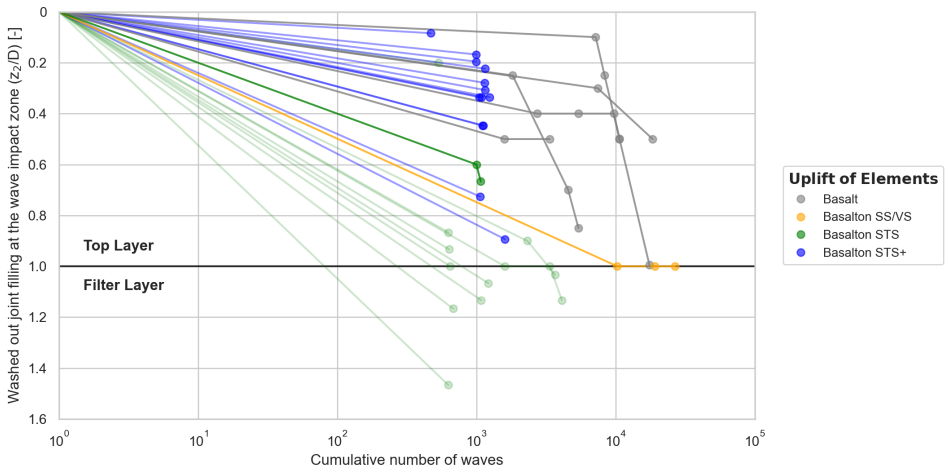

Figure 4.9: Loss of joint filling for the wave impact zone over time

Based on Figure 4.9, it becomes apparent that there are large differences between different experiments in how fast joint filling is being washed-out. It is expected that this is caused by the different intensities of wave loading and how well the revetment is washed in.

In the second part of the analysis, we will study the impact of washed-out joint filling on the uplift of elements. By combining the data from this section and the previous section on the uplift of elements, we can plot the location of the uplifted elements against the amount of washed-out joint filling as shown in Figure 4.10. The points are color-coded to indicate how large the measured uplift is based on Section 4.4.2.

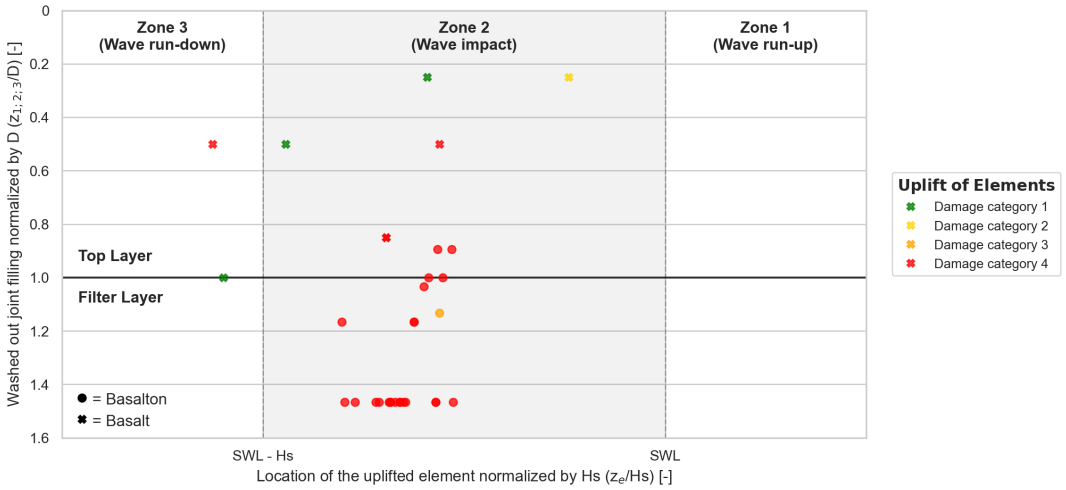

Figure 4.10: Location of the uplifted elements illustrated against amount of washed-out joint filling

From Figure 4.10, we can conclude that there is a significant reduction of joint filling for most uplifted elements. In some cases, even part of the filter layer is washed-out ($z_{1;2;3}$ > D). In this figure, we can see the number of points increasing for more washed-out joint filling. Therefore, we expect that elements become more prone to be lifted from the revetment when there is less joint filling left within the joints. To research this further, we illustrated all data on the average amount of washed-out joint filling for the wave impact zone (zone 2) against the dimensionless loading in Figure 4.11. Again, the points are color-coding is used to indicate how large the measured uplift is.

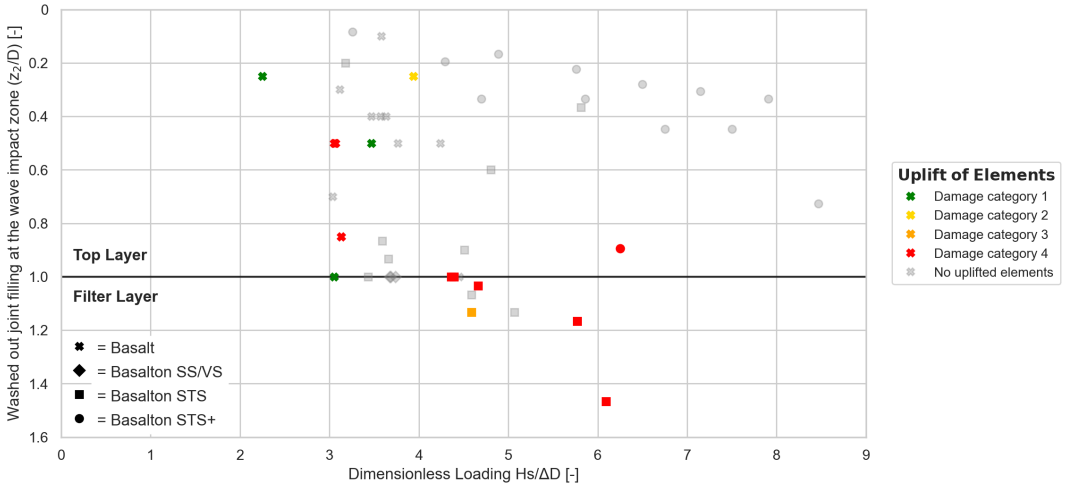

Figure 4.11: Loss of joint filling illustrated against the dimensionless loading with the corresponding uplift damage category

Figure 4.11 indicates that the amount of washed-out joint filling may have impact on the stability of the revetment. From this figure, it can be seen that experiments with a lot of washed-out joint filling tend to experience uplift of elements for a lower dimensionless loading which confirms our hypothesis of the previous paragraph. Those findings are expected and can be related to the physics as joint filling provides additional resistance by providing additional clamping.

4.4.4. Deformation of the revetment

The third type of damage is the deformation of the revetment. Deformation can occur due to various processes such as compaction and migration of the filter, subsidence, and settlement. In our analysis, we will assume all deformations occur solely due to compaction and migration of the filter. The deformation we will focus on is the S-profile. The deformation in the form of an S-profile occurs due to wave impacts and therefore has the most significant impact on column-type revetments. During a wave impact, the pressures compact the filter at the impact zone and cause the uplift of neighboring elements just above and below the wave impact zone. This uplift creates space below the elements, which causes the filter material to migrate. As a result, the revetment will deform into an S-shape, with the trough around the wave impact zone and the hump below the wave impact zone. Because no parameterization of the S-profile is available in the literature, we will first parameterize this type of damage based on old flume experiments. Then, we will assess the impact of the S-profile on the uplift of elements.

The data for this analysis is obtained by studying the reports of the research programs. In the reports of research programs (1), (2), and (6), data on deformations are obtained from 2D laser measurements of the revetment. In the other research programs, the data on deformations is obtained from measurements at fixed points. These programs measured and reported the deformation of 5 to 10 fixed locations for multiple cross-sections of the revetment. This way of measuring deformation makes it sometimes difficult to determine the exact shape of the S-profile as it is not directly clear where the start, center, and end of the S-profile are. This has been resolved by using spline interpolation on the data. Only data from the center of the flume is used to prevent any effects of the flume walls. For each experiments with an S-profile, the following data is collected (Figure 4.12):

- $\mathbf{z_{s;top}}$: The Z-coordinate of the top of the S-profile with respect to the flume bottom. The top location which is characterized by the point in the cross-section between the trough and the undamaged upper part of the revetment;
- $\mathbf{z_{s;mid}}$: The Z-coordinate of the center of the S-profile with respect to the flume bottom. The center location which is characterized by the point in the cross-section between the trough and the hump of the revetment;
- $\mathbf{z_{s;bot}}$: The Z-coordinate of the bottom of the S-profile with with respect to the flume bottom. The bottom location which is characterized by the point in the cross-section between the hump and the undamaged lower part of the revetment;
- $\mathbf{B_s}$: The width of the S-profile, characterized by the distance between $z_{s;top}$ and $z_{s;bot}$;
- $\mathbf{B_{s;trough}}$: The width of the trough of the S-profile, characterized by the distance between $z_{s;top}$ and $z_{s;mid}$;
- $\mathbf{B_{s;hump}}$: The width of the hump of the S-profile, characterized by the distance between $z_{s;mid}$ and $z_{s;bot}$.
- $\mathbf{a_s}$: The amplitude of the S-profile, characterized by half the difference between the maximum of the hump and the minimum of the trough;

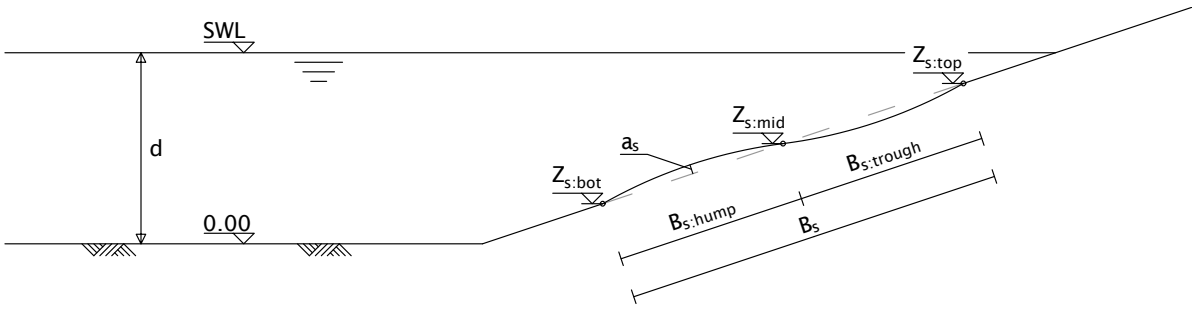

Figure 4.12: Parameterization of the S-profile

We divide our analysis of the S-profile into two parts. First, we will parameterize and quantify the S-profile, for which we will look at the location, width, and amplitude of the S-profile. Then, we will analyze the impact of the S-profile on the uplift of elements. All the collected data on the S-profile from the experiments is included in Appendix A.

The first part of the parameterization is to quantitatively compare the position of the S-profiles obtained from the different experiments. The position of a S-profile can be parameterized by three points, respectively the bottom of the S-profile $z_{s;bot}$, the center of the S-profile $z_{s;mid}$ and the hump of the S-profile $z_{s;top}$ (Figure 4.12). By analyzing old flume experiments, we found data on these points in 46 of the 56 Basalton experiments and in 26 of the 33 basalt experiments. Because the S-profile is formed due to wave impact, it is expected that the three points describing the location of the S-profile can best be made dimensionless with the significant wave height in respect to the still water level. The definitions of the dimensionless top, center, and bottom are shown in Equation (4.3).

$$z_{s;top;d} = \frac{z_{s;top} - d}{H_s} \qquad z_{s;mid;d} = \frac{z_{s;mid} - d}{H_s} \qquad z_{s;bot;d} = \frac{z_{s;bot} - d}{H_s} \tag{4.3}$$

First, we analyze if the different locations are correlated to each other. In Figure 4.13, we illustrated the dimensionless center against the dimensionless bottom in the left plot and against the dimensionless top in the right plot. Based on these plots, it can be concluded that the locations of these parameters are correlated to each other. Therefore, we will parameterize the location of the S-profile based only on the center points, which should make it easier to model the S-profile probabilistically later in the study.

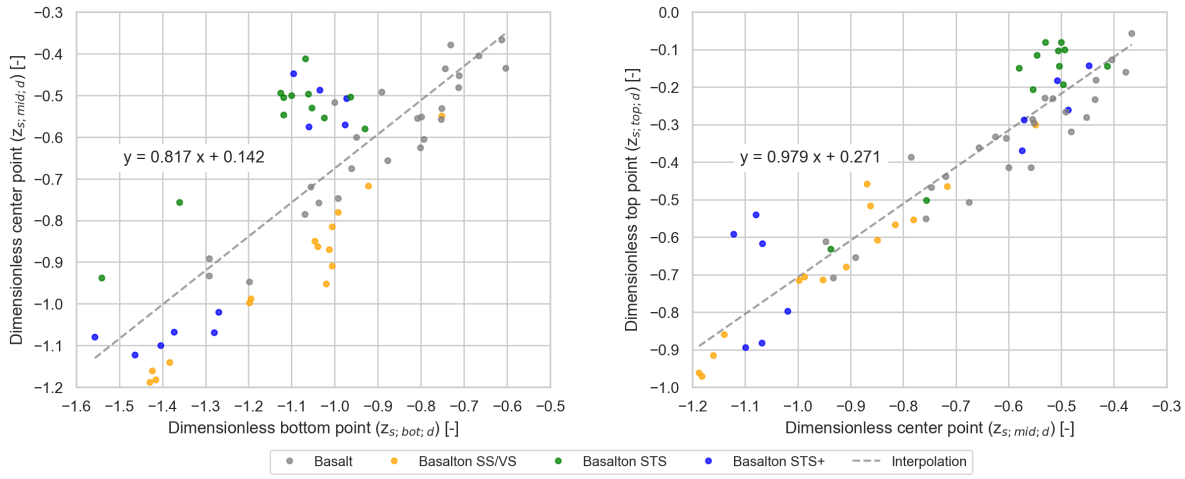

Figure 4.13: Correlation between the different locations of the S-profile

As earlier mentioned, it is expected that the location of the S-profile is related to the location of wave impact. In Section 2.2.2.4, the wave impact location equations by Schüttrumpf (2001) and Peters (2017) are both based on the Iribarren number. This suggests that the location of the S-profile may also be expressed based on the Iribarren number. Therefore we illustrated the dimensionless top, center, and bottom against the Iribarren number in Figure 4.14. For all three dimensionless locations, we find a negative correlation with the Iribarren number. This implies that for a larger Iribarren number, the location of the S-profile is lower on the slope. Those findings confirm our hypothesis that the location of the S-profile is related to the wave impact location.

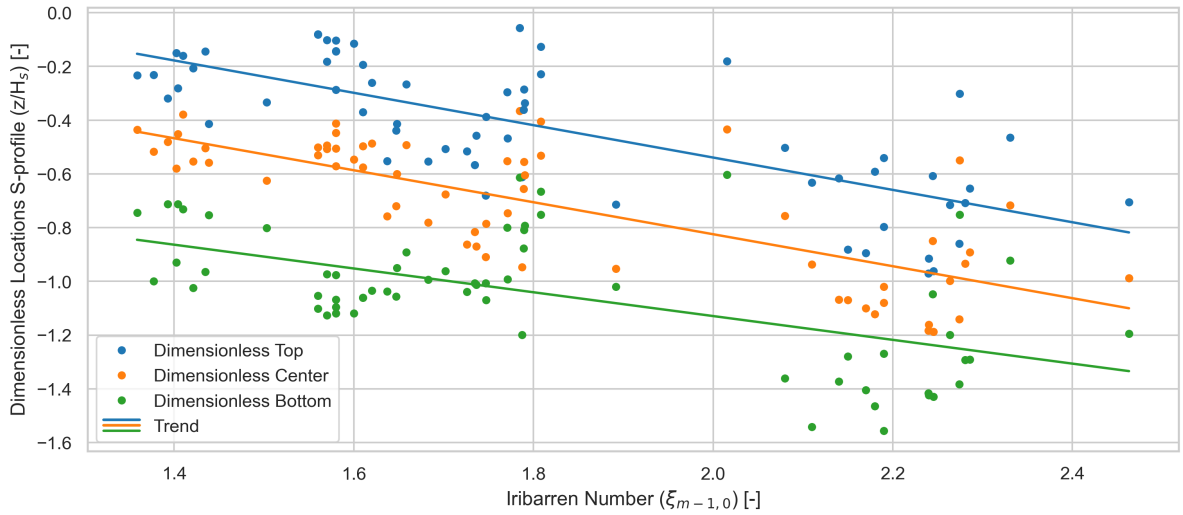

Figure 4.14: The dimensionless top, center and bottom against the Iribarren number with trend lines

Based on our findings, we suggest to express the location of the S-profile in terms of the dimensionless center. The dimensionless top and bottom can be estimated with use of the width of the S-profile, which will be studied later in this section. To define an expression, we plot the dimensionless center points against the Iribarren numbers in Figure 4.15. Based on this figure, we propose Equation 4.4 to estimate the location of the S-profile.

$$\frac{z_{s;mid;d}}{H_s} = -0.595 * \xi_{m-1,0} + \gamma_z \quad \text{with:} \quad \gamma_z \sim \mathrm{N}(0.358,\ 0.157) \tag{4.4}$$

Figure 4.15 suggest that there is no difference between the different top layer elements. This is as expected because the wave impact location primarily determines the location of the S-profile. During some series of experiments, the water level was raised. However, this was at most only a few decimeters. By analyzing the data, we found no evidence that small increases in the water level will impact the location of the S-profile. However, we expect a large increase in water level will affect the location of the S-profile, as the wave impact location will differ significantly. During the flume experiments, a large increase in the water level did not happen and is therefore out-of-scope for this study.

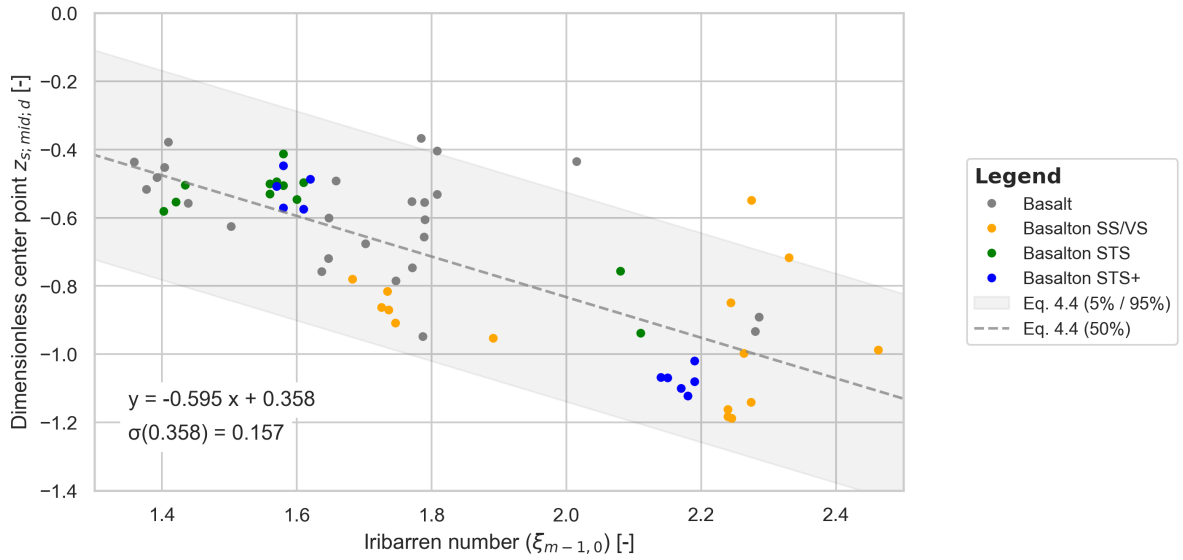

Figure 4.15: The dimensionless center point of the S-profile illustrated against the Iribarren number

Based on the analysis of the top, center and bottom locations of the S-profile, we can analyze the width of the S-profile. For the parameterization of the S-profile, we define the total width B_s, the width of the trough $B_{s;trough}$ and the width of the hump $B_{s;hump}$. In which total width is the sum of the latter two.

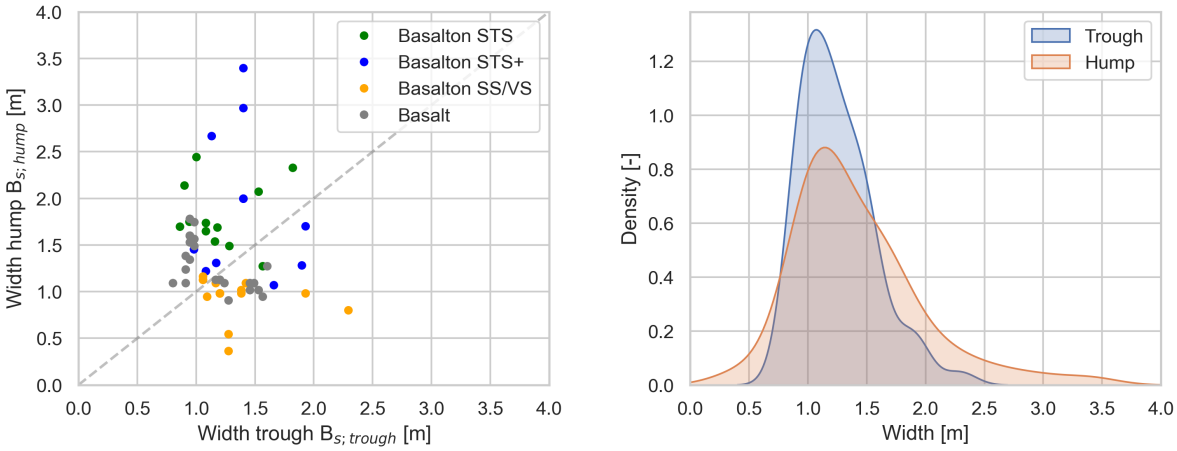

Figure 4.16: Width of the hump illustrated against the width of the trough of the S-profile.

In Figure 4.16, the width of the hump and trough are illustrated for all experiments. From the right figure, it can be seen that the width of the hump has a larger variation than the width of the trough. This phenomenon can also be observed in Figure 4.14, the trend lines show that for a larger Iribarren number, the width of the hump becomes smaller while the width of the trough stays more or less the same. We expect this happens because, for the analyzed range of Iribarren numbers, the maximum pressure by the wave impacts decreases for a larger Iribarren number based on the models discussed in Section 2.2.2.4. As a result, the revetments in the experiments with an Iribarren number of 1.4 experience a larger loading due to wave impact compared to the experiments with a larger Iribarren number. Consequentially, this also results in a larger residual loading on the elements resulting in more elements being lifted up during the wave impact allowing for a wider hump.

We can estimate the width of the trough based on the data from Figure 4.13. This figure showed a strong correlation between the dimensionless center point and top point. Therefore, we will derive an estimation using the equation obtained by the linear interpolation in the right plot of Figure 4.13. Next, we can rewrite this equation as shown in Equation 4.5.

$$\begin{aligned} \frac{z_{s;top\ 50\%}}{H_s} &= 0.979\ \frac{z_{s;mid\ 50\%}}{H_s} + 0.271 \\ \frac{z_{s;top\ 50\%}}{H_s} &\approx \frac{z_{s;mid\ 50\%}}{H_s} + 0.271 \\ \frac{\Delta z_{s;trough\ 50\%}}{H_s} &\approx 0.271 \\ \Delta z_{s;trough\ 50\%} &\approx 0.271\ H_s \end{aligned} \tag{4.5}$$

Based on this rewrite, we propose Equation 4.6 as a rule of thumb to estimate the width of the trough.

$$B_{s;trough\ 50\%} \approx\ 0.271\ \frac{H_s}{\sin(\alpha)} \tag{4.6}$$

Next, we derive an equation for the total width (B_s) of the S-profile. To find the key parameters, correlations between the total width and other parameters were analyzed. Based on this analysis, we found that the total width of the S-profile is best described by the filter layer thickness, the dimensionless loading, and the Iribarren number. The correlation with those parameters makes sense as the filter layer thickness directly impacts the loading within the leakage length. A larger leakage length will result induce a larger filter response which also reaches further down the slope. Consequentially, more elements will be lifted up allowing the hump to become wider. The same goes for the dimensionless loading. The correlation with the Iribarren number is discussed earlier in this section. As a result, we propose Equation 4.7 to estimate the total width of the S-profile. In Figure 4.17, the found equation is illustrated with all data on which the fit is made.

$$\frac{B_s}{b} = \gamma_B \left(\frac{H_s}{\Delta D \; \xi_{m-1,0}} \right)^{0.89} \qquad \text{with:} \quad \gamma_B \sim \mathrm{N}\,(12.43,\ 2.65) \tag{4.7}$$

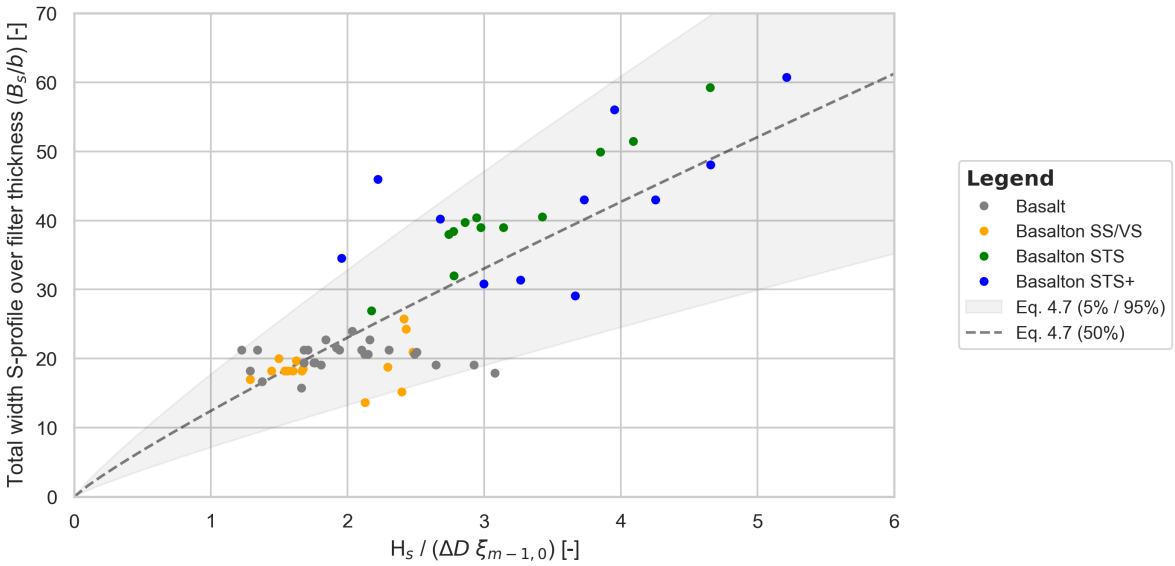

Figure 4.17: Estimation of the total width of the S-profile by Equation 4.7

To fully assess the impact of the S-profile, we also need to study the amplitude. In Figure 4.18, the development of the amplitude over the filter thickness is illustrated against the cumulative number of waves. Based on this data, it turns out that the revetment is quite stiff in the beginning, and almost no deformation occurs. In most cases, between 1,000 and 10,000 waves, the revetment will start deforming at an increasing pace. During most series of experiments, one or multiple elements are lifted from the revetment, and thus, the experiment stops.

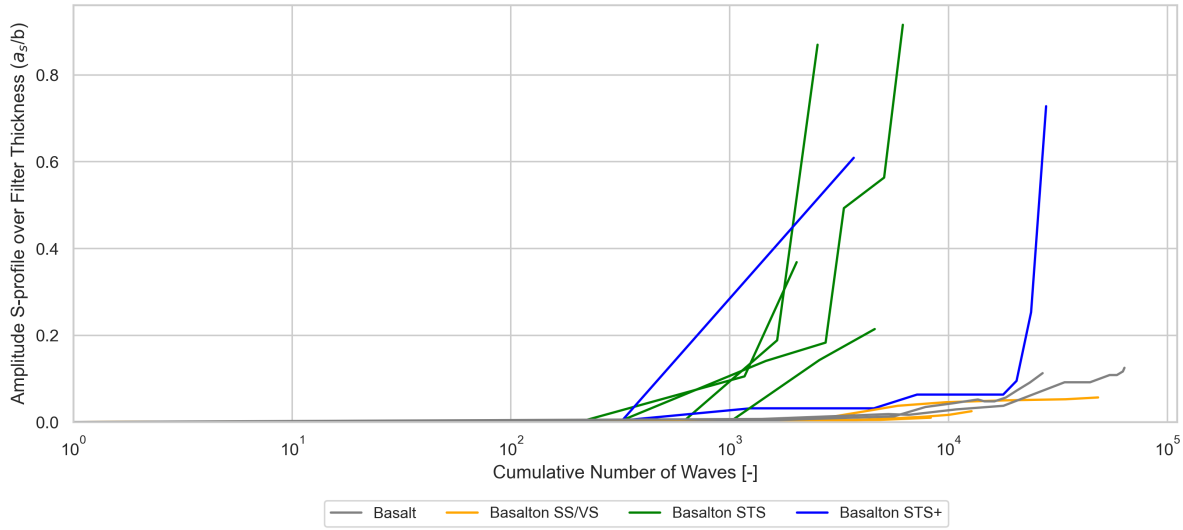

Figure 4.18: Development of the amplitude of the S-profile over the cumulative number of waves

In Figure 4.18, it stands out that the STS and STS+ variants of Basalton show larger deformations in comparison to Basalton SS/VS and basalt. This is probably due to the following two aspects. First, Basalton STS and STS+ variants are more heavily loaded during the flume experiments. While Basalton SS/VS and basalt are usually loaded to a dimensionless loading of 4 - 5, the STS and STS+ variants are loaded up to a dimensionless loading of 8. As a result, those higher loads may cause larger deformations. The second reason may be because the used elements in the STS experiments were smoother than usual. This is because they were specially made on a scale for those flume experiments using a different process (Wolters, 2016a).

The development of the amplitude is difficult to quantify. Primarily because it is dependent on many different aspects such as the loading, the loading history, properties of the revetment itself, other types of damage. Therefore, we will use Figure 4.18 as a reference in this study. As a result, we can only give the boundaries of the S-profile amplitude over the filter layer thickness, which is between 0 and 1. This is because we assume that the migration of the filter layer causes the deformation. A value of 1 would mean that all filter material under the trough has migrated into the hump.

In the second part of our analysis, we study the impact of the S-profile on the stability of the top layer. By combining the obtained data from this section and the previous section on the uplift of elements, we can determine where the elements were uplifted respective to the S-profile. This is shown in Figure 4.10, the points are color-coded to indicate how large the measured uplift is based on Section 4.4.2.

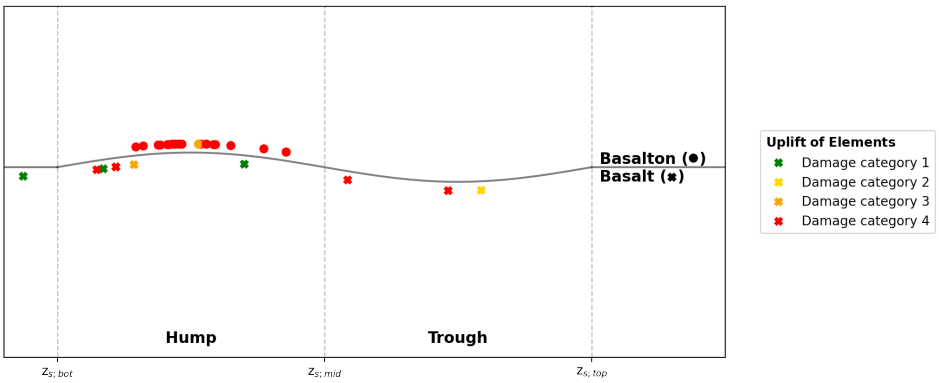

Figure 4.19: Location of uplifted elements with their respectively damage category on the S-profile

Based on earlier analysis and literature study, it is known that wave impact is expected somewhere between the bottom of the trough and the transition from trough to hump. In Figure 4.19, we see predominantly elements being uplifted from the hump of the S-profile below the wave impact location. This is notable, as Vrijling et al. (2001) and Peters (2017) both suggested that resistance of a revetment increases down the slope. Therefore, one should expect that elements above the wave impact location are more likely to be uplifted. However, based on the data from the flume experiments, this is not the case. This phenomena may be explained by three reasons:

1. **Washed-out of joint filling:** The zone below the wave impact tend to have less joint filling than the area above the wave impact due to the run-down of the wave. This may decrease clamping and thus making elements below the wave impact zone more vulnerable for uplift.

2. **The curvature of the S-profile:** Just above the impact zone, the trough of the S-profile is located while below the impact zone, the trough transitions into the hump. The shape of the trough provides a positive curvature, which will make the elements rotate towards each other, which increases clamping. The reverse can be found on the hump, in which negative curvature causes elements to rotate away from each other reducing clamping (Figure 4.20).

3. **Change in loading due to migrated filter material:** Migration of the filter material will affect locally the filter layer thickness. At the hump, the filter layer becomes thicker while at the trough the filter layer becomes thinner. From Section 2.2.3, it is known that the filter thickness has impact on the leakage length, which is an important factor determining the filter pressure. This difference in leakage length will cause the filter pressure to be higher than normal under the hump and lower than normal under the trough. Consequentially during wave impact, this leads to a higher residual loading on the elements on the hump, making those element more vulnerable to be uplifted from the revetment.

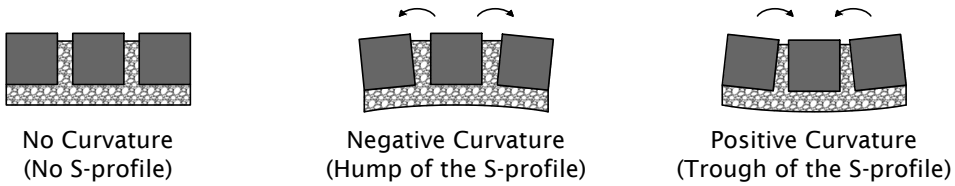

Figure 4.20: Impact of curvature on the elements

Next, we analyze the impact of the amplitude of the S-profile on the uplift of elements. In Figure 4.21, the amplitude over the filter layer thickness is illustrated against the dimensionless loading for all experiments. Again, the points are color-coding is used to indicate how large the measured uplift is.

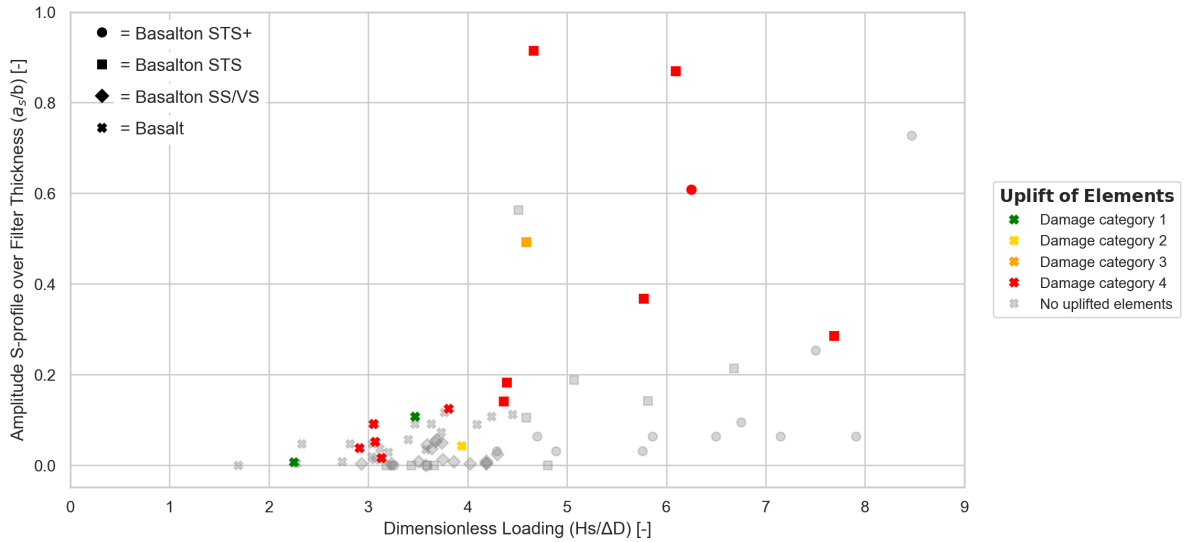

Figure 4.21: For each uplifted element the amplitude of the S-profile over the filter layer thickness.

Figure 4.21 shows that for most cases, a large amplitude of the S-profile will lead to the uplift of at least one element. However, one outlier had no uplifted elements for an amplitude over filter thickness ratio of 0.75, a dimensionless loading of 8.5. It is difficult to determine why this revetment did not experience any uplift of elements, mainly because no anomalies were reported. Therefore, in conclusion, we believe that S-profiles with larger amplitudes have a more negative impact on the stability of the revetment. However, many other factors also contribute to the stability of the revetment, and thus having an S-profile with a large amplitude does not always mean that this will lead to the uplift of elements.

4.5. Summary of Findings

The aim of this chapter is to parameterize and quantify damages based on data from old flume experiments. For this analysis, we collected data on damages from 56 experiments with a Basalton revetment and 33 experiments with an basalt revetment. The following three types of damage were analyzed: uplift of elements, washed-out joint filling and deformation in the form of an S-profile.

From the analysis of the uplifted elements can be concluded that all Basalton elements and most basalt elements were being uplifted around the wave impact zone. This suggests, the wave impact may be the primarily driver to cause the uplift of elements for those types of revetment. Some basalt elements were uplifted lower on the slope, near the wave run-down location. However, this is likely explained by the large natural variance of basalt elements causing weak spots.

Next, the washed-out joint filling is studied. For this analysis we collected data on the amount of washed-out joint filling for three zones on the slope: the wave run-down zone ($z < z_{SWL}$-H_s), the wave impact zone (z_{SWL}-$H_s < z < z_{SWL}$), and the wave run-up zone ($z > z_{SWL}$). From this analysis, it is concluded that more joint filling is washed-out in the wave impact zone than the other zones. This is likely caused by the large differences in pressure during the wave impact and the turbulence it creates on the top layer and within the joints. Furthermore, we studied the impact washed-out joint filling has on the uplift of elements. We found that in general, more washed-out joint filling leads to elements being uplifted by a lower dimensionless loading. Therefore, a revetment with washed-out joint filling has a lower stability number.

Finally, the last type of damage studied is deformation in the form of an S-profile. Within our study, we assume this type of damage occurs solely by migration of the filter material. During our analysis, we studied the location, width and amplitude of the S-profile. We found that the shape of the S-profile is predictable and proposed equations to estimate the location and the width. Because the wave impact location correlates with the Iribarren number, we found that we can express the location of the S-profile also with the Iribarren number, leading to Equation 4.4. Furthermore, we found that the width of the S-profile correlates to the loading on the elements during wave impact, therefore we were able to express the width of the S-profile based on the dimensionless loading, Iribarren number and filter thickness leading to Equation 4.7. Last, we found that the rate of which amplitude of the S-profile increases is likely dependent on the loading on the revetment as experiments with a higher loading showed a larger amplitude. In the last part of the analysis we studied the impact an S-profile has on the uplift of elements. This analysis showed that elements primarily were uplifted on the hump of the S-profile. Additionally, we believe that S-profiles with larger amplitudes have a more negative impact on the stability of the revetment. However, many other factors also contribute to the stability of the revetment, and thus having an S-profile with a large amplitude does not always mean that this will lead to the uplift of elements.

5

Impact of Damage on the Stability

In previous chapters, different types of damage on pattern-placed revetments were assessed and parameterized. This chapter aims to use those parameterizations and assess the impact of those damages on the stability with a finite element model, hereafter called FE-model. First, in Section 5.1 the methodology is discussed. Next, in Section 5.2 the FE-model is created and verified. In Section 5.3, the input and scenarios to be used with the model are listed. Then, in Section 5.4 the results of those scenarios are discussed and analysed. Last, in Section 5.5 a summary of findings is given.

5.1. Methodology

The two objectives of this chapter are to create and validate an FE-model and assess the impact of damage on the stability of pattern-placed revetments using this model. In order to achieve the first objective, we have to choose a finite element model suite. In order to accomplish the goals of this chapter and the next chapter, the suite must meet two requirements:

1. Because a pattern-placed revetment is made of many elements, and it is desirable to be able to model elements being lifted from the revetment, the suite must support an explicit analysis.
2. The suite must be able to have an integration with a scripting language. This is required as many different iterations of a pattern-placed revetment model will be used for the following two chapters. Therefore, we will automate the generation of an FE-model using a script to generate a model based upon a specific set of predefined parameters.

At the university at which this study is conducted, two FE-model suites were found which fulfill both requirements: Abaqus CAE and Ansys. Chosen is to work with Abaqus CAE because it supports integration with Python, and documentation is widely available online.

Using Abaqus and Python, we will create a script to generate a model of a pattern-placed revetment. Because this study requires running many simulations, it is critical to keep the computation time short. Therefore, some simplification will be used, which will be explained later in this chapter. Based on the parameterization in Chapter 4, different types of damage will also be implemented within the model. The model will be calibrated by performing pull-out tests and comparing those results to pull-out tests done on revetments in the Netherlands to calibrate the friction coefficient.

To accomplish the second goal, the impact of deformation (S-profile), reduced clamping, and a missing element is studied with the FE-model. Within this analysis, damage is studied by generating and simulating models with damage included within the initial conditions, hereafter called scenarios. In order to study the impact of a specific type of damage, multiple scenarios are generated, each with one parameter related to the studied type of damage slightly adjusted. This ‘one at a time’ approach will give insight into, for example, the effect of the amplitude of the S-profile. After the scenarios are simulated, the displacements within the model are analyzed with Python and compared with an undamaged scenario.

5.2. Creating the Finite Element Model

This section will discuss how the FE-model is created in four parts. First, in Section 5.2.1 the design choices regarding different aspects of the FE-model are substantiated. Next, in Section 5.2.2 it is explained how the different types of damage are implemented in the FE-model. Then, in Section 5.2.3, the default values of the parameters used in the FE-model are listed and substantiated. Last, in Section 5.2.4 the model is calibrated to data from pull-out experiments in the field.

5.2.1. Modelling of the Pattern-Placed Revetment

In the first part of this chapter, we design the FE-model for the pattern-placed revetment and substantiated the design choices on a theoretical level. For the creation of the model in Python and Abaqus, reference is made to Appendix B.

Geometry

The basic geometry of the model is defined by parameters shown in Figure 5.1. In which α is the slope angle, d the water depth, and B_m the width of the model expressed in total sets of Basalton STS+. The bottom of the revetment is supported over the whole thickness by a stiff toe. Finally, the top and bottom of the pattern-placed revetment is defined by the dimensionless top and bottom $z_{d;top}$ and $z_{d;bot}$ using Equation 4.1. The model is only able to put a whole set of Basalton STS+ on the slope. Therefore, we choose to fix the top coordinate and let the model adjust the bottom coordinate (z_{bot}). Solving it this way will allow us to study the impact of the location of the top of the revetment respective to the still water level. As a result, the model will start laying sets of elements at the revetment's top coordinate and then lay sets down the slope until it has reached the defined bottom coordinate. Because of this, the real bottom coordinate is often slightly lower than the defined bottom coordinate.

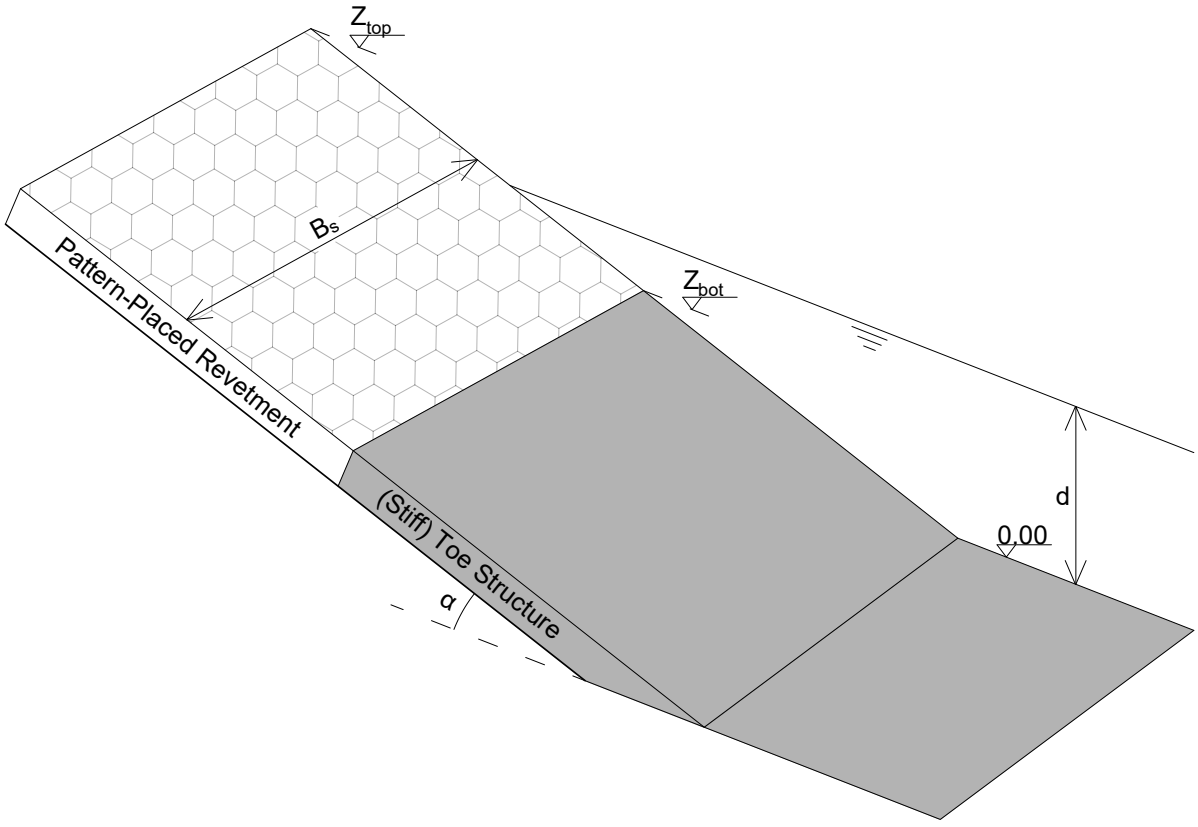

Figure 5.1: Parameters defining the geometry of the model

Top Layer

The set of elements used in the FE-model is the STS+ variant of Basalton manufactured by Holcim Coastal. This type is chosen because Basalton is commonly used in the Netherlands, and STS+ is the newest variant of Basalton. In Figure 5.2, a top view of the Basalton STS+ set is shown with numbered elements for further references.

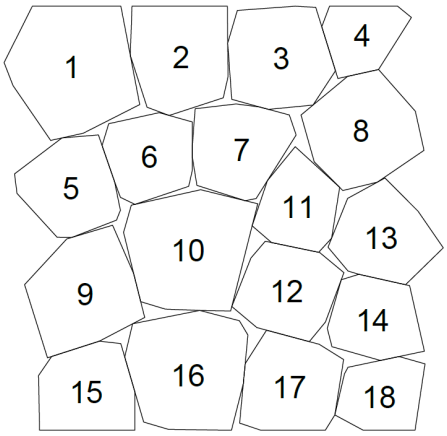

Figure 5.2: Basalton STS+ set with numbering for further references (Holcim Coastal, 2013)

The elements are modeled as 3D deformable bodies defined by the Young Modulus (E) and the Poisson Ratio (ν) within the FE-model. Next, the geometry of the elements is defined by the layer thickness (D) and the density of the concrete (ρ_s). During simulation, it is assumed that the elements around and below the wave impact location are submerged. Last, two friction coefficients are introduced to model the interaction between the element and the filter (μ_f) and to model the interaction between elements themselves (μ_e).

Almost all elements are able to translate and rotate in any direction. The only exceptions are the most left column (element 1, 5, 9 and 15) and the most right column (4, 8, 13, 14 and 18) of the revetment. In the field, those elements are next to other Basalton elements. Therefore boundary conditions are applied to the elements in these columns in order to constrain the translation and rotation. Those elements are indicated by the red color in Figure 5.3 and are constrained to translate only along the X' and Z' axis and rotate only around the Y' axis.

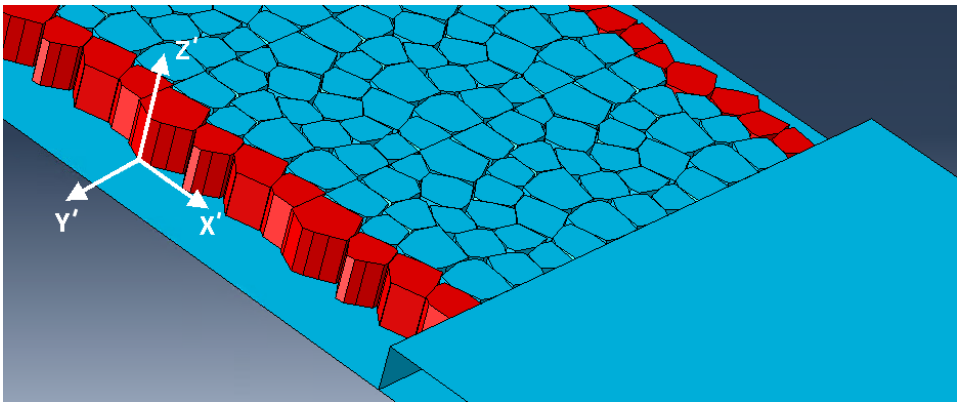

Figure 5.3: Constrained elements indicated by the red hatch

Filter Layer

The filter layer within the FE-model is not physically modeled. However, we included the impact of the filter layer on the filter response when determining the loading on the elements. The filter layer is included by two parameters: the permeability of the filter material and filter layer thickness. When deformation is applied, the thickness of the filter layer will become a function of the slope coordinate to model the difference in filter layer thickness.

A simplification of modeling the filter this way is that usually, the soil acts like a spring and would deform under wave loading. However, to reduce complexity, the surface below the elements is modeled as a rigid surface. From a physical view, this may slightly positively impact the stability of the elements as when the surface is rigid, small deformations due to the wave loading are neglected. However, because the model only simulates five waves, it is expected that the amount of deformation five waves will cause is minimal. Therefore, it is assumed that also the impact of this simplification is minimal.

Joint Filling

In the model, there are two methods to take into account the clamping due to joint filling. The first method is to generate 3D deformable bodies at the location of the joint filling. Those bodies will act as a spring to clamp the elements. As shown in Figure 5.4, this method will create 24 new bodies for each set of Basalton elements. Fourteen of those bodies, indicated by the green and red color, are required for each Basalton set, while the ten light blue and dark blue bodies are only required when the top or right side of the considered set is adjacent to another set. One significant implication of modeling joint filling this way is that during test runs with the model, the computation time increased by a factor of 30. This increase can be explained because of the increase of degrees of freedom and interactions in the model.

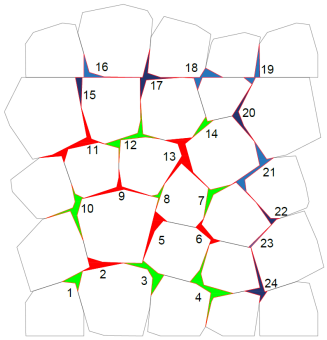

Figure 5.4: Basalton STS+ joint filling

Because the model has to run multiple times to assess different scenarios, a long computation time is not desirable. Therefore it is opted to model the joint filling as a modification of the friction coefficient between elements (μ_e). In Section 5.2.4 the model is calibrated and an estimation is made for the required friction coefficient μ_e.

Wave Loading

The wave loading is modelled by the wave impact profile defined by Peters (2017) and is introduced in Section 2.2.2.4. This model is defined in space and time, which makes is suitable for application within a FE-model. The first important step is to determine how many wave impacts are simulated. Two main aspects are important here, first, the number of wave impacts should be high enough in order to create damage. Second, the number of wave impacts should be minimized in order to reduce the required computation time. Based upon experiments with the FE-model, it turns out that with five large waves the revetment can be damaged. Therefore, five waves seems like a good compromise between computation time and accuracy.

In this section, we will give a summary of how those five waves are defined, an in-depth explanation of this methodology can be found in Appendix C. The aim of the used method is to compress a storm of 5000 waves into five waves by simulating only the part of the storm in which the revetment is the most heavily loaded. This is determined by the largest average wave height of five consecutive waves during a storm. As our main focus is to study the uncertainty due to structural changes, which are in this study the damages. We made some assumptions which allows for an easier quantification and to reduce the uncertainty of the loading:

- The wave steepness is constant for all five waves.
- The wave height of the five simulated individual waves are equal.
- The duration of the storm is 5000 waves (8 - 10 hours).
- It is assumed that the wave climate can be described by a Rayleigh distribution.

Using those simplifications, a Monte Carlo simulation is used to generate and analyze random storms in order to find a curve to estimate the largest average wave height of five consecutive waves during a storm over the significant wave height ($H_{n;w}/H_s$). Based on this curve, a general extreme value distribution is fitted and is shown in Figure 5.5. The quantile of this distribution is referred to as the storm intensity i_{st} and is used to take into account the uncertainty between two different storms. For the same significant wave height, a large storm intensity results in a relatively heavy storm, and a low storm intensity results in a relatively mild storm. The wave impact location is determined based upon Equation 2.7 in Section 2.2.2.4, which is a part of the same study as the wave impact model (Peters, 2017).

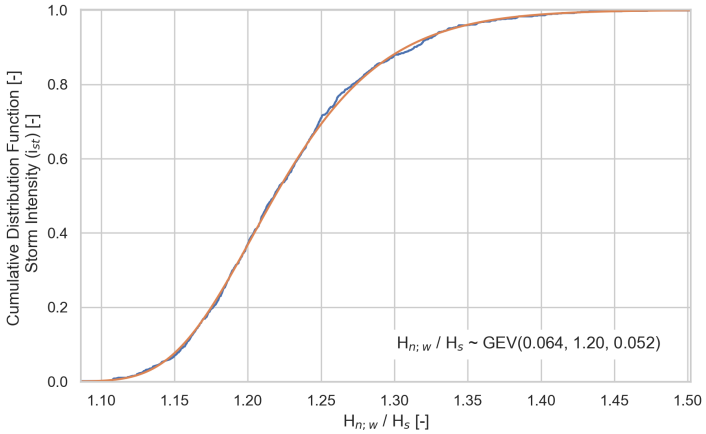

Figure 5.5: Expected ratio of the average individual wave height over the significant wave height for a certain storm intensity

Filter Response

With the wave loading defined, the filter response can be implemented. Together with the wave loading, the filter response determines the residual pressure on the elements. The filter response is based upon the leakage length as introduced in Section 2.2.3. The definition of the leakage length is shown in Equation 5.1.

$$\Lambda(x) = \sqrt{\frac{b(x)\ D\ k}{k'}} \tag{5.1}$$

Within the model, the filter layer thickness is assumed to be variable in order to model deformation caused by filter migration (e.g. for an S-profile). This allows for modelling the impact this type of deformations have on the filter response. It should be noted that this is not standard practice and within models like SteenToets, the leakage length is often assumed to be constant for the whole slope. To estimate the filter response based upon the pressures on the top layer, we use Equation 5.2 as, which models the filter pressure based upon 1D linear potential flow (Klein Breteler and Van der Werf, 2006).

$$\Lambda(x)^2 \frac{d^2\Phi_F(x,t)}{dx^2} - \Phi_F(x,t) = -\Phi_T(x,t) \tag{5.2}$$

In Equation 2.12, Φ_T(x,t) is the hydraulic head on the top layer and Φ_F(x,t) is the filter response. By taking the difference between these two variables, the residual pressure on the elements is obtained. Equation 2.12 is numerically solved using an implicit Euler scheme. The chosen time step is 0.01 seconds, and the chosen step in space is 0.01 meter. Those steps are sufficient to accurately model the wave impact duration. The loading on each element, which will be calculated based upon around 20 - 30 data points. Then, the calculated resulting pressure is interpolated and combined into an average pressure for each element for each time step as shown in Figure 5.6.

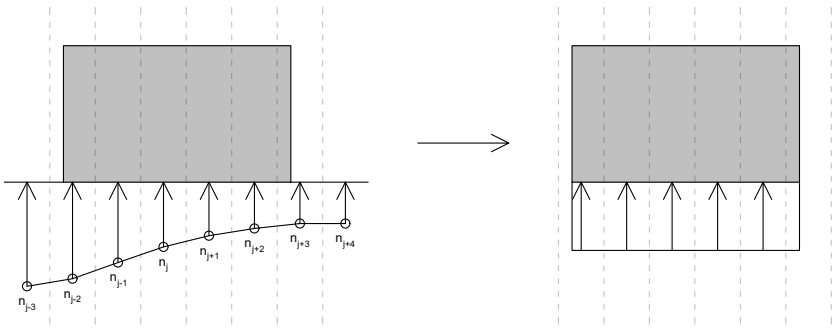

Figure 5.6: For each time step, the data points are combined to calculate the average pressure on an element

By using the described method to determine the residual pressure, the following assumptions are made:

- Inertia of the flow is not taken into account.
- By using the 1D linear potential flow to determine the filter response, the resistance/leakage length has to be linearized.
- Damage does not affect the simulated wave loading.
- The simulated initial damage does not affect the filter response, with the exception of deformation. The deformation is assumed to be caused by migration of the filter material, therefore the filter thickness and herewith the leakage length (Λ), vary along the slope coordinate.
- The influence of further damage of the top layer and increased filter layer thickness caused during the simulation is not taken into account within the filter response.
- The residual load on an element is averaged over the corresponding data points to model it as a uniform pressure (Figure 5.6).
- 2D effects due to lateral (coast parallel) variations in the load or structure are negligible.

In Figure 5.7, the wave impact pressure, filter response and residual pressure are shown as simulated by the model. In the left pane, the hydraulic head is shown during the peak of the wave impact over the slope coordinate, and in the right pane, the hydraulic head at the largest pressure point the over time.

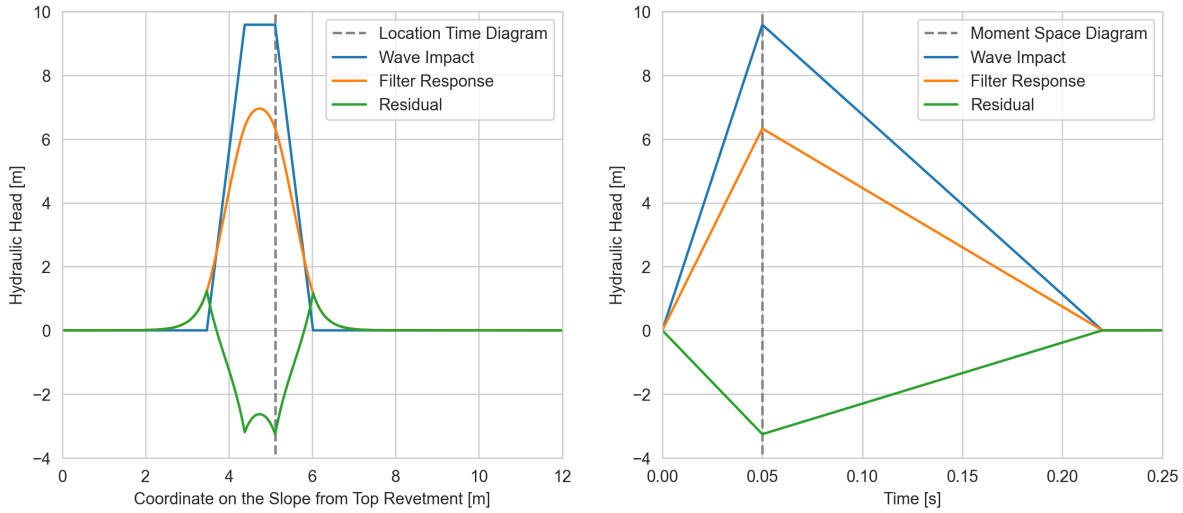

Figure 5.7: Modelled wave impact in space (left) and time (right)

Each simulation will simulate 12 seconds, in the first 2 seconds, no loading applied. This will give the elements time to find their steady-state position from their initial positions. Based on experimental runs with the model, it turns out each element needs about 1 second before the velocity off all elements is back to zero again. Just to be sure, a spin-up time of 2 seconds is applied before the first wave impact. After each wave impact, based on experimental runs, it is measured that elements need about 1 - 1.5 seconds to find their steady-state again. Therefore it is chosen to apply wave impacts with a 2 seconds interval.

5.2.2. Damages

Three types of damage are implemented within the FE-model. These damages are modelled based upon the findings of Chapter 4. An explanation of how each damage is implemented in the model is given below.

5.2.2.1. Deformation (S-profile)

The model can generate deformation in the form of an S-profile based on the analysis done in Chapter 4. The S-profile is defined based upon three parameters: the center point ($z_{s;mid}$), the total width (B_s) and the amplitude (a_s). The model assumes that the S-profile is the result of a migrated filter layer. Thus, the model will locally adjust the filter layer thickness around the S-profile, which impacts the leakage length locally, as discussed in the previous section. The S-profile is implemented according to the parameterization done in Chapter 4. The only simplification made on this parameterization is that width of the hump and trough are assumed to be equal to model the deformation by a single sine period. In reality, the hump is a little bit wider than the through for lower Iribarren numbers. However, this simplification is required to ensure a smooth transition in slope between the trough and the hump.

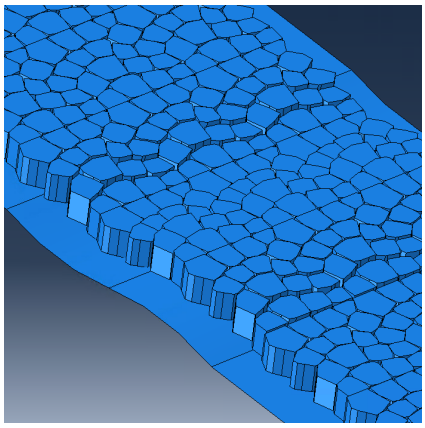

Figure 5.8: Modelled S-profile

5.2.2.2. Washed-out Joint Filling

Physically including joint filling as deformable 3D bodies will increase the computation time of the model by a factor of 30. Therefore, it is chosen to include the effect of joint filling within the friction coefficient between elements. In Section 5.2.4, the model is calibrated based upon a comparison of simulated pull-out tests and pull-out tests from the field. Two friction coefficients are calibrated, one based upon pull-out tests done on revetments with washed-out joint filling, and one based upon pull-out tests done on revetments which are well washed in. It is unknown, apart from the two calibrated cases, how the amount of joint filling left relates to the friction coefficient. Klein Breteler (2018) suggests that it is still possible to have a well clamped element if some joint filling is missing. Therefore, we will refer to this damage as 'reduced clamping' in the remainder of this study.

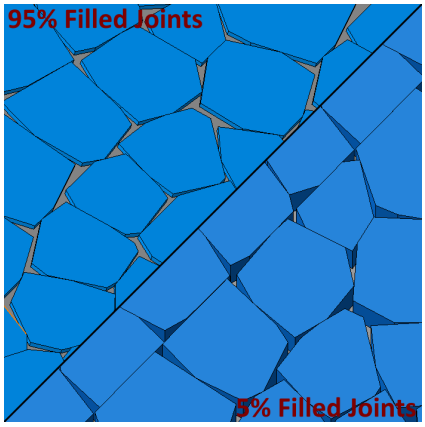

Figure 5.9: Modelled washed-out joint filling

5.2.2.3. Missing Elements

The model can remove elements in the revetment at a predefined location to simulate a missing element. The location of the missing element is given by an X and Z coordinate. If the X and Z coordinates fall between two elements, the model will select the element most close to the given X and Z coordinates. The only elements which cannot be removed are the elements at the boundary due to the boundary conditions given to those elements.

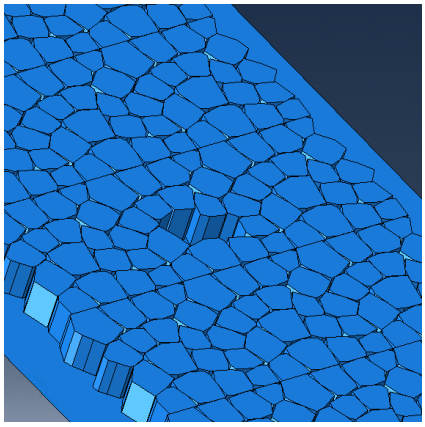

Figure 5.10: Modelled missing element

5.2.3. Parameters

In Table 5.1 a list with all parameters and used values in the model is shown. Unless specified otherwise, the listed values will be used as input for all models in this study. Below the table a justification is given for some of the most important parameters. For all other parameters, an explanation on why this value is chosen can be found in Appendix E.

Symbol	Description	Value	Units
Geometry			
B_m	Width of the model	3.00	[sets]
cot α	Slope	3.00	[-]
d	Water depth	5.00	[m]
$z_{d;top}$	Dimensionless top of the revetment	0.20	[-]
$z_{d;bot}$	Dimensionless bottom of the revetment	-0.55	[-]
g	Gravitational acceleration	9.81	[m/s^2]
Wave Loading			
H_s	Significant wave height	2.50	[m]
T_p	Peak period	5.66	[s]
s_{0p}	Offshore wave steepness	0.05	[-]
i_{st}	Storm Intensity (Appendix C)	0.90	[-]
ρ_w	Mass density of the water	1025	[kg/m^3]
Top Layer			
D	Thickness of the top layer	0.30	[m]
k'	Permeability of the top layer (10% open, Gravel 9/25 mm)	0.05	[m/s]
Λ	Leakage length	0.38	[m]
ρ_e	Mass density of the elements (without joints)	2240	[kg/m^3]
E_e	Young's modulus of the elements	50.0	[GPa]
ν_e	Poisson's ratio	0.20	[-]
μ_e	Friction between elements (with joint filling)	0.85	[-]
μ_f	Friction with the filter	0.60	[-]
Filter Layer			
b	Thickness of the filter layer	0.13	[m]
k	Permeability of the filter layer (Gravel 17/42 mm)	0.19	[m/s]
Numerical			
dx	Step in space for determining loading	0.01	[m]
dt	Step in time for determining loading	0.01	[s]

Table 5.1: Used parameters in the scenarios of Chapter 5 and 6 (unless otherwise specified)

Most values regarding the top layer, filter layer, and joint filling are based upon the flume experiments done by Kaste and Mourik (2016). The significant wave height is 2.50 meters, which is based upon a dimensionless loading ($H_s/\Delta D$) of 7.0 as during the flume experiments for a dimensionless loading of about 7.0, significant damages began to occur (Kaste and Mourik, 2016).

The leakage length of the revetment is 0.38 meters and is calculated based on the thickness of the top and filter layer and the permeability of the top and filter layer. Both permeabilities are calculated by Kaste and Mourik (2016) using the model used in SteenToets. With a joint filling gradation of 9/25 mm and about 10% open spaces, they calculated a top layer permeability of about 0.05 m/s. For the filter layer, they calculated a permeability of about 0.18 with a filter layer thickness of 0.13 meters and a gradation of 17/42 mm.

5.2.4. Calibration of the Model

The final step in the creation of the model is to calibrate the resistance of the revetment by determining the friction coefficient between elements (μ_e). This section aims to obtain a friction coefficient for a well washed in revetment and a friction coefficient for a revetment without joint filling.

The first step in this analysis is to study the normal force within the FE-model. Based on the left pane in Figure 5.11, it can be concluded that there is a limited initial normal force within the revetment at the start of the simulation. This is, however, as expected because the revetment has no loading history. Furthermore, the revetment is generated all at once, while a revetment in the field is built up layer per layer, providing some initial normal force. The right pane of the figure shows the normal pressure between two elements during the simulation. The development of the normal pressure shows similarities to the findings of research done by Wolters and Klein Breteler (2007) in which the development of normal force of a pattern-placed revetment is studied. This suggests that the FE-model can built up a realistic normal force as a result of wave loading. However, as only five waves are simulated, the generated normal force is minimal compared to revetments in the field.

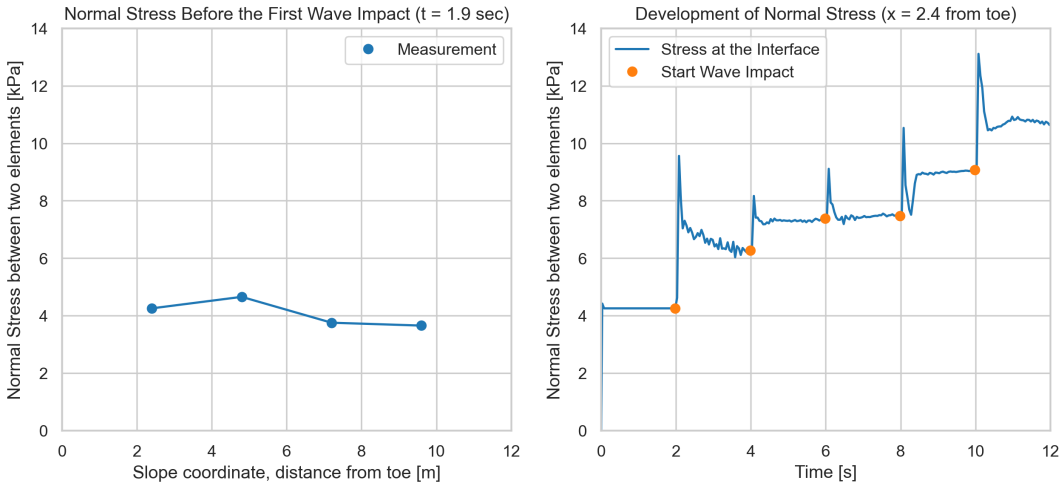

Figure 5.11: Left: Normal Stress at four different locations just before the first wave impact (t = 1.9 sec); Right: Development of normal stress between two elements (x = 2.4 from toe)

The lack of loading history will be compensated by calibration of the friction coefficient between elements. This calibration will be done by comparing results from simulated pull-out tests to pull-out tests done on Basalton revetments in the field. The simulated pull-out tests will be executed as described by Coeveld and Klein Breteler (2003). During the pull-out test a force is applied to an element normal to the slope, which gradually increases over 30 seconds from zero to four times the self-weight of the element. When an element exceeded a displacement of 0.02 meter, the measured force is reported and used to determine the clamping factor, which is defined in Equation 5.3 (Peters, 2017).

$$n_{fl} = \frac{F_u}{G \cos(\alpha)} \tag{5.3}$$

Numerous pull-out tests of Basalton revetments have been performed and/or analyzed by Coeveld and Klein Breteler (2003), Blom (2006) and Peters (2017). It is found that the clamping factor varies a lot between different experiments and revetments. The authors of the publications point out this is the result of many dependencies such as the age of the revetment, the temperature, and the location on the slope. As no firm conclusions are available on the clamping factor for Basalton, we estimate the lower bound of the clamping factor for a well washed in Basalton revetment to be 20. Furthermore, based on pull-out tests performed by Klein Breteler and Mourik (2014) on Basalton revetment with washed-out joint filling, we estimate the lower found of the clamping factor for a revetment without joint filling to be 15.

Next, pull-out tests are simulated based on the parameters presented in Table 5.2.3 and with different friction coefficients (μ_e). A total of seven series with eight pull-out experiments were done on various elements and locations on the slope. All tested elements are shown by a red hatch in Figure 5.12.

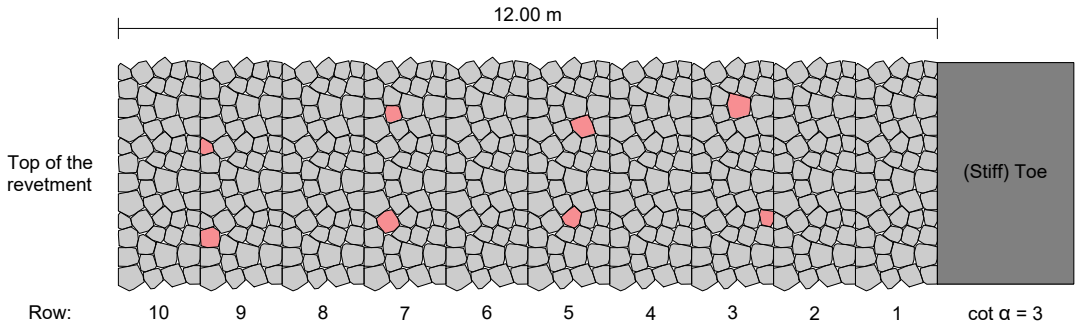

Figure 5.12: Elements on which the pull-out test is performed indicated by red hatch.

The results from the pull-out tests are shown in Figure 5.13. Based on this figure and the found clamping factors for revetments in the field, it is possible to derive the friction coefficients. For a well washed in revetment, a friction coefficient of 0.85 is derived, and for a revetment without joint filling, a friction coefficient of 0.60. It is important to note that the friction coefficients are larger than usual as they include next to the natural friction between elements, compensation for the lack of loading history, and the effect of joint filling.

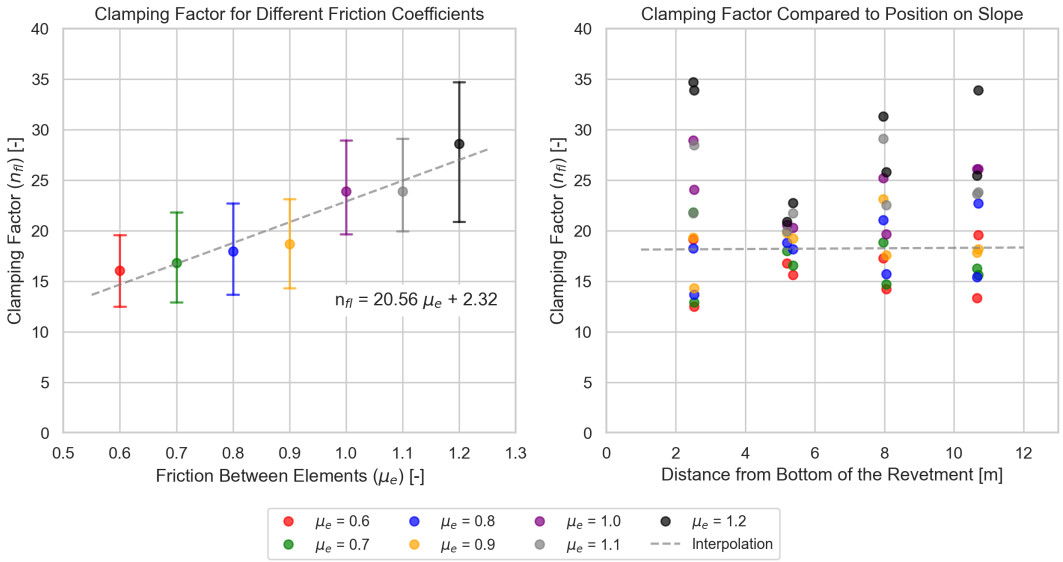

Figure 5.13: Clamping Factor for different friction coefficients (left) and position on the slope (right) (n = 8 for each serie of pull-out tests)

5.3. Scenarios

The scenarios for this chapter are divided into four groups with one or multiple simulations. All scenarios will have an identical set of parameters describing the geometry and loading of the revetment as defined in Table 5.1. Each group will be used to study a specific type of damage. In Table 5.2, the different types of damage and descriptions for each group and scenario can be found. The undamaged scenario will be used as a reference to compare against the scenarios with damage.

The consistency of the model output has been tested by running the same simulation multiple times. It was found that the results of each simulation were identical to each other. This implies that the results from the finite element model are deterministic, and thus no additional uncertainty is introduced by the finite element model suite.

Group 1: No Damage
The undamaged scenario has no changed or additional parameters compared to Table 5.1. Therefore, this group only consists out of one simulation.

Group 2: Deformation (S-Profile)
The scenarios in the second group contain revetments that have deformation in the form of an S-profile. It is assumed that the deformation solely occurs due to migration of the filter material. To model the S-profile, the Equations 4.4 and 4.7 are used to determine location and width. For each of those equations, the 50% exceedance value will be used. The group consists of six scenarios, each with an increasing amplitude of the S-profile ranging from an amplitude over filter thickness ratio from 0.1 to 1.0.

Group 3: Reduced Clamping
The scenarios in the third group contain revetments with reduced clamping to simulate the loss of joint filling. This reduction of clamping is simulated by adjusting the friction coefficient between elements. Based on the verification of the model in Section 5.2.4, the friction coefficient in this group will vary between 0.85 (with joint filling) and 0.60 (without joint filling). The group will consist out of 3 scenarios. The first scenario has a friction factor of 0.80, the second one 0.70, and the third one 0.60.

Group 4: Missing Elements
The scenarios in the last group contain revetments with a missing element. The group consists of two scenarios, in which the first scenario has an element missing just above the wave impact zone while the second scenario has an element missing just below the wave impact zone. In both scenarios, an element of similar size is removed. Both elements will be removed from the center column of Basalton STS+ sets to reduce the impact of the boundary conditions.

Model	Group	Description
1.01	No Damage	No damage will be introduced in this scenario
2.01	Deformation	Small S-profile (a_s/b = 0.1)
2.02	Deformation	Small S-profile (a_s/b = 0.2)
2.03	Deformation	Medium S-profile (a_s/b = 0.4)
2.04	Deformation	Medium S-profile (a_s/b = 0.6)
2.05	Deformation	Large S-profile (a_s/b = 0.8)
2.06	Deformation	Large S-profile (a_s/b = 1.0)
3.01	Reduction in clamping	Small reduction (μ_e = 0.8)
3.02	Reduction in clamping	Medium reduction (μ_e = 0.7)
3.03	Reduction in clamping	No joint filling (μ_e = 0.6)
4.01	Missing elements	Missing element above the wave impact (z = 4.43)
4.02	Missing elements	Missing element below the wave impact (z = 3.47)

Table 5.2: Summary with the description of damage for the different groups of scenarios

5.4. Results

All scenarios defined in Table 5.2 from the previous section are generated and simulated. Within this section, the results will be analyzed. This analysis will give insight into how different types of damage affect the top layer stability. However, before we discuss the impact of damages, we first need to define the output parameters, which will be obtained by analyzing the output of the FE-model with Python. It is chosen to measure the damage of each scenario in the following ways:

- **Number of fully uplifted elements per meter:** The model considers an element fully uplifted when the deformation of the element measured perpendicular to the slope exceeds the top layer thickness somewhere during the simulation.
- **Total maximum deformation per meter:** Is the sum of the deformation perpendicular to the slope of all elements during the peak of the last wave impact, divided by the width of the model. When an element is fully uplifted, the deformation for that element is capped at the top layer thickness.
- **Total final deformation per meter:** Is the sum of the deformation perpendicular to the slope of all elements two seconds after the last wave impact, divided by the width of the model. When an element is fully uplifted, the deformation for that element is capped at the top layer thickness.
- **Highest uplifted element:** The element with the largest deformation over the entire simulation. The deformation of an element is measured perpendicular to the slope. When an element is fully uplifted, the deformation for that element is capped at the top layer thickness.

The results of those output parameters for each scenario can be found in Table 5.3.

Model	Group	Parameter	Uplifted Elements [-]	Sum Max. Deformation [m/m]	Sum Final Deformation [m/m]	Max. Uplifted Element [m]
1.01	No Damage	-	0	0.3716	0.0919	0.20
2.01	Deformation	a_s/b = 0.1	0	0.5807	0.1701	0.24
2.02	Deformation	a_s/b = 0.2	3	0.9792	0.6693	0.30
2.03	Deformation	a_s/b = 0.4	4	1.1634	0.8842	0.30
2.04	Deformation	a_s/b = 0.6	8	1.4896	1.2099	0.30
2.05	Deformation	a_s/b = 0.8	11	2.1555	1.6858	0.30
2.06	Deformation	a_s/b = 1.0	6	2.7102	1.2871	0.30
3.01	Reduction clamping	μ_e = 0.8	0	0.5019	0.0967	0.20
3.02	Reduction clamping	μ_e = 0.7	1	1.1092	0.5114	0.30
3.03	Reduction clamping	μ_e = 0.6	7	1.9136	0.8733	0.30
4.01	Missing elements	z = 4.43	0	0.5315	0.1954	0.18
4.02	Missing elements	z = 3.47	1	0.5361	0.2033	0.30

Table 5.3: Summary of the scenarios for the different groups

5.4.1. No Damage

The scenario from the first group contains no initial damage. The maximum deformation of the revetment during the simulation is illustrated in Figure 5.14. Additionally, two plots are provided in Appendix E for each scenario, one showing the maximum deformation and one final deformation of the revetment.

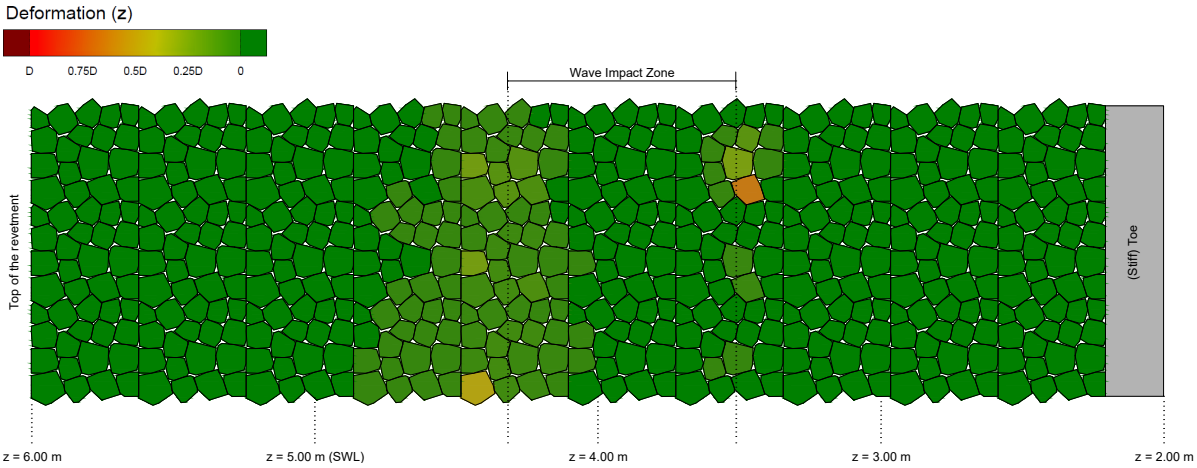

Figure 5.14: Maximum deformation of the revetment during the simulation (No damage)

Figure 5.14 shows that the revetment primarily deforms above and to a lesser extent below the wave impact location. This difference cannot be explained by the wave loading or filter response as the loading is symmetrical above and below the wave impact location (Figure 5.14). Therefore, it is expected that this difference is caused by the development of normal force within the revetment. As is discussed in Section 5.2.4, at the start, there is no difference in the normal force over the revetment. However, during wave loading, normal forces start to develop and becomes increases faster near the toe (Vrijling et al., 2001). At the moment of the snapshot in Figure 5.14, the revetment has already been loaded with a few waves. Therefore, it is expected that the difference in deformation may be explained by the development of normal force within the revetment.

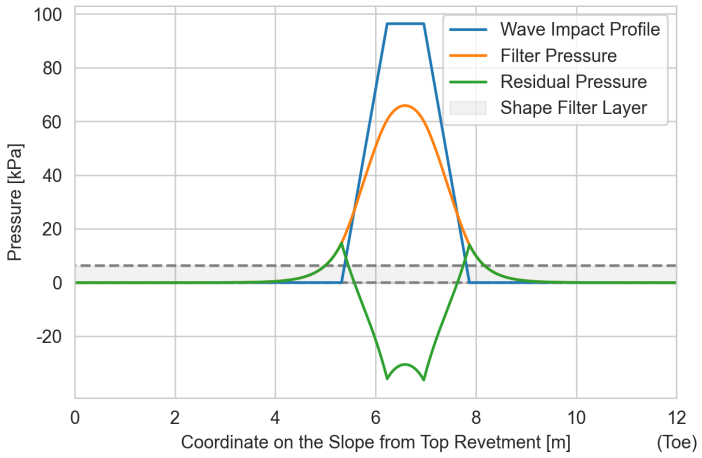

Figure 5.15: Pressures on the revetment during the peak of the wave impact

Although the results are in line with what is expected based upon the analysis of the flume experiments in Chapter 4, it is tricky to interpret the absolute results of the model. This is because it is challenging to verify the results from the FE-model to the flume experiments. Therefore, we will assess the relative impact of damages. Therefore, in the next sections, the impact of damage will be compared against the undamaged scenario, hereafter called the baseline scenario.

5.4.2. Deformation (S-profile)

The first type of damage which will be analyzed is deformation in the form of an S-profile. Figure 5.16 shows the maximum deformation of a medium-size S-profile (model 2.03), in which the amplitude over filter thickness ratio is 0.40.

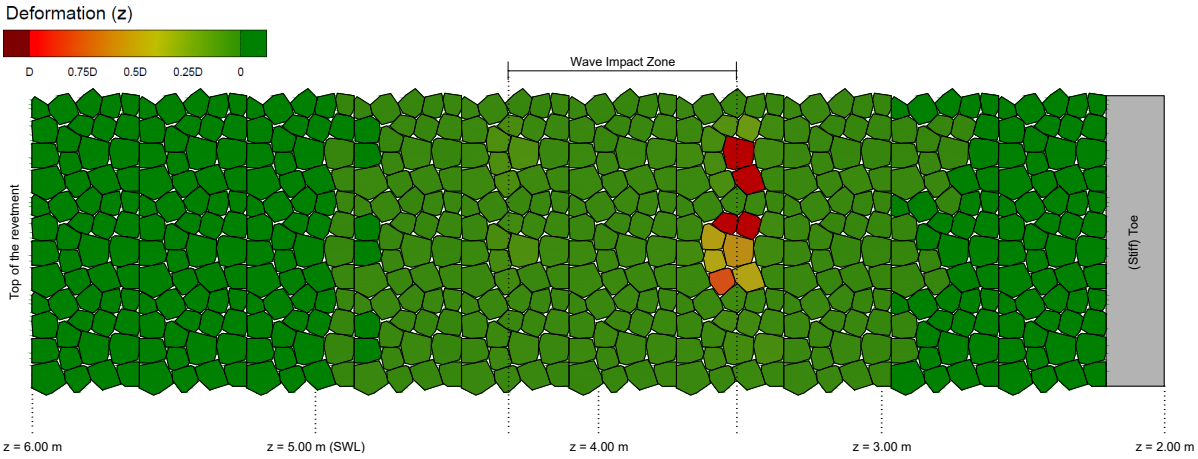

Figure 5.16: Maximum deformation of the revetment during the simulation (Deformation: a_s/b = 0.4)

The results of the simulations done with an S-profile show that the most damage occurs just below the wave impact location, on the hump of the S-profile. This is different from the findings for the baseline scenario, as for that scenario damage was occurring also above the wave impact location. The difference in the location on the slope were damages occurs for an S-profile is also observed during the analysis of the flume experiments in Figure 4.19 of Chapter 4. It turns out that for an S-profile, there is a difference in stability between the area below the wave impact location and above the wave impact location. It is assumed that the hump of an S-profile causes a reduction in stability while the trough of the S-profile causes an increase in stability. This may be explained in two ways:

1. Due to the deformation, the filter layer thickness is no longer constant over the length of the slope. As a result, the leakage length will also change, impacting how the filter responds to the wave impact. In the right pane of Figure 5.17, the loading on the elements is illustrated. It can be seen that due to the local variation in filter layer thickness, the filter response and residual pressure are about 33% larger at the hump than at the trough of the S-profile.
2. Due to the curvature of the revetment, an increase or decrease in clamping can affect the stability locally. As the positive curvature of the hump may induce a loss in clamping, while the negative curvature of the trough may induce an increase in clamping, as earlier discussed during the analysis of the flume experiments in Section 4.4.4.

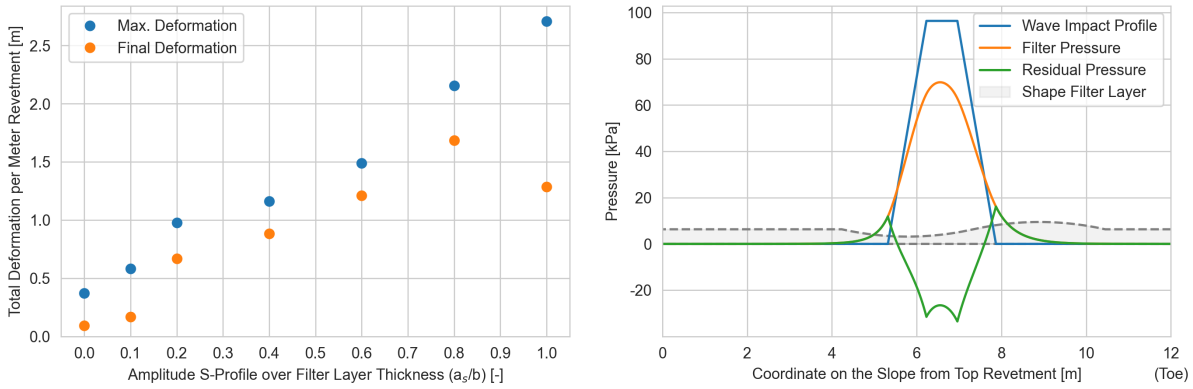

Figure 5.17: Left: Total deformation illustrated for different S-Profile amplitudes. Right: Pressures on the revetment during the peak of the wave impact

The left pane of Figure 5.17 shows the total and maximum deformation of all scenarios together with the baseline scenario. Based on this plot, we identify three different ranges in how damage develops. First, when the amplitude of the S-profile is low, there is a slight increase of about 1.6 times more total maximum deformation. The final state of the revetment is also slightly more deformed for this amplitude than the baseline scenario. The second range begins when the first element is lifted from the revetment ($a_s/b \approx 0.2$), for which the maximum deformation is about 3 - 4 times the baseline scenario. Finally, for large amplitudes ($a_s/b > 0.6$), the maximum deformation is about 4 - 6 times the baseline scenario. For those amplitude, the elements on the hump experience a significant reduction in clamping. As a result, the elements on the hump are not clamped anymore and the only resistance left is the self-weight.

5.4.3. Reduction in Clamping

The second type of damage which will be analyzed is the reduction in friction between the elements. As mentioned previously in Section 5.2.4, the joint filling is replaced with an adjusted friction coefficient between elements to significant reduce the time it takes to run the simulation. The maximum deformation from the scenario with no joint filling is illustrated in Figure 5.18.

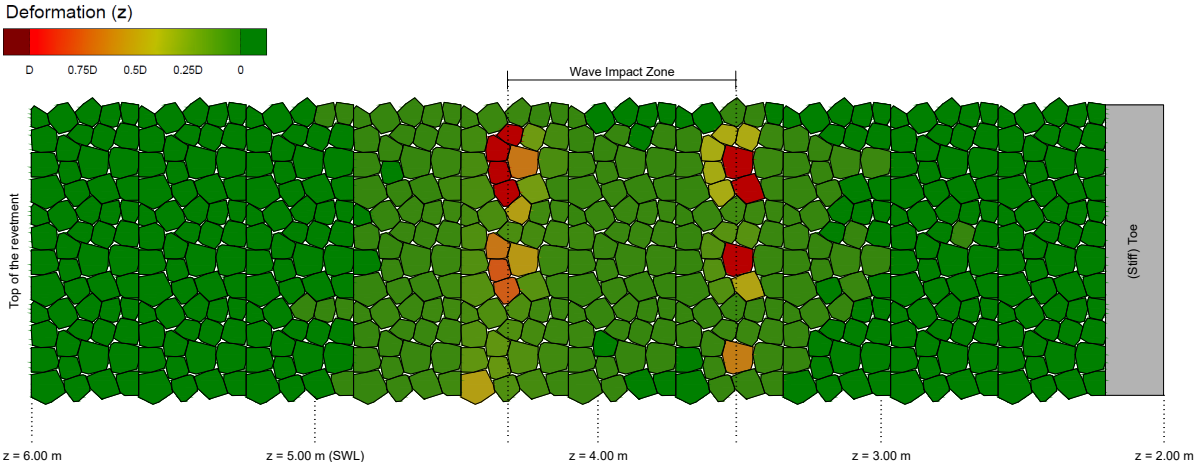

Figure 5.18: Maximum deformation of the revetment during the simulation (No joint filling: μ_e = 0.6)

Based on the physics, it is expected that a revetment with no joint filling is less stable than a revetment with joint filling. This reduction of stability can be explained because a reduction in the amount of joint filling reduces the clamping of an element. This reduction also becomes apparent when assessing the results from a revetment without joint filling. Seven elements were uplifted from the revetment: four elements above and three below the wave impact location. In Figure 5.19, the three scenarios from this group are illustrated together with the baseline scenario. Based on those results, the scenario with no joint filling experience 5.1 times more maximum deformation compared to the baseline scenario. For any cases between full and empty joints, it seems that the revetment linearly becomes weaker in relation to the friction coefficient. However, one should be careful as no data was found to substantiate a linear relationship between the friction coefficient and the amount of joint filling left. It is quite possible that if there is only a little of the joint filling left, the element is still tightly clamped by the normal force in the revetment, as noted by Klein Breteler (2018) within his guideline for maintenance on pattern-placed revetments.

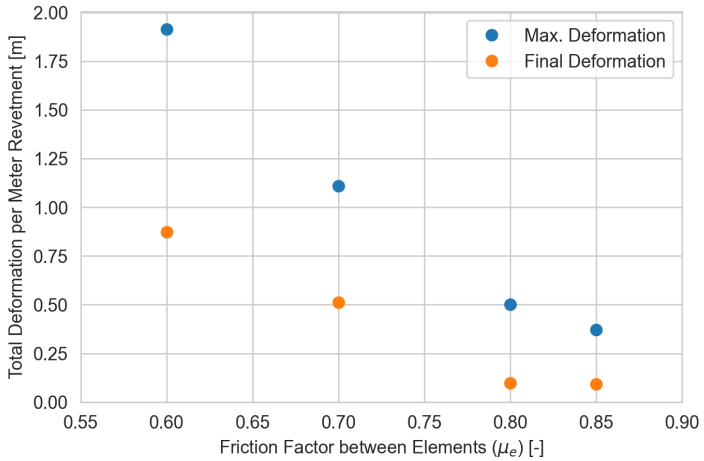

Figure 5.19: Total deformation illustrated for different friction coefficients μ_e.

5.4.4. Missing Elements

The third and last type of damage which will be analyzed is a missing element. In the first scenario an element just above the wave impact location is removed while in the second scenario an element just below the wave impact location is removed. The maximum deformation during the simulation of those scenarios is illustrated in Figure 5.20.

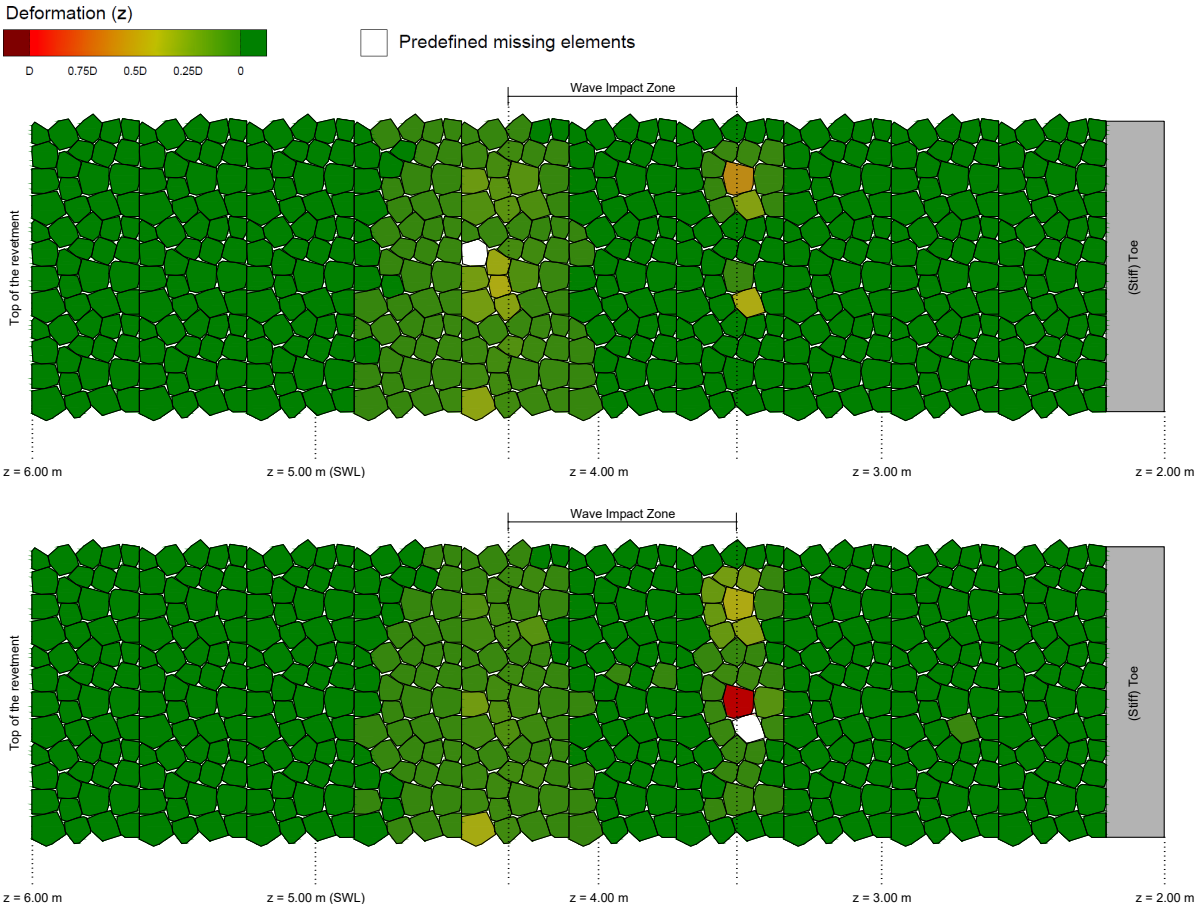

Figure 5.20: Maximum deformation of the revetment during the simulation (Missing element, top: z = 4.43, bottom: z = 3.47)

Based on physics, a revetment with a missing element is expected to be less stable. This reduction of stability is especially the case for the elements next to the missing element because they are negatively affected by the following two aspects:

1. Because one of the neighbouring elements is missing, the contact area of the element with other elements is less, resulting in less clamping.
2. Due to the missing element, the elements will arch around the missing element to redistribute the normal force. Therefore, especially elements below the missing element are at risk of losing a large part of the normal force in the revetment, resulting in less clamping.

In summary, elements around the hole of the missing elements are thus more prone to be fully lifted from the revetment. The latter is the case that happened in the second simulation, as can be seen in the bottom pane of Figure 5.20.

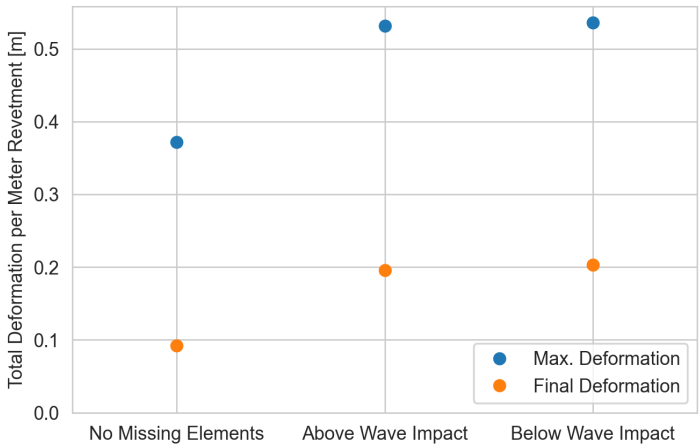

Figure 5.21: Total deformation illustrated for missing elements.

In Figure 5.21, the total deformation for both scenarios is illustrated together with the baseline scenario. Based on the results, it can be concluded that it does not matter whether the element is missing above or below the wave impact location for the total deformation. Generally, a revetment with a missing element will experience 1.4 times more total maximum deformation than a revetment without damage. The simulations show that a single missing element has less impact on the stability than the other analyzed damages. However, we would like to stress that the scenarios simulating a missing element were without any other types of damage. This means that those scenarios simulate a case in which an element is missing due to, for example, vandalism. In the other scenarios with revetments with deformation or reduced clamping, we also saw missing elements. It should be noted that in those cases, the revetment is a lot less stable than the scenarios with only a missing element. This is because those missing elements resulted from the initial simulated damage (deformation, reduced clamping). Therefore, it can be concluded that when it is observed in the field, it is crucial to study the cause of a missing element, as this is essential to avoid misjudging the consequences.

5.5. Summary of Findings

In this chapter, we created a finite element model (FE-model) to study the impact of damaged pattern-placed revetments under wave impact. In the FE-model, three of the most common types of damage are included based upon the parameterization done in Chapter 4. The first goal of this chapter is to find out whether it is possible to use a finite element model to model the behavior of (damaged) pattern-placed revetments. This turned out to be possible. In order to speed up the computation time and allow for more simulations, some simplifications are applied to reduce complexity. The three most important simplifications are listed below:

1. The wave loading is reduced to five wave impacts based on the largest average wave height of five consecutive waves during a storm defined by the significant wave height and storm intensity;
2. The loading of the model is reduced to a simple wave profile used with the filter equation to define a residual pressure on the elements over time and space;
3. The effect of joint filling is accounted for by an adjustment in the friction coefficient between elements. As a result, the joint filling does not have to be physically modeled and speeds up the computation time by a factor of 30.

For revetments in the field, normal force between elements will build up over time due to wave loading, which increases the clamping of the elements. Although the FE-model can also build up normal force due to wave loading, it is not possible to include the loading history within the initial conditions. In the FE-model, this is resolved by calibrating the friction coefficient based upon pull-out tests by Basalton revetments in the field.

The results of the undamaged revetment simulated by the FE-model are in line with what is expected based upon the analysis of the flume experiments in Chapter 4. Nevertheless, it is tricky to interpret the absolute results of the FE-model. This is because it is challenging to validate this model to a revetment in the field or flume experiment as the development of damage is dependent on many different factors. Therefore, the different types of damage are assessed relative to the undamaged scenario.

The second goal of this chapter is to analyze the impact of certain types of damage with the model. With the use of the FE-model, we analyzed three of the most common types of damage and found the following conclusions:

- Deformation (S-profile) will result in 1.5 – 5.8 times more maximum deformation depending on the amplitude. For the analysis is assumed that the S-profile is caused solely by the migration of the filter. Two possible explanations are found why a revetment with an S-profile is less stable. First, the curvature of the S-profile will cause a reduction in clamping. Second, the migration filter layer will cause a larger filter response under the hump of the S-profile.
- Reduced clamping (no joint filling) will result in 5.1 times more maximum deformation. For any cases between full and empty joints, it seems that the revetment linearly becomes weaker in relation to the friction coefficient. However, no relationship between the friction coefficient and the amount of joint filling between elements could be substantiated. It is believed that a small amount of joint filling can still cause relatively large clamping.
- A missing element above or below the wave impact location will result in 1.4 times more maximum deformation. Although the impact of one missing element on the stability seems relatively low, it is important to note that it is removed without any underlying damages, for example, vandalism. In case elements are being lifted out of the revetment due to damages like deformation, the impact on the stability may be a lot more significant. Therefore, when observing a missing element in the field, it is essential to find the cause of why it is missing.

The results of the simulated damaged revetments by the FE-model seem to be in line with the expectations based upon the physics. For example, the S-profile turned out to have the most impact on the stability. As described in the bullet points, we have also found two reasons to explain this based on the physics. This gives us confidence that we can use the FE-model results to estimate the impact of damages relative to a baseline scenario.

6

Impact of Damage on the Reliability

In this chapter, the finite element model created in the previous chapter will be used to assess the impact damages have on the reliability of a pattern-placed revetment. In Section 6.1, the methodology of this chapter is explained. Next, in Section 6.2, a sensitivity analysis is performed on undamaged revetments to find the most important uncertain parameters. After that, the found parameters are used within a sensitivity analysis in Section 6.3 to study the most important uncertain parameters for each type of damage. Based on the obtained samples, a model is created with the use of response surfaces in Section 6.4. With this model, the impact of damage on the stability number is studied in Section 6.5. Then, all findings from the chapter are applied to a case study in Section 6.6. Finally, in Section 6.7 a summary of the most important findings is given.

6.1. Methodology

The two objectives of this chapter are to investigate which uncertain parameters are the most important for failure and the impact of damages on the reliability of the revetment. The finite element model, hereafter called FE-model, created in the previous chapter, will be used to achieve both objectives.

The first objective is achieved in two parts. First, we investigate the most important uncertain parameters for an undamaged revetment. This analysis aims to reduce the number of uncertain parameters, which reduces the required number of samples for the second part. First, we select the most important input parameters of the FE-model and assign representative probability distributions. With Latin Hypercube Sampling, we generate samples and simulate them with the FE-model. Then, using a Fourier Amplitude Sensitivity Test (FAST), we analyze the samples to identify the most important uncertain parameters for a revetment with no damage. Chosen is to work with FAST because fewer samples are required as FAST only estimates the total order sensitivities. In the second part, we will study the most important parameters for a damaged revetment. In order to get more insight into the sensitivities, chosen is to use the variance-based sensitivity analysis, hereafter called the Sobol method. Although the Sobol method generally requires more samples than FAST to estimate the total effect, the benefit of the Sobol method is that first-order and second-order sensitivities are also obtained. For our analysis, we have one sample group without damage and three sample groups with different types of damage: deformation (S-profile), reduced clamping, and a missing element. For the sensitivity analysis, we include the most important uncertain parameters for an undamaged revetment and the parameters associated with the studied type of damage as probability distributions. As required for the Sobol method, the samples are generated based on a Sobol sequence. After the FE-model simulates the samples and the output is processed, we analyze those results with the Sobol method. All sampling and sensitivity analyses are based upon the Python Sensitivity Analysis Libary (SALib) by Herman and Usher (2017).

To achieve the second objective, we use response surfaces to create a model based upon the samples generated for the sensitivity analysis. The response surfaces are fitted with the use of the SciKit-Learn Python package by Pedregosa et al. (2011). Based on the response surfaces, we will study the impact of the Iribarren number and dimensionless leakage length on the stability number. Finally, we will

conclude the chapter by doing a case study and using the response surfaces to estimate the impact of damages on the failure probability of a revetment on a coastal dike.

6.2. Identification of Important Uncertain Parameters

This section aims to obtain the most important uncertain parameters affecting the outcome of an FE-model of an undamaged revetment. With an average computation time of three hours per sample, keeping the sample size as small as possible is vital. However, as the sample size increases for each input parameter assigned as a probability distribution, it is impossible to assign all 22 parameters by a probability distribution and obtain valuable results. Therefore, in this section, we try to reduce the parameters represented by a probability distribution to only the most important ones with the use of a sensitivity analysis. This will allow us in the next section to keep the number of parameters represented by a probability distribution and the sample size as small as possible.

6.2.1. Sample Group

From all parameters as listed in Table 5.1, we choose the six parameters we expect to have the most significant impact in the field on the development of damage. Table 6.1 lists those parameters, including the distribution over which will be sampled. All other non-listed parameters are assumed to be deterministic and defined as in Table 5.1.

Parameter		Distribution	Unit
H_s / ΔD	Dimensionless loading	*U(2.0; 8.0)*	[-]
Λ / D	Dimensionless leakage length	*U(0.5; 2.5)*	[-]
s_{0p}	Offshore wave steepness	*U(0.01; 0.05)*	[-]
i_{st}	Storm intensity	*U(0.0; 1.0)*	[-]
cot α	Slope	*U(2.5; 4.0)*	[-]
$z_{d;top}$	Dimensionless top of the revetment	*U(0.1; 0.3)*	[-]

Table 6.1: Used probabilistic distributions for the sensitivity analysis

All chosen probabilistic distributions are uniform. The choice to apply uniform distributions is to ensure the sample space is evenly sampled. The choice of the assigned probabilistic distributions for each parameter is briefly explained below:

- **Dimensionless loading:** The boundaries of the distribution are based upon the data collected from flume experiments in Chapter 4.
- **Leakage length over top layer thickness:** With a constant top layer thickness of 0.3 meters, the leakage length varies from 0.15 to 0.75 meters. Both boundaries of the distribution are defined based upon data collected from flume experiments with Basalton revetments in Chapter 4 and the flume experiment data on other column-type elements in the Ph.D. thesis of Peters (2017).
- **Offshore wave steepness:** The lower boundary of the distribution is based upon the wave steepness of swell waves, while the upper boundary is based upon the wave steepness rarely exceeded by wind waves as discussed in Chapter 2.
- **Storm intensity:** The boundaries of the distribution are chosen because the storm intensity as defined in Appendix C ranges between 0 and 1.
- **Slope:** The boundaries of the distribution are chosen based upon the most common slopes found in the field and during the flume experiments as found in Chapter 4.
- **Dimensionless top of the revetment:** With a water depth of 5 meters, the top of the revetment varies between 0.5 and 1.5 meters above still water level. The boundaries of the distribution are based upon the data collected from flume experiments in Chapter 4.

6.2.2. Results

Before applying the sensitivity analysis, we first generate and simulate the samples with the FE-model. Next, the output of the FE-model is analyzed with the use of Python. Again, the same output parameters as defined in Chapter 5 are obtained for each sample. To identify the most important uncertain parameters, assessing the process leading up to a damaged revetment is important. In this case, this is the displacement the elements experience during wave loading. Therefore, we choose is to work in the sensitivity analysis with the total maximum deformation per meter, which is defined as:

- **Total maximum deformation per meter:** Is the sum of the deformation perpendicular to the slope during the last wave impact of all elements divided by the width of the model. When an element is fully uplifted, the deformation for that element is capped at the top layer thickness.

Next, the output from the samples is used in a sensitivity analysis. We choose to work with the Fourier Amplitude Sensitivity Testing (FAST) for the sensitivity analysis. The main benefit is that FAST requires relatively few samples in order to predict the importance of parameters. The downside of using FAST is that the method can only estimate the first-order sensitivity indices (Saltelli and Ratto, 2008). The first-order sensitivity indices describe the contribution to the output variation due to a change in a parameter. Therfore, a higher sensitivity index does have a larger impact on the output variation, more on this in the next section. However, only knowing the first-order sensitivity indices is sufficient for this section to conclude which parameters are the most important. In the next section, a sensitivity analysis will be done with the Sobol method, which also provides the total-order and second-order sensitivity indices.

A total of 256 samples are simulated for the sensitivity analysis. The convergence of the sensitivity analysis is analyzed in Appendix F.1. In Table 6.2 the numerical results from FAST can be found. Those results are also plotted together with the 95% confidence interval in Figure 6.1.

Parameter		**First-Order Sensitivity Index (Best Estimate) [-]**	**Standard Deviation [-]**
$H_s/\Delta D$	Dimensionless loading	0.245	0.0835
Λ / D	Dimensionless leakage length	0.124	0.0708
s_{0p}	Offshore wave steepness	0.0525	0.0560
i_{st}	Storm intensity	-0.0143	0.0496
cot α	Slope	-0.00434	0.0474
$z_{d;top}$	Dimensionless top of the revetment	-0.0462	0.0487

Table 6.2: Results from the FAST analysis containing the first-order sensitivity indices and the standard deviation

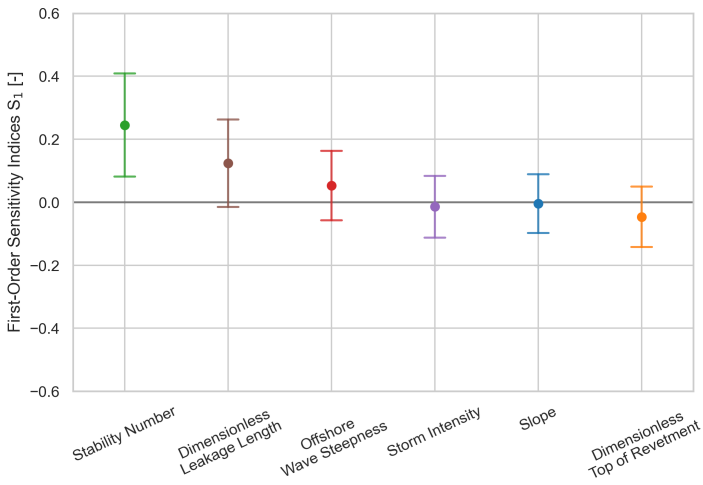

Figure 6.1: First-order sensitivity indices for each parameter together with the 95% confidence interval

Based on the results of the FAST, it turns out that the dimensionless loading, dimensionless leakage length, and the offshore wave steepness are the most important parameters. Therefore, we will include those parameters as random variables in the sensitivity analyses in the next section. The storm intensity, slope, and dimensionless top of the revetment will be replaced with the original constants as defined in Table 5.1.

In Figure 6.2, two plots are shown of all samples. The left plot is the traditional way of presenting flume experiments as a point of the dimensionless loading and Iribarren number. All points are color-coded by the maximum observed uplift of an element (z_e) as defined in Chapter 4:

- **Damage category 1**: Little uplift of an element ($0 < z_e/D < 0.33$);
- **Damage category 2**: Reasonable uplift of an element ($0.33 < z_e/D < 0.67$);
- **Damage category 3**: Much uplift of an element ($0.67 < z_e/D < 1$);
- **Damage category 4**: Element came loose ($z_e/D > 1$).

Based upon the importance of the different parameters, it makes more sense to express the results for those samples as a point of the dimensionless loading and the dimensionless leakage length (Figure 6.2, right plot). In comparison to the left plot, the right plot is a lot less chaotic. It shows that both the dimensionless loading and dimensionless leakage length significantly impact whether an element is fully lifted from the revetment. Some outliers are also visible and can be explained because the sample has either a small or large Iribarren number.

In reality, plotting the results of flume tests using the dimensionless leakage length is quite difficult as the leakage length is generally challenging to determine. In addition to this, it also can vary locally due to damages such as clogged top/filter layers, loss of joint filling, and deformations. The model simplifies this for an undamaged revetment by calculating the loading by assuming a specific uniform dimensionless leakage length.

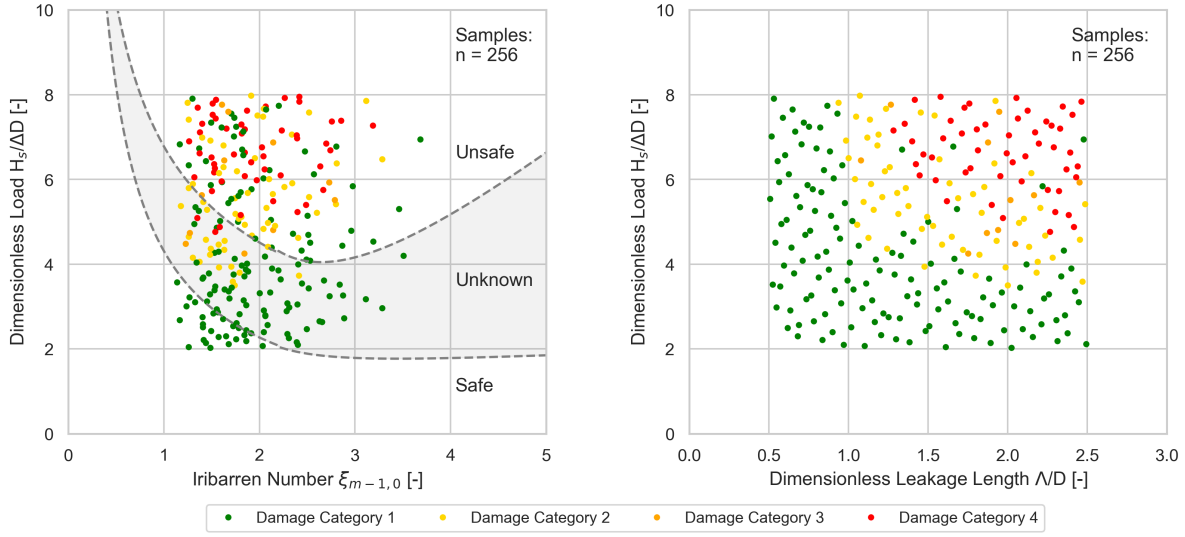

Figure 6.2: Results of the set of scenarios used in the qualitative sensitivity analysis with the VTV2004 stability model (Section 2.4).

6.3. Sensitivity Analysis

This section assesses the impact input parameters of the model have on damage development for four groups of physical states of a revetment, one without damage and three with damage. The three types of damage which will be assessed are deformation (S-profile), reduced clamping, and a missing element. To assess those groups, we will use the Sobol method, a sensitivity analysis that allows for an estimation of the first-order, second-order, and total-order sensitivity indices of all parameters.

6.3.1. Sample Groups

The four assessed groups within this section are revetments with no damage, deformation (S-profile), reduced clamping, and missing elements. In addition to the parameters introduced by the respective type of damage, for all groups also the three most important parameters from the previous section are introduced as probability distributions. An overview of all used probability distributions for the respective parameters can be found in Table 6.4. All the other parameters within the model are deterministic and based upon Table 5.1.

When using the Sobol method within SALib, it is required to sample with a Sobol sequence. For a Sobol sequence, the number of sample points is indicated by N. The Sobol sequence will sample for each sample point N_i a total of $2D + 2$ samples, in which D is the number of parameters assigned by probability distributions. The goal of $2D + 2$ samples for each sample point is to assess the local sensitivity at the sample point by varying each of the parameters one at a time (Saltelli and Ratto, 2008). In order to fulfill the convergence properties of the Sobol sequence and method, the number of samples N should be a base of 2 (Herman and Usher, 2017). For this study, N = 16 is used, giving sample sizes for each group as shown in Table 6.3.

Sample Group	**Parameters (D)**	**Model Realizations**		
		N = 8	**N = 16**	**N = 32**
Group 1: No Damage	3	64	128	256
Group 2: Deformation	6	112	224	448
Group 3: Reduced Clamping	4	80	160	320
Group 4: Missing Elements	5	96	192	384
Total:	-	352	704	1408

Table 6.3: Sample size required for a certain number of sample points N

Group 1: No Damage

The first group contains no damage in the initial conditions of the model. Therefore, the input parameters defined by probability distributions are only the dimensionless loading, the dimensionless leakage length, and the wave steepness. For those parameters, the identical probability distributions and reasoning from the previous section are applicable. This group will also act as a reference to compare against the results of groups with initial damage.

Group 2: Deformation (S-Profile)

In the second group, deformation will be added as an S-profile. The S-profile will add three new parameters based upon the parameterization done in Chapter 4. The following probability distributions define those three new parameters:

- **Uncertainty of the location of the S-profile:** The distribution used is based upon the derived equation for the location of the S-profile. (Equation 4.4, Chapter 4).
- **Uncertainty of the width of the S-profile:** The distribution used is based upon the derived equation for the width of the S-profile. (Equation 4.7, Chapter 4).
- **Ratio amplitude S-profile over filter layer thickness:** The distribution used is defined as a uniform distribution between 0 and 1. The lower bound is defined as the case when there is no S-profile, while the upper bound is defined as the maximum possible amplitude of the S-profile that can happen due to filter migration.

Group 3: Reduced Clamping
In the third group, reduced clamping will be assessed. Reduced clamping is a simplification to study the impact of the loss of joint filling. This type of damage will add one parameter in addition to the three most important parameters for an undamaged revetment. The following probability distribution defines this additional parameter:

- **Friction between elements:** In the previous chapter, this friction coefficient is analyzed. The analysis showed that a revetment with full joints could be approximated by a friction coefficient of 0.85, while empty joints can be approximated with a friction coefficient of 0.60. Those values are therefore chosen as lower and upper boundaries of the uniform distribution.

Group 4: Missing Element
The last group will assess the impact of missing elements. In each sample, one element will be removed based on a parameter z_e which corresponds to the height measured from the flume bottom, and a parameter x_e which is the offset from the center of the revetment. The element at those coordinates will be removed. When a sample point falls on one of the open spaces of the revetment, the element closest to the sample point is chosen. The following probability distributions defines those additional parameters:

- **Location on the slope in height:** The distribution used to select the height up the slope of the removed element is a uniform distribution between 2.5 and 5.0. Those values are chosen to allow the removal of an element under and above the wave impact location.
- **Offset from the centerline of the revetment:** The distribution used to select the offset of the removed element is a uniform distribution between -1.3 and 1.3. This range will allow the selection of any element within the revetment, excluding the outer columns of elements as they are required to impose boundary conditions.

Parameter		Distribution
General (Applicable to all groups)		
H_s / ΔD	Dimensionless loading	*U(2.0; 8.0)*
Λ / D	Dimensionless leakage length	*U(0.5; 2.5)*
s_{0p}	Offshore wave steepness	*U(0.01; 0.05)*
Group 2: Deformation (S-Profile)		
γ_z	Uncertainty of the location of S-Profile (eq. 4.4 for $z_{s;mid}$)	*N(0.358; 0.157)*
γ_B	Uncertainty of the width of S-Profile (eq. 4.7 for B_s)	*N(12.43; 2.65)*
a_s/b	Ratio amplitude S-profile over filter layer thickness	*U(0.0; 1.0)*
Group 3: Reduced Clamping		
μ_e	Friction between elements	*U(0.60; 0.85)*
Group 4: Missing Element		
z_e	Location on the slope in height	*U(2.5; 5.0)*
x_e	Offset from the centerline of the revetment	*U(-1.3; 1.3)*

Table 6.4: Used probability distributions within the different groups

6.3.2. Results

For all groups listed in the previous section, samples were generated using a Sobol sequence and are simulated with the FE-model. Next, the output of the model of each sample is analyzed to obtain the output parameter. Similar to the previous section, chosen is to use the total maximum deformation as the output parameter. For this sensitivity analysis for each group, we will use the Sobol method to obtain sensitivity indices for all parameters. First, we will briefly explain those indices by considering Equation 6.1, in which Y is the output of the model and $X_1, ..., X_D$ are parameters described by probability distributions.

$$Y = f(X_1, ..., X_D) \tag{6.1}$$

With the Sobol method, for each parameter X_i the total-order and first-order sensitivity indices are obtained. In addition to this, the Sobol method will also return a sensitivity index for each pair of parameters (resp. parameters X_i and X_j), which are the second-order sensitivity indices. The larger the sensitivity index, the larger the impact is on the output of the model (Saltelli and Ratto, 2008). Below, the obtained sensitivity indices are briefly described:

- **First-order sensitivity index ($S_{1;i}$):** accounts for the contribution to the output variation due to a change in parameter i. The first-order sensitivity indices are illustrated as light blue circles in the plots below.
- **Second-order sensitivity index ($S_{2;i;j}$):** accounts for the contribution to the output variation due to the interaction between parameter i and j. The second-order sensitivity indices are illustrated as lines between two parameters in the plots below.
- **Total-order sensitivity index ($S_{T;i}$):** accounts for all the contributions to the output variation due to a change in a parameter $S_{T;i} = \sum S_{n,i}$.

More information on the data processing can be found in Appendix D. Data from the sensitivity analysis can be found in Appendix F.

Group 1: No Damage

In Figure 6.3, the sensitivity indices are illustrated for the group without damage. Based on the sensitivity analysis, it can be concluded that the dimensionless loading and the dimensionless leakage length have the largest impact on the development of damage. This makes sense as for a higher dimensionless loading it is more likely that damage occurs. The same goes for the leakage length, as a larger leakage length will induce a higher residual pressure on the elements just below and above the wave impact location as discussed in section 5.4. The second-order sensitivity indices also give some important insight. Based on this analysis, there seems to be a significant non-linear effect between the dimensionless loading and the dimensionless leakage length. It is assumed that this non-linear effect is caused because the residual response defined by the filter equation in Equation 2.12 does not scale linearly with the leakage length. This phenomenon can also be seen in the right plot of Figure 6.2. Additionally, there is also a non-linear effect between the dimensionless loading and the offshore wave steepness. This phenomenon can be explained because wind waves generally induce more damage than swell waves (Schiereck and Verhagen, 2019). This can also be seen when studying Equation 2.9, which is used to determine the maximum pressure caused by the wave impact. This equation shows that wind waves cause a higher impact pressure than swell waves for the same wave height, resulting in a larger residual pressure on the elements.

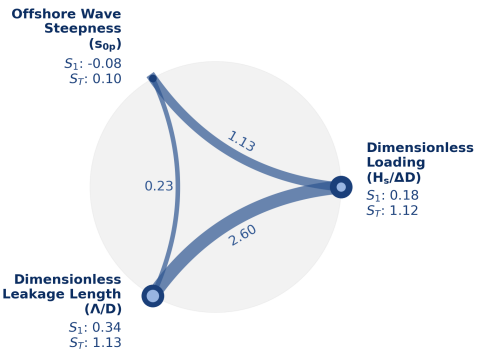

Figure 6.3: Sensitivity indices for group 1 (No Damage)

Group 2: Deformation (S-Profile)

In Figure 6.4, the sensitivity indices are illustrated for the group with deformation in the form of an S-profile. Based on the results, it turns out that the uncertainty of the location and the width does have little impact on the development of damage. However, the amplitude does affect the development of damage. The increase of damage for a larger amplitude was also seen in Chapter 5, in which simulations were done with different amplitudes. In that chapter, we proposed two different arguments why an S-profile causes a reduction in stability. First, due to the curvature, elements on the hump of the S-profile will experience less clamping. Second, because of the migrated filter material, the filter layer thickness varies underneath the S-profile, which affects the filter pressure response causing increased loading on the elements on the hump of the S-profile. If the first argument is the main cause, it is expected that a larger width of the S-profile would induce less curvature and thus more clamping, resulting in less damage. However, the sensitivity analysis shows that with the interaction between the amplitude and the width, more damage will occur for a larger width and amplitude. Therefore, we believe that the second argument is the main contributor to the reduced stability.

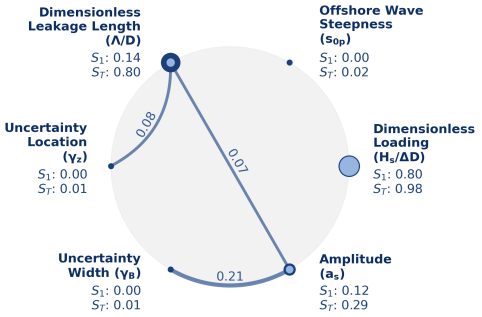

Figure 6.4: Results of the sensitivity for group 2

Group 3: Reduced Clamping

In Figure 6.5, the sensitivity indices are illustrated for the group with deformation in the form of an S-profile. The results show that the interaction between the friction coefficient and the dimensionless loading affects the development of damage. This suggests that having a larger friction coefficient becomes more important for higher stability numbers. In Chapter 5 we translated the impact of empty and full joints into an adjustment on the friction coefficient. From this, we can conclude that for lower stability numbers, the revetment should be able to withstand the loading without joint filling based on the clamping between elements and the self-weight of the elements. For higher stability numbers, joint filling becomes of greater importance to gain additional clamping to resist the larger wave loading.

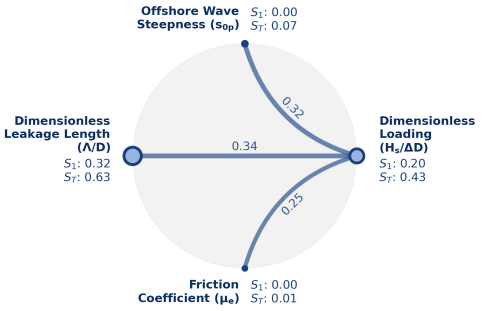

Figure 6.5: Results of the sensitivity for group 3

Group 4: Missing Element

In Figure 6.6, the sensitivity indices are illustrated for the group with deformation in the form of an S-profile. The results show relatively large importance of the X coordinate of the missing element. This may suggest that it may be of importance which element is missing. For example, a Basalton STS+ set consists of 18 different elements, and it may be possible that when an element with a large surface or contact area with other elements is missing, the impact is more significant. Furthermore, for the Z coordinate of the missing element, the impact on the development of damage is likely to be affected by how close the missing element is from the wave impact location. This is important as a missing element will induce a local reduction in clamping, especially for its neighboring elements. As determined in Chapter 5, the closer an element is near the wave impact location, the larger the residual pressure on the elements. Therefore, if an element is missing near the wave impact location, it will likely induce more damage than an element missing further away from the wave impact location.

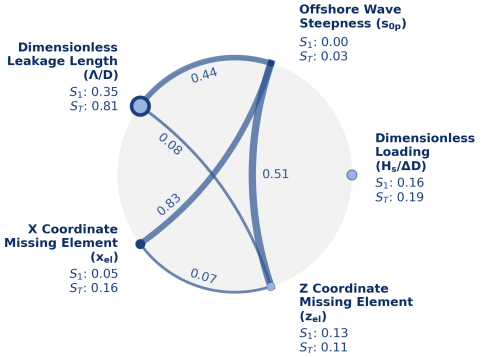

Figure 6.6: Results of the sensitivity for group 4

6.4. Definition of a Stability Model

In the section, we will create the models to estimate the impact on the failure probability based on the different groups of samples from the previous section. This is required because due to the high computational costs of obtaining samples, it is not feasible to do a Monte Carlo simulation with the FE-model to estimate the failure probability. Therefore, we will use the methodology described by Rajashekhar and Ellingwood (1993) in the paper 'A new look at the response surface approach for reliability analysis'. In this paper, Rajashekhar and Ellingwood describe a way to estimate the failure probability using response surfaces. With this approach, we can estimate the failure probability based on the samples obtained in the previous section.

Before we are able to create the response surfaces, first, we have to choose relevant output parameters to obtain from the samples. As the main focus is damage, we chose to look at the final state of the revetment. Therefore, similar to Chapter 5, the output parameters are defined as follows:

- **Total final deformation per meter:** Is the sum of the deformation perpendicular to the slope of all elements two seconds after the last wave impact, divided by the width of the model. When an element is fully uplifted, the deformation for that element is capped at the top layer thickness.
- **Number of fully uplifted elements per meter:** The model considers an element fully uplifted when the deformation of the element measured perpendicular to the slope exceeds the top layer thickness somewhere during the simulation.

The number of fully uplifted elements per meter is the most useful output parameter as it says the most about the failure of the revetment. However, the FE-model has a width of 3 sets of Basalton STS+ elements (3.27 meters). Therefore, this parameter contains out of a discrete set of values, starting at 0 and increasing with steps of about 0.306 (1/3.27). To solve this, we will relate the number of fully uplifted elements per meter to the final total deformation (Figure 6.7) and use the final total deformation to define our failure definition.

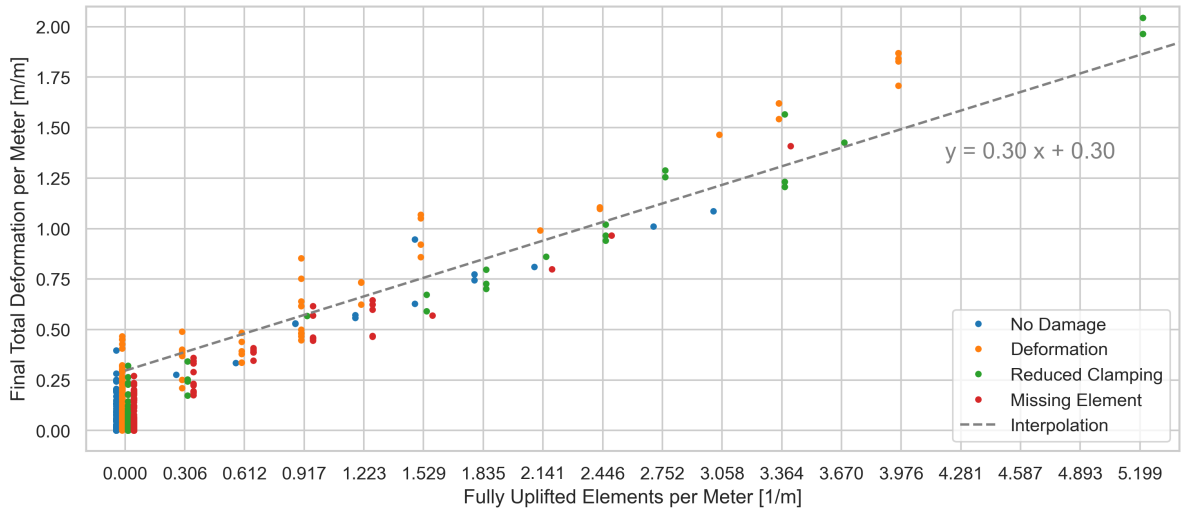

Figure 6.7: The total final deformation per meter illustrated versus the number of fully uplifted elements per meter

In our analysis, we define the revetment to be failed when on average, one element is fully uplifted every three meters of revetment. Although, it is difficult to pinpoint an exact criterion, we think that for this number of fully lifted elements per meter it becomes more difficult to keep the resistance provided by normal force. With the use of Figure 6.7, this translates to about final total deformation of 0.4 meters per meter.

It is important to note that this failure definition differs from the typical definition used in practice. In Section 2.4, we discussed several models. Compared to our failure definition, those models are all defined based on the criteria that no elements may be fully lifted from the revetment. Using Figure 6.7, this criterion would most likely translate into 0.1 meters per meter.

6.4.1. Fitting Response Surfaces

Next, we will fit four response surfaces to the samples of each of the four groups: no damage, deformation (S-profile), reduced clamping, and a missing element. In the previous section, those samples were generated using a Sobol sequence to perform a Sobol analysis. Because this sampling method focuses on a uniform sample space, those samples are also very suitable to fit response surfaces. A response surface typically consists out of a n^{th} order polynomial, in which n is equal or lower to the number of input parameters to prevent an ill-conditioned fit (Rajashekhar and Ellingwood, 1993). To fit a response surface to the sample data, we use Support Vector Regression (SVR) from the Python package SciKit-Learn (Pedregosa et al., 2011). SVR is an algorithm that uses supervised learning to regress data. Within the SVR, a polynomial kernel type was used as this turned out to give the best fits. In order to determine the correct order, all data was illustrated in a 3D environment. Then, based on the shape of the data points, it was chosen to apply a second-order polynomial kernel. After the regression analysis by SVR, a black-box model as shown in Equation 6.2 is obtained, which can be used to predict the final total deformation for any set of parameters. More information on the fit and the errors can be found in Appendix F.2.

$$\begin{aligned} Y_1 &= f_1\left(\frac{H_s}{\Delta D},\ \xi_{m-1,0},\ \frac{\Lambda}{D}\right) \\ Y_2 &= f_2\left(\frac{H_s}{\Delta D},\ \xi_{m-1,0},\ \frac{\Lambda}{D},\ \gamma_z,\ \gamma_B,\ s_a\right) \\ Y_3 &= f_3\left(\frac{H_s}{\Delta D},\ \xi_{m-1,0},\ \frac{\Lambda}{D},\ \mu_e\right) \\ Y_4 &= f_4\left(\frac{H_s}{\Delta D},\ \xi_{m-1,0},\ \frac{\Lambda}{D}\right) \end{aligned} \tag{6.2}$$

The response surface models and the training data is available on the GitHub of the author: https://github.com/nielsvandervegt/mscthesis/tree/main/DamageModels

In Section 6.5, we will use the response surfaces to study the impact of the Iribarren number and the dimensionless leakage length on the stability number.

6.4.2. Estimating the Failure Probability

The final step is to use the response surfaces to estimate the failure probability. In our analysis, we will use a Monte Carlo simulation to obtain and compare the failure probabilities for different types and intensities of damages. Before we can use the Monte Carlo simulation, we first have to define limit state functions as in Equation 6.3, in which the resistance is denoted by R and the loading by S.

$$Z = R - S \tag{6.3}$$

In Equation 6.3, the loading (S), will be defined by the function of the fitted response surfaces as in Equation 6.2. The resistance (R) will be defined as the maximum allowed final total deformation, and may vary and thus is denoted by R_{dam}. As discussed earlier, we suggest a value of 0.6 for total failure of the revetment and a value of 0.1 to prevent any elements from being lifted up. This will lead to the limit state functions shown in Equation 6.4.

$$\begin{aligned} Z_1 &= R_{dam} - f_1\left(\frac{H_s}{\Delta D},\ \xi_{m-1,0},\ \frac{\Lambda}{D}\right) \\ Z_2 &= R_{dam} - f_2\left(\frac{H_s}{\Delta D},\ \xi_{m-1,0},\ \frac{\Lambda}{D},\ \gamma_z,\ \gamma_B,\ s_a\right) \\ Z_3 &= R_{dam} - f_3\left(\frac{H_s}{\Delta D},\ \xi_{m-1,0},\ \frac{\Lambda}{D},\ \mu_e\right) \\ Z_4 &= R_{dam} - f_4\left(\frac{H_s}{\Delta D},\ \xi_{m-1,0},\ \frac{\Lambda}{D}\right) \end{aligned} \tag{6.4}$$

In Section 6.6, we will demonstrate this model within a case study of a coastal dike in the Netherlands.

6.5. Impact on the Stability Number

Based on the response surface models from the previous section, we are able to study the impact the leakage length and the Iribarren number have on the stability number of the revetment. All other stability models are based on the failure criterion that no elements may be lifted from the revetment. Therefore, to compare the results against the other models, we use a failure definition of 0.1 meter final total deformation per meter revetment (Figure 6.7). Using this failure definition, we created curves for the stability number for the different types of damage.

6.5.1. Deformation (S-profile)

In Figure 6.8 two sets of stability curves are shown, one for a varying dimensionless leakage length and one for a varying Iribarren number. The factors relating to the location and width of the S-profile are set to their expected values to only study the impact of the amplitude.

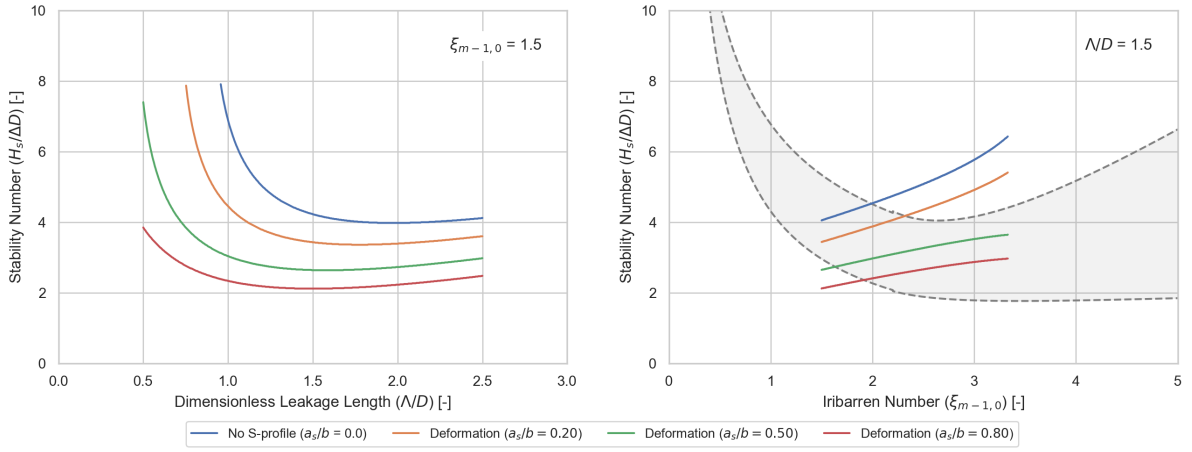

Figure 6.8: Design curves from the response surfaces for different deformations with the VTV2004 stability model (Section 2.4)

First of all, we consider the curve representing a revetment without damage. Based on the curve in the left pane of Figure 6.8, it can be concluded that a larger dimensionless leakage length will lead to a smaller stability number. This can be explained by the fact that for large dimensionless leakage lengths, the ratio between the overall permeability between the filter and top layer is large. Consequentially, the water in the filter is not able to flow fast out of the top layer, resulting in larger filter response (Cirkel et al., 2015). As a result, for the same wave height, a revetment with a higher dimensionless leakage length experience a larger residual pressures on the elements explaining the decrease in the stability number.

In the curve in the right pane of Figure 6.8, we see an increase of stability for a larger Iribarren number. Based on the wave impact models discussed in Section 2.2.2.4, we know that the largest wave impact pressure is expected for an Iribarren numbers between 1.5 and 2.0. For larger numbers, the wave impact pressure decreases for the same significant wave height as the breaker type changes from plunging to collapsing. This explains why for larger Iribarren numbers, the stability number increases.

For the curves describing the revetments with different intensities of deformation, we can see the same behaviour as we described for the no damage curves. However, for those curves the stability number is lower. This caused by a reduction in clamping and increase of loading caused by the deformation, as discussed in Section 5.4. The curves suggest that the decrease of stability number is more or less linear to the increase of the amplitude over filter thickness ratio of the S-profile. The only exception is the right end of the curve in the left pane of Figure 6.8, here the bottom two lines have a different curve. We were not able to relate this behaviour to any physical process, therefore we expect this may be an effect from the fitting.

6.5.2. Reduced Clamping

In Figure 6.9 two sets of stability curves are shown, one for a varying dimensionless leakage length and one for a varying Iribarren number.

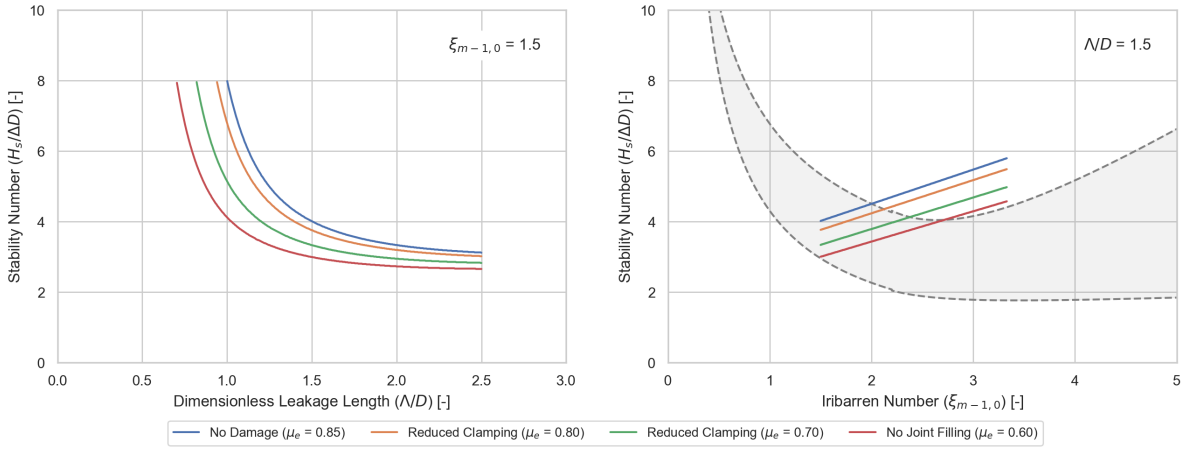

Figure 6.9: Design curves from the response surfaces for reduced clamping with the VTV2004 stability model (Section 2.4)

From Figure 6.10 we observe that a reduction in clamping or washed-out joint filling has less impact on the stability number than deformation has. Nevertheless, according to the model, washed-out joint filling still reduces the stability number with 25% for a revetment with a dimensionless leakage length of 1.5. The curves shows that the decrease of the stability number is more or less linear to the decrease of the friction coefficient.

6.5.3. Missing Element

In Figure 6.10 two sets of stability curves are shown, one for a varying dimensionless leakage length and one for a varying Iribarren number.

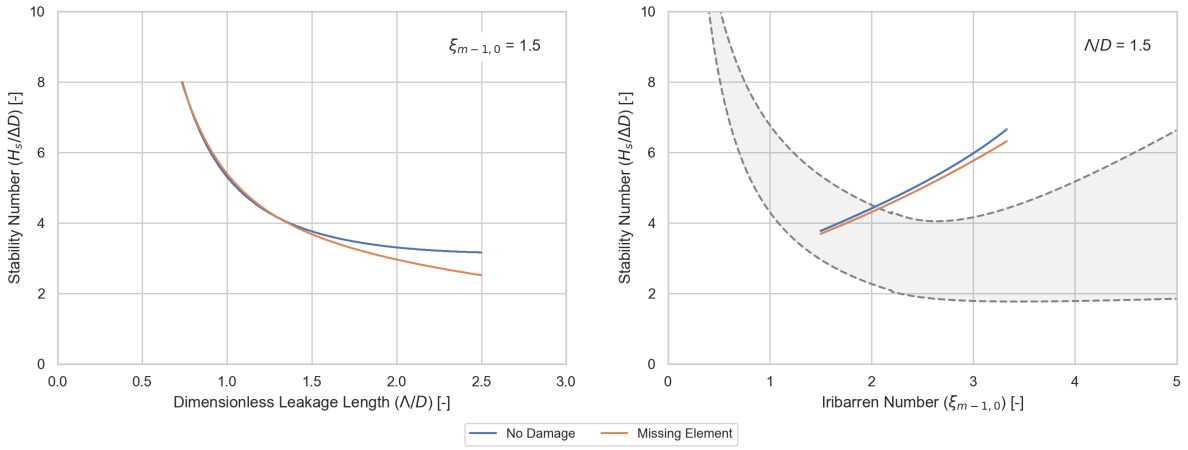

Figure 6.10: Design curves from the response surfaces with and without a missing element with the VTV2004 stability model (Section 2.4)

From Figure 6.10 can be seen that the differences between the revetments with and without a missing element are minimal, with the exception for a large dimensionless leakage length. For a larger dimensionless leakage length, the filter response reaches further away from the wave impact location, affecting a larger area of elements. Consequentially, this has a larger impact on the stability of the revetment and thus a larger resistance is required. We believe that due to the missing element, the resistance of a revetment with a missing element is lower, and therefore more affected by a wider filter response. As a result, this causes the curves to deviate from each other for larger dimensionless leakage lengths.

6.6. Case Study: The Impact of Damages on a Coastal Dike

In this section, we will apply the findings from the previous sections to a case study of a typical coastal dike in the Netherlands. Within the case study we will estimate the impact of damages for a dike at the coast of the North Sea, near Den Helder. First, we will introduce the case, then we will assess the different damages.

We will assess the pattern-placed revetment on the lower outer slope of the dike, a sketch of the cross-section of this part of the dike is shown in Figure 6.11. The outer slope of the dike has a berm, which is also used as a bike path. The lower outer slope has a slope of 1 in 4 and consists out a pattern-placed revetment made of Basalton which transitions just before the berm into a revetment of asphalt. The pattern-placed revetment is supported by a toe made of rubble mound penetrated with asphalt. The upper outer slope consists out of an asphalt on the lower part and a grass on the upper part. In our analysis we will only consider wave loading normal to the dike, which in this case, are waves coming from the west.

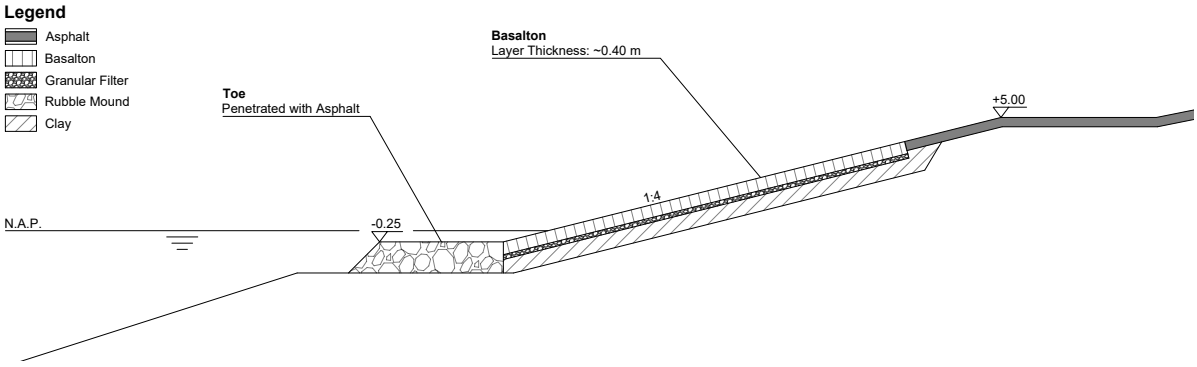

Figure 6.11: Sketch of the lower out slope (height data from Actueel Hoogtebestand Nederland, 2021)

The first step in our analysis is to define the input parameters related to the strength and loading of the assessed revetment. Each of the response surface models require at least the dimensionless loading $H_s/\Delta D$, the Iribarren number $\xi_{m-1,0}$ and the dimensionless leakage length Λ/D as input (Equation 6.4). The significant wave height in the dimensionless loading is defined using the Bretschneider equations, which are deterministic models to estimate the significant wave height and the peak wave period (TAW, 1989a). Over the years, there have been several variants of the Bretschneider equations developed. The variant we will use is from the computer program Hydra-NL (HKV, 2019) and is presented by Equations 6.5 and 6.6.

$$H_s = \frac{0.283\ u_{10}^2\ v_1}{g} \cdot \tanh\left(\frac{0.0125}{v_1}\left(\frac{g\ F}{u_{10}^2}\right)^{0.42}\right) \quad \text{with} \quad v_1 = \tanh\left(0.530\left(\frac{g\ d}{u_{10}^2}\right)^{0.75}\right) \tag{6.5}$$

$$T_p = \frac{2.592\pi\ u_{10}\ v_2}{g} \cdot \tanh\left(\frac{0.077}{v_2}\left(\frac{g\ F}{u_{10}^2}\right)^{0.25}\right) \quad \text{with} \quad v_2 = \tanh\left(0.833\left(\frac{g\ d}{u_{10}^2}\right)^{0.375}\right) \tag{6.6}$$

In which:

u_{10}	=	Wind speed 10 meter above water level	[m/s]
F	=	Fetch	[m]
d	=	Water depth	[m]
g	=	Gravitational acceleration	[m/s^2]

The Iribarren number $\xi_{m-1,0}$ is calculated based upon the results from the Bretschneider calculations as shown in Equation 6.7. The peak period is translated into the spectral period $T_{m-1,0}$ by using the rule of thumb: $T_p \approx 1.1\ T_{m-1,0}$ (EurOtop, 2018).

$$\xi_{m-1,0} = \frac{\tan\alpha}{\sqrt{\frac{H_{m0}}{L_{m-1,0}}}} \quad \text{with} \quad L_{m-1,0} = \frac{gT_{m-1,0}{}^2}{2\pi} \tag{6.7}$$

All input parameters and corresponding probability distributions for this dike can be found in Table 6.5. Below the table a justification is given for all parameters.

Parameters		Distribution	Unit
Distributions & Values			
u_{10}	Wind speed at 10 meter above water level	*Weibull(11.00; 3.50)*	[m/s]
F	Fetch	*Normal(250000; 5000)*	[m]
d	Water depth	*Normal(35; 3.5)*	[m]
Λ	Leakage length	*Normal(0.6; 0.06)*	[m]
Deterministic			
g	Gravitational acceleration	9.81	[m/s^2]
D	Top layer thickness	0.4	[m]
cot α	Slope	4	[-]
ρ_s	Mass density of the top layer elements	2800	[kg/m^3]
ρ_w	Mass density of the water	1025	[kg/m^3]

Table 6.5: The defined probability distributions and values for each parameter used in the case study

The following justifications belongs to the choice of values and distributions for the different parameters:

- **Wind speed (u_{10}):** The Weibull distribution is obtained from Hydra-NL and is based on wind data from Schiphol (HKV, 2019).
- **Fetch (F):** Is modelled by a Normal distribution and is based upon the measured distance between Den Helder and the United Kingdom in the westerly direction. A coefficient of variance of 2% is chosen because the fetch may differ depending on the exact angle of the westerly wind (270 $\pm$ 11.25 degrees).
- **Water depth (d):** Is modelled by a Normal distribution and based upon the bathymetry west of Den Helder. It is estimated that the average water depth is about 35 meters (Marine Regions, 2021). A coefficient of variance of 10% is chosen for the uncertainty.
- **Leakage length (Λ):** Is modelled as a Normal distribution and is based upon the analyzed data from the Basalton flume experiments in Section 4.3. It is expected that the dimensionless leakage length is about 1.5. This will result in an average value for Λ of 0.6, to account for variation a 10% coefficient of variance of applied.
- **Top layer thickness (D):** The top layer thickness is estimated to be 0.40 meters.
- **Slope (cot α):** The outer lower slope has a slope of 1 in 4 based on height data from Actueel Hoogtebestand Nederland (2021).
- **Mass density of the top layer elements (ρ_s):** The mass density of the top layer elements, excluding the open spaces, is assumed to be 2800 kg/m^3 based on the analyzed data from the Basalton SS/VS flume experiments in Section 4.3.
- **Mass density of the water (ρ_w):** Is assumed to be sea water with a mass density of 1025 kg/m^3.

6.6.1. Estimating the Impact of Damages

In the next part of the case study, the impact of different types and intensities of damage on the pattern-placed revetment are assessed. First, the different response surface models are compared against each other. Thereafter, for each type of damage, a probabilistic assessment will be done based on the methodology from Section 6.4.2.

Performance of the Response Surface Models

Before we analyze the impact on the failure probability by the different types of damage. First, we will compared the different response surface models, hereafter models, to each other. In Figure 6.12, failure probabilities are illustrated for a revetment without damage for different definitions of the resistance (R_{dam}) in the limit state function. The three curves are obtained for the no damage, deformation and reduced clamping models. For the latter two groups, the parameters relating to damage are defined such that they will predict the impact of a revetment without damage (amplitude S-profile over filter thickness is 0 and friction coefficient is 0.85). For the model relating to the missing elements, it is not possible to obtain results for a revetment without damage. This is because for this group, there are only samples with one missing element and therefore, a revetment without damage is not within the sample space.

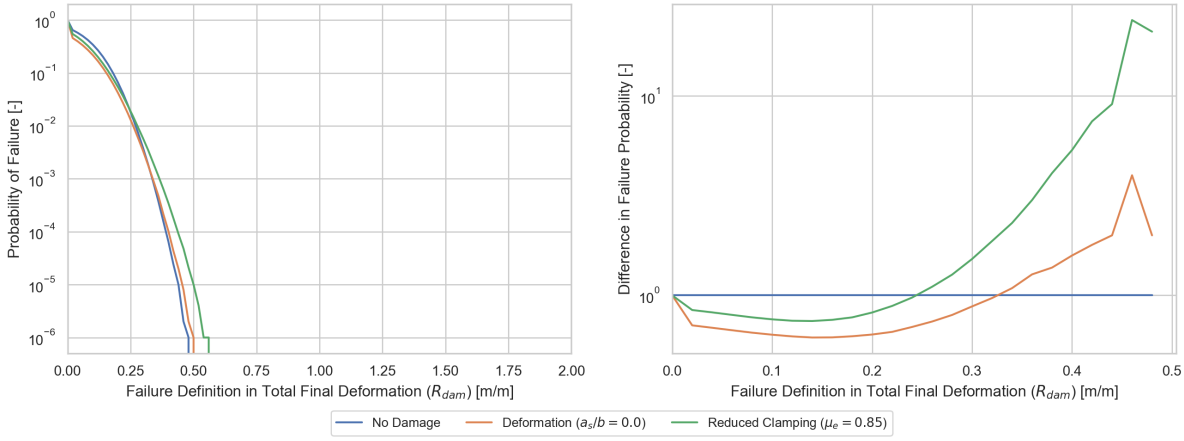

Figure 6.12: Probability of failure of the no damage scenario for different definitions of the resistance (R_{dam}) in the limit state function (step size = 0.02, n = 10^6 per step)

From Figure 6.12, it can be seen that there are some differences for lower failure probabilities between the different 'No Damage' scenarios based on the different response surfaces. This makes it tricky to compare results with a low failure probability from one group to another. As discussed in Chapter 5, the FE-model does not introduce any uncertainty when doing multiple runs with identical revetments. Therefore, it can be concluded that those differences can be attributed to the response surface fit. To resolve those differences, it is chosen to compare the impact of deformation and reduced clamping to a revetment without damage as predicted by the models itself. This is assumed to be a proper solution as within the deformation and reduced clamping group, the set of parameters relating to a revetment without damage is at the border of the sample space and can therefore be estimated by the models itself. For the response surface for revetments with a missing element, this is not possible. Therefore, we will compare that model to the model without any damage.

Finally, to validate the models for this case study, the design point is calculated for the undamaged scenario using the First-Order Reliability Method (FORM). By obtaining the design point, it can be checked if the most likely combination of parameters causing failure is within the sample range. If it is, this gives confidence that the obtained results are based upon the samples on which the response surface is fitted. Within the FORM analysis, we used the failure definition of 0.4 meters per meter final total deformation as defined in Section 6.4. The calculated design point contained a dimensionless loading of 6.55, an Iribarren number of 1.54, and a dimensionless leakage length of 1.76. Based on those results, it can be concluded that all values from the design point are within the sample space defined in Section 6.3.

Deformation (S-profile)
In Figure 6.13, the failure probabilities for different amplitudes of the S-profile are illustrated.

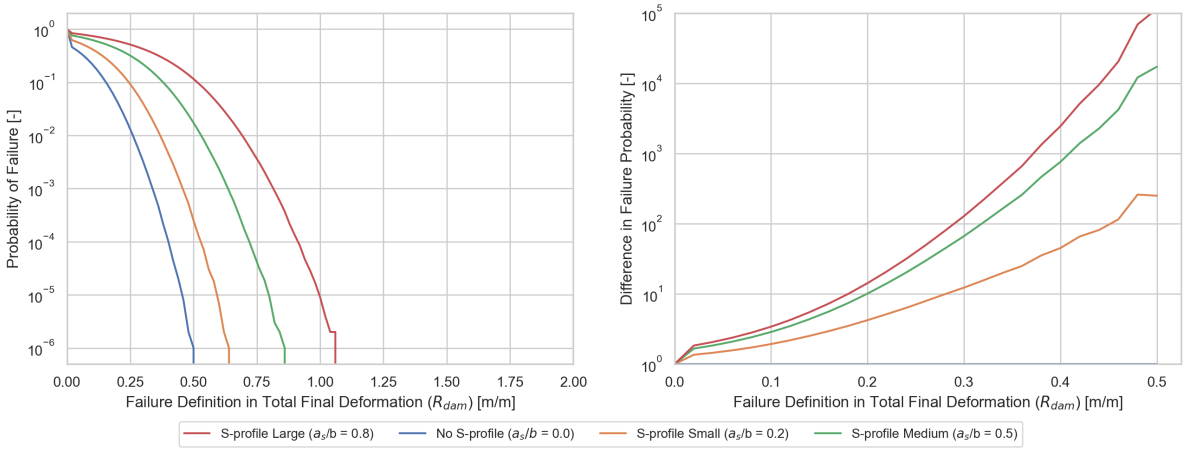

Figure 6.13: Probability of failure of different S-profile amplitudes for different definitions of the resistance (R_{dam}) in the limit state function (step size = 0.02, n = 10^6 per step)

From Figure 6.13, it can be concluded that for a larger allowable damage (R_{dam}), the impact on the failure probability increases. From all three studied types of damage, the S-profile can have the largest impact. Furthermore, the impact increases when the amplitude over filter thickness ratio becomes larger. If we apply a maximum allowable total final deformation of 0.4 meters per meter (Section 6.4), the failure probability of the revetment becomes 10^1 - 10^2 times as large for a small S-profile, and up to 10^3 - 10^4 as large for a large S-profile. An overview of the results is available in Table 6.6.

Reduced Clamping (No Joint Filling)
In Figure 6.14, the calculated failure probabilities for different friction coefficients applied to the elements are illustrated. The goal of the different friction coefficients is to simulate a revetment with joint filling (μ = 0.85), a revetment without joint filling (μ = 0.60) and two cases between those.

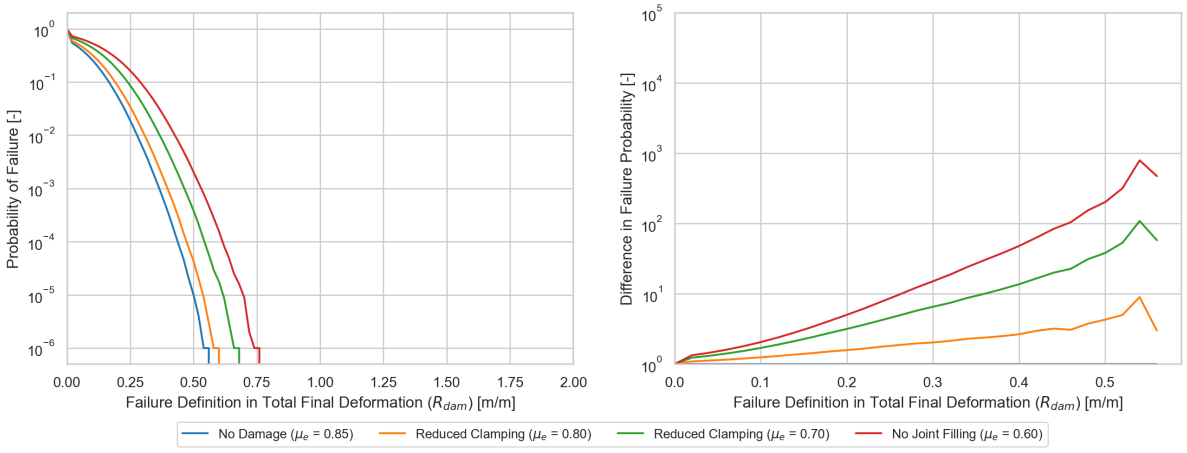

Figure 6.14: Probability of failure of different clamping reductions for different definitions of the resistance (R_{dam}) in the limit state function (step size = 0.02, n = 10^6 per step)

From Figure 6.14, it can be concluded that washed-out joint filling also has a large impact on the failure probability. Again, if we apply a final total deformation of 0.4 meters per meter as our failure definition. We see that when all the joint filling is washed-out, the failure probability increases by 10^1 - 10^2 times. An overview of the results is available in Table 6.7.

Missing Elements

In Figure 6.15, a failure probability curve is shown for revetments with one missing element. It is important to note that two different curves are obtained from two different models. The curve with no damage is obtained from the response surface model fitted on the samples without damage and the curve for the missing element is from the model fitted on the samples with a missing element.

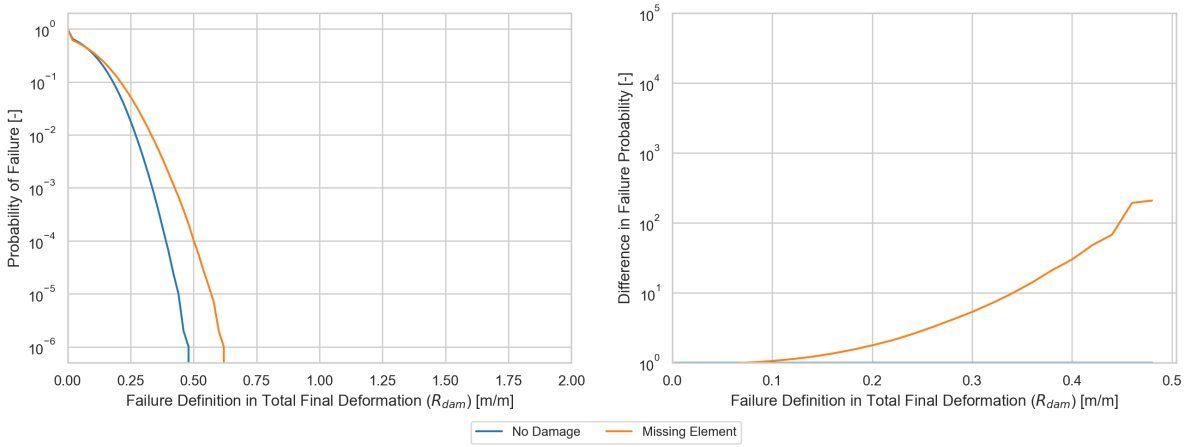

Figure 6.15: Probability of failure of a revetment with a missing element for different definitions of the resistance (R_{dam}) in the limit state function (step size = 0.02, n = 10^6 per step)

Based on Figure 6.15, a revetment with a missing element impacts the failure probability by a factor of 10^1 - 10^2 when the failure definition is defined as 0.4 meters per meter final total deformation. An overview of the results is available in Table 6.8.

6.6.2. Vulnerability

A final conclusion will be given based on the concept of vulnerability, which allows for quantification of the impact of the damages seen in the curves. As vulnerability is a relative indicator, it is particularly useful for this analysis. Lind (1995) defines the concept of vulnerability in his paper 'A measure of vulnerability and damage tolerance' as "The ratio of the failure probability of a damaged system to the failure probability of the undamaged system", shown by Equation 6.8.

$$V = \frac{P\,(r_d,\ S)}{P\,(r_0,\ S)} \tag{6.8}$$

The considered system is the top layer of the pattern-placed revetment during the most intense moment of the storm. In the analysis, we studied the final total deformation which we related to the average number of uplifted elements per meter revetment. The studied failure mechanism is therefore the uplift of elements as a result of pressure difference over the top layer. The damaged system is the same system with damages included within the initial conditions. Practically, this means that the damage is already present before the storm.

With the vulnerability, it is possible to assess the difference between the impact of different types of damage. The failure definition is defined based upon Section 6.4 and is 0.4 meters per meter final total deformation. Which is about one element fully lifted from the revetment per three meter of revetment (Figure 6.7). From the assessment of the different types of damage, the failure probabilities are collected and analysed for the vulnerability in Tables 6.6, 6.7 and 6.8. Based on those results, it can be concluded that deformation has the most significant impact on the failure probability with a vulnerability of 800 for a medium size S-profile. A small size S-profile (50) has about the same vulnerability as no joint filling (50) and a missing element (40).

Deformation (S-profile)	Parameter	Failure Probability	Vulnerability
No Damage	a_s/b = 0.0	$1.01 \cdot 10^{-4}$	1
Small S-profile	a_s/b = 0.2	$4.63 \cdot 10^{-3}$	50
Medium S-profile	a_s/b = 0.5	$7.82 \cdot 10^{-2}$	800
Large S-profile	a_s/b = 0.8	$2.52 \cdot 10^{-1}$	2500

Table 6.6: Failure probability and vulnerability for different intensities of deformation (n = 10^6)

Reduced Clamping	Friction	Failure Probability	Vulnerability
No Damage	μ_e = 0.85	$3.40 \cdot 10^{-4}$	1
Small Reduction Clamping	μ_e = 0.80	$8.72 \cdot 10^{-4}$	3
Large Reduction Clamping	μ_e = 0.70	$4.67 \cdot 10^{-3}$	15
No Joint Filling	μ_e = 0.60	$1.67 \cdot 10^{-2}$	50

Table 6.7: Failure probability and vulnerability for different intensities of reduction of clamping (n = 10^6)

Missing Element	Elements	Failure Probability	Vulnerability
No Damage	0	$5.20 \cdot 10^{-5}$	1
Missing Element	1	$1.88 \cdot 10^{-3}$	40

Table 6.8: Failure probability and vulnerability for different revetments with a missing element (n = 10^6)

6.7. Summary of Findings

In this chapter, we used the finite element model from the previous chapter to study the impact damages have on the reliability of the revetment. In the first part of the chapter, we analyzed the most important uncertainty parameters, and in the second part, we created models that can estimate the impact of damages on the failure probability. Finally, the chapter was concluded by a case study in which all findings were applied to estimate the failure probability of a damaged revetment.

The first goal of this chapter is to identify which uncertain parameters have the largest impact. Because the FE-model has a computation time of three hours per model, keeping the number of samples small is vital. Therefore in order to achieve this objective, we did two analyses. The goal of the first analysis was to identify the most important uncertain parameters for an undamaged revetment. As the sample size increases for each additional parameter, we chose the six parameters out of the 22 input parameters for an undamaged revetment, which we thought would have the most significant impact on the development of damage. Next, we did a sensitivity analysis using a Fourier Amplitude Sensitivity Test (FAST) with those six parameters. This test allows for a relatively accurate estimation of the first-order sensitivity index for each parameter for a small sample group. Based on the results of the FAST, it turns out that the dimensionless loading ($H_s/\Delta D$), the dimensionless leakage length (Λ/D), and the offshore wave steepness (s_{0p}) have the most significant impact and are therefore included again in the second analysis. The storm intensity (i_{st}), the slope ($\cot \alpha$), and the dimensionless top of the revetment ($z_{d;top}$) showed a relatively small impact and were therefore assumed to be a constant in the second analysis.

The goal of the second analysis was to identify the most important uncertain parameters for a damaged revetment. Similar to the previous chapter, we created four groups, one without damage and one for each of the following damages: deformation (S-profile), reduced clamping, and a missing element. For each group, we did a sensitivity analysis using the Sobol method. The results gave some interesting insights into the different types of damage. For each damage, the dimensionless loading and the dimensionless leakage length were the most important parameters. In addition to this, the results suggested that the main cause of the decreased stability of a deformed revetment is the increase in loading caused by the migrated filter material. Furthermore, the results for the group with the reduced clamping showed that the loss joint filling is mainly of concern for a larger dimensionless loading. Finally, for a missing element, the results suggested that an element close to the wave impact location is of larger concern than an element more down the slope.

The second goal of this chapter is to study the impact damages have on the failure probability of a revetment. To achieve this goal, response surface models were created using Support Vector Regression (SVR), an algorithm that uses supervised learning to regress data. With those models, the impact of the Iribarren number and dimensionless leakage length on the stability number is studied. From this analysis, it can be concluded that the impact of both parameters is logical and explicable based on the physics and literature. For deformation on a typical pattern-placed revetment, the stability number decreased from 4 to 2-3 depending on the amplitude of the S-profile. For reduced clamping, the stability number decreased from 4 to 3. We found a difference between smaller and larger leakage lengths for a missing element as this type of damage seems to affect primarily revetments with larger leakage lengths. We expect that this happens because, for a larger dimensionless leakage length, the filter response reaches further away from the wave impact location affecting a larger area of elements. As a result, the elements around the hole are all affected at once and require more resistance.

Finally, we applied all findings from this chapter to a case study for a coastal dike near Den Helder. Using a Monte Carlo analysis, the failure probability for a revetment with different types of damage on the lower slope of a dike is calculated. The impact the different damages and intensities have is expressed with the concept of vulnerability. For deformation, vulnerabilities were found ranging from 50 for a small S-profile ($a_s/b = 0.2$) up to 2500 for a large S-profile ($a_s/b = 0.8$). The vulnerability for a revetment without joint filling is 50 and with a missing element 40.

7

Discussion

This study aims to answer whether it is possible to estimate the impact of damages on the stability and reliability of a pattern-placed revetment with the use of a model. Within the study, first, a qualitative assessment of the different types of damage is done. Based on this assessment, the uplift of elements, deformation, and washed out joint filling is further analyzed with data from old flume experiments. Finally, these damages are implemented within a finite element model (FE-model) to estimate the impact the damages have on the stability and reliability. It turned out that deformation (S-profile) has the most significant impact on the stability and the failure probability, followed by washed out joint filling and a missing element.

We will divide the discussion into two parts. First in Section 7.1, we will discuss the methodology used to estimate the impact of damages. Next, in Section 7.2, we discuss the implications of the results on the daily practice.

7.1. Discussion on the Model

In the first part of the discussion, we will discuss the effect of the different simplifications used within the FE-model and the parameterization of the damages. First, we will discuss the assessment of pattern-placed revetments in the Netherlands and how the obtained model related to that. Next, the modeling of the wave loading and filter response is discussed. Finally, the parameterization and implementation of the different types of damage are discussed.

Assessment of Pattern-Placed Revetments

Within the Netherlands, SteenToets is usually used to assess pattern-placed revetments. The program assesses revetments using four different loading schematizations: two wavefronts, and two wave impacts. The wave impact schematizations are identified by type 1 and 2 (Figure 2.28), and the main difference is that type 1 does have a trough, and type 2 does not (Klein Breteler and Van der Werf, 2006). Within the FE-model, the wave impact schematization from the thesis of Peters (2017) is used. This schematization is similar to type 1 of the schematizations used within SteenToets (Klein Breteler and Kaste, 2019). This raises the question of whether a simulation of type 2 is also required to get a complete picture of the strength of a revetment. Peters (2017) suggests in his thesis that the type 2 schematization mainly is applicable for waves impacting the slope at a degree of 70 degrees or less. He adds that this is usually only the case for small waves with a relatively high velocity breaking on a shallow slope. Within this study, we only simulate rather large waves on steep slopes. Therefore those waves are best represented by a type 1 schematization or, for this study, the wave model from Peters (2017). Consequentially, we expect that the assessment done by the FE-model is in line with the evaluation done by SteenToets.

Wavefronts are neglected within the FE-model as it is primarily a failure mechanism for revetments with a large leakage length under wave loading with large Iribarren numbers, such as revetments made of blocks (Klein Breteler and Van der Werf, 2006). However, based on the performance of simulating wave

impacts, we think that the FE-model can also be used to study the effect of wavefronts. However, because the FE-model does a dynamical analysis, first, a wavefront loading schematization should be defined in time and space before it can be added to the FE-model.

Wave Loading
Whereas applications as SteenToets assess the impact of wave loading on the revetment statically, the finite element does this dynamically. As it is not feasible to simulate a whole storm within a relatively short time, another way had to be found to load the revetment. It is important that the loading contains enough wave impacts to create damage, also the number of wave impacts should be minimized to decrease computation time. Therefore, it is opted to simulate five individual waves with an identical wave height and steepness. The wave height is statistically derived based on the expected largest average wave height of five consecutive waves in a storm of 5000 waves, generated based on a given significant wave height. As the main focus of this study is to investigate the uncertainty due to structural changes, those simplifications allow for a more straightforward quantification of the loading. Nevertheless, those simplifications also have implications. Within a storm, the wave height and steepness vary per wave. Therefore, certain combinations of wave height and steepness may result in heavier loading than simulated by the model. Additionally, not every storm consists out of 5000 waves. Consequentially, when a storm has more waves, the loading will increase as it is more likely that five consecutive large waves will load the revetment. On the contrary, for a storm with fewer waves, the loading decreases.

Filter Response
Last, we will discuss the simplifications made for the filter response of the revetment. Within the FE-model, the filter response is modeled as 1D linear potential flow. This is a typical way to determine the filter response used by SteenToets or other stability models. An important simplification by modeling the filter response this way is that it requires the leakage length to be linearized by assuming that the flow of water through the top layer and filter material is laminar (Klein Breteler and Van der Werf, 2006). However, in reality, flow through gravel is often classified between laminar and turbulent (Schiereck and Verhagen, 2019). As the flow through the top layer and within the filter layer is between laminar and turbulent, the actual permeability is lower than predicted, and therefore, the actual leakage length is also lower. As a result, the loading within the model is slightly overestimated (TAW, 1989b). Next, the leakage length is assumed constant for most of the simulations. The only exception in which the leakage length varies is when initial deformation is applied, for which the leakage length is calculated based upon the varying filter thickness. In reality, the leakage length may vary along the slope due to deformation, washed-out joint filling, uplifted elements, or other types of damage. During the simulation of the revetment, the leakage length will not change for any damages which may occur. It is expected that this simplification does not have a significant impact on the five simulated waves. However, if more waves are simulated, it may have an effect because damages, such as deformation, may increase in intensity during the storm.

Modelling of Deformation (S-profile)
The first type of damage we discuss is the deformation in the form of an S-profile. Within the FE-model, the S-profile is implemented based upon three parameters: the location of the center, the total width, and the amplitude of the S-profile. To achieve a smooth implementation within the FE-model, the S-profile is modeled by a single sine period. Although this is correct for larger Iribarren numbers, the data from the flume experiments showed that the hump is generally a bit wider than the trough for lower Iribarren numbers (Figure 4.14). Within this study, it is assumed that deformation is caused solely by the migration of filter material. Therefore, based on the conservation of the filter material, if the hump is wider than the trough, the amplitude of the hump is lower than the trough. It is difficult to substantiate this argument as most experiments only report the amplitude of the S-profile based upon the difference between the maximum and minimum of the S-profile. However, we believe this is a logical consequence of the differences in width. The sensitivity analysis in Chapter 6 showed that the increase of filter layer thickness primarily causes the increase of the loading under the hump. Therefore, if the amplitude of the hump is, in reality, smaller than modeled, the increase of the filter response under the hump is also less. Based on this, we can conclude that the FE-model predicts most likely an upper bound, and is the most accurate when the Iribarren number is large.

Modelling of Washed-Out Joint Filling
The second studied type of damage with the FE-model is washed-out joint filling. A loss of joint filling impacts the clamping between elements and therefore reduces the stability of the revetment. The effect joint filling has within the model is included within the calibration of the friction coefficients. This friction coefficient has been calibrated based on simulating pull-out tests and comparing the results to pull-out tests done in the field. The effect of joint filling is included by deriving one friction coefficient for a revetment with sufficient joint filling and one for a revetment without joint filling. The calibration of the friction coefficients introduces two important uncertainties. First, to obtain an accurate result from the simulated pull-out tests, a sample size of about 150 pull-out tests is required (Coeveld and Klein Breteler, 2003). However, only eight pull-out tests were used to determine the clamping factor within the model due to the computation time. Second, reports on pull-out tests show a wide range of clamping factors for Basalton revetments. This is primarily because the strength of a revetment is dependent on many different aspects and can even vary from day to day (Blom, 2006). It is challenging to estimate a clamping factor due to the widely different predictions of clamping factors. Therefore, it is chosen to define the clamping factor more conservatively. Consequentially, the FE-model predicts most likely an upper bound. This implies that most revetments are generally more stable than the FE-model will predict.

Modelling of a Missing Element
The third and last studied type of damage with the FE-model is a missing element. A missing element will leave a hole in the revetment, which causes a reduction of clamping. Within the FE-model, a missing element is simulated by removing an element before the start of the simulation. This is an important fact because, during the first two seconds of the simulation, the elements within the revetment displace from their initial position to their steady-state position. Although the displacements caused by this reordering of elements are minimal (< 1 mm), this allows the revetment to arch a bit of the normal force around the missing element. In reality, when an element is removed because of, for example vandalism, it will take some wave impacts before the elements around the hole reorder and arches the normal force around the missing element. As a result, over time, the revetment becomes stronger. The FE-model is not capable of studying the direct impact of a missing element. Instead, the simulation resembles a revetment that survived the initial impact caused by a missing element and was able to reorder and arches a bit of the normal force around the missing element. Based on this argument, it is believed that the FE-model predicts most likely a lower bound.

7.2. Discussion on Implications of the Results

In the second part of the discussion, the results are interpreted and the implications are discussed for daily practice. In Chapter 3, we identified eight different types of damage for pattern-placed revetments, three of which we assessed further by an analysis of old flume experiments and simulations with an FE-model. Based on the analysis of old flume experiments in Chapter 4, it is shown that basalt revetments are subject to identical types of damage as for Basalton revetments. Therefore, it is believed that the findings within this study apply to a broader range of top layer elements with similar characteristics to Basalton (e.g. basalt, C-Star, and Hydroblocks).

The results from Chapter 5 and 6 showed that deformation in the form of an S-profile has the most significant impact on the stability and reliability of a pattern-placed revetment. Within this study, we assume that the migration of the filter material solely causes deformation. In reality, deformation can be caused by multiple root causes related to the core of the dike or soil underneath, such as consolidation, creep, or liquefaction. If instead of migration of the filter material, deformation is caused by these root causes, it is expected that the consequences will be less severe. When we compared two revetments with deformation against each other, of which one has migrated filter material, and the other has an equal filter layer thickness, the total displacement of elements decreased by 20%. The sensitivity analysis from Chapter 6 shows that the decreased stability caused by deformation is primarily driven by an increase in loading due to a difference in filter layer thickness. Although geotechnical deformations are not affected by an increase in loading, they still affect the resistance as the positive curvature of the deformation (e.g., shaped like a hump) negatively affects the clamping between the elements and makes it easier for joint filling to be washed-out. Finally, if a damage has not been ob-

served during inspection, the damage is also not repaired. Klerk et al. (2021) studied the probability of detection (PoD) for various damages on revetments. Although no PoD was derived for a deformed pattern-placed revetment, a PoD of 0.3 is derived for a deformed grass slope. Assuming that this PoD is related to spotting deformation in general, those findings suggest it is difficult to spot deformations. This could be caused by the fact that a deformation stands out less as it generally has a relatively small height difference compared to the total length of the slope. This raises the question if a visual inspection is accurate enough to be able to observe deformations. Based on this PoD, we think there are other better ways to inspect revetments, such as surveying the slope using a drone.

Next to an S-profile, the results show that washed-out joint filling also significantly impacts the stability and reliability of pattern-placed revetments. Several root causes are found which may cause washing out of joint filling, such as the growth of woody vegetation, pressure differences over the top layer, and vandalism. For the finite element model, we included the effect of joint filling within the friction coefficient. It should be noted that the amount of joint filling left within the joints is expected not to have a linear relationship with the friction coefficient of the elements. On the contrary, with some joint filling washed-out, it is likely that the elements are still well clamped (Klein Breteler, 2018). However, the results also show that it is vital to keep the revetment well washed in. According to the sensitivity analysis, the resistance caused by the clamping from the joint filling becomes more critical for larger loading.

The last type of damage studied with the FE-model is a missing element. It is important to note that there are two primary reasons why an element could be missing. The first reason is that the element could be missing due to vandalism. Within the FE-model, this is the scenario that is simulated. Based on the results from Chapter 5 and 6, the consequences of a missing element due to vandalism seem to be limited. Those mild consequences are also observed during a flume experiment with a Basalton revetment in which three elements were removed to study the development of damage. After a few experiments, of which one with a slightly larger hole of two missing elements, no other damage than washed-out joint filling and migrated filter material was observed (Klein Breteler and Eysink, 2007). The second reason that can cause a missing element is when the element is uplifted due to any underlying damage. In this case, those missing elements indicate the beginning of failure of the revetment, and therefore immediate maintenance intervention is required. In conclusion, it is vital that when a missing element is observed during an inspection, the location is not only reported but also if there might be a reason why an element is missing.

Another observation done during the qualitative analysis of damages is related to the root causes of the growth of non-woody vegetation and the growth of woody vegetation. The only damage caused by the growth of non-woody vegetation is clogging of the top and filter layer. This seems to be insignificant. However, it is crucial to limit the growth of non-woody vegetation for two reasons. First, it becomes more difficult to inspect the revetment. Second, the growth of non-woody vegetation will eventually cause, if not maintained, the growth of woody vegetation (Klein Breteler, 2018). Contrary to non-woody vegetation, woody vegetation can cause many damages, such as (partial) uplift of elements, washed-out joint filling, and wider joints, and therefore may have a significant impact on the stability of the revetment.

This study mainly focuses on the impact of only one type of damage on a revetment. However, in the field, it is common to observe revetments with different types of damage. Therefore, one of the questions raised from this study is, what is the effect of combinations of damages? We think an important driver for vulnerable combinations of damages are the so-called progressive damages. Progressive damage is characterized by the fact that it affects one of its own root causes, which could lead to a domino effect. For example, suppose one element is uplifted from the revetment due to pressure differences over the top layer. In that case, it becomes a lot more likely for the neighboring elements also to be lifted from the revetment due to the reduced clamping caused by the hole in the revetment. Based on the qualitative assessment of damage in Chapter 3, we identified two progressive damages in this study: deformation and the uplifted elements. If one of those progressive damages occurs together with one of the other damages, it is believed that the revetment will fail earlier. An example of such a combination is deformation with washed-out joints. The washed-out joints cause easier uplift of the elements on the hump; this allows for more space for the filter material to migrate, resulting in faster growth of the deformation.

8

Conclusion and Recommendations

8.1. Conclusion

This research aimed to study whether it is possible to estimate the impact of damage on the stability and reliability of a pattern-placed revetment using a model. This study clearly shows that it is possible to create a finite element model that can estimate the impact damage has on the stability and reliability of a pattern-placed revetment. The obtained results have the potential of being used within the daily practice as part of risk-based maintenance and within further research to assess other types of damage. For risk-based maintenance, this study provides a way to obtain a first indication of the impact of missing elements, deformation, and washed-out joint filling. Additionally, the developed methodology can be used to obtain the impact of other types of damage. Although Basalton is the primarily investigated type of top layer, analysis of the flume experiments showed that basalt revetments are subject to identical types of damage. Therefore, it is expected that the findings within this study can be applied to a broader range of top layer elements with similar characteristics to Basalton (e.g. basalt, C-Star, and Hydroblocks).

A framework has been created to evaluate damage by relating it to the root cause and impact. Based on a literature review, eight different types of damage were identified. It is found that there are two ways in which the damage can affect the stability of the revetment. First, it can affect the resistance of the revetment if it impacts the self-weight of the element, the clamping between the elements, or the friction with the filter layer. Second, it can affect the filter response of the revetment if it impacts the leakage length. Additionally, the damages deformation and missing elements turned out to be progressive, as they can provide a positive feedback loop by affecting their own root cause. This results in a faster progression of the damage when the intensity of the damage becomes larger.

Data from old flume experiments are collected and analyzed to obtain insight into the damages: (partial) uplift of elements, deformation, and washed-out joint filling. Based on an analysis of all uplifted elements, it can be concluded that all Basalton elements and most basalt elements were uplifted caused by wave impact. Furthermore, the amount of joint filling in the different experiments is analyzed. The results show that most joint filling is washed-out around the wave impact zone, followed by the wave run-down and wave run-up zones. Additionally, the data indicates that a lower loading is required for elements to be lifted from the revetment when less joint filling is left in the joints. Last, it turned out that the revetment deforms as an S-shape near the wave impact zone caused by the wave impact, hereafter called S-profile. Models are being defined to estimate the location and the width of the S-profile as no models were available in the literature. A dependency of the S-profile location is found with the Iribarren number. A dependency of the width of the S-profile is found with the dimensionless loading, Iribarren number, and filter thickness. Analysis of the S-profile with the different uplifted elements showed that most elements were uplifted from the hump of the S-profile.

A finite element model, hereafter FE-model, is created, which allows for simulation of wave impacts on a Basalton revetment. The insights and parametrizations of damages obtained from the analysis of the flume experiments are used to model damages within the FE-model. Multiple scenarios with different

types and intensities of damage are simulated to assess the impact damages have. The results are presented in Table 8.1. Based on the results, it turns out that the S-profile has the most significant impact on the total deformation measured. Two reasons are found why this may be the case. First, the model assumes that the S-profile is caused solely by the migration of filter material. Therefore, the filter layer under the hump is thicker than under an undamaged part of the revetment. This thicker filter layer allows for a locally larger leakage length and, therefore, a larger residual loading on the elements. Second, due to the curvature of the S-profile, the clamping is reduced on the hump. For a revetment with no joint filling, it was found that it also had a significant impact on the total deformation of the revetment. Finally, a relatively low impact is observed on the total deformation for revetments with a missing element. Important to note is that the simulation of a revetment with a missing element resembles the effect similar to when an element is taken out of the revetment by vandalism. This is different than when an element is missing due to underlying damage, in which the consequences are expected to be more severe.

A sensitivity analysis is done to obtain the most important uncertain parameters. Four different groups were defined: undamaged, deformation (S-profile), reduced clamping, and a missing element. The sensitivity analysis for the undamaged revetments shows the most important parameters are the dimensionless leakage length, the dimensionless loading, and the offshore wave steepness. The sensitivity analysis for the groups with different types of damage shows that the earlier defined parameters for the undamaged case are still important. Furthermore, it turned out some other parameters related to damage are also important. The first important parameter is the amplitude of the S-profile, which shows that the primary reason for the reduced stability caused by an S-profile is the increase in loading due to the migrated filter layer. Second, the interaction between the friction coefficient of the elements and the dimensionless loading reveals that joint filling becomes more important for larger loading. Last, the Z-coordinate of the missing elements shows that if an element is missing near the wave impact location, it will result in more damage than when an element is missing more down the slope.

Based on the samples used within the sensitivity analysis, response surface models are created. With those response surfaces, the impact of the dimensionless leakage length and the Iribarren number on the stability number is studied. Based on this analysis, it is found that missing elements are in particular affected by large dimensionless leakage lengths. The impact of the stability number for different types of damage is summarized in Table 8.1. The study is concluded by a case study of a pattern-placed revetment on a coastal dike in Den Helder. For this revetment, the impact on the failure probability is determined for different types of damage and intensities of damage using the response surface models. The impact is measured in terms of vulnerability, which is defined as the failure probability of a damaged system over the failure probability of an undamaged system (1995). Within the analysis, the vulnerability of top layer during the most intense moment of the storm is determined. From this, it is concluded that a small S-profile, no joint filling, and a missing element all have about the same impact on the reliability of the revetment. A summary of the results is presented in Table 8.1.

Damage	**Damage Parameter**	**Maximum Total Deformation [m/m]**	**Decrease of Stability Number [1]**	**Vulnerability Case Study [2]**	**Estimation [3]**
No Damage	N/A	0.37	-	-	-
Small S-profile	$a_s/b = 0.20$	0.98	20%	50	Upper bound
Medium S-profile	$a_s/b = 0.50$	1.32	35%	800	Upper bound
Large S-profile	$a_s/b = 0.80$	2.16	50%	2500	Upper bound
No Joint Filling	$\mu_e = 0.60$	1.91	25%	50	Upper bound
Missing Element	No. = 1	0.54	0% - 25% [4]	40	Lower bound

Table 8.1: Quantification of the impact of damages on the stability and reliability of column-type pattern-placed revetments

[1]: Estimated impact for a revetment with a dimensionless leakage length (Λ/D) of 1.5 and an Iribarren number ($\xi_{m-1,0}$) of 1.5.

[2]: Vulnerability based upon the case study done in Section 6.6.

[3]: The estimations of the upper and lower bound are based upon the discussion in Section 7.2.

[4]: Depends on the dimensionless leakage length and is especially vulnerable for revetments with larger leakage lengths.

8.2. Recommendations

Based on the results, discussion and conclusion recommendations can be made. The recommendations are divided into two parts. First, recommendations will be made for implementing findings from this study into the daily practice. Second, recommendations will be made for the application of the finite element model. Last, recommendations will be done for further research.

Inspection and Maintenance of Damages

1. **Deformation (S-profile)**
   This study shows that deformation in the form of an S-profile has the most significant impact on the stability and reliability of the three studied damages. Therefore, it is important to be well aware of the impact this damage can have as the impact is larger than is generally thought. An additional risk with the S-profile is that deformations have a relatively low probability of detection (Klerk et al., 2021). As discussed in Section 7.2, a visual inspection may not be sufficient enough, and one may consider other ways to assess the more poorly visible damages. An alternative to inspect for deformations could be by surveying the slope using a drone.

2. **Washed-Out Joint Filling**
   This study shows that the additional friction obtained from joint filling becomes increasingly more important for a larger wave loading. Therefore, although the revetment is still relatively well-clamped if some joint filling is washed-out, it is vital to keep it well washed in for maximum clamping.

3. **Missing Element**
   Within this study, we defined two causes that lead to a missing element. The first type is due to vandalism or because the element is pushed out by woody vegetation. Simulations showed that for the first type, the revetment is still relatively stable. However, the second type is the uplift of elements due to underlying damage. In this case, it is expected that the revetment is near failure, and an immediate maintenance intervention is required. Based on these findings, when a missing element is observed during an inspection, it is recommended to investigate the root cause of the missing element to get an idea of the severity of the damage.

4. **Non-Woody Vegetation**
   Although the growth of non-woody vegetation has a relatively small impact on the stability of a revetment, if not maintained well, the growth of non-woody vegetation will eventually cause the growth of woody vegetation (Klein Breteler, 2018). Contrary to non-woody vegetation, woody vegetation can cause many damages, such as (partial) uplift of elements, washed-out joint filling, and wider joints, and therefore may have a significant impact on the stability of the revetment. (Section 4.5)

Finite Element Model

1. **Use of the Finite Element Model as a Tool**
   The FE-model as developed within this study may be a valuable tool next to flume experiments that can give a quick estimation of different types of damages. Additionally, with the developed methodology and model, extending this concept to other types of damages and/or other types of revetment is quite straightforward. (Section 7.1)

2. **Block Revetments**
   The current finite element model is capable of simulating wave impacts. However, by expanding the model with wavefronts, it will also be capable of assessing revetments loaded by wave run-down. This is particularly useful when it is desirable to assess also (damaged) block-type revetments with the model.

Further Research

1. **Beam Model**
   Deformation and washed-out joint filling are both able to be modeled within a beam model. By assessing those damages using a beam model, the physical impact may be better understood and may lead to more accurate results. Additionally, a beam model will be more accessible to use than a finite element model.

2. **Flume Experiments**
   This study uses old flume experiments, which results in that data is not always available or complete. Further research can include flume experiments designed to study the development of damages such as the S-profile, washed-out joint filling, and a missing element. The obtained data will lead to a more accurate parameterization of the studied damages and a more accurate representation within the finite element model. Additionally, it may also be useful to validate the finite element model.

3. **Toe Deformation**
   Toe deformation and thereby the sliding and rotation of elements (kammen) is, according to Section 3.4 capable of affecting the clamping and the friction with the filter. Because this damage is common for pattern-placed revetment in the field and is expected to impact the stability significantly, it is recommended to do further research into the effect of toe deformation.

Bibliography

Actueel Hoogtebestand Nederland. (2021). Digital height maps for the netherlands. https://www.ahn.nl/ahn-viewer

Altena Infra-materialen. (2019). Altena infra-materialen [[Online; accessed February 15, 2021]]. https://altena-infra.nl/

Battjes, J. (1974). Surf similarity. *Coastal Engineering Proceedings*, *1*(14), 466–480. https://doi.org/10.9753/icce.v14.26

Bezuijen, A., Burger, A., & Klein Breteler, M. (1990). *Taludbekleding van gezette steen, samenvatting van onderzoeksresultaten 1980 - 1988*. Rijkswaterstaat Dienst Weg- en Waterbouwkunde.

Blok, R. (2014). *Tabellen voor bouwkunde en waterbouwkunde*. ThiemeMeulenhoff.

Blom, J. (2006). *Veldproeven op steenzettingen in zeeland*.

Bosboom, J., & Stive, M. (2015). *Coastal dynamics 1*. Delft Academic Press.

Buijs, F., Hall, J., Sayers, P., & Gelder, P. V. (2009). Time-dependent reliability analysis of flood defences. *Reliability Engineering & System Safety*, *94*(12), 1942–1953. https://doi.org/10.1016/j.ress.2009.06.012

CIRIA. (2007). *The rock manual. the use of rock in hydraulic engineering (2nd edition)*. C683, CIRIA, London.

CIRIA. (2013). *The international levee handbook*. CIRIA; Ministry of Ecology; USACE.

Cirkel, J., Van Dam, C., Van Den Akker, E., & Nell, J. (2015). *Handreiking dijkbekledingen* (tech. rep.). Deltares. Ministerie van Infrastructuur en Milieu, Rijkswaterstaat.

Coeveld, E. (2003). *Invloed van golfklappen op stabiliteit: Literatuurstudie* (tech. rep.). Rijkswaterstaat, Dienst Weg- en Waterbouwkunde.

Coeveld, E., & Klein Breteler, M. (2003). *Invloed klemming: Statische analyse trekproeven* (tech. rep.). Delft Hydraulics. Rijkswaterstaat, Dienst Weg- en Waterbouwkunde.

CUR. (1995). *Design manual for pitched slope protection* (Vol. 155). Balkema A.A. Publishers.

De Waal, J., Klein Breteler, M., & Den Adel, H. (1995). *Taludbekledingen van gezette steen, golfdruk op het talud, deel b* (tech. rep.). Waterkundig Laboratorium. Dienst Weg- en Waterbouwkunde.

Delta Committee. (1960). *Eindverslag en interimadviezen* (tech. rep.). Delta Committee. Staatsdrukkerij 'S Gravenhage.

DeltaExpertise. (2020). Zeeweringenwiki [[Online; accessed August 17, 2021]]. https://www.zeeweringenwiki.nl/wiki/index.php

Dorst, K., Provoost, Y., & Verhagen, H. (2012). *Stability of pattern placed revetment elements*. PIANC.

EurOtop. (2018). *Manual on wave overtopping of sea defences and related structures*. Van der Meer, J.W.; Allsop, N.W.H.; Bruce, T.; De Rouck, J.; Kortenhaus, A.; Pullen, T.; Schüttrumpf, H.; Troch, P.; Zanuttigh, B. www.overtopping-manual.com

Eysink, W., & Klein Breteler, M. (2003). *Deltagootonderzoek naar stabiliteit van basalt, fase 1 en 2* (tech. rep.). Delft Hydraulics. Rijkswaterstaat, Directie Zeeland.

Faber, M. H. (2002). Risk-based inspection: An introduction. *Structural Engineering International*, *12*(3), 186–186. https://doi.org/10.2749/101686602777965261

Flikweert, J. (2003). *Tr-25b technisch rapport steenzettingen* (tech. rep.). TAW and Royal Haskoning Nederland bv. Ministerie van Verkeer en Waterstaat, Directoraat-Generaal Rijkswaterstaat.

Gier, F., Schuttrumpf, H., Monnich, J., Van der Meer, J., Kudella, M., & Rubin, H. (2012). Stability of interlocked pattern placed block revetments. *Coastal Engineering Proceedings*, *1*(33), 46. https://doi.org/10.9753/icce.v33.structures.46

Haringman Betonwaren. (n.d.). Hydroblocks [[Online; accessed February 15, 2021]]. https://www.haringman-beton.nl/assortiment/zeewering/hydroblocksr-0

Herman, J., & Usher, W. (2017). SALib: An open-source python library for sensitivity analysis. *The Journal of Open Source Software*, *2*(9). https://doi.org/10.21105/joss.00097

Hillblock BV. (2018). Hillblock [[Online; accessed February 15, 2021]]. https://www.hillblock.nl/

HKV. (2019). *Hydra-nl v2.7 gebruikershandleiding* (tech. rep.). HKV. Rijkswaterstaat.

Holcim Coastal. (2013). Holcim coastal productoverzicht.

Holthuijsen, L. (2007). *Waves in oceanic and coastal waters*. Cambridge University Press.

Jongejan, R., & Klein Breteler, M. (2015). *A semi-probabilistic assessment rule for the stability of block revetments under wave attack* (tech. rep.). Deltares. Rijkswaterstaat.

Kaste, D., & Mourik, G. (2016). *Stabiliteit van basalton 30 sts+ steenzetting bij golfaanval* (tech. rep.). Deltares.

Klein Breteler, M. (2018). *Onderhoudseisen voor steenbekledingen op dijken* (tech. rep.). Deltares.

Klein Breteler, M. (2020). *Handleiding steentoets* (tech. rep.). Deltares. Rijkswaterstaat.

Klein Breteler, M., & Eysink, W. (2005). *Langeduursterkte van steenzettingen* (tech. rep.). Delft Hydraulics.

Klein Breteler, M., & Eysink, W. (2007). *Reststerkte van steenzetting met zuilen na initiële schade* (tech. rep.). Delft Hydraulics.

Klein Breteler, M., & Kaste, D. (2019). *Documentatie steentoets v19.1.1* (tech. rep.). Deltares. Rijkswaterstaat.

Klein Breteler, M., & Mourik, G. (2014). *Invloed kwaliteit zetwerk opstabiliteit steenzetting, trekproeven op slecht zetwerk* (tech. rep.). Deltares.

Klein Breteler, M., Mourik, G., & Bosters, M. (2014). *Stabiliteit van steenzettingen bij golfaanval* (tech. rep.). Deltares. Rijkswaterstaat.

Klein Breteler, M., & Van der Werf, I. (2006). *Kennisontwikkeling t.b.v. steentoets2006* (tech. rep.). Delft Hydraulics. Rijkswaterstaat Zeeland, Projectbureau Zeeweringen.

Klein Breteler, M., Van der Werf, I., & Wenneker, I. (2012). *Kwantificering golfbelasting en invloed lange golven* (tech. rep.). Deltares. Onderzoeksprogramma Kennisleemtes Steenbekledingen.

Klerk, W., Kanning, W., Kok, M., Bronsveld, J., & Wolfert, A. (2021). Accuracy of visual inspections of flood defences [[Accepted for publication]]. *Structure and Infrastructure Engineering*.

Kok, M., Jongejan, R., Nieuwjaar, M., & Tánczos, I. (2016). *Handreiking ontwerpen met overstromingskansen* (tech. rep.). directoraat-generaal Ruimte en Water van het ministerie van Infrastructuur en Milieu en het Expertise Netwerk Waterveiligheid.

KOMO. (2018). Productcertificaat basalton [[Online; accessed April 25, 2021]]. https://www.holcim.nl/sites/netherlands/files/documents/MAN_Brochure_Coastal_NL_LR_v2.pdf

LBN Beton. (2020). Verkalit(r) interlock-zetstenen productinformatie. https://www.lbn.nu/lbn/producten/innovaties/dijkbekleding/verkalit

LBN Betonproducten. (n.d.). Lbn betonproducten [[Online; accessed February 15, 2021]]. https://www.lbn.nu/

Lind, N. C. (1995). A measure of vulnerability and damage tolerance. *Reliability Engineering & System Safety*, *48*(1), 1–6. https://doi.org/10.1016/0951-8320(95)00007-o

Marine Regions. (2021). Bathymetry of the north sea. https://www.marineregions.org/

Ministerie van Infrastructuur en Milieu. (2015). Kader zorgplicht primaire waterkeringen.

Ministry of Infrastructure and Water Management. (2004). *De veiligheid van de primaire waterkeringen in nederland; voorschrift toetsen op veiligheid voor de tweede toetsronde 2001 - 2006* (tech. rep.). Ministry of Infrastructure and Water Management.

Nationaal Park Oosterschelde. (2020). Dikes [[Online; accessed February 12, 2021]]. https://www.np-oosterschelde.nl/en/over-het-park/landschap/dijken.htm

Pedregosa, F., Varoquaux, G., Gramfort, A., Michel, V., Thirion, B., Grisel, O., Blondel, M., Prettenhofer, P., Weiss, R., Dubourg, V., Vanderplas, J., Passos, A., Cournapeau, D., Brucher, M., Perrot, M., & Duchesnay, E. (2011). Scikit-learn: Machine learning in Python. *Journal of Machine Learning Research*, *12*, 2825–2830.

Peters, D. (2007). *Kennisontwikkeling t.b.v. steentoets; het implementatie gereed maken van het klemmingsonderzoek* (tech. rep.). Royal Haskoning DHV.

Peters, D. (2017). *Design of pattern-placed revetments* (Doctoral dissertation). Delft University of Technology. https://doi.org/10.4233/uuid:0b67a0dd-a951-46f3-bbaa-86270e546c4e

Pilarczyk, K., Klein Breteler, M., & Bezuijen, A. (1995). Wave forces and structural response of placed block revetments. *International Conference on Coastal Engineering 1995*.

Rajashekhar, M. R., & Ellingwood, B. R. (1993). A new look at the response surface approach for reliability analysis. *Structural Safety*, *12*(3), 205–220. https://doi.org/10.1016/0167-4730(93)90003-j

Rijksoverheid. (1958). Deltawet. https://wetten.overheid.nl/BWBR0002283/2004-07-01

Rijksoverheid. (2017). Waterwet. https://wetten.overheid.nl/BWBR0025458/2021-07-01

Rijkswaterstaat. (2007). *Hydraulische randvoorwaarden 2006* (tech. rep.). Ministerie van Verkeer en Waterstaat.

Rijkswaterstaat. (2019). *Programmaplan boi 2023* (tech. rep.). Rijkswaterstaat Ministerie van Infrastructuur en Waterstaat.

Saltelli, A., & Ratto, M. (2008). *Global sensitivity analysis. the primer*. John Wiley and Sons Ltd.

Schiereck, G., & Verhagen, H. (2019). *Introduction to bed, bank and shore protection*. Delft Academic Press.

Schoen, S. (2004). *Onderzoek naar liggerwerking bij steenzettingen*.

Schüttrumpf, H. (2001). *Wellenüberlaufströmung bei seedeichen* (Doctoral dissertation). Technischen Universität Carolo-Wilhelmina. https://doi.org/https://doi.org/10.24355/dbbs.084-200511080100-46

Stenen zoeken.nl. (2020). Wat is basalt? [[Online; accessed February 12, 2021]]. https://www.stenenzoeken.nl/

STOWA. (2021). *Technische vergelijking tussen de overschrijdingskans en overstromingskans* (tech. rep.). Stiching Toegepast Onderzoek Waterbeheer (STOWA). Stichting Toegepast Onderzoek Waterbeheer.

TAW. (1984). *Tr-02 leidraad cementbetonnen dijkbekleding* (tech. rep.). Technisch Adviescommissie voor de Waterkeringen (TAW). Rijkswaterstaat, COW.

TAW. (1989a). *Leidraad voor het ontwerpen van rivierdijken deel 2* (tech. rep.). Technisch Adviescommissie voor de Waterkeringen (TAW); Expertise Netwerk Waterveiligheid (ENW).

TAW. (1989b). *Leidraad voor het ontwerpen van rivierdijken, deel 2* (tech. rep.). Technische Adviescomissie voor de Waterkeringen (TAW). Uitgeverij Waltman.

TAW. (2002). *Technisch rapport asfalt voor waterkeren* (tech. rep.). TAW. Rijkswaterstaat.

Van der Meer, J. (1988). *Rock slopes and gravel beaches under wave attack* (Doctoral dissertation). Delft University of Technology. Delft Hydraulics Laboratory.

Van der Meer, J., & Klein Breteler, M. (1991). *Easurement and computation of wave induced velocities on a smooth slope* (tech. rep.). American Society of Civil Engineers. https://doi.org/10.1061/9780872627765.016

Van Der Meer, M., & Moens, M. (1990). *Schadecatalogus voor dijkbekledingen* (tech. rep.). Rijkswaterstaat, Diens Weg- en Waterbouwkunde.

Van der Meer, M., Niemeijer, J., Post, W., & Heemstra, J. (2004). *Technisch rapport waterspanningen bij dijken waterkeringen* (tech. rep.). TAW. Rijkswaterstaat.

Van Steeg, P. (2016). *Stabiliteit taludbekleding van hillblock 2.0, drainageblock en grassblock* (tech. rep.). Deltares. Deltares.

Vrijling, J., Van der Horst, C., Van Hoof, P., & van Gelder, P. (2001). The structural analysis of the block revetment on the dutch dikes. https://doi.org/10.1061/40549(276)156

Waterschapshuis, H. (2019). Digigids [[Online; accessed February 08, 2021]]. http://digigids.hetwaterschapshuis.nl/

Wolters, G. (2016a). *Stabiliteit van basalton 30 sts steenzetting bij golfaanval* (tech. rep.). Deltares.

Wolters, G. (2016b). *Stabiliteit van c-star steenzetting bij golfaanval* (tech. rep.). Deltares. Deltares.

Wolters, G., & Klein Breteler, M. (2007). *Normaalkracht in steenzetting met blokken op hun kant* (tech. rep.). Delft Hydraulics. Projectbureau Zeeweringen.

Wolters, G., & Klein Breteler, M. (2011). *Reststerkte van een dijk met steenzetting op een kleilaag* (tech. rep.). Deltares.

List of Tables

List of Figures

A

Data on Damages from Flume Experiments

In this appendix the data from the flume experiments can be found. First, a table is presented with the different experiments and the found numerical parameters for the damages. Second, for each experiments with uplifted elements a list of the position of the elements is given. Not for all experiments, all data is available on the different studied damages. Therefore, if no data is available, it is noted in the tables as 'unk' (unknown).

A.1. Data on Damages

All data retrieved from the analysed experiments can be found in Table A.1 on the next page. The following data is given for each analysed experiment:

- **Ref:** Reference to the research program of which the experiment is part of:
    1. Stability of a Basalton 30 STS revetment under wave loading (Wolters, 2016a)
    2. Stability of a Basalton 30 STS+ revetment under wave loading (Kaste and Mourik, 2016)
    3. Residual strength of a pattern-placed revetment with initial damage (Klein Breteler and Eysink, 2007)
    4. Long-term strength of pattern-placed revetments (Klein Breteler and Eysink, 2005)
    5. Flume research to the stability of basalt, phase 1 and 2 (Eysink and Klein Breteler, 2003)
    6. Residual strength of a clay dike with a pattern-placed revetment (Wolters and Klein Breteler, 2011)
- **Exp:** Experiment ID as indicated by the research program;
- **Type:** Used type of top layer element;
- **Scale:** Scale of the experiment;
- **Slope:** Slope of the revetment;
- **SWL:** Still water level (relative to bottom of flume);
- **D:** Top layer thickness;
- **b:** Filter layer thickness;
- **H_s:** Significant wave height;
- **U_{-Hs}:** Average wash-out in the zone below the wave impact ($z < SWL-H_s$);
- **U_{WI}:** Average wash-out in the zone below the wave impact ($SWL-H_s < z < SWL$);
- **U_{SWL}:** Average wash-out in the zone above the wave impact ($z > SWL$);
- **a_s:** Amplitude of the S-profile;
- **z_{bot}:** The Z-coordinate of the bottom of the S-profile (relative to bottom of flume);
- **z_{mid}:** The Z-coordinate of the S-profile between the trough and hump (relative to bottom of flume);

- **z_{top}:** The Z-coordinate of the top of the S-profile (relative to bottom of flume);
- **Lifted:** Total number of elements fully uplifted;
- **Cat.** Damage category as indicated in Section 4.4.2.

A.2. List of Uplifted Elements

In Table A.2 all reported uplifted elements are listed with the total uplift u_n and the location on the slope indication by the Z-coordinate z_n. The table can be found after the table with the general experiment and damage information from the previous section. Note that there are two rows (p1 and p2) for P07 from research program (1) because a total of 15 elements were uplifted in this experiment.

Report			Experiment Data						Washed-out Joint Filling			Deformation (S-profile)				Uplift	
Ref	Exp	Type	Scale	Slope	SWL	D	b	H_s	U_{-Hs}	U_{WI}	U_{SWL}	a_s	z_{bot}	z_{mid}	z_{top}	Lifted	Cat.
[−]	[−]	[−]	[−]	[−]	[REF]	[m]	[m]	[m]	[m]	[m]	[m]	[m]	[REF]	[REF]	[REF]	[#]	[−]
(1)	P01	STS	2.0	3	4.55	0.15	0.095	0.62	0.020	0.030	0.035	0.000	n/a	n/a	n/a	0	a
(1)	P02	STS	2.0	3	4.7	0.15	0.095	0.89	0.100	0.160	0.035	0.010	3.33	3.87	4.14	0	a
(1)	P03	STS	2.0	3	4.7	0.15	0.095	1.12	0.100	0.175	0.040	0.035	3.18	3.85	4.14	3	d
(1)	P04	STS	2.0	3	4.55	0.15	0.069	0.67	0.000	0.150	0.030	0.000	n/a	n/a	n/a	0	a
(1)	P05	STS	2.0	3	4.7	0.15	0.069	0.71	0.000	0.140	0.040	0.000	n/a	n/a	n/a	0	a
(1)	P06	STS	2.0	3	4.7	0.15	0.069	0.98	0.000	0.170	0.070	0.013	3.66	4.21	4.51	0	a
(1)	P07	STS	2.0	3	4.7	0.15	0.069	1.18	0.220	0.220	0.220	0.060	3.44	4.21	4.53	15	d
(1)	P08	STS	2.0	3	4.7	0.15	0.071	0.70	0.000	0.130	0.050	0.000	n/a	n/a	n/a	0	a
(1)	P09	STS	2.0	3	4.7	0.15	0.071	0.85	0.050	0.150	0.050	0.010	3.75	4.24	4.60	1	d
(1)	P10	STS	2.0	3	4.7	0.15	0.071	0.85	0.100	0.150	0.100	0.013	3.75	4.27	4.61	1	d
(1)	P11	STS	2.0	3	4.7	0.15	0.071	0.89	0.080	0.170	0.090	0.035	3.72	4.25	4.63	1	c
(1)	P12	STS	2.0	3	4.7	0.15	0.071	0.87	0.089	0.135	0.060	0.040	3.72	4.27	4.61	0	a
(1)	P13	STS	2.0	3	4.7	0.15	0.071	0.90	0.085	0.155	0.060	0.065	3.75	4.22	4.63	1	d
(2)	B01	STS+	1.6	3	5.42	0.18	0.079	0.76	0.013	0.015	0.015	0.000	n/a	n/a	n/a	0	a
(2)	B02	STS+	1.6	3	5.62	0.18	0.079	0.99	0.020	0.035	0.020	0.003	4.17	4.51	5.03	0	a
(2)	B03	STS+	1.6	3	5.62	0.18	0.079	1.13	0.010	0.030	0.025	0.003	3.86	4.40	5.01	0	a
(2)	B04	STS+	1.6	3	5.62	0.18	0.079	1.33	0.025	0.040	0.035	0.003	3.79	4.20	4.80	0	a
(2)	B05	STS+	1.6	3	5.62	0.18	0.079	1.51	unk	0.050	0.030	0.005	3.50	3.96	4.27	0	a
(2)	B06	STS+	1.6	3	5.62	0.18	0.079	1.66	unk	0.055	0.040	0.005	3.51	3.93	4.30	0	a
(2)	B07	STS+	1.6	3	5.88	0.18	0.079	1.83	unk	0.060	0.035	0.005	3.54	3.92	4.27	0	a
(2)	B08	STS+	1.6	3	5.62	0.18	0.079	1.09	0.010	0.060	0.035	0.005	unk	unk	unk	0	a
(2)	B09	STS+	1.6	3	5.62	0.18	0.079	1.36	0.005	0.060	0.045	0.005	4.30	4.93	5.37	0	a
(2)	B10	STS+	1.6	3	5.82	0.18	0.079	1.56	0.010	0.080	0.050	0.008	4.30	4.93	5.37	0	a
(2)	B11	STS+	1.6	3	5.93	0.18	0.079	1.74	0.030	0.080	0.050	0.020	4.09	4.93	5.29	0	a
(2)	B12	STS+	1.6	3	6.01	0.18	0.079	1.96	unk	0.130	unk	0.058	3.98	5.06	5.50	0	a
(2)	B13	STS+	1.6	3	5.42	0.18	0.078	0.75	unk	unk	unk	0.000	n/a	n/a	n/a	0	a
(2)	B14	STS+	1.6	3	5.62	0.18	0.078	1.45	0.050	0.160	0.060	0.048	4.03	4.97	5.41	2	d
(3)	P501	SS/VS	1.0	3.5	4.8	0.20	0.12	1.47	unk	unk	unk	0.001	3.30	3.40	3.75	0	a
(3)	P1001	SS/VS	1.0	3.5	4.79	0.20	0.12	1.53	unk	unk	unk	0.001	3.25	3.40	3.75	0	a
(3)	P1501	SS/VS	1.0	3.5	4.79	0.20	0.12	1.53	unk	unk	unk	0.001	3.20	3.47	4.00	0	a
(3)	P2001	SS/VS	1.0	3.5	4.8	0.20	0.12	1.53	unk	unk	unk	0.001	3.25	3.47	4.10	0	a
(4)	P4201	SS/VS	1.0	3.5	4.2	0.20	0.12	1.22	unk	unk	unk	nb	unk	unk	unk	0	a
(4)	P4202	SS/VS	1.0	3.5	4.2	0.20	0.12	1.31	unk	unk	unk	0.000	n/a	n/a	n/a	0	a

Report			Experiment Data						Washed-out Joint Filling			Deformation (S-profile)				Uplift	
Ref	Exp	Type	Scale	Slope	SWL	D	b	H_s	U_{-Hs}	U_{WI}	U_{SWL}	a_s	z_{bot}	z_{mid}	z_{top}	Lifted	Cat.
[−]	[−]	[−]	[−]	[−]	$[REF]$	$[m]$	$[m]$	$[m]$	$[m]$	$[m]$	$[m]$	$[m]$	$[REF]$	$[REF]$	$[REF]$	[#]	[−]
(4)	P4203	SS/VS	1.0	3.5	4.2	0.20	0.12	1.23	unk	unk	unk	nb	unk	unk	unk	0	a
(4)	P4204	SS/VS	1.0	3.5	4.2	0.20	0.12	1.33	unk	unk	unk	0.005	3.20	3.47	3.80	0	a
(4)	P4401	SS/VS	1.0	3.5	4.42	0.20	0.12	1.35	unk	unk	unk	nb	unk	unk	unk	0	a
(4)	P4402	SS/VS	1.0	3.5	4.41	0.20	0.12	1.31	unk	unk	unk	0.006	3.20	3.47	3.80	0	a
(4)	P4601	SS/VS	1.0	3.5	4.63	0.20	0.12	1.37	0.200	0.200	unk	0.006	3.20	3.47	3.80	0	a
(4)	P4801	SS/VS	1.0	3.5	4.82	0.20	0.12	1.36	unk	unk	unk	nb	unk	unk	unk	0	a
(4)	P4802	SS/VS	1.0	3.5	4.83	0.20	0.12	1.34	unk	unk	unk	nb	unk	unk	unk	0	a
(4)	P4803	SS/VS	1.0	3.5	4.81	0.20	0.12	1.34	0.200	0.200	unk	0.006	3.20	3.47	3.85	0	a
(4)	P5001	SS/VS	1.0	3.5	5.02	0.20	0.12	1.42	unk	unk	unk	nb	unk	unk	unk	0	a
(4)	P5002	SS/VS	1.0	3.5	5.02	0.20	0.12	1.33	unk	unk	unk	nb	unk	unk	unk	0	a
(4)	P4804	SS/VS	1.0	3.5	4.83	0.20	0.12	1.36	unk	unk	unk	nb	unk	unk	unk	0	a
(4)	P4805	SS/VS	1.0	3.5	4.81	0.20	0.12	1.35	0.200	0.200	0.050	0.007	3.20	3.48	3.86	0	a
(4)	1	Basalt	1.0	3.5	4.2	0.20	0.12	0.66	unk	unk	unk	0.000	n/a	n/a	n/a	0	a
(4)	2	Basalt	1.0	3.5	4.19	0.20	0.12	0.89	unk	unk	unk	0.001	3.25	3.55	3.80	0	a
(4)	3	Basalt	1.0	3.5	4.36	0.20	0.12	1.07	unk	unk	unk	0.001	3.25	3.55	3.77	0	a
(4)	4	Basalt	1.0	3.5	4.33	0.20	0.12	0.97	unk	unk	unk	unk	unk	unk	unk	0	a
(4)	4A	Basalt	1.0	3.5	4.32	0.20	0.12	1.20	unk	unk	unk	0.002	3.25	3.73	4.00	0	a
(4)	5	Basalt	1.0	3.5	4.58	0.20	0.12	1.4	unk	0.020	unk	0.004	3.25	3.74	4.00	0	a
(4)	6	Basalt	1.0	3.5	4.78	0.20	0.12	1.54	unk	0.050	unk	0.005	3.30	3.74	4.00	1	b
(4)	7	Basalt	1.0	3.5	4.72	0.20	0.12	1.1	unk	unk	unk	unk	unk	unk	unk	0	a
(4)	7A	Basalt	1.0	3.5	4.72	0.20	0.12	1.1	unk	unk	unk	0.006	3.30	3.74	4.00	0	a
(4)	8	Basalt	1.0	3.5	4.85	0.20	0.12	1.26	unk	unk	unk	unk	unk	unk	unk	0	a
(4)	8A	Basalt	1.0	3.5	4.85	0.20	0.12	1.2	0.100	0.100	unk	0.006	3.30	3.73	4.00	1	d
(4)	13	Basalt	1.0	3.5	4.21	0.20	0.12	0.91	unk	unk	unk	0.006	3.30	3.74	4.00	0	a
(4)	14	Basalt	1.0	3.5	4.19	0.20	0.12	1.19	unk	unk	unk	0.006	3.32	3.74	4.00	0	a
(4)	15	Basalt	1.0	3.5	4.31	0.20	0.12	1.33	unk	unk	unk	0.007	3.32	3.73	4.00	0	a
(4)	16	Basalt	1.0	3.5	4.39	0.20	0.12	1.46	unk	unk	unk	0.009	3.35	3.73	3.98	0	a
(4)	17	Basalt	1.0	3.5	4.49	0.20	0.12	1.6	unk	unk	unk	0.011	3.35	3.72	3.98	0	a
(4)	18	Basalt	1.0	3.5	4.69	0.20	0.12	1.74	unk	0.200	unk	0.014	3.38	3.72	3.97	0	a
(5)	20	SS/VS	1.0	3.5	4.69	0.20	0.12	0.7	unk	unk	unk	unk	unk	unk	unk	0	a
(5)	21	SS/VS	1.0	3.5	4.68	0.20	0.12	1.07	unk	unk	unk	0.001	3.20	3.46	3.76	0	a
(5)	22	SS/VS	1.0	3.5	4.84	0.20	0.12	1.18	unk	unk	unk	0.001	3.16	3.47	3.76	0	a
(5)	23	SS/VS	1.0	3.5	4.99	0.20	0.12	1.28	unk	unk	unk	0.001	3.16	3.47	3.76	0	a
(5)	24	SS/VS	1.0	3.5	5.1	0.20	0.12	1.37	unk	unk	unk	0.002	3.16	3.48	3.77	0	a

Report			Experiment Data						Washed-out Joint Filling			Deformation (S-profile)				Uplift	
Ref	Exp	Type	Scale	Slope	SWL	D	b	H_s	U_{-Hs}	U_{WI}	U_{SWL}	a_s	z_{bot}	z_{mid}	z_{top}	Lifted	Cat.
[−]	[−]	[−]	[−]	[−]	$[REF]$	$[m]$	$[m]$	$[m]$	$[m]$	$[m]$	$[m]$	$[m]$	$[REF]$	$[REF]$	$[REF]$	[#]	[−]
(5)	25	SS/VS	1.0	3.5	4.56	0.20	0.12	1.41	unk	unk	unk	0.001	3.16	3.46	3.78	0	a
(5)	26	SS/VS	1.0	3.5	4.74	0.20	0.12	1.57	unk	unk	unk	0.003	3.16	3.46	3.85	0	a
(5)	P4010	Basalt	1.0	3.5	4.04	0.20	0.12	0.879	0.060	0.050	0.000	0.001	3.10	3.35	3.70	1	b
(5)	P4210	Basalt	1.0	3.5	4.22	0.20	0.12	1.202	unk	unk	unk	unk	unk	unk	unk	0	a
(5)	P4211	Basalt	1.0	3.5	4.2	0.20	0.12	1.187	unk	0.140	unk	0.002	3.41	3.72	4.05	0	a
(5)	P4410	Basalt	1.0	3.5	4.4	0.20	0.12	1.225	0.040	0.170	0.050	0.002	3.41	3.72	4.05	2	d
(5)	P4411	Basalt	1.0	3.5	4.41	0.20	0.12	1.251	unk	unk	unk	0.004	3.41	3.72	4.04	0	a
(5)	P4610	Basalt	1.0	3.5	4.63	0.20	0.12	1.219	0.000	0.060	0.050	0.005	3.42	3.72	4.06	0	a
(5)	P4810	Basalt	1.0	3.5	4.82	0.20	0.12	1.138	unk	unk	unk	0.005	3.42	3.72	4.07	1	d
(5)	P4811	Basalt	1.0	3.5	4.84	0.20	0.12	1.221	unk	unk	unk	unk	unk	unk	unk	0	a
(5)	P4812	Basalt	1.0	3.5	4.83	0.20	0.12	1.193	0.200	0.100	0.050	0.011	3.40	3.70	4.10	2	d
(5)	P4215	Basalt	1.0	3.5	4.22	0.20	0.12	1.42	0.000	0.080	0.050	0.011	3.35	3.70	4.14	0	a
(5)	P4415	Basalt	1.0	3.5	4.42	0.20	0.12	1.356	0.000	0.080	0.050	0.011	3.40	3.70	4.11	0	a
(5)	P4615	Basalt	1.0	3.5	4.63	0.20	0.12	1.396	0.000	0.080	0.050	unk	unk	unk	unk	0	a
(5)	P4616	Basalt	1.0	3.5	4.61	0.20	0.12	1.357	0.040	0.100	0.050	0.013	3.42	3.72	4.12	1	b
(5)	P4418	Basalt	1.0	3.5	4.42	0.20	0.12	1.657	0.050	0.100	0.010	0.013	3.42	3.70	4.12	0	a
(5)	P4618	Basalt	1.0	3.5	4.6	0.20	0.12	1.472	0.050	0.100	0.010	0.014	3.42	3.68	4.11	0	a
(5)	P4619	Basalt	1.0	3.5	4.6	0.20	0.12	1.488	unk	unk	unk	0.015	3.42	3.70	4.10	1	d
(6)	P01	STS	1.0	3.5	4.4	0.15	0.07	1	0.000	0.090	0.050	0	n/a	n/a	n/a	0	a
(6)	P02	STS	1.0	3.5	4.5	0.15	0.07	1.21	0.000	0.055	0.055	0.01	3.26	3.83	4.25	0	a
(6)	P03	STS	1.0	3.5	4.6	0.15	0.07	1.39	unk	unk	unk	0.015	3.26	3.9	4.4	0	a
(6)	P04	STS	1.0	3.5	4.7	0.15	0.07	1.6	unk	unk	unk	0.02	3.26	3.9	4.4	1	d

Ref	Report Exp	Type	Location [mREF] and displacement [m] of uplifted elements															
			z_1	u_1	z_2	u_2	z_3	u_3	z_4	u_4	z_5	u_5	z_6	u_6	z_7	u_7	z_8	u_8
(1)	P03	STS	3.80	0.15	4.00	0.15	4.00	0.15										
(1)	P07 (p1)	STS	4.08	0.15	4.03	0.15	4.03	0.15	3.92	0.15	3.91	0.15	3.93	0.15	3.89	0.15	3.76	0.15
(1)	P07 (p2)	STS	3.79	0.15	3.85	0.15	3.86	0.15	3.89	0.15	3.89	0.15	3.94	0.15	3.92	0.15		
(1)	P09	STS	4.20	0.15														
(1)	P10	STS	4.23	0.15														
(1)	P11	STS	4.20	0.14														
(1)	P13	STS	4.16	0.15														
(2)	B14	STS+	4.80	0.18	4.85	0.18												
(4)	6	Basalt	4.41	0.09														
(4)	8A	Basalt	3.50	0.20														
(5)	P4010	Basalt	3.52	0.04														
(5)	P4410	Basalt	3.55	0.20	3.55	0.20												
(5)	P4810	Basalt	4.37	0.20														
(5)	P4812	Basalt	3.52	0.02	4.16	0.20												
(5)	P4616	Basalt	3.33	0.03														
(5)	P4619	Basalt	3.52	0.20														
(6)	P04	STS	4.14	0.15														

B

Creating the (Stochastic) Finite Element Model

This appendix explains how the finite element model was created and used. First, an introduction is given how Python can be used to create models with Abaqus. Next, an explanation on how the finite element model is created. Last, how the finite element model is expanded to a stochastic finite element model. The Python code of the model can be found in Appendix B.4.

B.1. Using Python with Abaqus

The model is made with Abaqus 2019 for which the license was provided by the TU Delft. Abaqus 2019 can only work with Python 2, therefore the Python code for the model is written for Python 2.7. Abaqus provides an option to run Python scripts and also provides a Python library which can be used to create models.

There are two options in order to build a model in Python. First, there is the documentation related to the Abaqus Python library. However, this may be quite overwhelming due to the amount of information and functions. Second, whenever saving an Abaqus model, Abaqus will create a .cae file, which contains the model information and a .jnl file, which contains a complete replica of the model in Python code. Therefore by creating step-by-step the model in Abaqus, it is quite easy to find the right Python functions to create a Python Abaqus script. Mainly the second method was used to create the finite element model for this study.

B.2. Creating the Finite Element Model

In this section is explained how the finite element model is created. First the generation of the geometry is covered, after that the generation of the revetment. Next, the generation of the loading and finally, how different damages are applied to the model.

B.2.1. Geometry

The geometry of the model consists out of three elements (indicated by the numbers in Figure B.1):

1. **The flume bottom** which is applied at z = 0, this is a rigid surface of which the purpose is to catch the elements when the roll down the slope;
2. **The toe structure** is the structure at between the flume bottom and the bottom side of the revetment. In this model the toe structure is rigid.
3. **The surface underneath the elements** is the surface on which the revetment is placed. The surface is rigid and has the shape of the filter layer and thus may contain a deformation when the S-profile is applied.

Furthermore, the geometry has a slope of 1 on cot α and the geometry is a little bit wider than the width of the revetment in order to prevent elements from falling off the side. All three elements have the 'Encastre' boundary condition applied to prevent displacement or rotations.

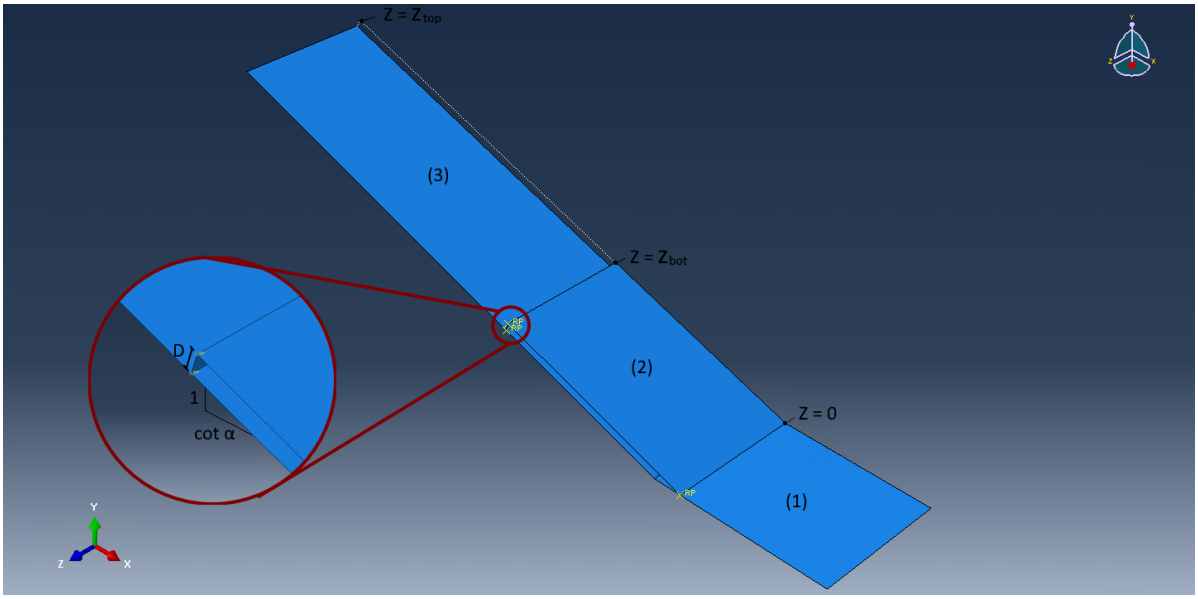

Figure B.1: Geometry of the model with corresponding parameters

The water depth (d) is also measured from the bottom of the flume and is important in order to find the top and bottom of the revetment (z_{top} and z_{bot}) based on the dimensionless top and bottom ($z_{d;top}$ and $z_{d;bot}$).

B.2.2. Elements

In the second step, the elements from the Basalton STS+ set are generated on the slope (Figure B.2). For each element in the Basalton STS+ set, there is a text file width the following information:

1. **Area of the element** which will not be used in the generation of the model, but is handy to have for analysis of the results;
2. **Length of the element** defined as the difference between the maximum and the minimum of the y out of the point data from the element;
3. **Relative center** which is the center of the element in the y direction measured from the origin of the Basalton STS+ set (origin at the left bottom of the set).
4. **Point data (x, y) of the boundaries of the element**, which are used to generate the exact topdown shape of the element as a part in Abaqus. The point data is relative to the origin of the Basalton STS+ set and is based upon a drawing provided by the manufacturer of Basalton, Holcim Coastal.

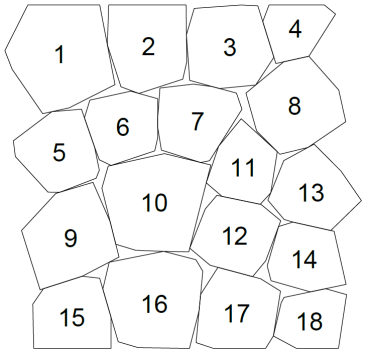

Figure B.2: Basalton STS+ elements (Holcim Coastal, 2013)

This data will be used throughout the model to determine the exact place and rotation, when a S-profile is applied, of each element on the slope. It is also used to determine the loading on the element.

After all elements are loaded into Abaqus, a material called 'Basalton' is added. This material is created as an elastic material with a density. Next, this new material is added to a section to create a homogeneous solid section called 'Sec-Basalton'. This section is applied to all elements.

The elements are placed in B_s columns and the amount of rows being able to fit on a slope between z_{top} and z_{bot}. The model can only place whole sets of Basalton on a revetment. Therefore before placing the elements on the slope, the model adjusts the bottom of the revetment z_{bot} in order to be able to fit a whole number of sets on the slope. The model will always adjust the model such that the corrected z_{bot} is always lower than the given z_{bot}. It is chosen to adjust the bottom of the revetment instead of the top because the normal force in the revetment is dependent on the position in the slope from the top of the revetment (Vrijling et al., 2001). Therefore, by adjusting the bottom, the top is always the same as the given input and thus the impact of the top location of the revetment can be studied. When the effect of toe deformation would be studied, it makes sense it fix the bottom of the revetment and adjust the top of the revetment. However, that is outside the scope of the study.

Next, the boundary conditions are applied. To prevent elements from moving in the lateral direction to the slope (Y' in Figure B.3), symmetric boundary conditions are added which prevent the elements at the outsides of the revetment displacement in the Y' direction and prevents rotation over the Z' and X' axes (ZSYMM). The elements with boundary conditions applied are shown in red in Figure B.3

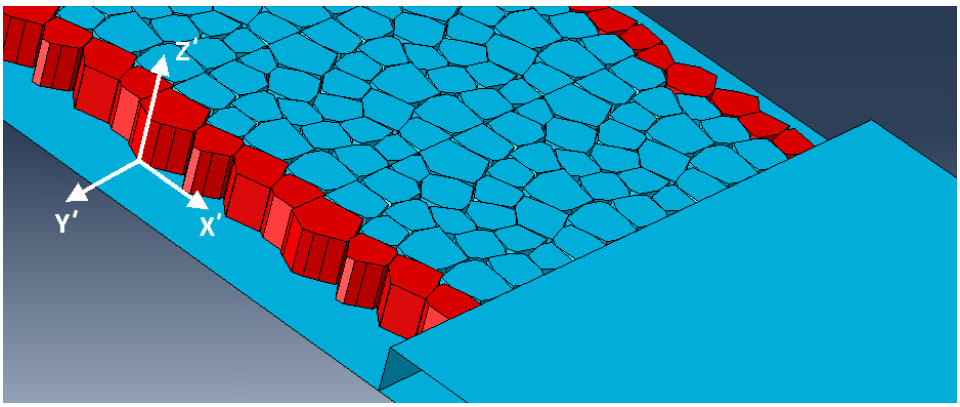

Figure B.3: Elements with boundary conditions applied (ZSYMM) in red

The last step is to model the interaction of the elements. Within the model there are two kinds of interactions for the elements, block-block and block-filter. It is important to seperate those as this allows for defining different friction coefficients to the different interactions. To prevent defining thousands of interactions between all elements in the model, the block-block interaction is the default. This is justified as most elements do only have interaction with either other blocks or the filter. The interaction is modelled as a 'NormalBehaviour' which allows for seperation of an element with its surroundings, it is also modelled as a 'TangentialBehaviour' in order to incooporate the friction coefficient μ_e. The second type of interaction is between the blocks and the filter. To model this interaction, for each element a seperate interaction with the filter is modelled, otherwise the interaction would be the same as for block-block. This interaction is modelled in the same way as block-block with the only exemption of the friction coefficient, which is for block-filter μ_f.

With the same method it was also tried to model joint filling. The generation of joint filling was successful, however, the number of degrees of freedom increased so much that the computation time increased thirty-fold. Therefore, it was decided to model joint filling as a correction to the friction coefficient.

B.2.3. Loading

There are two types of loading applied to the model. The first type of loading is the gravity and is definied as an uniform load which is present from the beginning to the end of the model. The standard gravity module in Abaqus is used for gravity.

The second load is the loading on the elements due to the wave loading. The wave loading within the model consists out of five wave impacts of an equal wave height H. This wave height H is based upon the most intense moment during a storm and can be retrieved from the significant wave height H_s and storm intensity i_{st}. The method behind determining the wave height for the wave loading can be found in Appendix C.

The wave impact model to be used is the model by Peters (2017). To use this model with an individual wave height, a representative significant wave height H_s is calculated such that $H = H_{2\%}$. The center of the wave impact will be located at -0.7 H_s below still water level based upon the literature review done in Chapter 4.

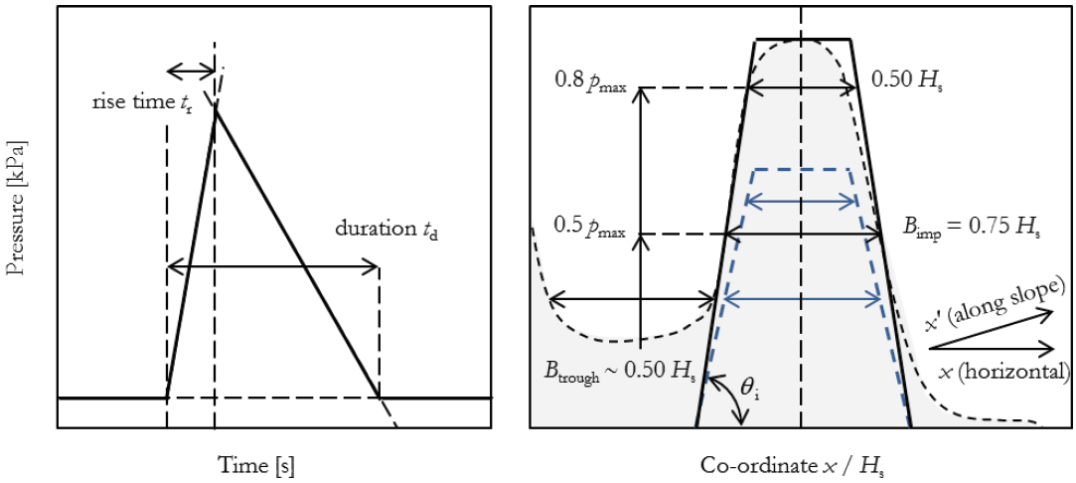

Figure B.4: Wave impact profile in space and time by Peters (2017)

The wave impacts are modelled into a 2 dimensional array in space and time with a time step of dt and a spacial step of dx. Reference is made to Section 2.2.2.4 in which the used equations are written down. For further reference, this array is denoted by the parameter $\phi_T(x,t)$.

Next, the leakage length will be determined. If there is no deformation the leakage length is constant over the whole length of the revetment. When the revetment is deformed, the deformation will be taken into account in the leakage length by varying the filter layer thickness b(x) corresponding to shape of the deformation (Equation B.1).

$$\Lambda(x) = \sqrt{\frac{D\ b(x)\ k}{k'}} \tag{B.1}$$

Based on the loading on the top layer $\phi_T(x,t)$ and the leakage length $\Lambda(x)$ it is possible to determine the filter response $\phi_F(x,t)$ with Differential Equation B.2.

$$\Lambda(x)^2 \frac{\partial^2 \phi_F(x,t)}{\partial x^2} - \phi_F(x,t) = -\phi_T(x,t) \tag{B.2}$$

This differential equation is solved using an implicit Euler scheme. This scheme is chosen because it is easy to implement and is unconditionally stable. At the boundary conditions it is assumed that the filter pressure $\phi_F(0,t)$ and $\phi_F(L,t)$ are both zero. However, because the differential equation has only space derivatives no diffusion will take place, the wave impact also never comes close to one of both boundaries therefore the impact of those boundary conditions are negliable.

After the filter response is calculated, the difference between the wave loading and the filter response is used to define the residual loading $\phi_R(x,t)$. To use the residual loading as a pressure $P_R(x,t)$ it is multiplied by the gravitational constant g and the density of the water ρ_w. The model then loops through each element to find which data points are in range of the length of the considered element and calculates the average pressure for each time step and combines it into a table (Figure B.5). After this, the model will apply a pressure to each element with magnitude -1 and as amplitude the earlier defined table. This will allow to change the magnitude of the pressure over time to simulate the residual force on the elements.

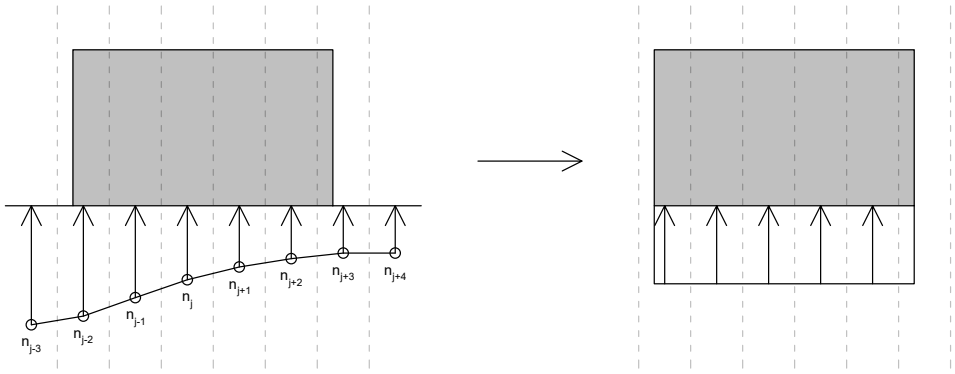

Figure B.5: Representation of the numerical grid

After this, the model is ready. In the next section is explained how damages are added to the model.

B.2.4. Damages

Next, damages will be added to the model. Generally, the work method explained in the previous section still applies when generating a revetment with damage. Deviations in the process will be reported per type of damage.

B.2.4.1. Deformation (S-profile)

To incorporate deformation two major things are changed to the model. First, the model assumes deformation is due to migration in the filter layer. As a result, when applying a S-profile, at the hump the filter layer is thicker than below the trough. This is when the spacial variation in the filter layer thickness b(x) is applied. As a result, the leakage length is no longer constant over the whole slope and thus the calculated residual pressure $P_f(x,t)$ will change.

Second, a deformation is applied to the position of the elements and the surface below the elements. To keep the model simple, the equations from Chapter 3 are applied to calculate the location and the total width of the S-profile based upon the given input parameters. The deformation in the surface below the elements is modelled as a sine wave. The elements above the deformation are either moved up or down until contact is made with the new deformed surface (Figure B.6). This all is done by mathematical models during the generation of the model before the simulation has been started.

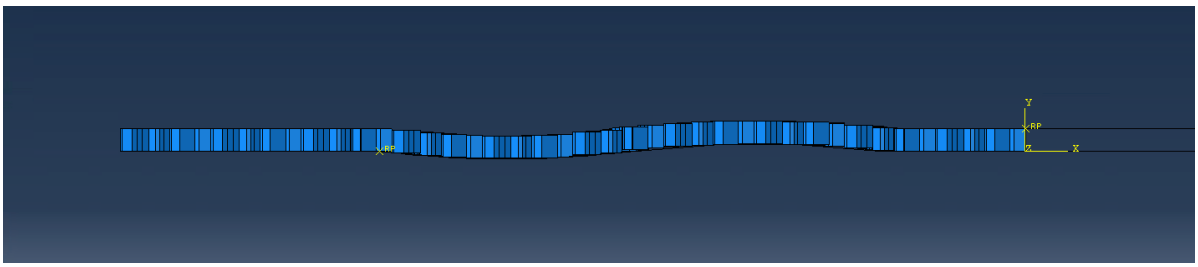

Figure B.6: A deformed revetment (a_s/b = 0.8)

B.2.4.2. Loss of Clamping

A loss of clamping is modelled by adjusting the block-block friction coefficient μ_e. This change is made immediately when the elements are generated.

B.2.4.3. Missing Elements

Missing elements are defined by a height z, which is the absolute height measured from the revetment bottom and offset x, which is the offset of the centerline of the revetment (Figure B.7). When this point (x, z) falls on an open space of the revetment, the model will choose the element which is the nearest to this point.

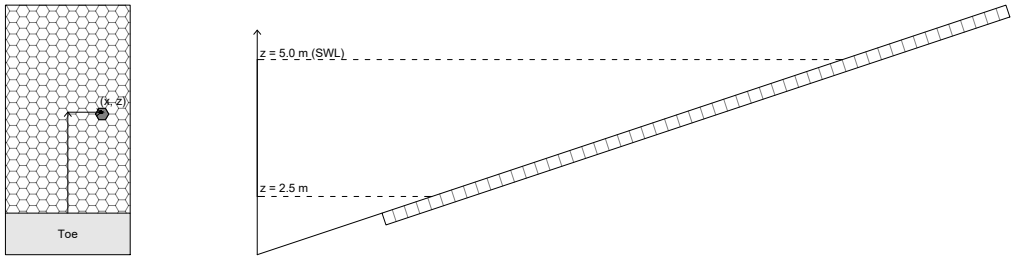

Figure B.7: Interpretation of the x and z variables for the fourth sample group

After the revetment is almost generated, the model will check whether an element has to be removed. If this turns out to be true, it will project the given x and z coordinates on the slope and determine the element which has to be removed. After this it will remove the element, the block-filter interaction corresponding to this element, the loading and the amplitude of the loading. This is all required to prevent Abaqus from showing errors.

B.3. Adding Random Parameters

The generation of samples is done by the Python package SALib by Herman and Usher (2017). The results of those samples are combined into one Excel files denoted by 'sample.xlsx' (Figure B.8). This Excel file is read by the Python script and will generate a model for each row. When a model is generated, it will be automatically saved as an .inp file, which is an input file that can be used when running simulations with Abaqus Command. This is especially handy when using a desktop to generate models and a high performance computer to run the models as only the .inp files has to be transferred between both computers.

	A	B	C	D	E	F	G	H	I	J	K	L	M	N	O	P	Q	R	S	T	U	V	W	X	Y	Z
1	ModelName	Slope	Zdtop	Zdbot	Hs	S0p	SI	D	d	Λ	k/k'	ρw	ρs	μf	με	H1	H2	H3	H4	H5	Order	Smid coef	Sb coef	S amp	Gz	Gx
2	Model-1001	3	0.2	-0.55	0.71122	0.01	0.5	0.3	5	0.15	0.576923	1025	2240	0.6	0.85	0.86569	0.86569	0.86569	0.86569	0.86569	11111	0.099758	8.071138	0.05	0	0
3	Model-1002	3	0.2	-0.55	1.778049	0.03	0.5	0.3	5	0.45	5.192308	1025	2240	0.6	0.85	2.164224	2.164224	2.164224	2.164224	2.164224	11111	0.358	12.43	0.5	0	0
4	Model-1003	3	0.2	-0.55	2.311463	0.02	0.5	0.3	5	0.3	2.307692	1025	2240	0.6	0.85	2.813492	2.813492	2.813492	2.813492	2.813492	11111	0.264152	10.84594	0.275	0	0
5	Model-1004	3	0.2	-0.55	1.244634	0.02	0.5	0.3	5	0.3	2.307692	1025	2240	0.6	0.85	1.514957	1.514957	1.514957	1.514957	1.514957	11111	0.264152	10.84594	0.275	0	0
6	Model-1005	3	0.2	-0.55	1.511341	0.025	0.5	0.3	5	0.525	7.067308	1025	2240	0.6	0.85	1.839591	1.839591	1.839591	1.839591	1.839591	11111	0.512525	15.03822	0.8375	0	0
7	Model-1006	3	0.2	-0.55	2.578171	0.045	0.5	0.3	5	0.225	1.298077	1025	2240	0.6	0.85	3.138125	3.138125	3.138125	3.138125	3.138125	11111	0.313123	11.67252	0.3875	0	0
8	Model-1007	3	0.2	-0.55	2.044756	0.015	0.5	0.3	5	0.675	11.68269	1025	2240	0.6	0.85	2.488858	2.488858	2.488858	2.488858	2.488858	11111	0.402877	13.18748	0.6125	0	0
9	Model-1008	3	0.2	-0.55	0.977927	0.015	0.5	0.3	5	0.675	11.68269	1025	2240	0.6	0.85	1.190323	1.190323	1.190323	1.190323	1.190323	11111	0.402877	13.18748	0.6125	0	0
10	Model-1009	3	0.2	-0.55	1.11128	0.0225	0.5	0.3	5	0.7125	13.01683	1025	2240	0.6	0.85	1.35264	1.35264	1.35264	1.35264	1.35264	11111	0.335789	12.05511	0.44375	0	0
11	Model-1010	3	0.2	-0.55	1.644695	0.0225	0.5	0.3	5	0.7125	13.01683	1025	2240	0.6	0.85	2.001908	2.001908	2.001908	2.001908	2.001908	11111	0.335789	12.05511	0.44375	0	0
12	Model-1011	3	0.2	-0.55	2.17811	0.0425	0.5	0.3	5	0.4125	4.362981	1025	2240	0.6	0.85	2.651175	2.651175	2.651175	2.651175	2.651175	11111	0.553735	15.73381	0.89375	0	0
13	Model-1012	3	0.2	-0.55	2.711524	0.0425	0.5	0.3	5	0.4125	4.362981	1025	2240	0.6	0.85	3.300442	3.300442	3.300442	3.300442	3.300442	11111	0.553735	15.73381	0.89375	0	0
14	Model-1013	3	0.2	-0.55	1.377988	0.0175	0.5	0.3	5	0.3375	2.920673	1025	2240	0.6	0.85	1.677274	1.677274	1.677274	1.677274	1.677274	11111	0.380211	12.80489	0.55625	0	0
15	Model-1014	3	0.2	-0.55	0.844573	0.0175	0.5	0.3	5	0.3375	2.920673	1025	2240	0.6	0.85	1.028007	1.028007	1.028007	1.028007	1.028007	11111	0.380211	12.80489	0.55625	0	0
16	Model-1015	3	0.2	-0.55	2.444817	0.0375	0.5	0.3	5	0.6375	10.42067	1025	2240	0.6	0.85	2.975809	2.975809	2.975809	2.975809	2.975809	11111	0.162265	9.126191	0.10625	0	0
17	Model-1016	3	0.2	-0.55	1.911402	0.0375	0.5	0.3	5	0.6375	10.42067	1025	2240	0.6	0.85	2.326541	2.326541	2.326541	2.326541	2.326541	11111	0.162265	9.126191	0.10625	0	0
18	Model-1017	3	0.2	-0.55	0.91125	0.02875	0.5	0.3	5	0.43125	4.76863	1025	2240	0.6	0.85	1.109165	1.109165	1.109165	1.109165	1.109165	11111	0.41454	13.38434	0.640625	0	0
19	Model-1018	3	0.2	-0.55	1.844726	0.02875	0.5	0.3	5	0.43125	4.76863	1025	2240	0.6	0.85	2.245383	2.245383	2.245383	2.245383	2.245383	11111	0.41454	13.38434	0.640625	0	0
20	Model-1019	3	0.2	-0.55	1.978079	0.04875	0.5	0.3	5	0.73125	13.71094	1025	2240	0.6	0.85	2.4077	2.4077	2.4077	2.4077	2.4077	11111	0.220532	10.10967	0.190625	0	0
21	Model-1020	3	0.2	-0.55	0.777896	0.04875	0.5	0.3	5	0.73125	13.71094	1025	2240	0.6	0.85	0.946848	0.946848	0.946848	0.946848	0.946848	11111	0.220532	10.10967	0.190625	0	0
22	Model-1021	3	0.2	-0.55	2.511494	0.01875	0.5	0.3	5	0.28125	2.028345	1025	2240	0.6	0.85	3.056967	3.056967	3.056967	3.056967	3.056967	11111	0.531633	15.36076	0.965625	0	0

Figure B.8: Excel parameter file which acts as input for the Python model

B.4. Revetment Model Code

The used code to generate the finite element model can be found at the GitHub repository of the author: https://github.com/nielsvandervegt/mscthesis/tree/main/FEModel

C

Determining the Wave Loading

In this appendix is substantiated how the loading is defined in the finite element model. As it is vital to keep the computation time low, it is opted to only simulate a few waves. The question is how many wave impacts are required in order to be able to analyse the impact of the different types of damage included in the initial conditions of the model. Two main aspects are important here, first, the number of wave impacts should be high enough in order to create damage. Second, the number of wave impacts should be minimized in order to reduce the required computation time. Based upon experiments with the finite element model, it turns out that for five large waves the revetment can be damaged. Therefore, five extreme waves seems like a good compromise between computation time and accuracy. The next step is to statistically determine those five waves. Therefore during this analysis, the main question is: what is the worst possible combination of five waves during a storm and how can we statistically define this. For this analysis we assume a constant storm duration of N_{storm} is 5000 waves (8-10 hours).

Within this analysis, in Section C.1 is defined what is the worst possible combination of five waves during a storm. Next, in Section C.2, the wave height for those five waves are quantified.

C.1. Defining the Worst Possible Combination of Five Waves

The first step in the analysis is to determine, what defines the worst possible combination of five waves for a storm. To answer this question, we have to look at the residual pressure on the elements. The higher this pressure, the more likely it is for an element to be fully uplifted from the revetment. The residual pressure is defined as the difference between the filter response and the wave impact pressure. As the filter response is solely determined by properties of the revetment and are assumed to not change during the storm, we have to look into the wave impact pressure. Within the finite element model, the wave impact profile of Peters (2017) is used for which the wave impact pressure for this profile is defined in Equation C.1.

$$\frac{P_{max2\%}}{\rho_w \; g \; H_s} = 8 - 1.6 \; \xi_{m-1,0} - \frac{2}{\left(\xi_{m-1,0} - 0.2\right)^2} \tag{C.1}$$

In Equation C.1, the pressure is defined as the peak value exceeded not more than by 2% of the waves. For the finite element method, we will assess individual waves, therefore we will substitute the significant wave height H_s with a representative significant wave height $H_{s;rep}$. Holthuijsen (2007) suggests that individual wave heights in a storm follow the cumulative Rayleigh distribution function shown in Equation C.4. By rewriting Equation C.4, we find that $H_{2\%}/H_s \approx 1.4$. Based on this finding, the representative significant wave height can be calculated such that the calculated individual wave height H_n is about $H_{2\%}$ (Equation C.2).

$$H_{s;rep} = \frac{H_n}{1.4} \tag{C.2}$$

Substituting Equation C.2 into Equation C.1, yields Equation C.3. This equation is used within the finite element model to determine the maximum pressure caused by an individual wave n.

$$\frac{P_{max;n}}{\rho_w \; g \; H_n} = 8 - 1.6 \; \xi_{m-1,0} - \frac{2}{\left(\xi_{m-1,0} - 0.2\right)^2} \tag{C.3}$$

Equation C.3 shows that P_{max} is dependent on the individual wave height H_n, mass density of the water, gravitational acceleration and the Iribarren number. The mass density of the water and gravitational acceleration are both defined by a constant and do not change between models. The Iribarren number will change between models. However, for each model it does not change between the five simulated waves. With this, we assume that the wave steepness, and hereby the Iribarren number, for all five waves are identical, this allows us to study the impact of the wave steepness later in the analysis. This means that only the individual wave height H_n is unknown. In Figure C.1, the impact of different individual wave heights are illustrated.

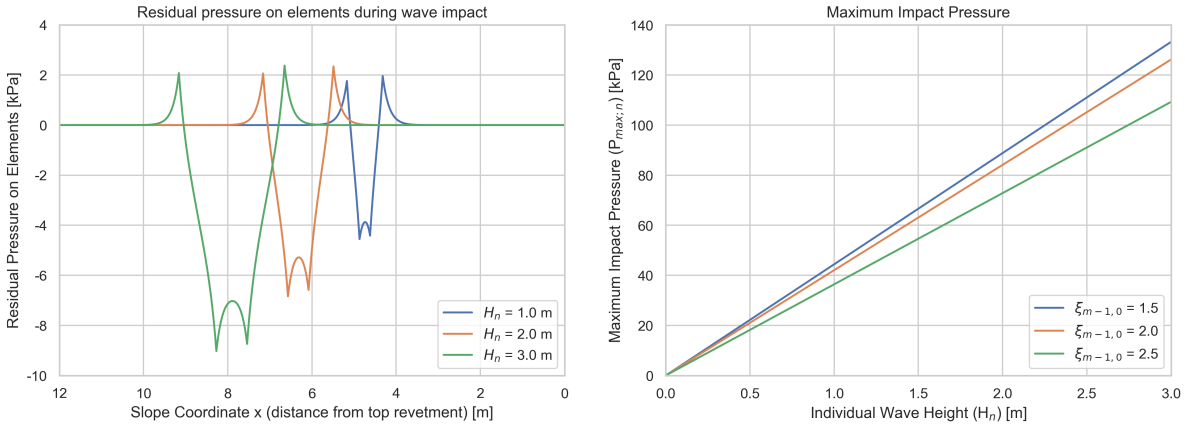

Figure C.1: The residual pressure on the elements illustrated for different individual wave heights (Left) $P_{max;n}$ illustrated against the individual wave height illustrated for different Iribarren numbers (Right)

In Figure C.1, we observe a linear relation between the maximum pressure and the individual wave height H_n for a constant Iribarren number. Based on this, we can conclude that for our model, the worst possible combination of five waves during a storm are the five consecutive waves with the largest combined individual wave height. In the next section, we will discuss a method to statistically obtain the worst possible combination of five waves during a storm.

C.2. Defining the Individual Wave Heights

The goal of this section is to statistically determine the worst possible combination of five waves during a storm based upon a predetermined significant wave height. In order to define this relation, we first have to statistically define a storm with individual waves. As mentioned in the previous section, Holthuijsen (2007) suggests that individual wave heights in a storm follow the cumulative Rayleigh distribution function shown in Equation C.4.

$$P\left\{\overline{H} < H\right\} = 1 - \exp\left(-\frac{H^2}{8m_0}\right) \tag{C.4}$$

We can rewrite Equation C.4 to a model we can use to generate a random wave field. First we assume $H_s \approx H_{m0} \approx 4\sqrt{m_0}$, and substitute it into Equation C.5.

$$P\left\{\overline{H} < H\right\} = 1 - \exp\left(-2\frac{H^2}{H_s^2}\right) \tag{C.5}$$

By replacing the term left of Equation C.5 by an uniform distribution ranging between 0 and 1, a random individual wave height H can be generated based solely on the significant wave height. Rewriting this equation will give Equation C.6.

$$H = H_s \sqrt{-\frac{1}{2}\ln\left(U(0,1)\right)} \tag{C.6}$$

By looping Equation C.6 for 5000 times, we can generate a storm with 5000 waves based upon a significant wave height. From the previous section, we know within those 5000 waves, we are looking for the five consecutive waves with the largest combined individual wave height. In reality, wave heights will normally vary from wave to wave. However, within this study focuses on the uncertainty due to structural changes, which are the damages. Therefore, we will define the individual wave height of the worst case scenario $H_{n;w}$ as the largest average wave height of five consecutive waves during a storms. This way we exclude the uncertainty of the order in which the waves are simulated and differences between the individual wave heights.

$$\frac{H_n}{H_s} = \sqrt{-\frac{1}{2}\ln\left(U(0,1)_n\right)} \tag{C.7}$$

Because the waves within a storm are generated based upon a probability distribution, the generated storms differ between each other. Therefore, a Monte Carlo simulation is done with Equation C.7 to find the expected largest average wave height of five consecutive waves during a storm $H_{n;w}$, hereafter average individual wave height. In order to use the result for any significant wave height, we study the expected ratio of the average individual wave height over the significant wave height ($H_{n;w}/H_s$). The results are shown in Figure C.2.

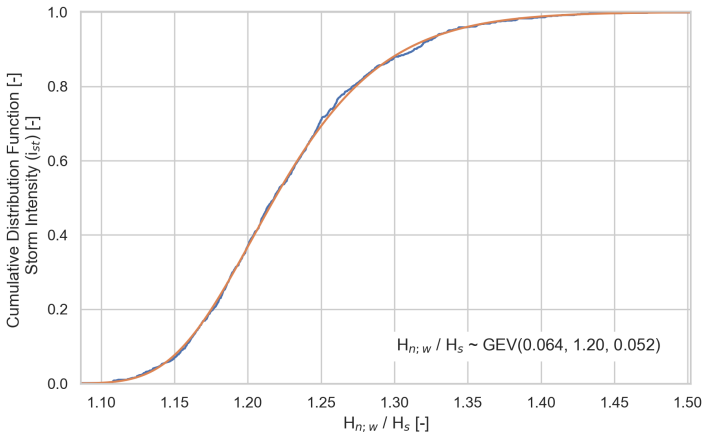

Figure C.2: Expected ratio of the average individual wave height over the significant wave height

Based on this Monte Carlo simulation, it was found that this ratio could be estimated by a generalized extreme value distribution. Within the finite element model we will use the obtained distribution to estimate the individual wave height of the five waves simulation in the model ($H_n = H_{n;w}$). To account for the variation between different storms, we introduce the storm intensity i_{st}. Which is the quantile of the found distribution used to include the uncertainty between different storms. Consequentially, a higher storm intensity will lead to a larger ratio $H_{n;w}/H_s$ and vice versa.

D

Data Processing of the (Stochastic) Finite Element Model Results

This appendix describes how the data from the Abaqus models is processed. For every Abaqus simulation, Abaqus will give an output database file (.odb). This file contains all information regarding the output of the simulation and can be loaded into Abaqus without requiring the original model file. However, because of the amount of sample, this study will analyse the data with the use of Python through the Abaqus command prompt.

For each sample group, all output database files are collected in one folder. The Python script will loop through all output database files and check whether the output database file is already processed or is currently being processed by another instance of the script. If neither applies the script will load the output database file.

The Python script will check the magnitude (Equation D.1) of the total displacement of each element (i) for a given set of time steps. The total displacement is the difference between the considered time step and the first time step before the very first wave impact. Chosen is to not use the first time step of the simulation as the first two seconds of the simulation are intended to allow the elements to displace from the initial conditions to the steady-state condition, which can add (minor) additional; displacements.

$$||u|| = \sqrt{u_{x;i}^2 + u_{y;i}^2 + u_{z;i}^2} \tag{D.1}$$

The Python script will collect four different data points from the output. The first data point is the total deformation of each element, which is determined at the last time step of the simulation. The second data point is the maximum deformation, which is determined by looping through a predefined set of relevant time steps to find the time step when the total deformation is the largest. This predefined set of relevant time steps consists out of a grid in which each second the whole revetment is analysed together with a finer grid of 0.01 seconds during the wave impact. Combining both grids will lead to a time step set of about 200 points, which will take about 15 minutes per sample to analyse. The last two data points are the total amount of elements per meter being lifted from the revetment and the largest deformation of an element. During the analysis, the total deformation of an element is capped at the top layer thickness as it is assumed when an element exceeds the top layer thickness, it is fully lifted from the revetment.

Finally, the Python script will write the results into a separate text file for each simulation. This text file will contain a header with data on the amount of fully lifted elements and the largest deformation of an element. Underneath the header is a list of values for the maximum and final deformation of each element including the column, row and element ID. Next, those text files can be loaded into a Python script to further analyse the data.

E

Results from the Finite Element Model

In the first part of this appendix, a justification is given for all parameters used in the model in Chapter 5 and partly Chapter 6. The second part of this appendix will present the all the results from the model runs of Chapter 5. For each model run two plots are made. The first plot is the maximum deformation of the revetment during the fifth and last wave impact and the second the deformation at the end of the simulation.

E.1. Parameters

Table E.1 with the parameters is reproduced below. Underneath the table each of the chosen values for the parameters are justified.

Symbol	Description	Value	Units
Geometry			
B_m	Width of the model	3.00	[sets]
cot α	Slope	3.00	[-]
d	Water depth	5.00	[m]
$z_{d;top}$	Dimensionless top of the revetment	0.20	[-]
$z_{d;bot}$	Dimensionless bottom of the revetment	-0.55	[-]
g	Gravitational acceleration	9.81	[m/s^2]
Wave Loading			
H_s	Significant wave height	2.50	[m]
T_p	Peak period	5.66	[s]
i_{st}	Storm Intensity (Appendix C)	0.90	[-]
s_{0p}	Offshore wave steepness	0.05	[-]
ρ_w	Density of the water	1025	[kg/m^3]
Top Layer			
D	Thickness of the top layer	0.30	[m]
k’	Permeability of the top layer (10% open, Gravel 9/25 mm)	0.05	[m/s]
Λ	Leakage length	0.38	[m]
ρ_e	Mass density of the elements (without joints)	2240	[kg/m^3]
E_e	Young’s modulus of the elements	50.0	[GPa]
ν_e	Poisson’s ratio	0.20	[-]
μ_e	Friction between elements (with joint filling)	0.85	[-]
μ_f	Friction with the filter	0.60	[-]
Filter Layer			
b	Thickness of the filter layer	0.13	[m]
k	Permeability of the filter layer (Gravel 17/42 mm)	0.19	[m/s]

Numerical			
dx	Step in space for determining loading	0.01	[m]
dt	Step in time for determining loading	0.01	[s]

Table E.1: Used parameters in the scenarios of Chapter 5 and 6 (unless otherwise specified)

Width of the model (B_s): The model consists out of three columns of Basalton STS+ sets which is based on a trade-off between simulation time and 2D effects.

Slope (cot α): The slope is chosen to be 1 in 3 because in the field the most common slope will be around 1 in 3 to 1 in 4. Also the Basalton STS+ experiments analysed in Chapter 4 had a slope of 1 in 3.

Water depth (d): The water depth is chosen to be 5 meter as during flume tests and in practice during a storm, the water depth near the toe is often in the order of magnitude of this depth.

Dimensionless top of the revetment ($z_{d;top}$): The dimensionless top of the revetment is 0.20, this value is based upon the analysis of the flume experiments done in Chapter 4.

Dimensionless bottom of the revetment ($z_{d;bot}$): The dimensionless bottom of the revetment is -0.55, this value is based upon the analysis of the flume experiments done in Chapter 4.

Gravitational acceleration (g): The gravitational acceleration is assumed to be 9.81 m/s^2.

Significant wave height (H_s): The significant wave height is based upon a dimensionless loading of 7. Kaste and Mourik (2016) showed during flume experiments with Basalton STS+ that for a dimensionless loading of 7, as during those experiments around this dimensionless loading large damages begin to occur.

Peak period (T_p:) The peak period is set to be 5.66 seconds. Together with a wave height of 2.50 this will give a wave steepness of 0.05.

Storm intensity (i_{st}): The storm intensity is set to be 0.50, which means that the most intense moment of 50% of all storms exceed this storm for the given significant wave height. This will result in 5 times a wave with a wave height of 3.04 meter. More can be found in Appendix C.

Wave steepness (s_{0p}): The wave steepness is assumed to be 0.05, as wind waves during storms tend to be more steeper than wind waves in normal conditions. (Chapter 2.2.2)

Mass density of the water (ρ_w): The density of the water is 1025 kg/m^3 which is based on seawater.

Thickness of the top layer (D): Basalton STS+ is available in a top layer thickness from 0.15 meter up to 0.50 meter. The top layer thickness for the model runs in this study is determined to be 0.30 meter.

Permeability of the top layer (k'): The permeability of the top layer is determined to be around 0.05 m/s based on the Basalton STS+ flume experiments (Kaste and Mourik, 2016). Kaste and Mourik (2016) determined this permeability with the model in SteenToets by measuring the percentage of open spaces, which is around 10% and the diameter of the joint filling material (D_{i15}), which is around 9.3 mm.

Leakage length (Λ): The leakage length is 0.38 meter and is calculated based upon the input for the top layer and filter layer thickness, and the top layer and filter layer permeability. Because all inputs are similar to the flume experiments by Kaste and Mourik (2016), the leakage length is also the same.

Mass density of the elements (ρ_e): The density of the elements is based on the Basalton STS+ elements which have a density of 2240 kg/m^3 (Holcim Coastal, 2013).

Young's modulus of the elements (E_e): The young's modulus of the elements is determined to be 50 GPa, which is typical for concrete (Blok, 2014).

Poisson's ratio of the elements (ν_e): Poisson's ratio of the elements is determined to be 0.2, which is typical for concrete. (Blok, 2014)

Friction between the elements (μ_e): The friction between the elements is determined to be 0.85 based on the calibration done in Section 5.2.4.

Friction with the filter (μ_f): The friction between the elements and the filter layer is determined to be 0.6 based on experiments done by Schoen (2004).

Thickness of the filter layer (b): The thickness of the filter layer is determined based on the entered leakage length, thickness of the top layer and permeability of the top and filter layer with the equation for the leakage length (Equation 2.11). In order to achieve a leakage length of 0.38 meter, this filter layer is determined to be 0.13 meter.

Permeability of the filter layer (k): The permability of the filter layer is 0.19 meter per second, and is based on the permeability of the granular filter layer used in the Basalton STS+ flume experiments (Kaste and Mourik, 2016). Kaste and Mourik (2016) calculated this permeability with the model in SteenToets by measuring the filter layer thickness, which is 0.13 meters and the diameter of the filter material (D_{f15}), which is around 17 mm.

Step in space (dx): The space step was chosen to be 0.01 meters, which should be sufficient to have enough data points to accurately determine the residual force on the elements.

Step in time (dt): The time step is chosen to be 0.01 seconds, this is based on the wave impact profile as the wave impact takes about 0.25 seconds. This gives about 25 time steps during the wave impact, which should be sufficient to model the impact quite accurately.

E.2. Group 1: No Damage

Model 1.01 - No Damage

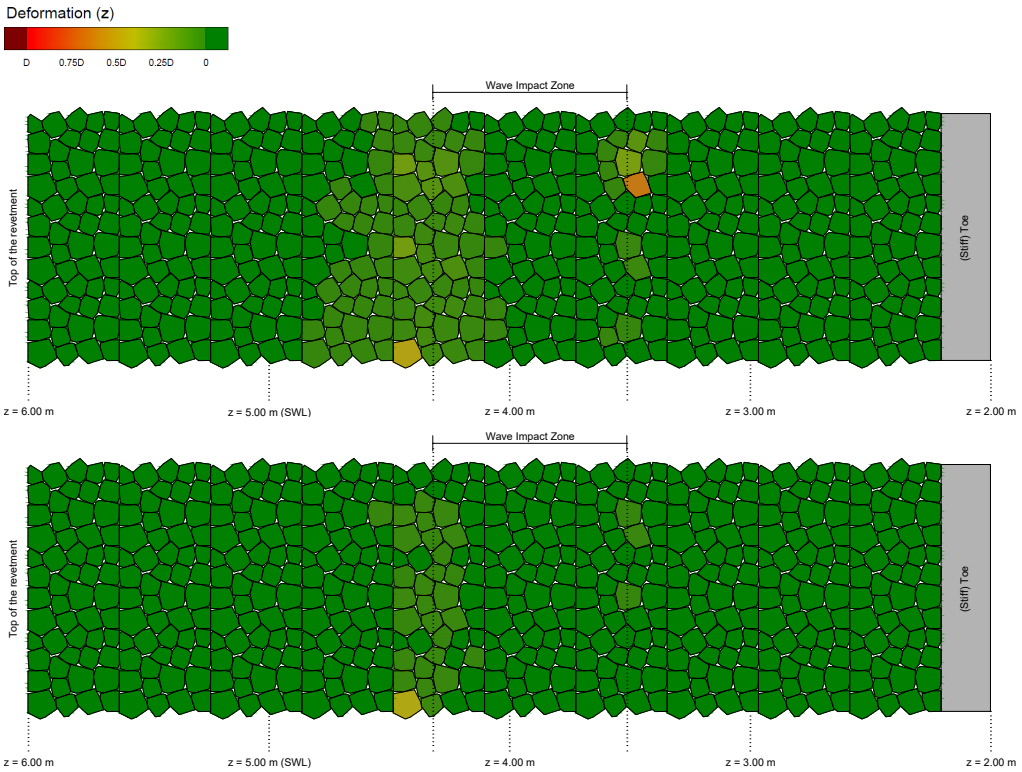

Figure E.1: Deformation plots for model 1.01 (top: maximum deformation of the revetment during the simulation, bottom: deformation at the end of the simulation)

E.3. Group 2: Deformation (S-Profile)

Model 2.01 - Small S-Profile (a_S/b = 0.1)

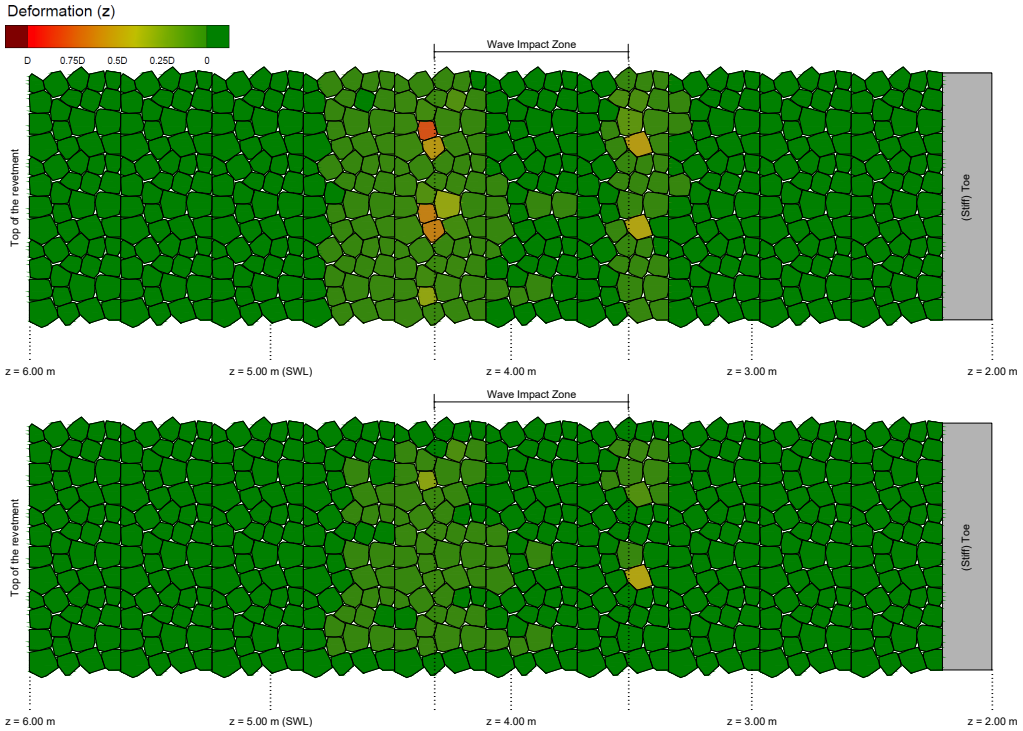

Figure E.2: Deformation plots for model 2.01 (top: maximum deformation of the revetment during the simulation, bottom: deformation at the end of the simulation)

Model 2.02 - Small S-Profile (a_S/b = 0.2)

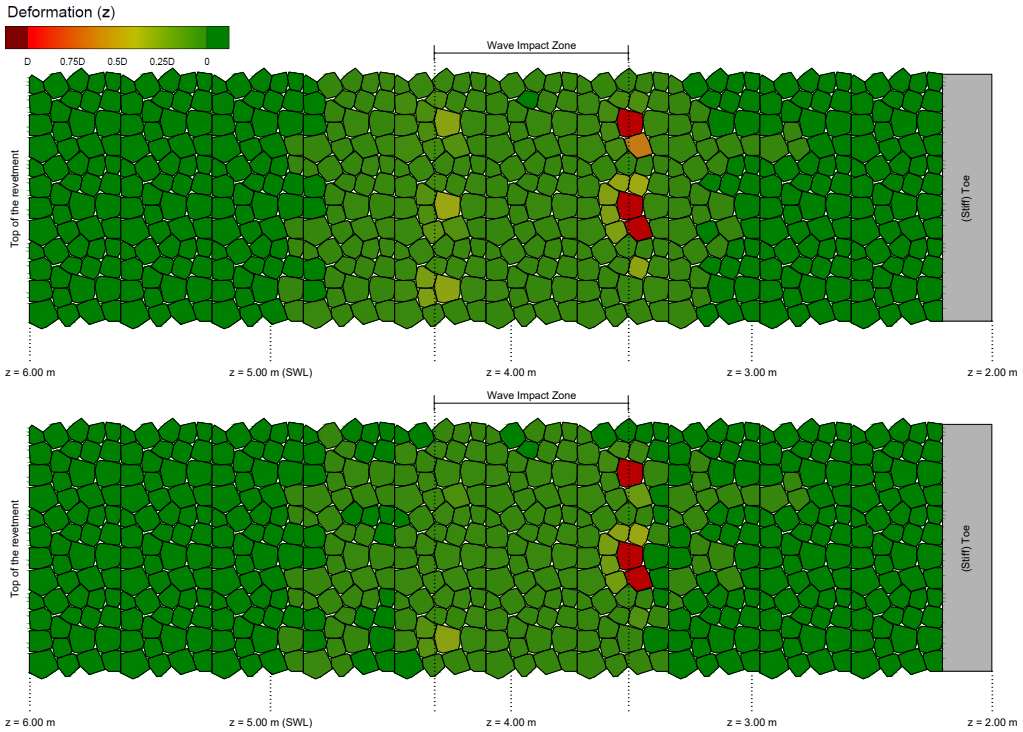

Figure E.3: Deformation plots for model 2.02 (top: maximum deformation of the revetment during the simulation, bottom: deformation at the end of the simulation)

Model 2.03 - Medium S-Profile (a_s/b = 0.4)

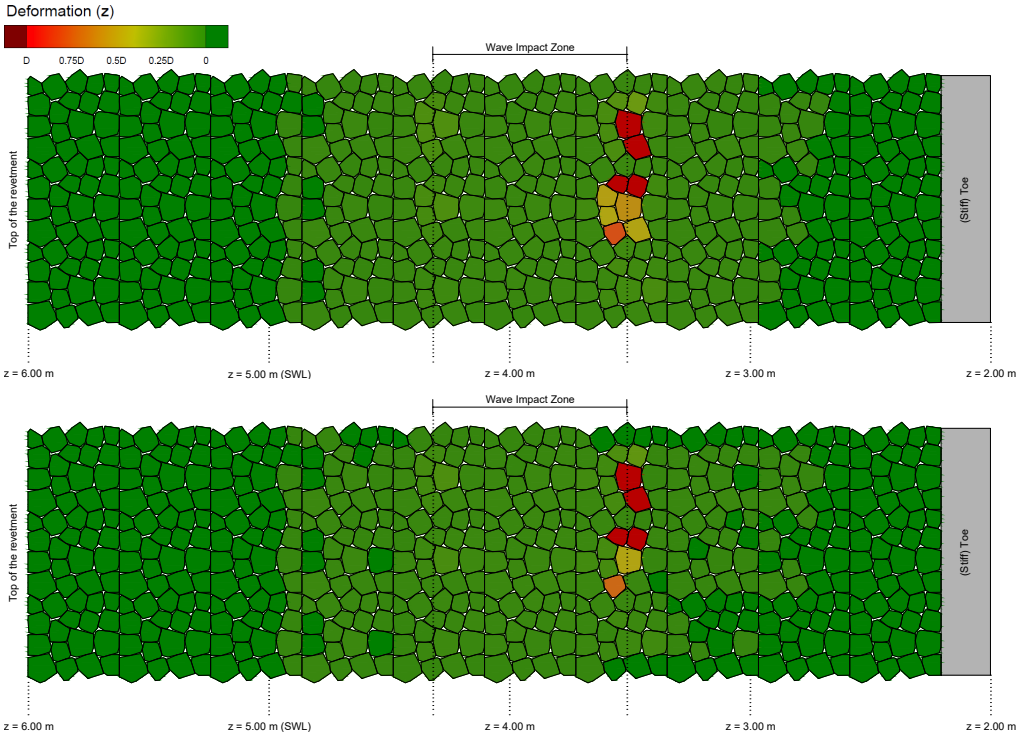

Figure E.4: Deformation plots for model 2.03 (top: maximum deformation of the revetment during the simulation, bottom: deformation at the end of the simulation)

Model 2.04 - Medium S-Profile (a_s/b = 0.6)

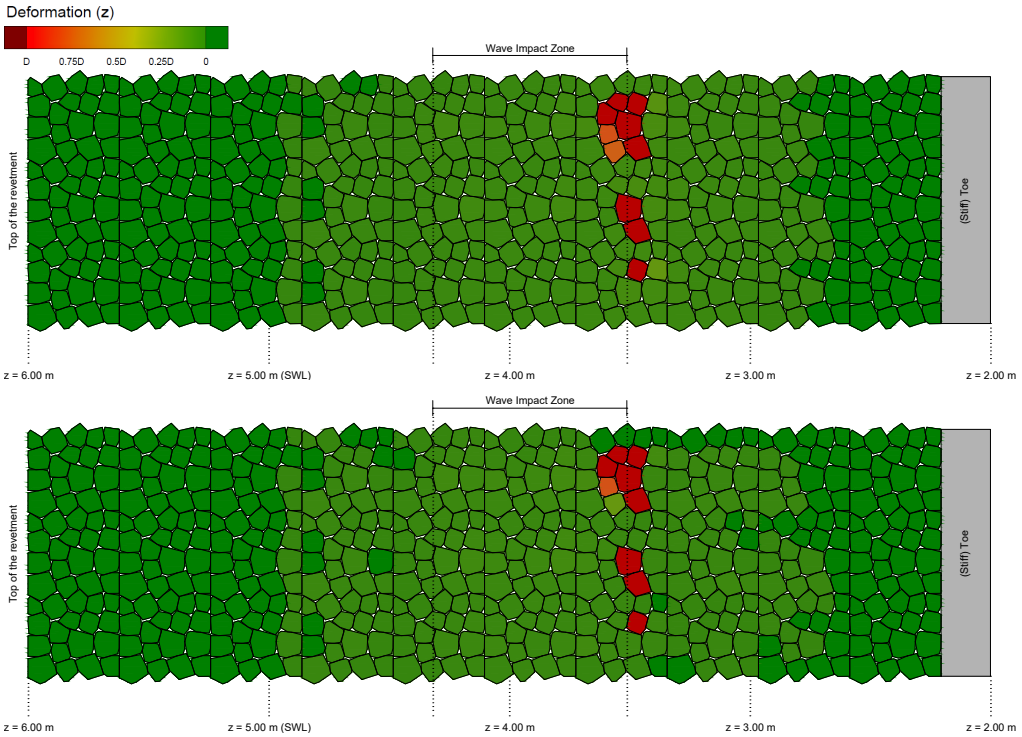

Figure E.5: Deformation plots for model 2.04 (top: maximum deformation of the revetment during the simulation, bottom: deformation at the end of the simulation)

Model 2.05 - Large S-Profile (a_s/b = 0.8)

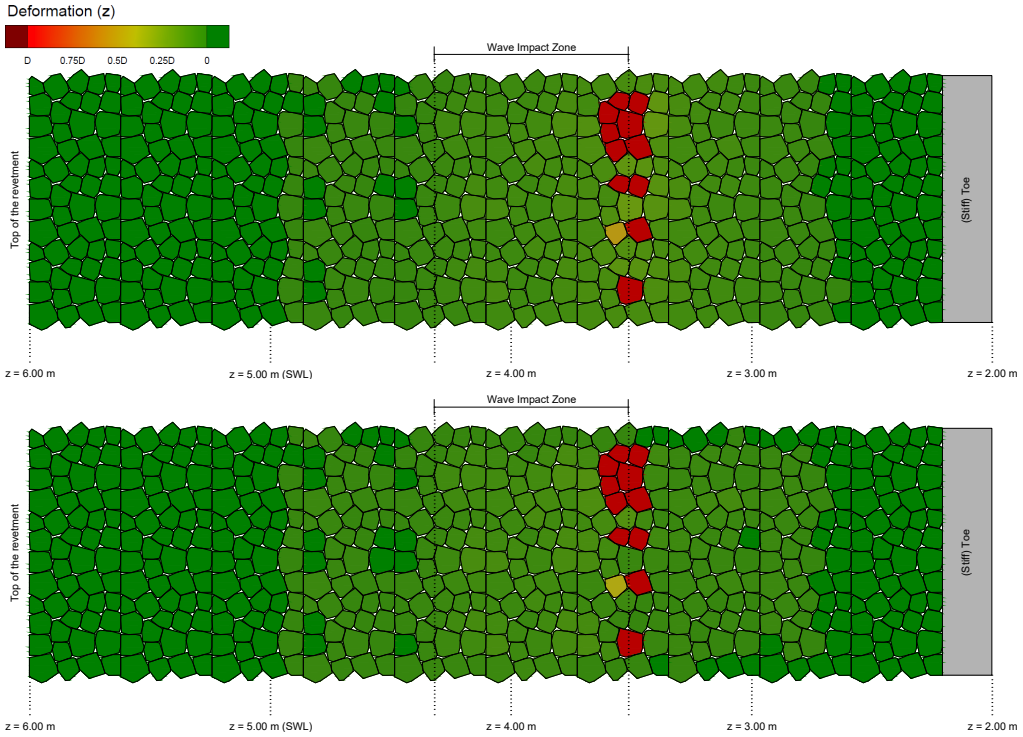

Figure E.6: Deformation plots for model 2.05 (top: maximum deformation of the revetment during the simulation, bottom: deformation at the end of the simulation)

Model 2.06 - Large S-Profile (a_s/b = 1.0)

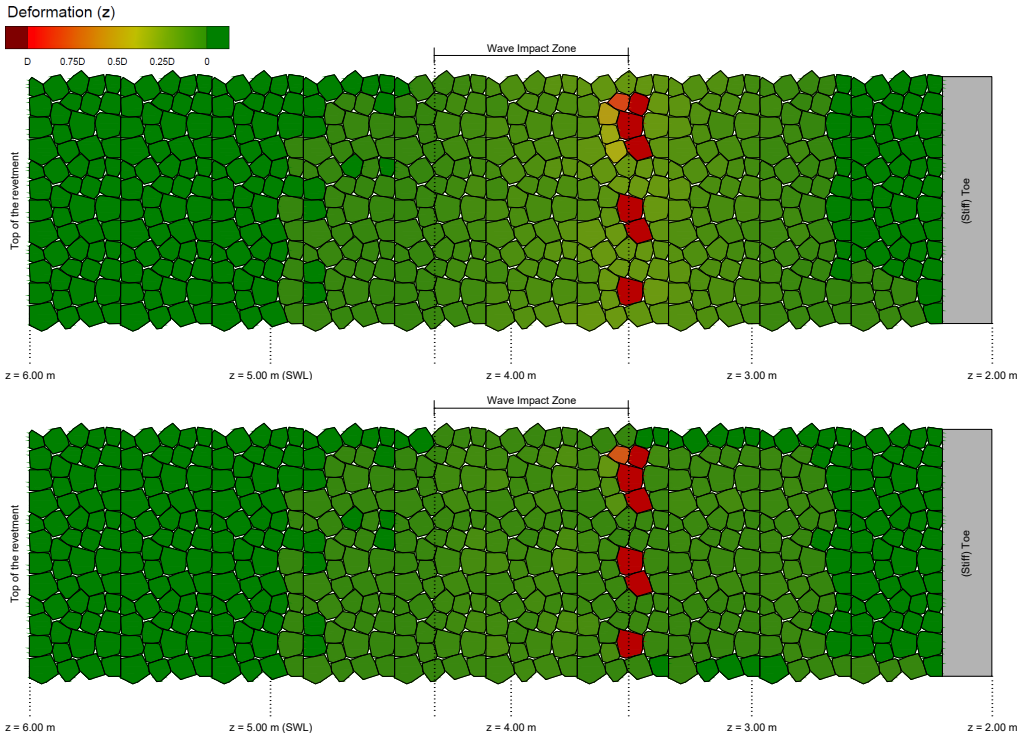

Figure E.7: Deformation plots for model 2.06 (top: maximum deformation of the revetment during the simulation, bottom: deformation at the end of the simulation)

E.4. Group 3: Reduction in Clamping

Model 3.01 - Small Friction Reduction (μ_e = 0.8)

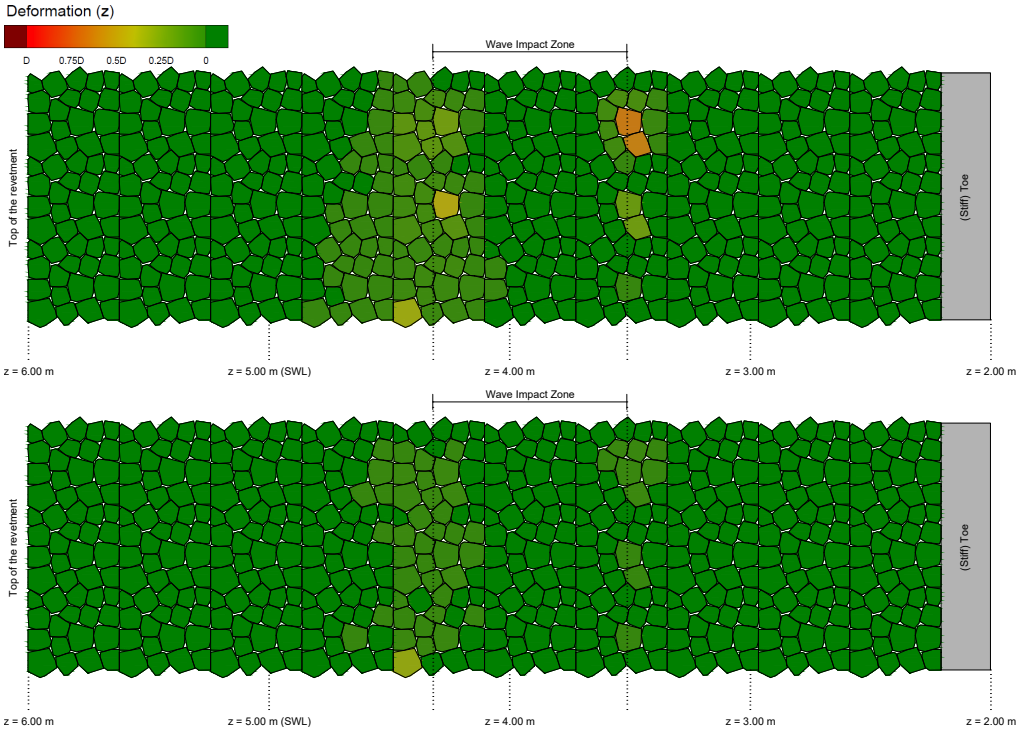

Figure E.8: Deformation plots for model 3.01 (top: maximum deformation of the revetment during the simulation, bottom: deformation at the end of the simulation)

Model 3.02 - Medium Friction Reduction (μ_e = 0.7)

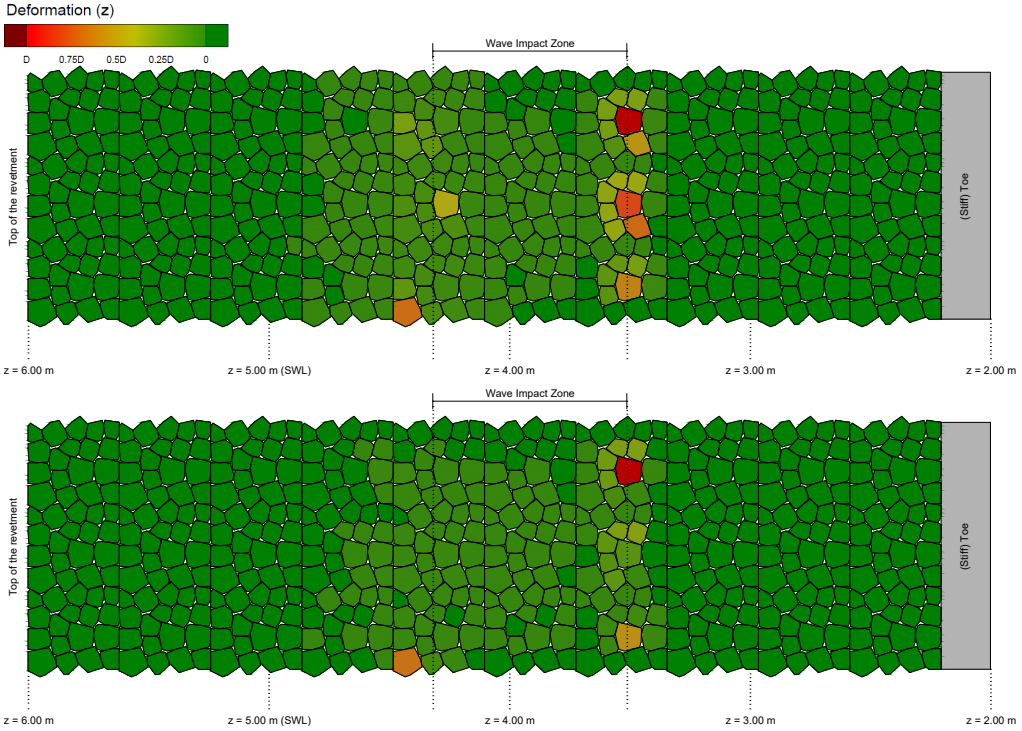

Figure E.9: Deformation plots for model 3.02 (top: maximum deformation of the revetment during the simulation, bottom: deformation at the end of the simulation)

Model 3.03 - No Joint Filling (μ_e = 0.6)

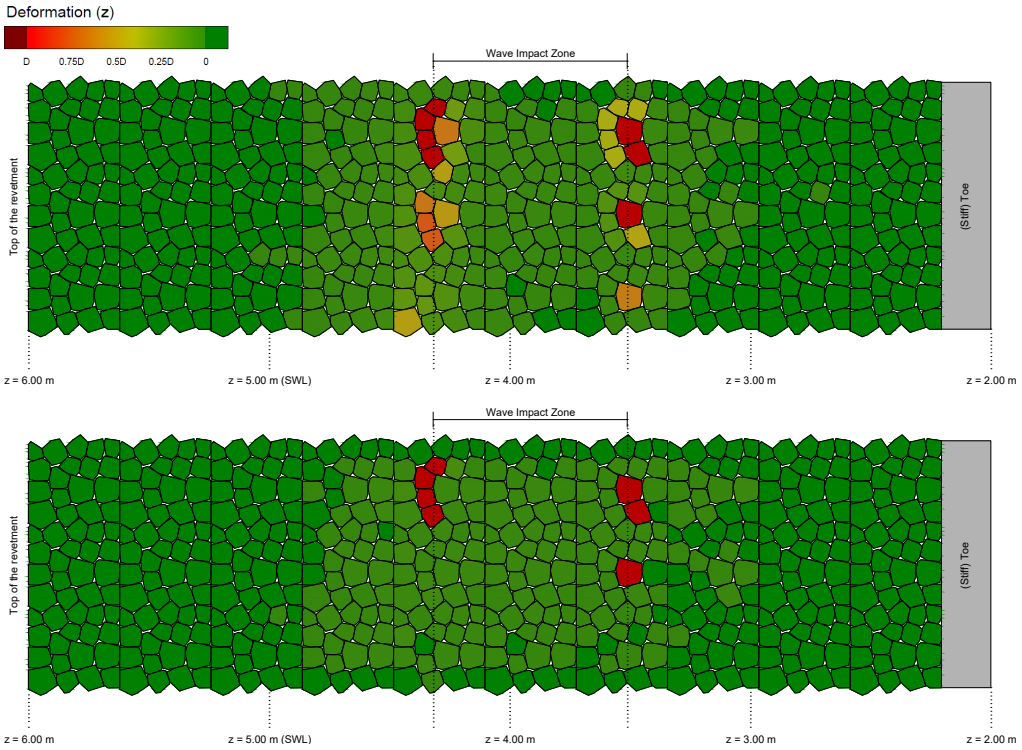

Figure E.10: Deformation plots for model 3.03 (top: maximum deformation of the revetment during the simulation, bottom: deformation at the end of the simulation)

E.5. Group 4: Missing Elements

Model 4.01 - Missing Element above Wave Impact (z = 4.43)

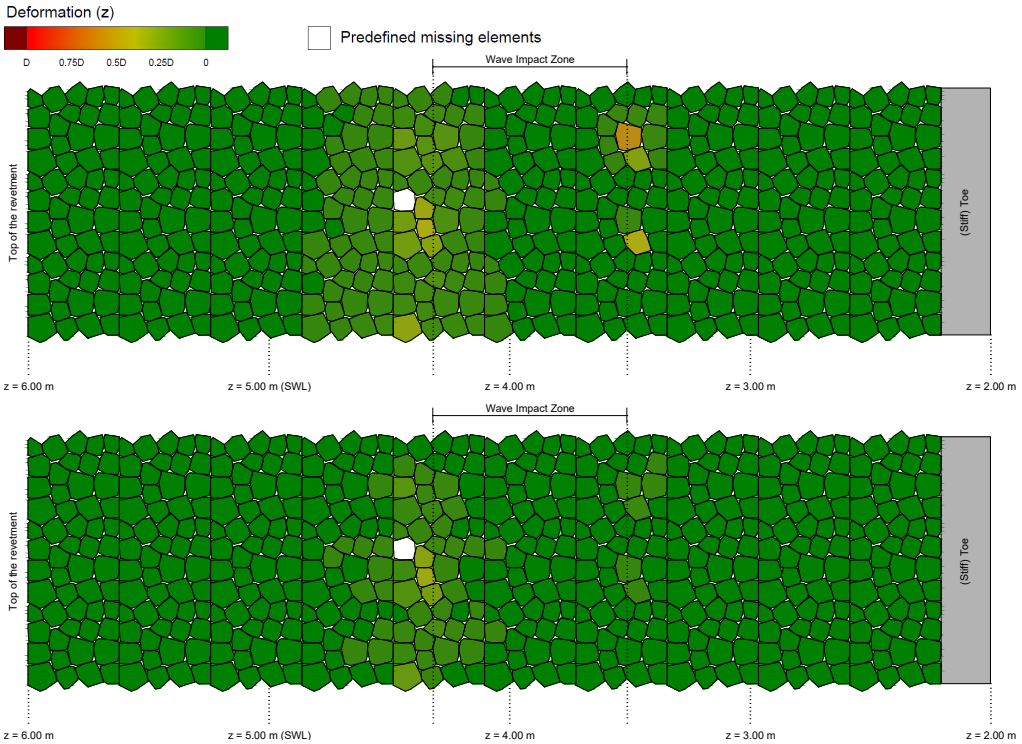

Figure E.11: Deformation plots for model 4.01 (top: maximum deformation of the revetment during the simulation, bottom: deformation at the end of the simulation)

Model 4.02 - Missing Element below Wave Impact (z = 3.47)

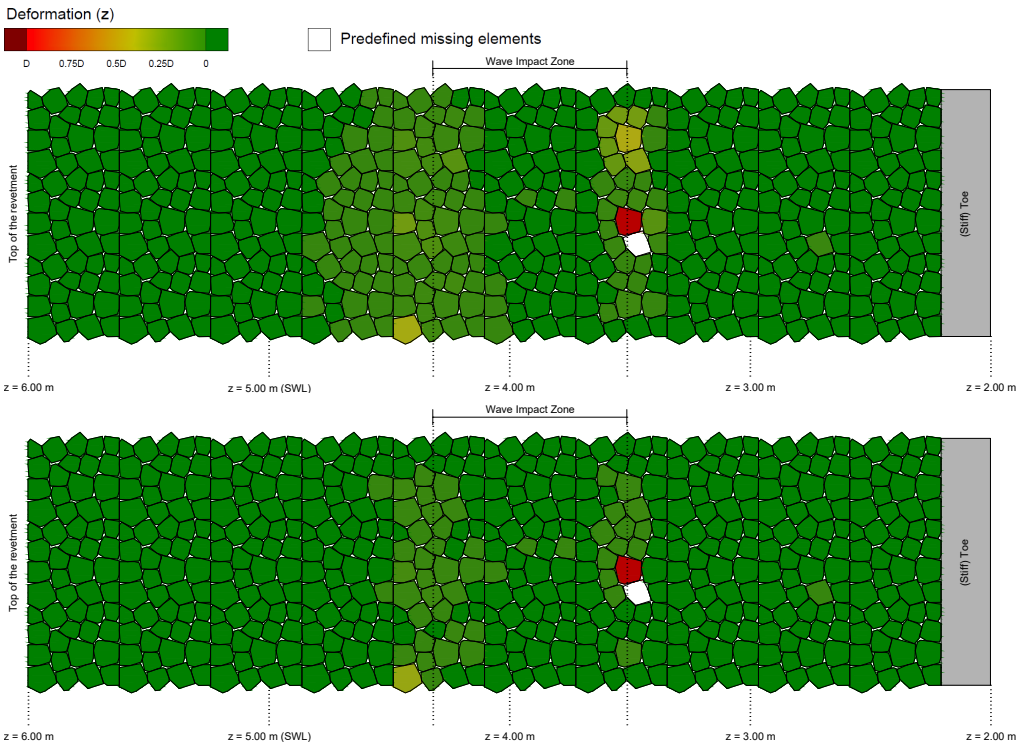

Figure E.12: Deformation plots for model 4.02 (top: maximum deformation of the revetment during the simulation, bottom: deformation at the end of the simulation)

Results from the Stochastic Finite Element Model

In this appendix, results from the stochastic finite element model are presented. In the first section, the qualitative sensitivity analysis results from the identification of the main parameters are shown (Section 6.2). Thereafter, more information is given on the response surface models (Section 6.4).

F.1. Qualitative Sensitivity Analysis

In this section the results from the qualitative sensitivity analysis of Section 6.2 are presented. First, a convergence plot for all parameters is shown in Figure F.1, thereafter, a more detailed convergence plot and sensitivity plot are presented for each random parameter.

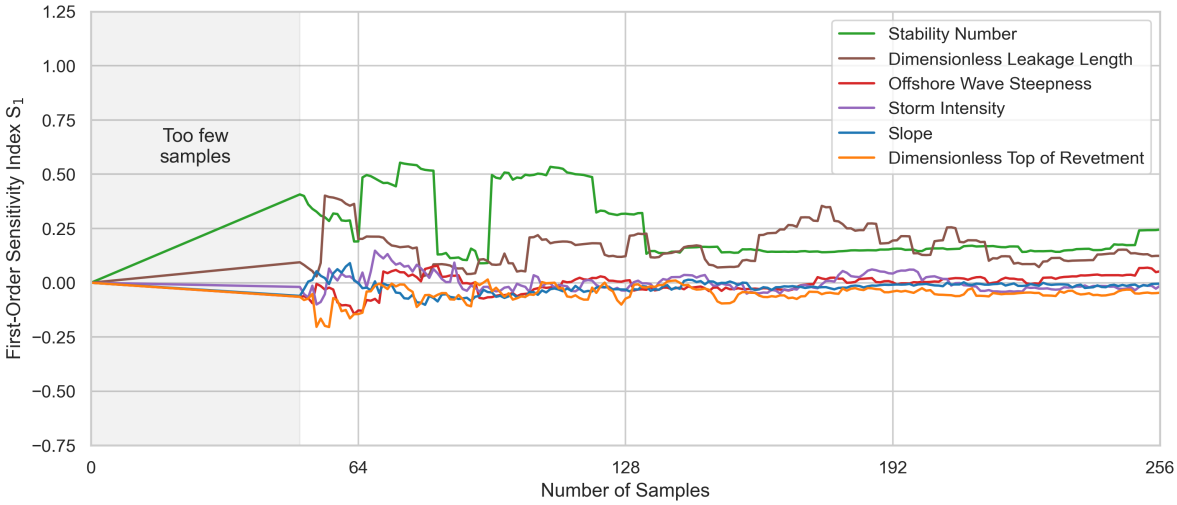

Figure F.1: Convergence plot for all research parameters

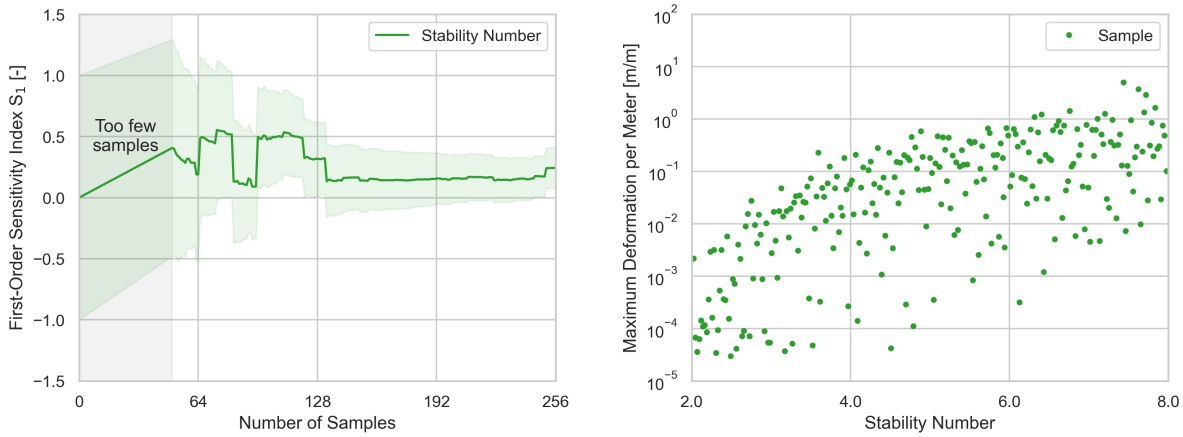

Figure F.2: Convergence plot (left) and sensitivity plot (right) for the stability number

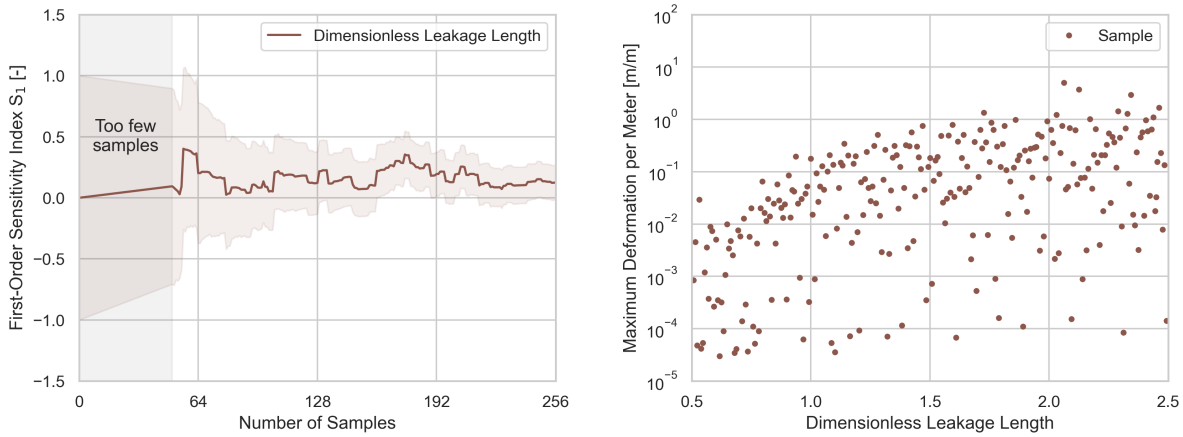

Figure F.3: Convergence plot (left) and sensitivity plot (right) for the dimensionless leakage length

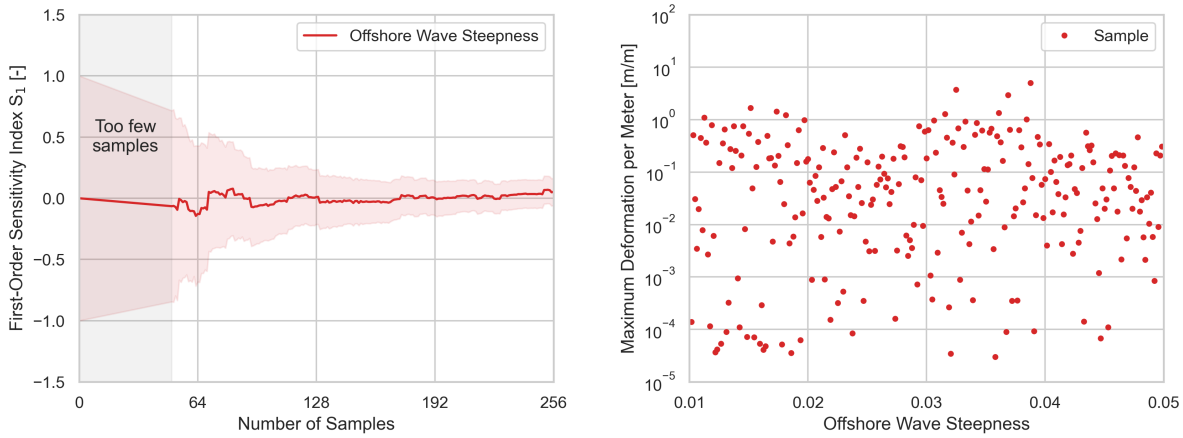

Figure F.4: Convergence plot (left) and sensitivity plot (right) for the offshore wave steepness

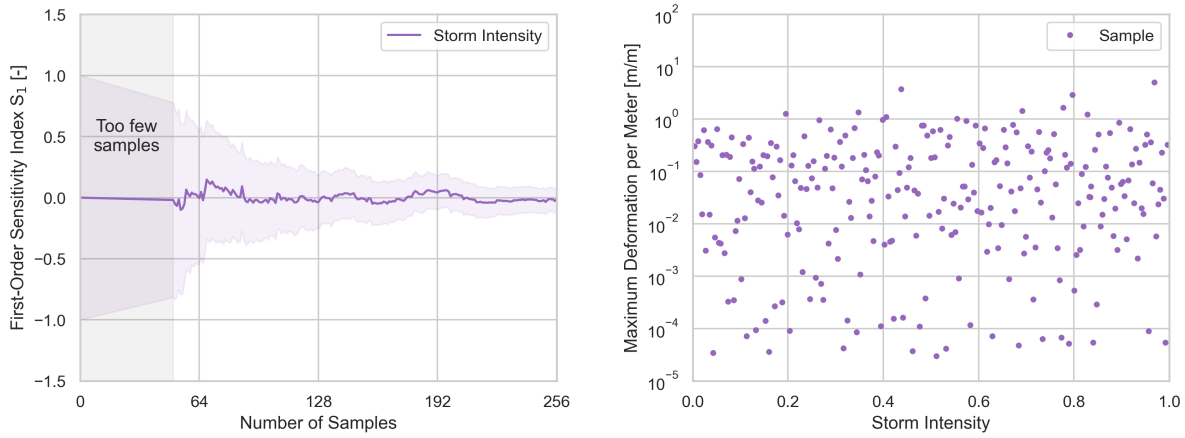

Figure F.5: Convergence plot (left) and sensitivity plot (right) for the storm intensity

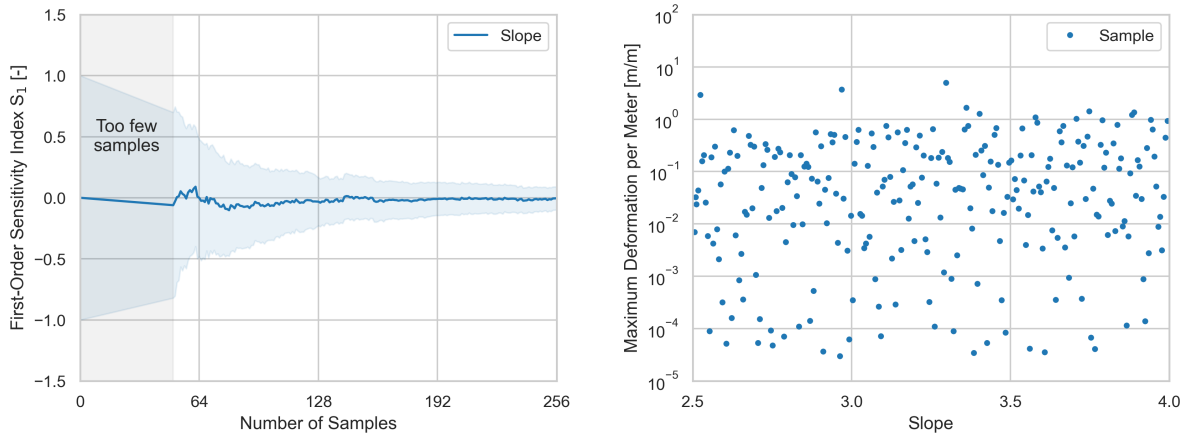

Figure F.6: Convergence plot (left) and sensitivity plot (right) for the slope

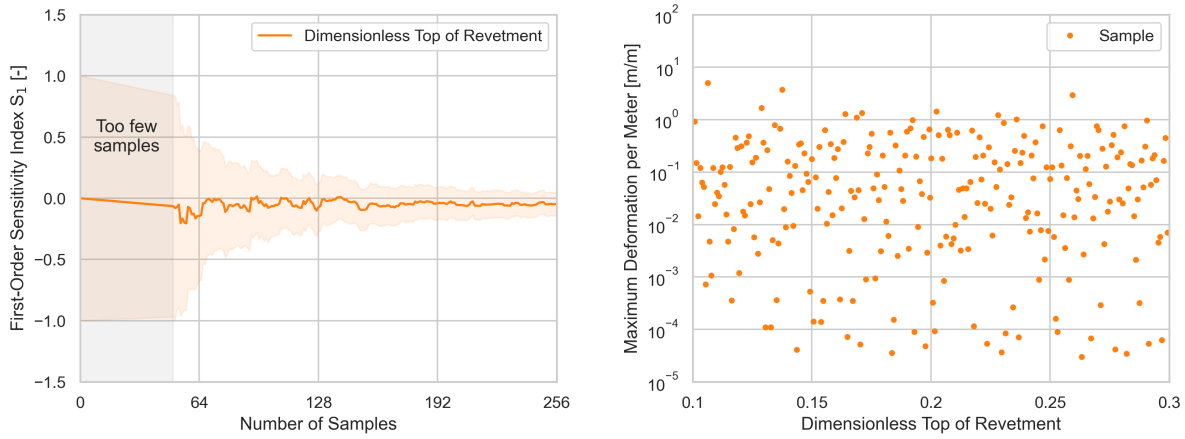

Figure F.7: Convergence plot (left) and sensitivity plot (right) for the dimensionless top of the revetment

F.2. Response Surfaces

For the assessment of the response surfaces, the score function of SciKit-Learn is used. This function assess the fit based upon the Equation F.1, in which u is defined as the residual sum of squares and v is defined as the total sum of squared (Pedregosa et al., 2011). The best possible score is 1.

$$R^2 = 1 - \frac{u}{v} \tag{F.1}$$

The fitted surfaces in Chapter 6 have the scores presented in Table F.1.

Surface	Score R^2
No Damage	0.68
Deformation (S-profile)	0.65
Reduced Clamping	0.65
Missing Elements	0.73

Table F.1: Scores of the response surface fits

The response surface models and the training data is available on the GitHub of the author: https://github.com/nielsvandervegt/mscthesis/tree/main/DamageModels